Laser 3D printing of Diamond-based Composite Materials for Thermal Management Applications

Loic Constantin

THÈSE EN COTUTELLE PRÉSENTÉE

POUR OBTENIR LE GRADE DE

DOCTEUR DE L'UNIVERSITÉ DE BORDEAUX ET DE L'UNIVERSITÉ DE NEBRASKA LINCOLN

ÉCOLE DOCTORALE UBX

SPÉCIALITÉ : Physico-Chimie de la Matière Condensée

ÉCOLE DOCTORALE DE UNL

SPÉCIALITÉ : Génie Electrique

Par Loic Constantin

IMPRESSION 3D DE MULTI-MATERIAUX A BASE DE DIAMANT POUR LA GESTION THERMIQUE

Sous la direction de Dr. Jean-François Silvain
Et Pr. Yong Feng Lu

Soutenue le 1er juillet 2020

Membres du jury :

M. Maglione, Mario, Directeur institut, ICMCB,	Président
Mme. Brunet, Véronique, Maitre de Conférence Université de Poitiers	Rapporteur
M. Alexander, Denis, Professeur Université de Nebraska-Lincoln	Examinateur
M. Wang, Jian, Maitre de Conférence Université de Nebraska-Lincoln	Examinateur
Mme Debiemme-Chouvy, Catherine, Directeur de rechercher, CNR	Examinateur
M. Silvain, Jean-François, Directeur de rechercher, CNR	Invité
M. Lu, Yong Feng, Professeur Université de Nebraska-Lincoln	Invité

3D LASER PRINTING OF DIAMOND-BASED COMPOSITES FOR THERMAL MANAGEMENT APPLICATIONS

by

Loic Constantin

A DISSERTATION

Presented to the Faculty of

The Graduate College at the University of Nebraska

and

The Graduate College of the University of Bordeaux, France

In Partial Fulfillment of Requirements

For the Degree of Doctor of Philosophy

Major: Electrical Engineering

Major: Physical-Chemistry of Condensed Matter

Under the Supervision of Professors Yongfeng Lu and Jean-Francois Silvain

Lincoln, Nebraska

July 2020

3D LASER PRINTING OF DIAMOND-BASED COMPOSITES FOR THERMAL MANAGEMENT APPLICATIONS

Loic Constantin, Ph.D.

University of Nebraska Lincoln - University of Bordeaux, 2020

Advisors : Yongfeng Lu and Jean-Francois Silvain

The constant increase of the working frequency of semiconductor-based devices with their miniaturization led to severe overheating, which affect their lifetime and reliability. Hence, thermal management has become a significant concern for the microelectronic area and needs to be addressed. Diamond (D) is known to be an excellent material for thermal dissipation as it possesses one of the highest thermal conductivity (TC) of any natural material and has a high electrical resistivity. D can cool electronic chips in two ways. When used in the form of a film, D acts as a heat spreader. When utilized in powder-form, Ds can be introduced into metals to enhance their TC and bring dimensional stability at elevated temperatures. The resulting metal/D composite materials are thus, excellent component to form heat sinks. Naturally, the thermal performances of heat sinks are closely related to their surface area. Although the attractiveness of D-based materials in term of thermal performance, they often exhibit simple geometry mostly due to the complexity of machining D-based materials into intricated designs. In this study, the laser 3D printing of copper/D composite materials is proposed to fabricate highly complex Cu/D structures which could remodel their applications. Before additively manufactured Cu/D composite materials, several challenges need to be addressed. First, the additive manufacturing of pure Cu is optimized and characterized. Then, due to a lack of a chemical affinity between Cu and D, the Cu-D interfacial zone is introduced in the composite material. Later, a molten salt coating process is studied to produced graded and multilayer coating of oxide/carbide and carbide/carbide, respectively, on carbon materials. Next, the additive manufacturing of highly sophisticated Cu/D composite structures is presented. Finally, the deposition of D films is performed by laser-assisted combustion flame. The effects of introducing ultraviolet lasers into the combustion flame are characterized in terms of chemical reaction and D film quality and growth rate.

IMPRESSION 3D DE MULTI-MATERIAUX A BASE DE DIAMANT POUR LA GESTION THERMIQUE

Loic Constantin, PhD

Université de Nebraska Lincoln- Université de Bordeaux, 2020

Advisors : Yongfeng Lu and Jean-Francois Silvain

L'augmentation de la fréquence de travail des dispositifs à base de semi-conducteurs avec leur miniaturisation a conduit à une surchauffe sévère, qui affecte leur durée de vie et leur fiabilité. Par conséquent, la gestion thermique est devenue une préoccupation importante dans le domaine microélectronique et doit être abordée. Le diamant (D) est connu pour être un excellent matériau pour la dissipation thermique car il possède l'une des conductivités thermiques les plus élevées de tous les matériaux naturels et possède une résistivité électrique élevée. D peut refroidir les puces électroniques de deux manières. Lorsqu'il est utilisé sous forme de film, D agit comme un diffuseur de chaleur. Lorsqu'ils sont utilisés sous forme de poudre, les Ds peuvent être introduits dans les métaux pour améliorer leur conductivités thermiques (TC) et apporter une stabilité dimensionnelle à des températures élevées. Les matériaux composites métal/D résultants sont ainsi d'excellents composants pour former des dissipateurs thermiques. Malgré l'attrait des matériaux à base de D en termes de performances thermiques, ils présentent souvent une géométrie simple, principalement en raison de la complexité d'usiner des matériaux à base de D dans des formes complexes. Dans cette étude, l'impression 3D laser de matériaux composites cuivre/D est proposée pour fabriquer des structures complexes de Cu/D qui pourraient remodeler leurs applications. Premièrement, la fabrication additive de Cu pur est optimisée et caractérisée. Puis, faute d'une affinité chimique entre Cu et D, une interphase est introduite dans le matériau composite. Plus tard, un procédé de revêtement de sel fondu est étudié pour produire un revêtement gradué et multicouche d'oxyde / carbure et de carbure / carbure, respectivement, sur des matériaux carbones. Ensuite, la fabrication additive de structures composites Cu/D est présentée. Enfin, le dépôt des films D est réalisé avec une flamme oxyacétylénique assistée laser. Les effets de l'introduction de lasers ultraviolets dans la flamme sont caractérisés en termes de réaction chimique, de qualité du film D et de taux de croissance.

“The best way to predict the future

is to invent it”

ALAN Kay, 1971

ACKNOWLEDGEMENT

My gratitude goes first to my French and American advisors, Dr. Jean-Francois Silvain from the ICMCB and Prof. Yongfeng Lu from the College of Engineering of the University of Nebraska-Lincoln. They both have been incredibly supportive, patient, and resourceful since the beginning of the program. Thank you very much for your time and your immense contribution to this work, but also for all your support, trust, and help outside of the scientific scope.

I want to thank the Direction General de l'Armement (DGA), for their financial support at the University of Bordeaux and Dr. Bruno Mortaigne. I also would like to thank the director of the ICMCB, Dr. Mario Maglione, for welcoming me to the institute.

I want to thank Professors, Natale Ianno, Dennis Alexander and Jian Wang at the University of Nebraska Lincoln, as well as Dr. Veronique Gauthier from the University of Poitiers, Dr. Catherine Debiemme-Chouvy from La Sorbonne, Prof. Hansang Kwon from the University of Tohoku, and Prof. Jean-Marc Heintz for the University of Bordeaux for being part of my supervisory committee and taking time to judge my thesis.

I also would like to thank Dr. Lisha Fan for the numerous advices, help, and time she provided during all the years. Also, I would like to thank Zhipeng Wu, and Nada Kraiem for their contribution to this work. I want to thank Prof. Jean-Luc Battaglia for his contribution and help on the thermal conductivity measurement and Prof. Bai Cui for providing free access to his labs. I want to thank Prof. Jerome Roger for his help and impact to the work.

I want to thank all my dear colleagues from the University of Nebraska Lincoln, Aofei Mao, Xi Wang, Lei Lu, Peixun Fan, Timothy Carlson, Nan Li, and from the ICMCB, Benjamin Thomas, Mael Pontoreau Clio Azina, Adrien Morvan and Nan Chamroune. Also, I would like to thank Pamela Weise, Laurie Prettyman, and Teresa Ryans, which were always available to answer questions and help.

Finally, I would like to dedicate a special thanks to my family and friends for being present and supportive during this program.

RESUME DES TRAVAUX DE THESE

Les industries et les systèmes de transport reposant sur l'énergie électrique ont connu une croissance rapide depuis les années 1950. Les dispositifs semi-conducteurs représentent le cœur des systèmes électroniques de puissance. Ils permettent de contrôler l'énergie électrique en la distribuant, la générant, la stockant et la convertissant. Ces systèmes se trouvent dans les transports, tels que l'automobile, les chemins de fer et l'aéronautique, et dans les systèmes de production, de conversion et de distribution d'électricité.

Au cours du dernier demi-siècle, des progrès significatifs ont été réalisés pour réduire leurs dimensions du micromètre à l'échelle nanométrique. Une telle miniaturisation permet d'intégrer un grand nombre de puces extrêmement proches les unes des autres, réduisant ainsi la longueur du trajet du signal et contribuant à des fréquences de fonctionnement plus élevées.

Cependant, l'augmentation constante de la puissance électrique et la miniaturisation des appareils ont conduit à des problèmes de gestion thermique dus à des densités de flux de chaleur critiques. Le flux thermique était de 0,5 W/cm^2 dans les années 1980, 40 W/cm^2 dans les années 2000, et atteint maintenant souvent 150 W/cm^2. De plus, la température d'une puce de silicium (Si) par exemple, doit être maintenue en dessous de ~ 150 °C pour éviter l'instabilité et la défaillance. Il apparaît donc que la capacité de refroidir un appareil est essentielle pour déterminer sa durée de vie, sa fiabilité et son efficacité. En effet, plus de la moitié des pannes électroniques sont liées à la surchauffe, tandis que 6%, 19% et 20% sont attribuables à la poussière, à l'humidité et aux vibrations. Par conséquent, la gestion thermique est devenue un des facteurs limitants du développement de la puissance électronique.

Pour répondre à ces défis, nous proposons d'utiliser l'impression laser tridimensionnelle (3D) pour fabriquer des composite Cu/D ainsi que des films de diamant (D). Cette thèse se concentre sur la fabrication de dissipateurs de chaleur à base de D. Les sujets suivants sont traités : 1) la fabrication additive de matériaux Cu et Cu/D et 2) le dépôt de films de D assisté par laser ultraviolet (UV).

Cette thèse résulte d'une collaboration internationale dans le cadre d'un double doctorat. Les deux partenaires sont le laboratoire de nano-ingénierie assistée par laser (LANE), qui fait partie du département de génie électrique et informatique de l'Université du Nebraska-Lincoln (UNL) aux États-Unis et le groupe de recherche sur les composites et la céramique de l'Institute de chimie et de la matière condensée de Bordeaux (ICMCB) à l'Université de Bordeaux (UBX) en France.

La thèse comprend sept chapitres. Dans le chapitre 1, les motivations et le plan de la thèse sont présentés. Dans le chapitre 2, l'état de l'art lié à aux travaux de thèse sont passés en revue. Il a été montré que l'absence d'affinité chimique entre Cu et D se traduit par des liaisons interfaciales faibles et poreuses, conduisant à un mauvais transfert thermique. L'importance d'avoir une liaison interfaciale robuste est discutée. Il est montré qu’une interphase chimique joue un rôle crucial dans les propriétés thermiques globales des composites.

Par la suite, les méthodes de fabrication et de production de composite métalliques sont discutées. Il est montré que seules des géométries simples sont possible avec les méthodes

conventionnelles et des étapes de post-traitement sont nécessaires pour fabriquer des structures de conception complexe.

Ensuite, des méthodes de fabrication additive assistées par laser sont présentées, telles que la Selective Laser Sintering (SLS), Selective Laser Melting (SLM) et Laser-Directed Energy Deposition (LDED). Les principaux défauts induits dans les matériaux au cours de chacun de ces processus sont présentés ainsi que les phénomènes physiques qui leur sont liés. Enfin, les progrès de l'impression laser 3D de structures complexes pour des applications de gestion thermique sont revus.

Au chapitre 3, la fabrication additive de Cu pur par les procédés SLM est décrite. Dans cette étude, des pièces fonctionnelles en Cu sont imprimées. Une enquête sur les paramètres d'impression est effectuée pour optimiser la qualité d'impression et comprendre les mécanismes de formation. Ensuite, des dissipateurs thermiques en Cu avec diverses conceptions structurelles sont fabriqués en utilisant les paramètres d'impression optimisés. Leurs propriétés physiques et leurs performances thermiques sont étudiées. Les dissipateurs de chaleur présentent une conductivité thermique de 368 W/m.K. Les performances thermiques des dissipateurs thermiques imprimés sont ensuite comparées à celles du commerce en étudiant leur capacité de refroidir une puce électronique. Il est montré que les dissipateurs thermiques imprimés avec des structure complexes surpassent de 45% la dissipation thermique du dissipateur du commerce (**Figure 1**).

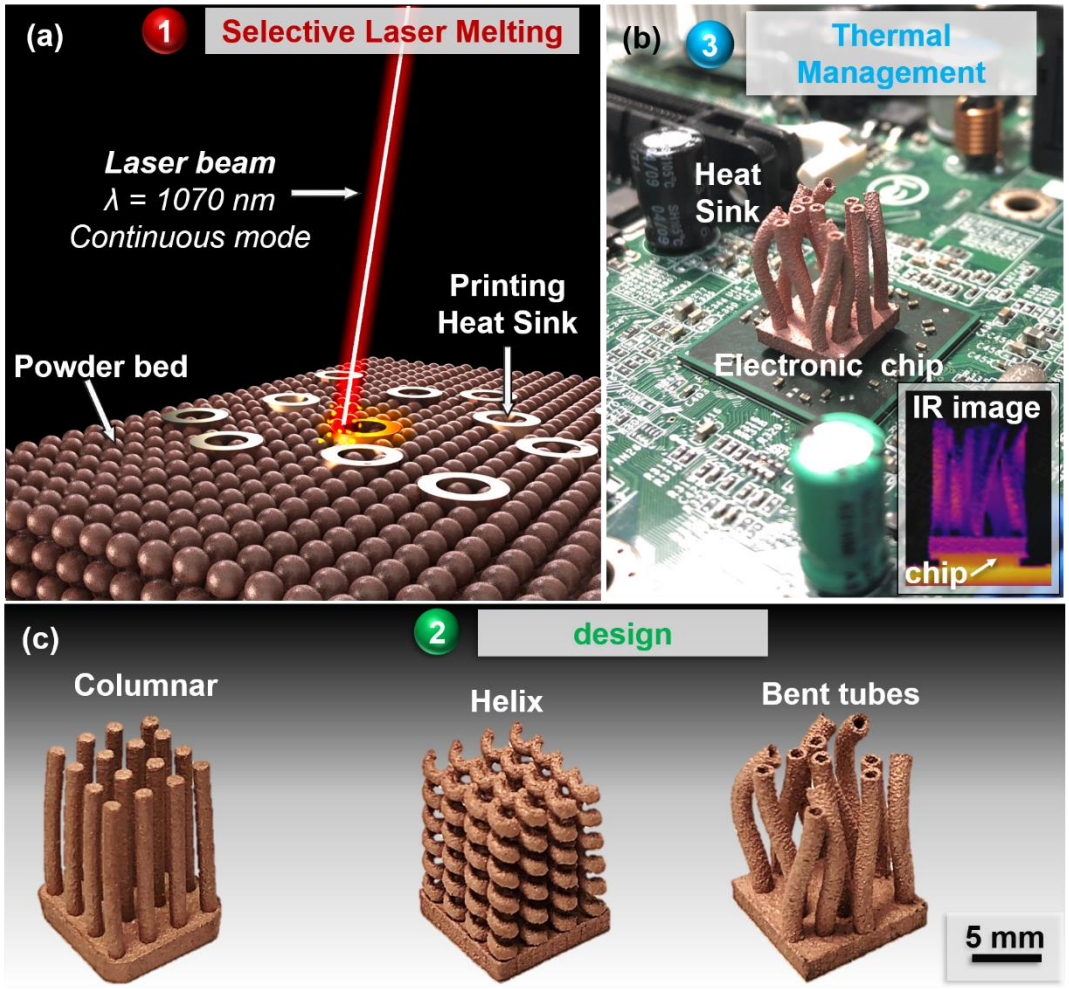

Figure 1. (a) Illustration du processus SLM pour imprimer des dissipateurs de chaleur en Cu, **(b)** photo d'un dissipateur de chaleur imprimé sur une puce électronique avec une image thermique dans l'insert, et **(c)** photos de trois dissipateurs de chaleur imprimées avec des forme complexe : colonnes, hélices, tubes coudés.

Au chapitre 4, des revêtements TiO_y-TiC_x sont synthétisés sur des fibres de carbone (CFs). Le revêtement de carbure riche en oxyde présente une mouillabilité significativement améliorée avec le Cu liquide par rapport aux couches riches en carbure. Notamment, l'angle de mouillage pour les échantillons TiO_y-TiC_x-CF préparés à 800 ºC est

de ~ 80 ° ± 5 ° avec une couverture de surface en Cu de ~ 50% contre ~ 115 ° et ~ 10% pour ceux des échantillons TiC_x-CF préparés à 950 ºC (**Figure 2**).

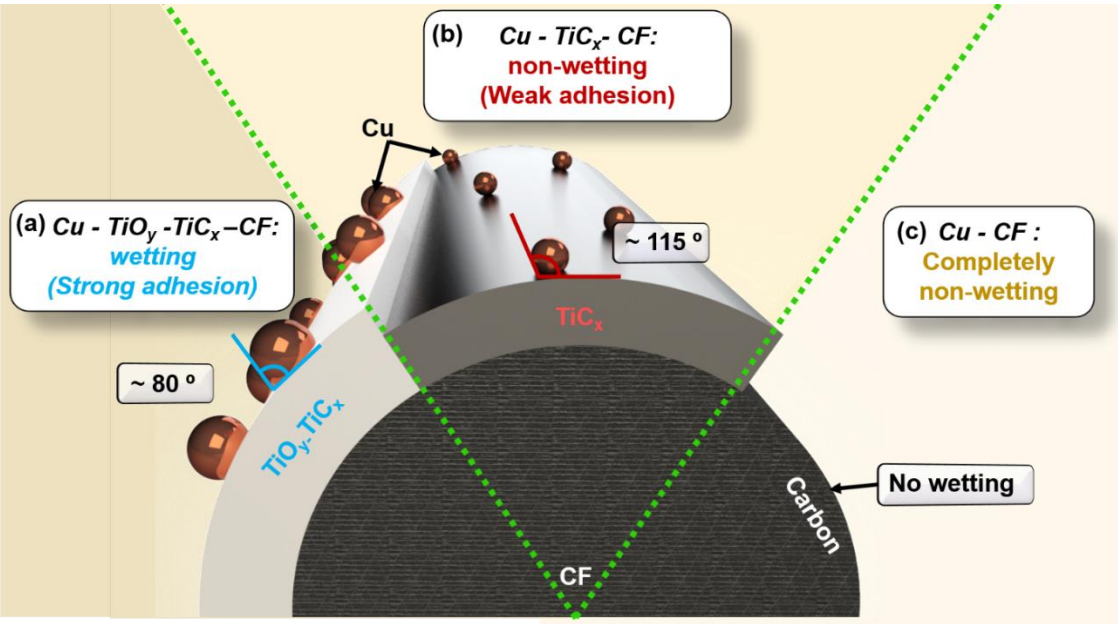

Figure 2. Illustration du mouillage de Cu sur les CF avec différentes interphases : **(a)** TiOy-TiCx, **(b)** TiCx et **(c)** CF.

Par la suite, en faisant varier la température (800 à 950 ºC) et la durée (1 à 5 h) de réaction mais aussi en utilisant une trempe thermique, les mécanismes de formation du dépôt de TiO_y-TiC_x sont étudiés. Les résultats indiquent un processus en trois étapes : 1) une courte période d'induction contrôlée par une dissolution rapide du Ti dans le sel fondu, 2) un transport de masse rapide du Ti dans le sel fondu et une réaction rapide aux surfaces des CFs, et 3) un transport de masse à travers la couche de revêtement contrôlée par une compétition de diffusions Ti et C (**Figure 3**).

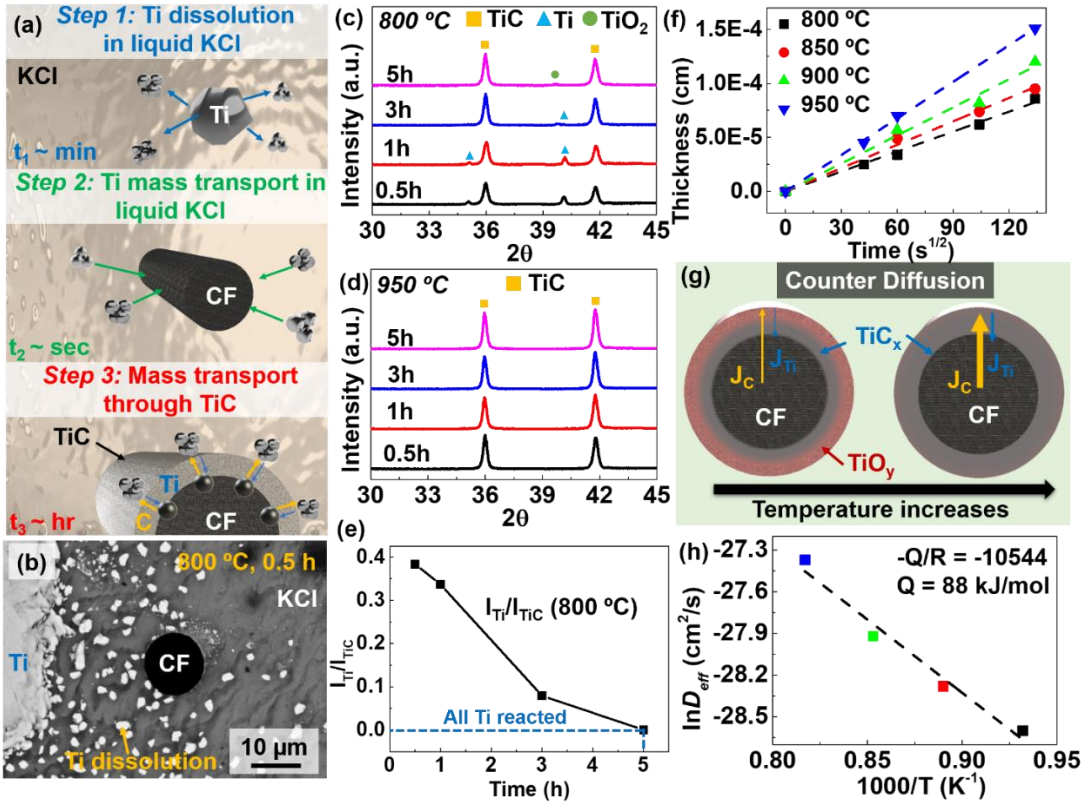

Figure 3. (a) Schéma des trois étapes principales d'un processus de revêtement au sel fondu, **(b)** Micrographies SEM de sel rapidement trempé à 800 ºC pendant 0,5 h, diffractogrammes XRD des CF lavés pour des temps de revêtement allant de 0,5 à 5 h à **(c)** 800 ºC et **(d)** 950 ºC, et **(e)** rapport ITi / ITiC XRD en fonction du temps de revêtement. **(f)** Épaisseur du revêtement en fonction de la racine carrée du temps pour différentes températures de revêtement ; **(g)** représentation schématique de l'effet de la température sur la couche revêtue de TiOy-TiCx gradué ; **(h)** Graphique d'Arrhenius du logarithme naturel de Deff en fonction de l'inverse de la température de revêtement ;

Enfin, les couches de TiO_2-TiC graduées développées sur CFs sont appliquées sur des particules D. On montre que des résultats similaires sont obtenus. Une couche de TiO_2 se forme sur les surfaces D. On constate que la concentration d'oxyde de Ti est liée à la

température du revêtement. Une température de revêtement plus basse conduit à une diffusion plus faible du réactif résultant en un revêtement partiellement oxydé. Le revêtement à base de Ti sera utilisé plus tard dans l'impression 3D laser de matériaux composites Cu/D.

Dans le chapitre 5, les effets des stratégies d'impression ; fusion unique, redéposition et refusion sont comparés en termes de qualité du lit de poudre, de densité des pièces et de microstructure pour impression 3D laser de composites Cu/D. Il est montré que la présence de D influence la dynamique du bain de fusion pendant le SLM, générant une grande quantité d'éjections. Plus tard, il est montré que les projections perturbent l'homogénéité du lit de poudre et conduit à la formation de matériaux composites poreux. De plus, la faible absorption laser du Cu provoque une réflexion du faisceau laser importante et limite la vitesse de balayage du laser à un minimum de 200 mm/s. Pour obtenir un matériau composite dense, les stratégies de redéposition et de refusion sont introduites pendant le SLM. Il est montré que seulement la refusion réduit l'éjection de poudres en supprimant les défauts d'impression. Ainsi des composites Cu/D denses (~ 96%) sont fabriqués. Enfin, des structures complexes en 3D sont imprimées pour des applications de gestion thermique (**Figure 4**). Des nids d'abeilles en Cu/D avec différents obturations et structures D sont fabriqués.

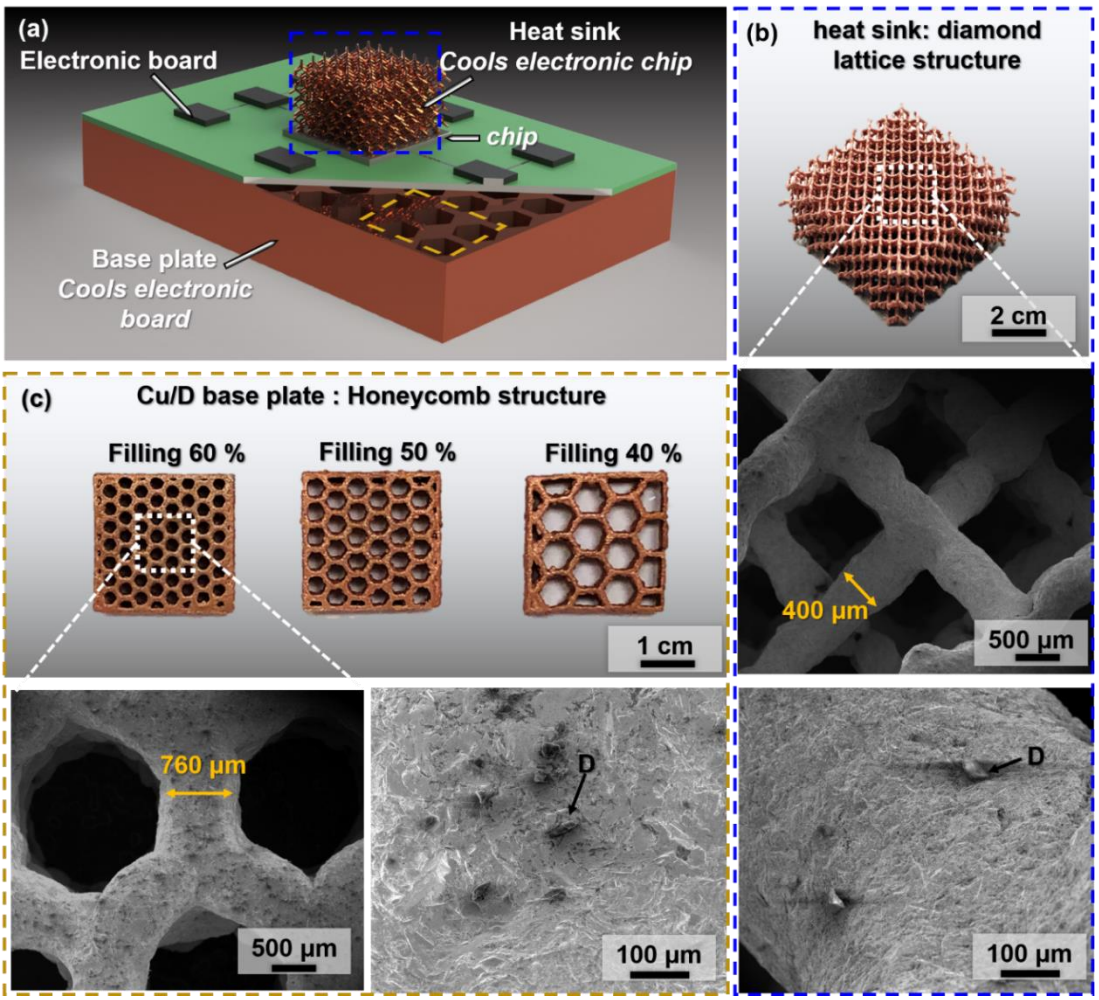

Figure 4. (a) Conductivité thermique des composites Cu/D imprimés avec les stratégies de fusion unique, redéposition et refusion. **(b)** illustration de composites Cu/D pour des applications microélectroniques, **(c)** photographie et micrographies SEM d'une structure D, et **(d)** structures en nid d'abeille.

Dans le chapitre 6, l'influence de la photolyse induite par laser UV sur la croissance de D est étudiée. L'Optical Emission Spectroscopy (OES) et la Laser-induced Fluorescence (LIF) de la flamme indiquent que la photolyse induite par laser UV produisait de grandes quantités de radicaux réactifs. Ces réactifs contribuent directement à la promotion de la croissance D. L'étude du processus de nucléation suggère que l'irradiation au laser excimère KrF modifie la croissance du diamant de manière à favoriser la formation de

diamant et à supprimer l'accumulation de carbone amorphe. Cela conduit donc à un taux de dépôt de diamant amélioré et à une qualité de diamant améliorée (**Figure 5**). De plus, la couche de transition est réduite de 700 nm sans laser à 5 nm avec irradiation laser UV.

Finalement, dans le chapitre 7, les travaux de thèse sont résumé suivi de future axes de recherche.

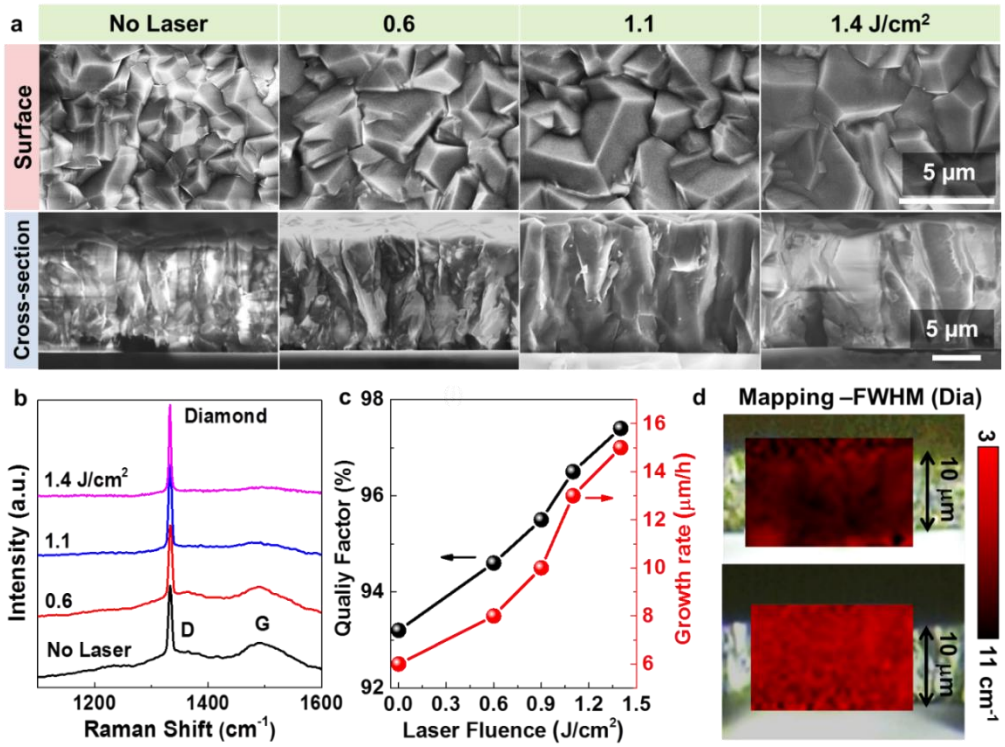

Figure 5 (a) Micrographies SEM de la surface et des morphologies en coupe transversale des films D déposés sans et avec irradiation laser excimère KrF à différentes fluences laser et 35 Hz. **(b)** Spectres Raman des films D correspondants. **(c)** Le taux de croissance et le facteur de qualité du film en tant que fonctions de la fluence laser. **(d)** Cartographie Raman du pic D demi-maximum pleine largeur (FWHM) des films D préparés (haut) sans et (bas) avec irradiation laser KrF excimer à 1,4 J / cm^2.

TABLE OF CONTENTS

TABLE OF FIGURES AND TABLES

1 Motivations and Outline

1.1 Motivations

Industries and transportation systems relying on electrical energy and power electronics have undergone rapid growth since the 1950s.[1] Acting as electrical energy converters, semiconductor devices represent the heart of power electronics systems. They enable the change of an electrical current from direct to alternating and modification of the potential and the current intensity. Hence, semiconductor devices allow electrical energy to be controlled by distributing, generating, storing, and converting it. These systems are found in transportation, such as automotive, railway, and aeronautics, and in electrical production, conversion, and distribution systems.

In the past half-century, significant progress has been made to reduce devices from microscale to nanoscale; and the aim of future technology is to reach sizes below ten nanometers.[2] Such miniaturization will permit a large number of chips to be integrated extremely close to each other, thereby reducing the signal path length and contributing to higher operating frequencies.[3,4] Hence, increasing the density of transistors and other integrated circuits (ICs) will enhance their performance. In 1958, Gordon E. Moore, the co-founder of Intel, noticed that the number of transistors per IC doubled every two years. He predicted that the trend would continue for decades. This is known as Moore's law and has been the driving force for miniaturization and the performance improvement of IC devices.[5] In 2003, Moore mentioned that the exponential increase in the component number would eventually reach saturation.[6]

On the other hand, the constant increase in the electrical power and miniaturization of devices has led to thermal management issues due to critical heat flux densities. Heat flux was 0.5 W/cm^2 in the 1980s, 40 W/cm^2 in the 2000s, and now often reaches 150 W/cm^2.[7,8] Moreover, the temperature of a silicon (Si) chip for example, must be maintained below ~150 °C to avoid instability and failure.[9] It thus appears that the capacity to cool a device to maintain a relatively low temperature is critical to determining its lifetime, reliability, and efficiency. Indeed, more than half of electronic failures are related to overheating, while 6%, 19%, and 20% are from dust, moisture, and vibration, respectively.[7] Consequently, thermal management has become the important limiting factor in further development of power electronics.

In power electronic modules, various substrate materials are attached to the chip to conduct and dissipate the heat. As shown in **Figure 1.1-1**, the chip is mounted on a ceramic substrate to insulate the module and limit electrical losses. The module is then connected to a copper (Cu) base plate and heat sink allowing the heat produced to dissipate.[10] The heat dissipation capability of the package is restricted to its thermal resistance, in other words, the sum of the thermal resistance of each component.[11] Thus, the thermophysical properties of each part need to be carefully analyzed to preserve their reliability. A significant concern is the formation of thermomechanical stress between two adjacent layers due to thermal expansion mismatches (coefficients of thermal expansion (CTEs)). If a significant CTE difference between two materials is introduced, tensile or compressive stresses are generated upon thermal cycling, affecting the mechanical integrity of the package and, potentially, eventual failure.[12]

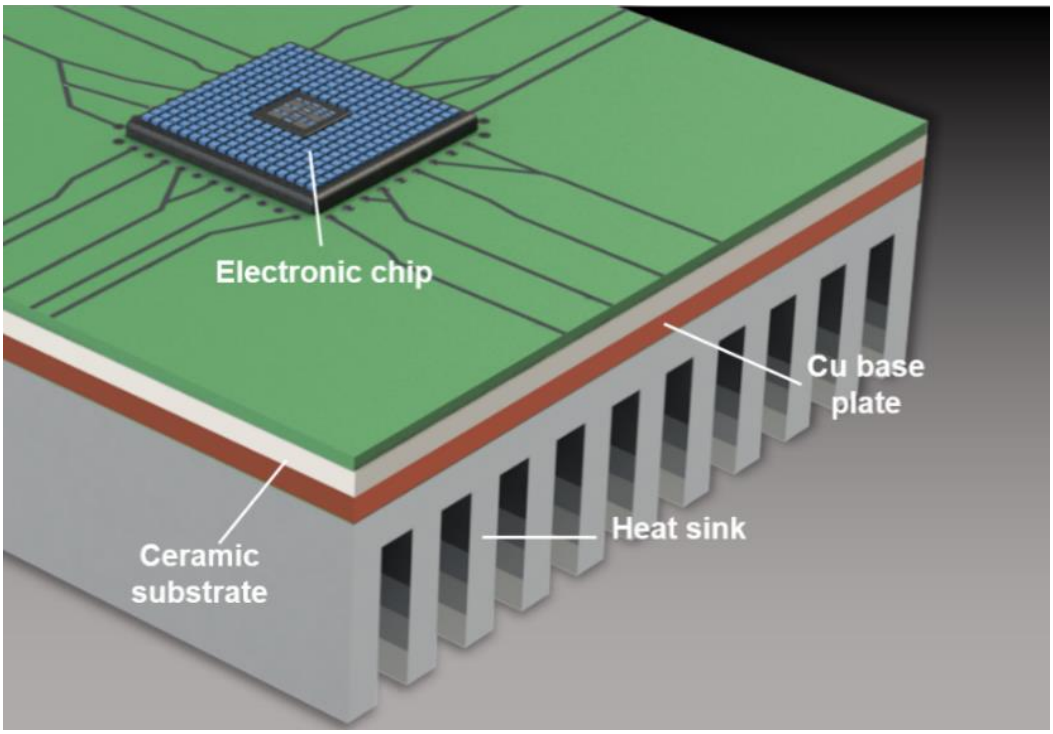

Figure 1.1-1 Illustration of a multichip power electronics module.

Cooling can be divided into two main categories: passive and active. A passive cooling system consists of a natural convection and conduction process. On the other hand, active cooling involves forced convection.[7,13] Cooling devices are usually made of highly thermally conductive materials with tailored CTEs. Copper metal matrix composites (MMCs) are among the most advanced materials for thermal management applications. Diamond (D) is often used as a reinforcement in the MMCs due to its high thermal coefficient (TC) (up to 2000 W/m.K) and low CTE (0.8 $x10^{-6}$/K).[14] Copper/diamond composite materials have demonstrated exceptionally high TC with low CTE and show promise for applications in thermal management.[10,11] However, the presence of D particles makes it difficult to machine these materials into complex geometries withdraw their applications as heat sinks. Additionally, D is an excellent candidate for use as an insulating layer in electronic packaging due to its unique thermal properties and high electrical

resistivity.[15] Often D films are grown by chemical vapor deposition (CVD), but either the growth rate or crystallinity of the film is altered.[16]

To answer these challenges, we proposed using three-dimensional (3D) laser printing to fabricate intricate Cu/D composite designs. In addition, laser-assisted CVD of D film is intended to grow high-quality D films in a relatively short time frame. This dissertation focuses on the fabrication of D-based heat sinks and heat spreader materials. The following topics are covered: 1) additive manufacturing of Cu and Cu/D composites and 2) ultraviolet (UV) laser-assisted D film deposition.

1.2 Overview of the dual Ph.D. program

This thesis results from an international collaboration in the framework of a dual Ph.D. program. The two partners are the Laser-Assisted Nano-Engineering (LANE) lab, part of the Department of Electrical and Computer Engineering at the University of Nebraska-Lincoln (UNL) in the U.S. and the Composite and Ceramics research group at the Institute of Condensed Matter Chemistry of Bordeaux (ICMCB) at the University of Bordeaux (UBX) in France.

My work in the U.S. and France concerned 3D laser printing of Cu/D composites, processing of graded and multilayer coatings on carbon-based materials for Cu/D composites, and deposition of diamond films. The supervisors for these research activities were Professor Yongfeng Lu at UNL and Professor Jean-François Silvain at ICMCB/UBX. This four-year program was divided into two years in the U.S. and two years in France, as shown in **Figure 1.2-1**.

Figure 1.2-1 Schedule for the four-year dual Ph.D. program.

1.3 Dissertation outline

The most significant contributions of this dissertation carried out at the LANE lab at UNL and ICMCB at UBX are:

1. Development of a selective laser sintering (SLS) technology to print dense, crack-free Cu structures.
2. Fabrication of complex Cu heat sink structures via selective laser melting (SLM) with high heat-dissipation performance.
3. Development of an innovative coating process for carbon-based materials.
4. Investigation of the kinetics of a molten-salt process to form carbide coatings.
5. Synthesis of a new titanium (Ti)-based coating for Cu/D composite via a molten-salt process.
6. Single-step deposition of multilayer carbide coatings on carbon-based materials via the molten-salt process.

7. Investigation of different printing technologies (laser direct energy deposition (LDED) and SLM) and optimization of printing parameters for manufacturing Cu/D composites
8. Development of UV laser-assisted CVD for diamond deposition.
9. Understanding the influence of the UV laser wavelength on diamond growth and quality.

The dissertation includes seven chapters. In Chapter 1, the motivations and the dissertation outline are presented. In Chapter 2, the state of the art related to this work and background information is reviewed. In Chapter 3, the additive manufacturing of pure Cu by the SLS and SLM processes is described, including the effect of the printing parameters. In Chapter 4, the development of a Ti-based coating on carbon fibers and D particles is shown as well as the synthesis of multilayer carbide coating on carbon fibers. In Chapter 5, LDED and SLM of Cu/D composite materials is presented along with the fabrication of intricate designs. In Chapter 6, the deposition of diamond films by laser-assisted CVD is presented with an emphasis on the effect of the UV laser wavelength on D growth. Finally, Chapter 7 is a summary of the work followed by future research directions.

2. State of the art

2.1 Introduction

The constant increase in power and packing densities in power electronic devices has led to heat dissipation issues. Significant demand for developing efficient heat-dissipating materials with high TC and a low CTE has appeared over the past decades.[17] To answer this demand, it is necessary to fabricate materials compatible with electronic chips to ensure the reliability of the power modules. Metal matrix composites have long been studied because they offer the possibility of combining the properties of two or more components resulting in hybrid properties (i.e., low CTE and high TC). Among the large number of MMCs, Cu is the most advanced matrix for composites in thermal management applications (i.e., base plate, heat sink, and exchanger). On the other hand, carbon (C) materials, such as carbon fibers (CFs), D, graphene, or carbon nanotubes (CNTs), are often added to the Cu matrix because of their high TCs and low CTEs. Copper/carbon composite materials have already demonstrated their superior properties compared to current electronic packaging. Lower and tailorable CTEs have been observed depending on the volume fraction of the reinforcement (e.g., CTE decreases when C concentration increases). High heat dissipation capability has been shown to surpass commercial heat exchangers.[18,19] Moreover, depending on the reinforcement nature (i.e., fibers or particles), anisotropic CTEs and TCs can be achieved.

In this chapter, the synthesis methods and properties of diamond materials are discussed, as they are an essential constituent of this work. Then, the current state-of-the-art Cu/D MMCs for thermal management are reviewed. Additionally, the remaining challenges associated with these materials are presented, such as the creation of a chemical bond

between the Cu and the D and the difficulty of manufacturing sophisticated Cu/D material structures. Finally, additive manufacturing processes are introduced as a potential alternative to current synthesis methods.

2.2 Synthesis of diamond and properties

Diamond has fascinated humankind for thousands of years because of its stunning beauty and was first used as a gemstone. Later, a growing interest among the scientific community appeared due to its outstanding properties. Diamond is a unique material in the sense that it combines extreme hardness and wear resistance, high thermal conductivity and electrical resistivity, low coefficient of thermal expansion, chemical inertness, and high optical transparency. Its excellent properties make it attractive for numerous applications, such as drilling and cutting, optics, heat sinks, and electronic packaging.[20]

2.2.1 Diamond synthesis

Catalytic high-pressure and high-temperature diamond

The catalytic high-pressure and high-temperature (HPHT) approach is the most advanced method of producing a large quantity of synthetic D powders. This method consists of applying high pressure (5 to 7 GPa) and temperature (1300 to 2000 ºC) to high-purity graphite powders. The graphite-to-diamond conversion is assured by adding transition metals (e.g., iron (Fe), nickel (Ni), cobalt (Co), manganese (Mn)), which serve as solvents and catalyzers. At high temperature, the molten metal dissolves the graphite; then, under high pressure, homogenous nucleation of D particles occurs.[21] The growth of nuclei into D powders is then governed by the diffusion of C atoms across the molten metal.

Often, cubic, cubo-octahedral, or octahedral D are obtained. Their sizes can go from micrometric up to centimeter depending on the time and conditions of the HPHT process.[20]

Chemical vapor deposition

Chemical vapor deposition differs from the HPHT method mainly because D is synthesized at low pressure (atmospheric) and low temperature (> 1000 ºC). In the CVD method, the reaction is driven by a chemical reaction in a gas phase. The nucleation and growth of D occurs on a substrate.[20] The gas mixture is usually composed of hydrogen (H), oxygen (O), and hydrocarbons (e.g., ethylene (C_2H_4), acetylene (C_2H_2)).[22] The decomposition of hydrocarbons into reactive species (e.g., -CH_2-) allows the epitaxial growth of sp^3 and sp^2 carbon species. Later, H and O etch the nondiamond-bonded species and eliminate the incorporation of impurities.[23]

Many CVD systems have been developed over the past decades, such as hot filament, plasma jet assisted, microwave, and combustion flame.[24,25] The CVD deposition of D is a competition between growth rate and D quality. Among the CVD systems, combustion synthesis was studied extensively due to its fast growth rate (up to 60 μm/h), as illustrated in **Figure 2.2-1(a)**.[25] In this process, molecules undergo different excitations, such as translations, rotations vibrations, and electronic excitations. Laser-assisted combustion synthesis was introduced to enhance D quality while maintaining or improving the growth rate. Molecular vibrations are in the infrared (IR) range; and hence, by shining an IR laser through the torch, vibrational energy can be selectively provided to reactive species. The laser-assisted combustion of D was demonstrated using a carbon dioxide (CO_2) laser. It was shown that the vibrational excitation of C_2H_4 can be achieved in a combustion flame, as shown in **Figure 2.2-1(b)**.[26–29] The laser wavelength needs to precisely match the

vibrational modes of molecules i.e., 10.532 μm for C_2H_4. In addition, the D growth rate and quality were both improved. Notably, a 10% enhancement of the D quality was reported with a growth rate three times faster.[10,30]

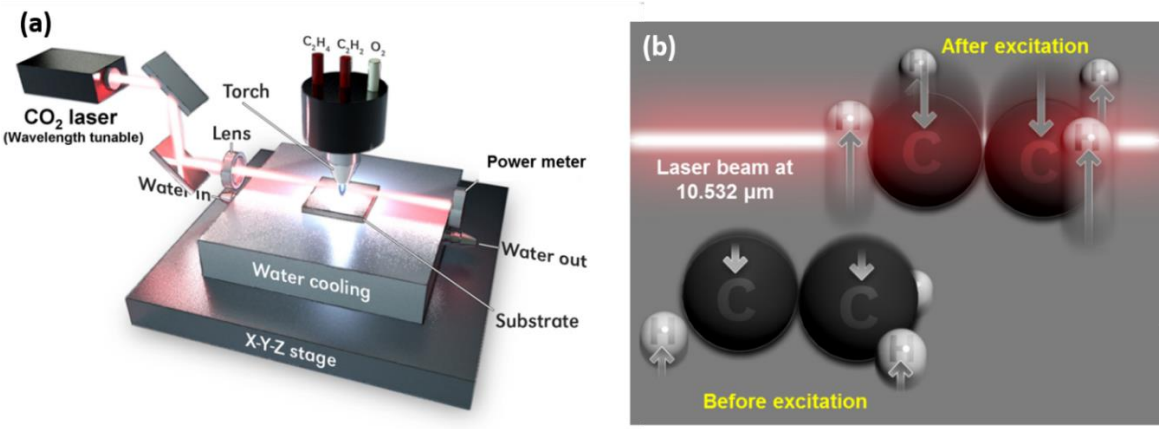

Figure 2.2-1 Illustration of **(a)** the combustion flame setup and **(b)** IR laser vibrational excitation of C_2H_4 molecules.[10]

2.2.2 Mechanical and thermal properties

Mechanical properties

It is well known that diamond is the hardest natural material with a ten on the Mohs hardness scale (1 to 10). This property is essential due to its high atomic packing density (1.77×10^{23} atoms/cm^3). This stunning hardness makes it an excellent material as a protective coating against wear. Also, D has a high Young's modulus with a value of about 1050 GPa, approximatively fives time superior to that of steel. Its high modulus also signifies that it has low compressibility and a Poisson's ratio of 0.07.[20]

Thermal properties

In addition to its mechanical properties, D has the highest thermal conductivity of any natural material, making it the predominant material in thermal management applications. The thermal conductivity of high-purity D can go as high as 2200 W/m.K at room temperature, which is more than five times that of pure Cu (400 W/m.K). This remarkably high thermal conductivity results from strong covalent bonding and low phonon scattering. However, this value was measured on a pure D crystal. Synthetic D films exhibit thermal conductivities between 300 and 700 W/m.K (**Figure 2.2-2**).[31–33] The lower thermal conductivity of D films compared to the pure single crystal is essentially due to the presence of impurities, grain boundaries (polycrystalline films), and crystallographic defects (dislocations, twin boundaries). Phonons carry heat in the D crystal lattice and are scattered in multiple directions due to the presence of defects (i.e., impurities, grain boundaries, etc.), resulting in lower thermal conductivity.[34] Note that most of the D films obtained via CVD show a black color, indicating the presence of nondiamond C. Nonetheless, CVD diamonds, with their preferred crystallographic orientation, allow the phonon-free path inside the film structures to be enhanced, making them valuable for thermal management applications in electronics.

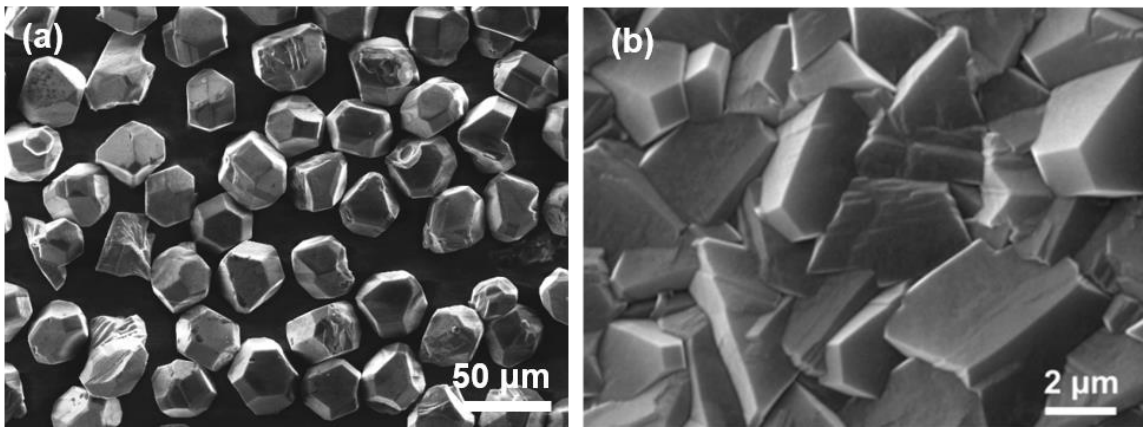

Figure 2.2-2 Scanning electron microscopy (SEM) micrograph of **(a)** D powder and **(b)** CVD diamond film.[10]

Furthermore, D has the lowest heat capacity in nature with a value of 6.19 J/mol.K in a temperature range of ~0 to 800 K, about four times smaller than Cu (24.2 J/mol.K). The low heat capacity of CVD diamond makes it a perfect material for a heat spreader. In other words, a heat sink needs to sustain a large amount of heat while maintaining its temperature (i.e., high heat capacity).[20] However, D has low heat capacity and high thermal conductivity, thus it will spread the heat efficiently when combined with a heat sink.

Finally, D presents a low CTE, from 0.8 x 10^{-6} to 4 x 10^{-6}/K in a temperature range from 300 to 1200 K. The low CTE makes D a desirable material not only for heat spreaders on Si chips (CTE = 2.6 x 10^{-6}/K) but also as reinforcement in MMCs. In general, metals have high CTEs (< 10 x 10^{-6}/K), causing the metal heat sink to peel off from electronic chips after multiple cycles (on and off cycle, heating, and cooling). Thus, using D as a reinforcement could lower the CTEs of MMCs and increase their thermal conductivity.[20]

2.3 Copper/diamond composites

Copper provides an efficient way to remove heat in microelectronics because of its high TC. However, the CTE mismatches between Cu (17 x 10^{-6}/K) and ceramics substrates (4-9 x 10^{-6}/K) leads to delamination, which causes electronic components to overheat. The fabrication of components with high TC, low CTE, and intricate shapes is thus crucial for the development of highly efficient heat-exchanging components for microelectronic industries.[35,36] Creating a composite material consisting of two highly thermally conductive elements, such as Cu and D, may fulfill these unmet needs.[37] However, the lack of chemical affinity between Cu and D, together with the difficulty of mechanically processing D-based materials into complex shapes, presents significant challenges.[38,39]

2.3.1 Cu/D, a nonreactive system

A reactive system is defined as the assembly of two chemically active phases. In other words, the two components can react with each other. However, Cu and C are a nonreactive system. This means that there is no chemical affinity and almost no solubility leading to a high wetting angle (~145º).[40] Several studies report low TCs (> 230 W/m.K) for Cu/D composites. The degradation of the TC is due to the weak affinity between Cu and D and the creation of pores at the interface, as shown in **Figure 2.3-1**. Thus, the synthesis of the interphase between the Cu and C reinforcement is essential to achieve high thermal conductivity.[41,42]

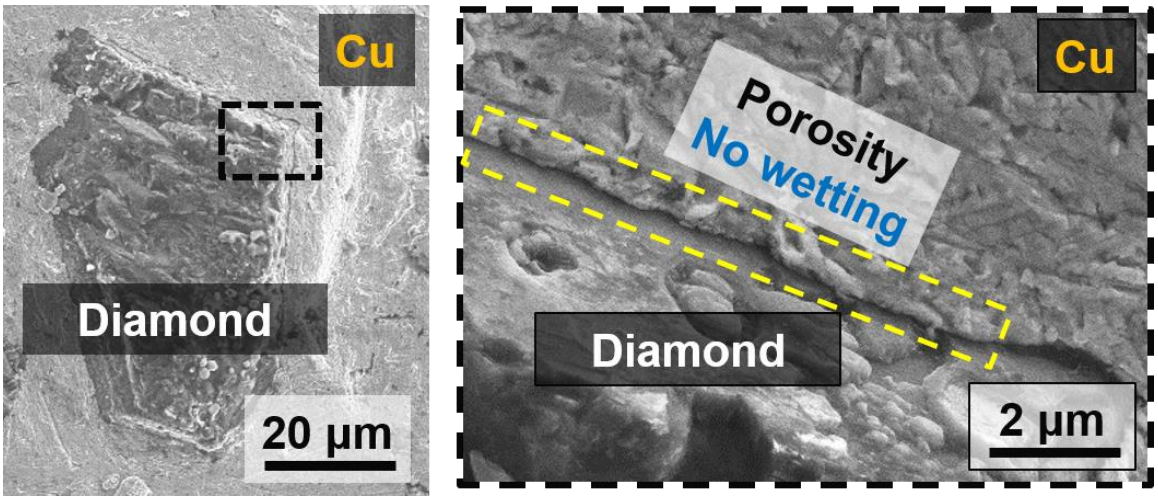

Figure 2.3-1 SEM micrographs of the Cu-D interface.

2.3.2 In situ formation of the interphase between Cu and D

Adding an alloying element was considered to improve the wettability of Cu and C during the sintering of the composite materials. Mortimer et al. studied the wettability of Cu and Cu alloys on C and showed improvement in the contact angle compared to pure Cu.[43] Notably, the alloying element reacted with the C substrate and formed a carbide layer, permitting the formation of chemical bonds.[43] A. Veillère et al. demonstrated that the addition of chromium (Cr) into a Cu and C powder mixture led to the creation of chromium carbide (Cr_3C_2) at the interphase after an annealing step.[44] Others reported on liquid sintering, which consists of adding an alloying element having a lower melting point than Cu, and thus turning it into a liquid during the sintering process. [45] The liquid-phase sintering of Cu/C composites containing a small amount of alloying element, molybdenum (Mo), tungsten (W), or Ti, showed the formation of carbide interphases between the Cu and C reinforcement.[45] However, the properties were severely degraded due to inhomogeneous dispersion of the alloying elements at the interfaces. In addition, traces of

alloying elements remained in the Cu matrix, resulting in a lower TC compared to that of pure Cu.

2.3.3 Ex situ formation of interphases for Cu/D composites

Another approach is to coat the D or C reinforcements before the sintering step. Multiple processes were studied, such as sputtering, microdeposition, or molten-salt synthesis. Liu et al. studied the formation of molybdenum carbide (Mo_2C) and titanium carbide (TiC) via a molten-salt process on carbon fibers (CFs).[46] They demonstrated the fabrication of a homogenously coated layer. Next, the manufacturing of Cu/CF composite was performed via spark plasma sintering (SPS). The TC of the Cu/CF without interphase was measured to be 206 W/m.K. However, with Mo_2C and TiC, the TC increased up to 290 and 297 W/m.K, respectively. Li et al. manufactured Cu/D composites via a gas pressure infiltration with a Ti-based coating on D particles. A TC of 716 W/m.K was achieved with a D volume fraction of 65 vol.% and a size of about 70 μm.[47] Kang et al. demonstrated the deposition of Cr_3C_2 on D particles via a molten-salt process. The resulting Cu/D prepared by vacuum pressure infiltration containing 65 vol.% of D (70 μm) exhibited a thermal conductivity of 562 W/m.K.[48] Interphase is thus vital to achieving highly thermally conductive Cu/D composites.

2.3.4 Fabrication of Cu/D composites

A large variety of processes have been used to fabricate MMCs, which can be divided into solid and liquid manufacturing. The conventional fabrication of MMCs uses powder metallurgy, which is a solid process. In this method, the densification is realized by sintering. Multiple metallurgy methods have been developed, depending on the heating

sources, such as hot pressing ((HP), induction coil), SPS (electric current in the material), or microwave sintering (microwave). In all of these methods, the powder mixtures are densified at a temperature lower than the melting point and under high pressure (uniaxial), as illustrated in **Figure 2.3-2**. The pressure enhances the powder packing density and creates dislocations in the metal powders, helping the densification. In these methods, the powders are placed into a mold (usually graphite). Thus, the mold design defines the final shape of the MMCs. The geometry is usually simple (i.e., cubes, cylinder) to obtain a homogenous pressure during the sintering. Subtractive manufacturing is widely employed to fabricate more sophisticated shapes.[10]

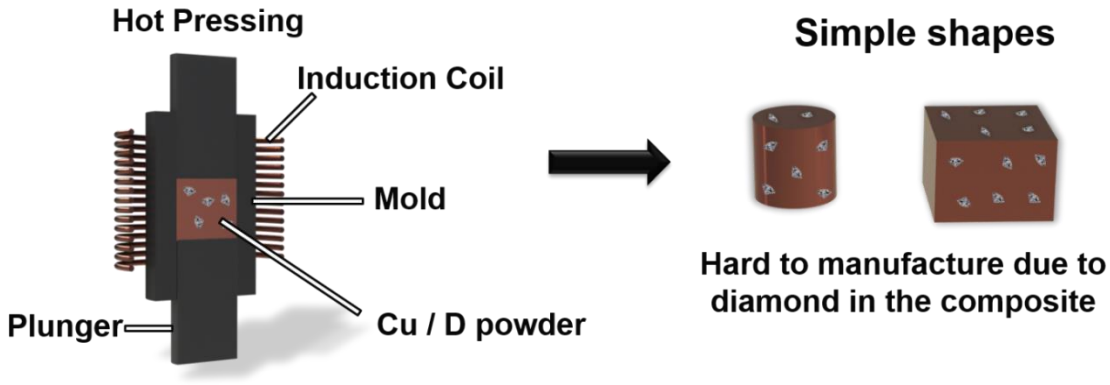

Figure 2.3-2 Illustration of the powder metallurgy route (e.g., uniaxial hot pressing).

Metal matrix composites can also be manufactured via liquid processes, such as stir casting or infiltration. In stir casting, the metal powders containing the reinforcement are totally melted and poured into a mold. However, due to the density difference between the two components, heterogeneous dispersion of the reinforcement may occur. In the infiltration process, a preform made of reinforcement is fabricated first using binders. Then a liquid metal is infiltrated into the preform via capillarity force and/or pressure. Nevertheless, contamination from the binders may remain in the materials. Once again, the

shape of the MMCs is limited by the shape of the mold. Hence, the manufacturing of complex shapes remains challenging; and a new process needs to be developed.[14,36]

2.4 Laser-assisted additive manufacturing: an overview

Additive manufacturing (AM), or 3D printing, was conceptualized back in the 1970s by David E.H. Jones in a paper published in the *New Scientist* journal and quickly developed for polymer materials.[49] In the 1980s, the concept of using a laser as a heat source to fuse powders was introduced on polymer powders. But it was only in the late 1990s that the research on AM of metals via laser sintering and melting started. Later in the 2000s, 3D printing of metals matured; and commercial printers became available.[50] Since the start of 3D printing back in the 1970s, a large selection of materials have been 3D printed (polymers, metals, ceramics, and composites) using different technologies (selective laser melting or sintering, direct energy deposition, etc.).

2.4.1 Selective laser sintering/melting

Selective laser sintering or melting refers to a powder bed technology. In this technique, the powders are added layer upon layer, as illustrated in **Figure 2.4-1**.[50] First, a thin powder layer is deposited onto the working area. Then, the laser selectively melts or sinters the powders into the designed shape. Next, the build plate is lowered; and a new layer is deposited. By repeating the process several times, complex 3D objects can be manufactured. Also, the printing chamber is filled with shielding gas to prevent oxidation of the metallic powders during the laser-matter interactions. The design of the 3D part is done using CAD software, which is then sliced into a print file and loaded into the printer.

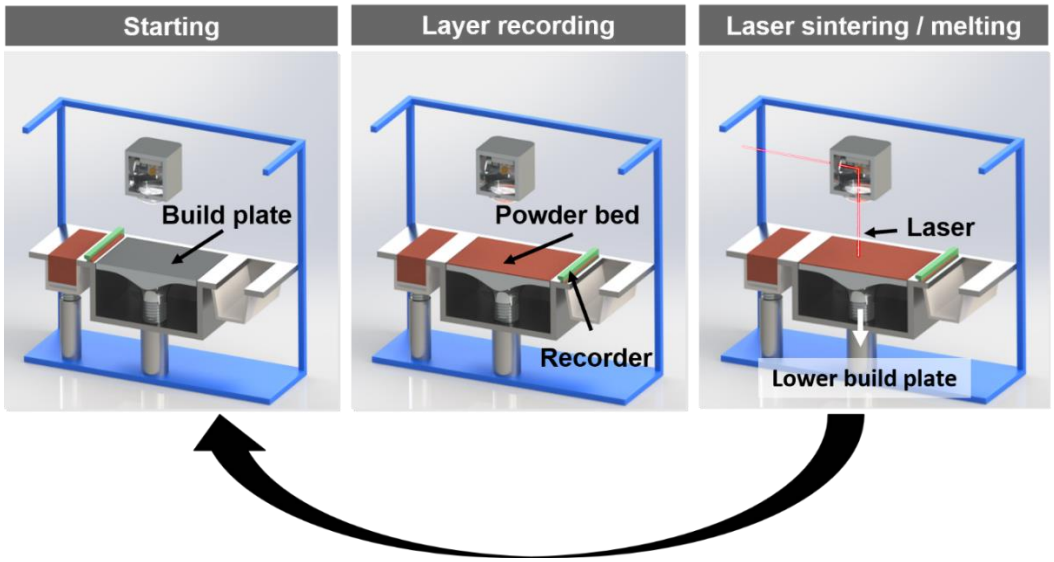

Figure 2.4-1 Illustration of the SLM/SLS processes.

In SLS, the laser beam lasts a few milliseconds on powder particles, which implies that the sintering time is too short to obtain a dense material.[51,52] One solution is to decrease the particle size, which leads to a faster sintering rate (i.e., lowering the surface area is the driving force of sintering). Also, small particles provide higher surface areas and increase laser absorption energy, working temperature, and, thus, sintering kinetics. However, when the size is too small, particles form agglomerates; and the high surface-to-volume ratio is lost.[53] Another solution to overcome this issue is liquid phase sintering. In this sintering process, a second component (called a binder) with a lower melting point than the main component is added in the powder bed. Due to the lower melting point, the binder liquifies during the pass of the laser. Then metal powders are embedded in the binder, and a dense part is obtained.[54]

The densification by liquid sintering can be divided into three steps: 1) when the liquid phase appears, there is a rapid bonding due to the capillary forces exerted on the liquid,

called the rearrangement; 2) densification by solution reprecipitation, and 3) solid sintering which causes further densification. Steps 2 and 3 occur by atomic diffusion and, thus, require time to occur. In the SLS process, due to a short laser-matter interaction time, only the rearrangement plays a significant role. During laser sintering, the liquid flows and fills the pores between the metal particles and cools down to form a solid.[55]

In SLM, however, the metal powders melt to form a transit pool of the molten material which induces several phenomena.[56] During the laser-matter interactions, a spheroidal molten pool is created in a few milliseconds. The presence of liquid metal induces the presence of a plasma jet or plume (i.e., metal vapor) above the molten pool. This gas generates a recoil pressure on the molten pool, which can induce spatter ejection. In addition, a temperature gradient forms inside the pool due to the temperature gradient between the center and the edges. A metal flow from the hot to the cold area arises in the pool, called the Marangoni effect.[57,58] The pool dynamic is thus a significant parameter when considering the printing of dense and smooth structures. In addition, the metal viscosity and surface tension of the liquid metal with the surrounding atmosphere and metal parts plays a vital role in the pool stability and is discussed in the next section.[59,60]

Printing defects are the major limitation of 3D laser printing technologies (i.e., SLS and SLM) as they degrade the properties of the printed part. When the laser strikes the powders, it locally heats them and induces the creation of a thermal gradient. The top layers (hot) tend to expand, while the bottom layers (colder) restrict this expansion.[61] This results in compressive stresses on the top layer and may cause plastic deformation. Later, when the material cools down, those stresses are converted into tensile stresses and may induce cracks.[62] Varying the laser scan strategy plays a crucial role in the distribution of heat and

thermal stresses.[50] Balling is ubiquitous in SLM and is due to insufficient wettability with the previous layers and to the molten metal surface tension. The formation of ball-like metallic powders can aggregate in subsequent layers and cause defects on the powder bed.[56] Finally, the porosity is one of the most critical issues, both in SLM and SLS. Pores often lead to a degradation in physical properties. They are classed into two categories: 1) powder-induced—during atomization of the powders, gas can be trapped into them and released during the process, leading to the formation of spherical pores; and 2) process-induced—if the applied energy is not enough to melt the metal (lack of fusion) or if the energy is too high, spatter ejection phenomena appear (keyhole formation).[63] The formation of process-induced porosity is related to the printing parameters. Thus, it is essential to optimize the printing parameters and understand how defects are formed. By using an optimal set of parameters, the density of the material can reach 99% of the theoretical density.[64,65]

2.4.2 Laser-directed energy deposition

Another common laser-assisted AM is LDED. In this AM technology, the laser melts the powders as in SLM; but the part is built by melting a surface (build plate) and simultaneously applying the metal powder, as shown in **Figure 2.4-2**. The powders are blown through a nozzle, encounter the laser, melt, and deposit.[66] Cracks, porosity, and balling are the significant defects in LDED, similar to SLM. The advantage of LDED over powder-bed technology is that LDED provides a faster building rate and larger building volumes. However, the surface finish is not as neat as that in powder-bed technology; and post-AM processing is often necessary. This technology is commonly used to coat and repair parts via cladding.[67]

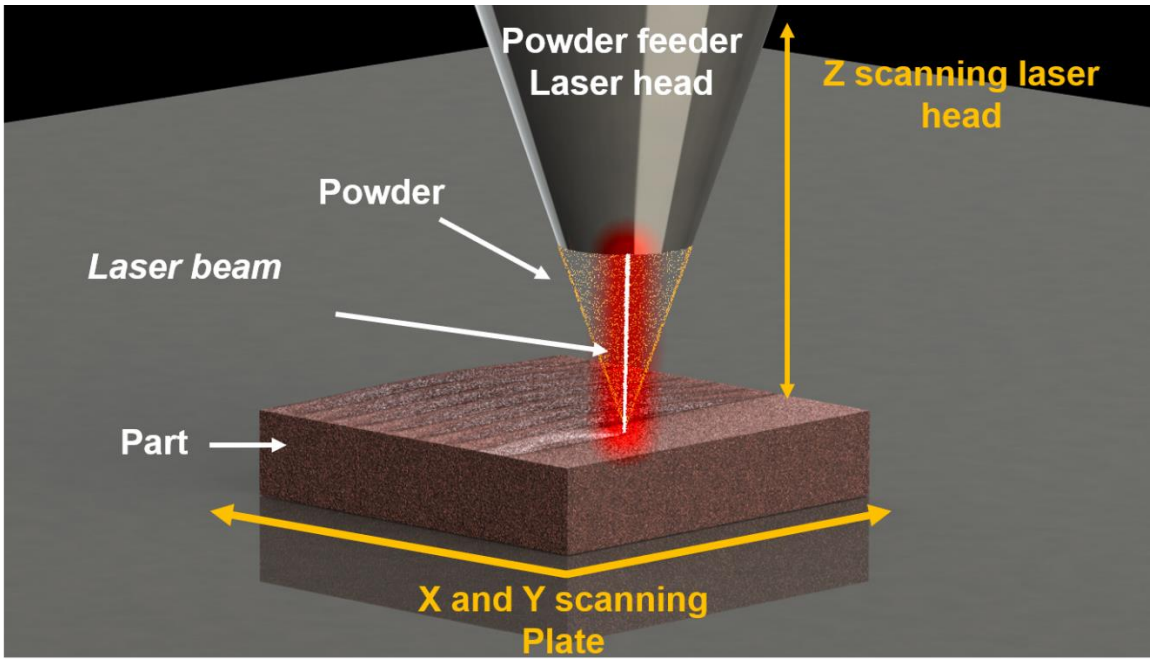

Figure 2.4-2 Illustration of LDED.

2.4.3 Wettability and viscosity

Wetting is a crucial aspect of the AM of metal parts. The wettability of a solid by a liquid is related to the surface tension of the liquid-solid, solid, vapor, and liquid-vapor interfaces.

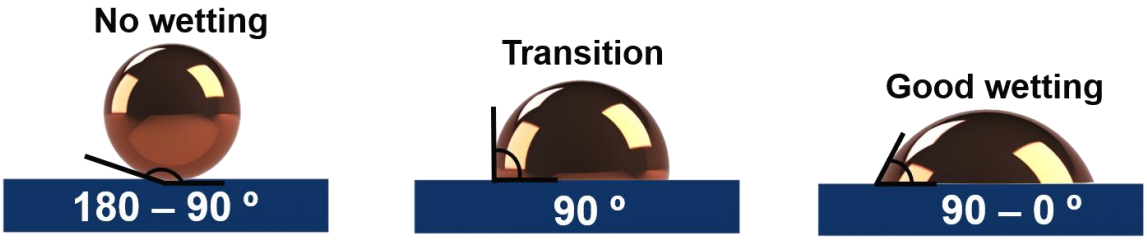

Figure 2.4-3 Illustration of the different wetting behaviors.

Wettability is defined by a contact angle θ, as can be seen in **Figure 2.4-3**, where an angle higher than 90° indicates a nonwetting behavior and lower than 90° indicates good wetting between the components. Wettability is expressed as a function of the surface tension of each phase by the following equation.[68]

$$\cos\theta = \frac{\gamma_{SV}-\gamma_{SL}}{\gamma_{LV}}, \quad \textbf{(1)}$$

where γ_{SV}, γ_{SL}, and γ_{LV} are the surface tension between solid-vapor, solid-liquid, and liquid-vapor, respectively. The surface tension depends on the temperature and can be expressed, in the case of Cu powders, as [69]

$$\gamma = 1330 - 0.23(T - 1085), \quad \textbf{(2)}$$

In SLM and LDED, the wettability between a solid and a liquid is influenced by the viscosity (i.e., temperature), the shielding gas, and the presence of impurities.[68] The viscosity of the molten pool is another significant concern in AM. The viscosity of the liquid phase must be low enough for it to flow and fuse with the surrounding particles but high enough to avoid the balling effect (i.e., surface tension). The viscosity of molten metal can be expressed by[70]

$$\mu = \mu_0\left(1 - \frac{1-\varphi_L}{\varphi_m}\right), \quad \textbf{(3)}$$

where μ_0 is the base viscosity and includes a temperature term, φ_L is the volume fraction of the liquid phase, and φ_m is the critical volume fraction of solids above which the mixture has an infinite viscosity. If the metal is totally liquid, the dynamic viscosity of the liquid is defined by the following equation.[69]

$$\mu = \frac{16}{15}\sqrt{\frac{m}{kT}}\gamma, \quad \textbf{(4)}$$

where m is the atomic mass, k is the Boltzmann constant, T is the temperature, and γ is the surface tension of the liquid. As can be seen in the previous equations, the viscosity decreases when the working temperature increases; thus, rheological properties are enhanced. During 3D laser printing, the laser power, scan speed, and layer thickness will influence the temperature of the molten metal and thus affect the rheological properties.

2.4.4 Laser absorption by metallic powders

Laser-matter interactions are an essential parameter in AM for the determination of the processing parameters, such as laser wavelength, power, and scan speed. Two primary mechanisms of light absorption are possible in the case of metal powders. The first is called multiphoton ionization and involves the simultaneous absorption of multiple photons by electrons, which then are ejected from the conduction band (wavelength lower than 1 μm). The second mechanism is the absorption of laser radiation by free electrons called the photothermal process through inverse bremsstrahlung (e^- (slow) + $h\nu \rightarrow e^-$ (fast)).[71] For most metals, the thermalization time (time to transfer energy to phonons) ranges from 10^{-12} to 10^{-10} s. Thus, if the laser-induced excitation rate is lower than the thermalization rate, the laser energy absorbed is directly transformed into heat. In addition, the laser absorption of metals decreases when the wavelength increases but increases with the temperature.[72]

The mixing law can estimate laser absorption in a powder mixture with an error rate of 10% using the absorbance of each component and its volume fraction, as expressed in the following equation.

$$A = A_1.\gamma_1 + A_2.\gamma_2, \quad \textbf{(5)}$$

where A_i and γ_i are, respectively, the absorptance and the volume fraction of component i, respectively.

2.4.5 Additive manufacturing of complex structures for thermal management applications

The ability to manufacture highly complex shapes is revolutionizing many industries, such as the defense, aerospace, and medical industries.[73] Much research has been conducted on the fabrication of thin, sophisticated lattice structures made of Ti and aluminum (Al) alloys and steel, [74–77] as shown in **Figure 2.4-4**. Lattice structures are studied extensively for their unique mechanical, thermal, and acoustic properties but also for their lightweight and high energy absorption.[78] This type of structure has applications in numerous areas and presents significant advantages for heat dissipation applications (i.e., high surface aspect).

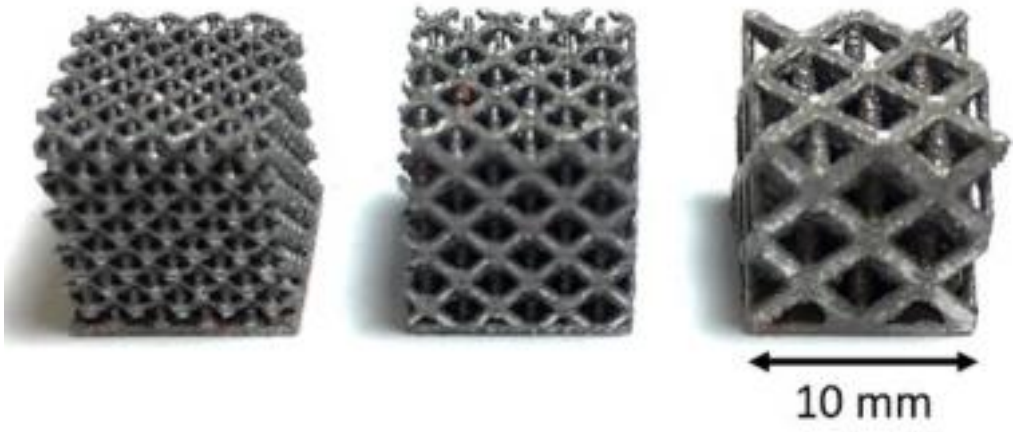

Figure 2.4-4 Photograph of aluminum silicon (Al-Si) 10 mg lattice structures, reported by K.K Wong et al.[77]

Few reports study the potential of using SLM to manufacture complex heat dissipaters, as shown in **Figure 2.4-5**. Heat sinks with different arrays and lattice structures were printed.[79] The high surface ratio provided by the intricate lattice structure enhances the thermal dissipation performance compared to commercial types of array heat sinks. M. Wong et al. showed that a diamond lattice structure heat sink enhances thermal dissipation by more than 60% compared to an array heat sink.[80] Yet, the printed parts are made of low thermal conductivity metals and alloys, such as steel, Ti, and Al alloys.[36,79,81] The additive manufacturing of high TC materials presents several challenges due to their excellent thermal dissipation and often low laser absorption in the near-infrared (NIR) domain.

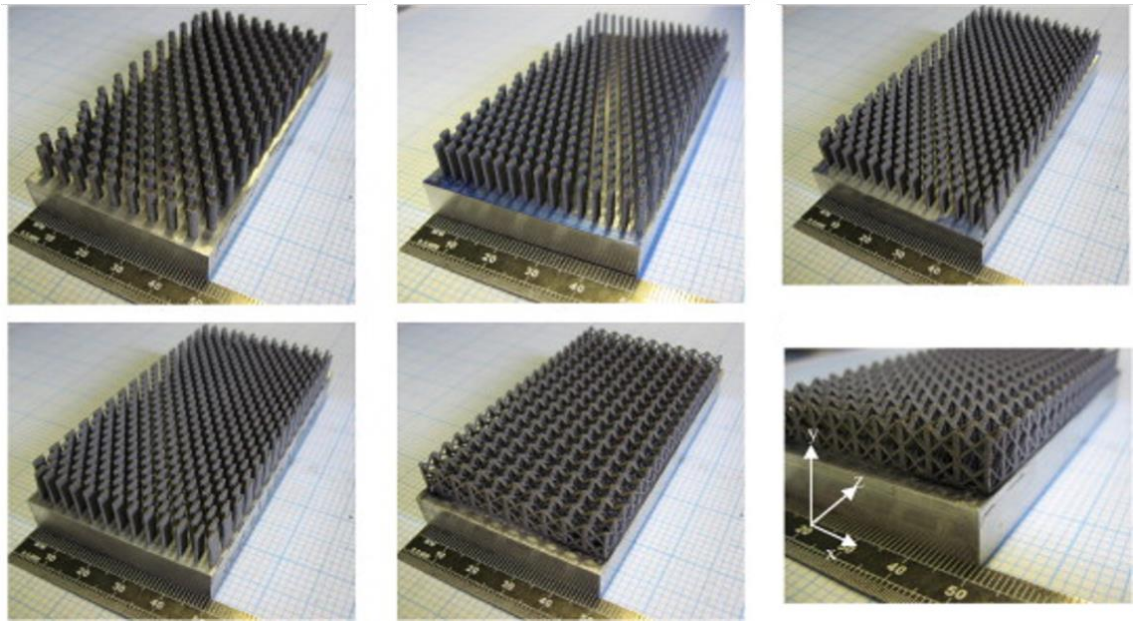

Figure 2.4-5 Photographs of 3D-printed heat sinks made of Al-Si10Mg, by M Wong et al.[66]

There are difficulties with laser-assisted AM of Cu due to its high thermal conductivity and low laser absorption in the IR domain (> 5 % at $\lambda = 1$ μm).[82] Over the last few years,

attempts were undertaken to 3D laser print Cu parts. Reports show that high laser power is necessary to densify the powder during the SLM process.[83–86] SD Jadhav et al. reported the manufacturing of dense Cu parts (98%) using a laser power of 800 W (λ = 1080 nm). Yet, they only demonstrated SLM of a simple geometry (i.e., cube).[85] In addition, a part of the laser power was reflected in the laser optics and caused severe damage. Axel Hess et al., studied the 3D laser printing of Cu using two sets of lasers, a green laser (λ = 515 nm) to heat and thus increase the laser absorption of Cu, followed by an IR laser (λ = 1030 nm) which melted the powders.[87] They showed that the use of a green laser improved densification compared to a single IR laser. However, they did not demonstrate the manufacturing of 3D objects. C. Silbernagel et al. studied the SLM of intricate Cu parts using, as shown in **Figure 2.4-6**, a moderated laser power. In this study, a laser power of 200 W was used to print complex Cu coils. However, the low laser power resulted in the fabrication of porous Cu parts (density = 85%). Thus the electrical conductivity (i.e., TC) of the printed part was severely degraded and only reached about 50% of the International Annealed Copper Standard (IACS).[88]

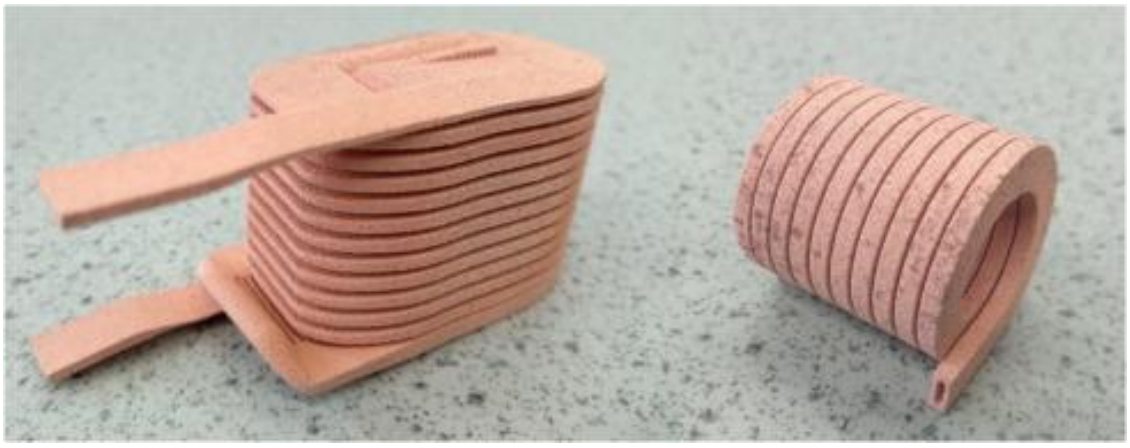

Figure 2.4-6 Photograph of Cu coil printed by C. Silbernagel et al.[88]

2.5 Conclusions

The objective of manufacturing a heat dissipater for microelectronics is to obtain a material with a low CTE and high TC. Diamond-based materials are an excellent choice due to their unique thermal properties as a polycrystalline film or reinforcement in a metal matrix.

Diamond CVD has a low CTE and heat capacity and high TC. Thus, it is an excellent material for use as a heat spreader when combined with a heat sink. Also, the simplicity, fast growth rate, and cost-effectiveness of using a combustion flame to synthesize D films make it an ideal method for producing heat spreaders. However, the presence of defects during the D growth degrades the thermal properties of the films. Using a laser-assisted combustion flame to grow D appears to be a promising way to improve D quality while maintaining a fast growth rate.

It has been shown that the absence of chemical affinity between Cu and D results in weak and porous interfacial bonds, leading to poor thermal transfer. The importance of having robust interfacial bonding plays a crucial role in the overall thermal properties of the composites. Therefore, it is necessary to produce a chemical bond between the Cu and D reinforcement through interphase. Different carbide interphases and synthesis methods were reviewed, such as MO_2C, TiC, and Cr_3C_2, and made in situ and ex situ. In addition, coating the C reinforcement before the Cu/D manufacturing allows homogenously coated layers to be produced and avoids the inclusion of impurities in the Cu matrix. The manufacturing method of producing MMCs was discussed, such as solid and liquid syntheses. However, it was shown that only simple MMC geometries have been built; and post-processing steps are necessary to fabricate intricately designed structures.

Laser-assisted AM methods were presented, such as SLS, SLM, and LDED. The primary defects induced during each of these processes were presented (i.e., cracks, porosity, and balling) as well as the physics phenomena related to them (i.e., thermal gradient, wettability, and viscosity). Finally, progress on the 3D laser printing of complex structures for thermal management applications was presented. It was shown that intricate structures are allowed to increase the surface ratio and thus promote heat dissipation performance but are currently limited to low thermal conductivity materials.

3 Additive Manufacturing of Pure Copper

3.1 Introduction

The high thermal conductivity (TC) (~ 400 W/m.K) of pure Cu makes it an essential material for thermal management applications in numerous industries, such as microelectronics, power plants, and aerospace industry.[14,35,89–91] However, the shape (i.e., surface area) of heat sinks plays a crucial role in heat dissipation, and is often a simple geometry due to the current fabrication limitation.[92,93] Recently, the development of additive manufacturing (AM), such a selective laser sintering or melting (SLS or SLM), has attracted tremendous attention due to its ability to efficiently manufacture geometrically complex metal parts while minimizing wastes and post-processing steps.[86,93] The thin and sophisticated features enabled by AM and the excellent properties of bulk Cu have the potential to significantly enhance the performance of heat sinks components.[36,94]

SLS of metal-based powders uses a laser as the heat source to heat the powders above the softening temperature. In the conventional sintering (CS) process, bonding occurs when the metal particles form interlinked necks through atomic diffusion at elevated temperatures.[95,96] However, solid-state diffusion is a slow process, which is difficult to initiate during SLS due to the very fast heating rates and short sintering times (~milliseconds).[97] To accelerate the binding process, liquid sintering is widely used in SLS by adding a binder that turns to liquid during the sintering.[98,99] Liquid sintering occurs as a result of liquid flow and rearrangement.[100] Many research groups have reported the manufacturing of Cu-based metal parts by SLS using various systems (copper-tin (Cu-Sn), copper-iron (Cu-Fe), copper-tin-nickel (Cu-Sn-Ni)) with properties comparable to those obtained by CS.[101–103] Although fast sintering for fabrication of metals or alloys can be

achieved by adding a binder to the powder mixtures,[104–106] sintering of a single metal remains a challenge due to the necessity of using a large quantity of binders.[107]

More recently, attempts have been undertaken to additively manufacture pure Cu via SLM.[82] Silbernagel et al. and SD Jadlhav et al. studied the fabrication of Cu parts by SLM using low laser powers of 200 and 300 W, respectively.[85,108] Low-density parts (86%) with low TC of 202 W/m.K were reported. The low-density parts resulted from insufficient laser energy deposited on powders due to the fast heat dissipation rate and the low laser absorption by Cu in the near-infrared (IR) range .[87,109] A high laser power (800 W) was employed to overcome this issue, and dense Cu parts were printed (97%) with a TC of 336 W/m.K.[83,84] Nevertheless, the high reflectivity of Cu at this laser wavelength can severely damage the laser sources and optics, leading to high maintenance and operation costs.[85] Another approach is to print Cu alloys that have much stronger absorption at the laser wavelength than pure Cu. Serval studies report the production of fully dense Cu-alloys such as Cu-Cr, Cu-Sn, or Cu-Zn.[110–112] However, a post-processing step is required for the as-built Cu alloys to reach electrical and thermal properties close to those of the bulk Cu.[110,111] Despite these impressive results, SLM of pure Cu, with properties comparable to bulk Cu without post-processing, remains challenging.

This chapter describes the AM of pure Cu using the SLS and SLM technologies. First, a binder-free SLS is developed to fabricate dense, and high-quality Cu parts. For that, a 532 nm Nd:YAG laser is chosen because Cu has a high optical absorptivity (about 40% at 532 nm). Next, the SLM of pure Cu is investigated using an IR fiber laser (λ = 1070 nm) with a moderate power (400 W). Dense, crack-free, and complex shaped heat sinks are fabricated by SLM after optimizing the printing parameters as shown in **Figure 3.1-1**

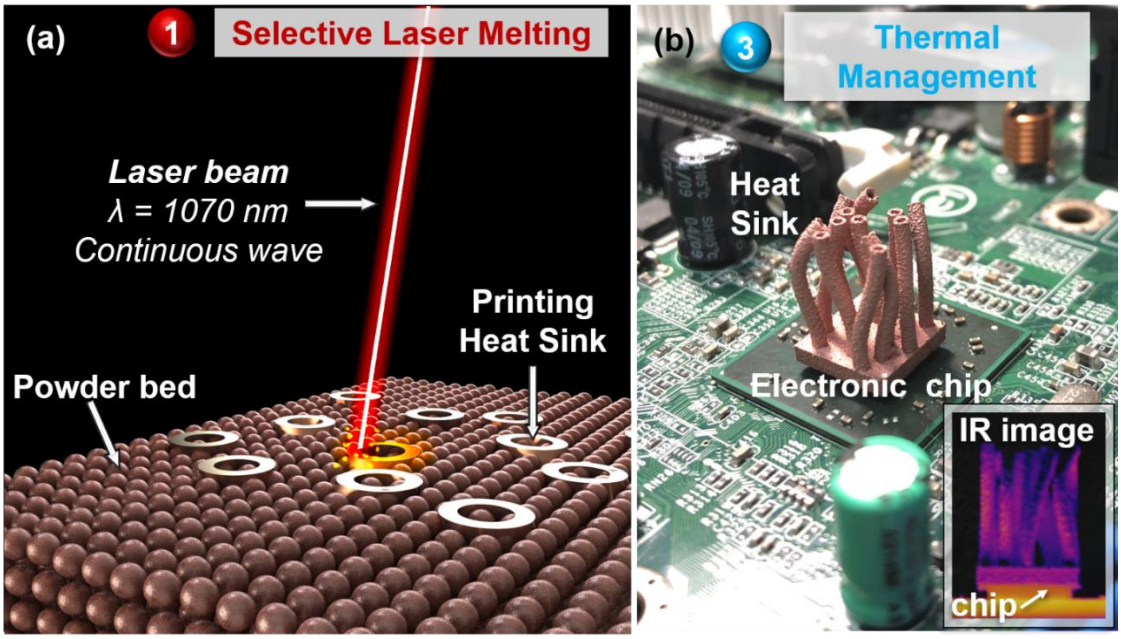

Figure 3.1-1 (a) Schematic illustration of the SLM process to print Cu heat sinks, **(b)** photo of a printed heat sink on an electronic chip with the thermal image in the insert.

3.2 Experimental set-up and procedures

3.2.1 Selective laser sintering (SLS)

Figure 3.2-1 (a) schematically shows the home-built SLS setup used in this work. A continuous-wave (CW) Nd:YAG laser (Coherent Verdi-G Series), with a wavelength of 532 nm and a maximum output power of 5 W, was used as the heat source. An optical objective lens (5× Mitutoyo M Plan Apo) was used to focus the laser beam into a spot with a diameter of 20 µm. A charge-coupled device (CCD) camera was used to monitor the printing process. The Cu powder was placed in a chamber which was filled with nitrogen (N_2) gas on a 3D moving stage with a step resolution of 2.5 µm. The chamber pressure was kept at 130 Pa under a N_2 flux of 10 cm^3/min for all of the experiments. Next, a simple line scanning pattern was used for the SLS. A line spacing of 10 µm (50% overlap) was used

to promote the atomic diffusion on each Cu layer, as illustrated in **Figure 3.2-1 (b)**. The sintering temperature was measured by an infrared camera (FLIR E85 ®) with the emissivity of Cu set as $\varepsilon = 0.07$. It was found that the temperature climbed up quickly to 700 ℃ within 5 s and reached around 780 ℃ after 20 s as shown in **Figure 3.2-1 (c)**.

Spherical Cu powders (Eckart Granulate Velden GmbH, 99% purity) with a diameter of 5 μm were used as the initial raw material. The powder was stored in a glove box to prevent surface oxidation. The Cu powders were cold pressed using a hydraulic press with a pressure of 100 MPa for 5 min. The thickness and the diameter of the prepared disc were about 50 μm and 50 mm, respectively. Scanning electron microscopy ((SEM) XL 30, Philips Electronics) was performed to study the microstructures and the fracture behaviors of the SLS materials. The density of the sintered Cu parts was estimated by measuring their weight and volume. An optical surface profiler (Zygo NewView™ 8300) was used to evaluate the surface roughness. Elements characterization was performed by X-Ray diffraction (XRD) (PANalytical X'pert PRO MPD, λ =1.5405 Å)

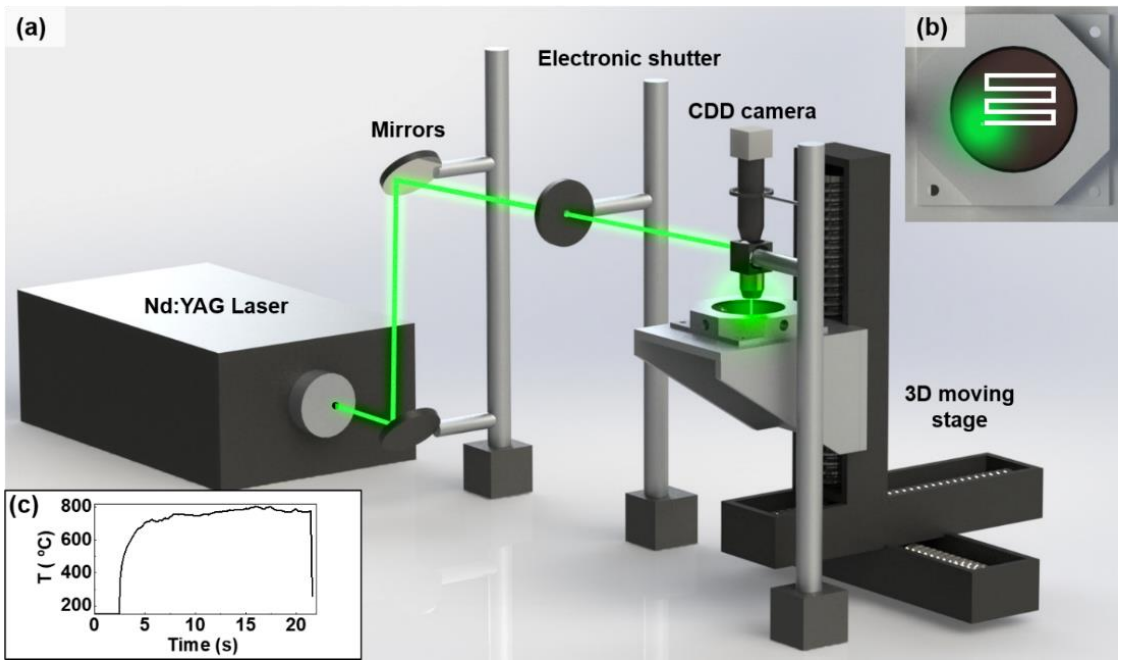

Figure 3.2-1 (a) Schematic of the homemade SLS system, **(b)** line scanning strategy of the laser sintering, and **(c)** temperature profile of the sintering pool.

3.2.2 Selective laser melting (SLM)

Cu parts were fabricated by SLM using an SLM 125® 3D printer (SLM Solutions). The printing parameters are summarized in **Figure 3.2-2 (a)**. The printer is equipped with a CW fiber laser (IPG photonics, YLM, Yb:YAG, λ = 1070 nm). The maximum output power is 400 W with a spot diameter of 70 μm on the powder-bed surface. Spherical Cu powders with an average size of 45 μm were used in this study (US Nano, Cu 99.5%). The size of the powder and dispersity of the powder were determine based on the powder flowability (spherical), bed compaction (high dispersity), and requirements of the SLM 125 printer (10 to 50 μm). A SEM micrograph of the powders is shown in **Figure 3.2-2 (b)**. The powder was stored under agon to prevent surface oxidation. The printing chamber was filled with argon (Ar) (99.9%, Matheson) to reduce an oxygen level below 0.09%. A

constant pressure of 18 mbar was maintained during all experiments. The printing parameters were optimized by adjusting the hatch distance from 0.08 to 0.12 mm, and the scan speed from 200 to 600 mm/s. The laser power and layer thickness were kept constant at 400 W and 0.03 mm, respectively, throughout the study. A stripe scan strategy was used in this study, as illustrated in **Figure 3.2-2 (c).** The structures printed were designed using SolidWork®. Magics® software was used to prepare print jobs and establish the printing parameters. The parts were printed on a stainless-steel building plate (stainless steel, 123 × 123 × 25 mm^3). The density of the samples was measured using the Archimedes method (Mettler Toledo AT201). The microstructure of the printed parts was characterized using an SEM (FEI Quanta 200 Environmental SEM). The cross-sectional views of polished samples were observed using an optical microscope (Nikon Eclipse E600). The average surface roughness was measured using an optical surface profiler (Zygo NewView 8000). The crystalline phases of the powders and parts printed were analyzed by X-Ray diffraction (XRD, Bruker-AXS D8 Discover Diffractometer, Cu Kα = 0.154 nm). Energy dispersive X-Ray (EDX) was performed on the Cu powders and parts using a Helios NanoLab™ 660 equipped with EDAX™ detector. The electrical resistance of the printed material was measured using a four-point probe method (Keithley 2400 Source Meter) with a current ranging from -0.03 to 0.03 A. The thermal conductivity was calculated from the electrical conductivity using the Wiedemann-Franz law. Sample hardness was measured by Vickers hardness test (Wilson Tukon™ 2500-3), using a load and dwell time of 0.5 Kg and 10 s, respectively. The physical properties of the heat sinks printed were compared to a commercial heat sink (Enzotech Mosfet MOS-C10). The thermal-dissipation performances of the printed heat sinks were evaluated by simulating the thermal management situation

of microelectronics using an IR camera (FLIR E85 24º). The heat sinks were attached to an electronic chip with a thermal tape (3M™ 8815 Thermal Tape). Using a hot plate, the memory card and the heat sink were heated to 100, 150, and 200 ºC, respectively, with a fan, which was placed 10 cm above the heat sink for airflow.

(a) Parameters	Values
Spot Size	70 µm
Laser Power	400 W
Scan Speed	200 to 600 mm/s
Hatch Distance	0.08 to 0.12 mm
Layer thickness	30 µm
Powder size	45 µm

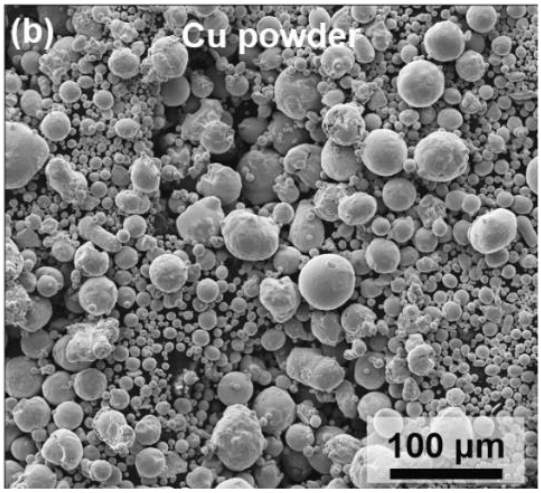

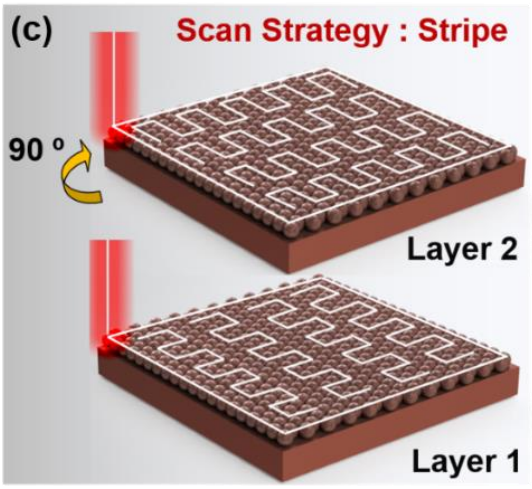

Figure 3.2-2 (a) SLM parameters used in this study, **(b)** SEM micrographs of the copper powders, and **(c)** schematic illustration of the stripe scan strategy.

3.3 Selective laser sintering (SLS) of pure copper

3.3.1 Effect of cold pressed powders in SLS of pure Cu

To enhance the particle contact and thus the surface diffusion, the effect of cold pressing on the SLS process was investigated as illustrate on **Figure 3.3-1**. Both a loosely packed Cu powder bed and a cold-pressed Cu pellet were sintered using an Nd:YAG laser at a constant laser scan speed of 125 µm/s and laser power of 5 W. The density of the loose powder and the cold-pressed pellet were estimated to be about 30 % and 63 %, respectively.

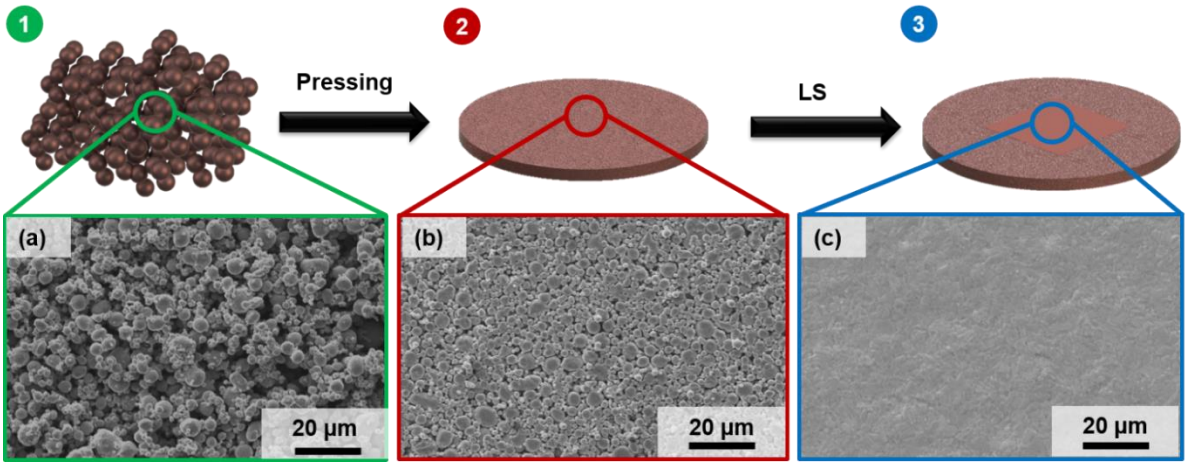

Figure 3.3-1 Powder metallurgy steps to obtain dense Cu parts: **(a)** raw powders, **(b)** after cold pressing, and **(c)** after the SLS process.

Figure 3.3-2 (a) shows the SEM micrographs of parts fabricated from the loose-powder bed and the cold-pressed pellet. The part obtained from the loose-powder bed has a porous surface with discontinuous laser scan tracks and Cu particles, which formed at the surface. This phenomenon is attributed to a poor fusing among the loosely packed Cu particles and the splashing of Cu particles during the SLS process.[113,114] The density of the sintered part was estimated to be about 79 %. In contrast, a part fabricated from the cold-pressed pellet

has an estimated density of about 91%. The number of pores and the pore sizes decreased significantly. Besides, Cu particles ejected were not observed, and laser scan tracks became continuous in the part fabricated from the cold-pressed pellet. The cold-pressed Cu pellet with a better packing density and more intimate contact between the Cu particles facilitates the SLS process by preventing particle ejection, as shown in **Figure 3.3-1 (a**) and **(b)**.

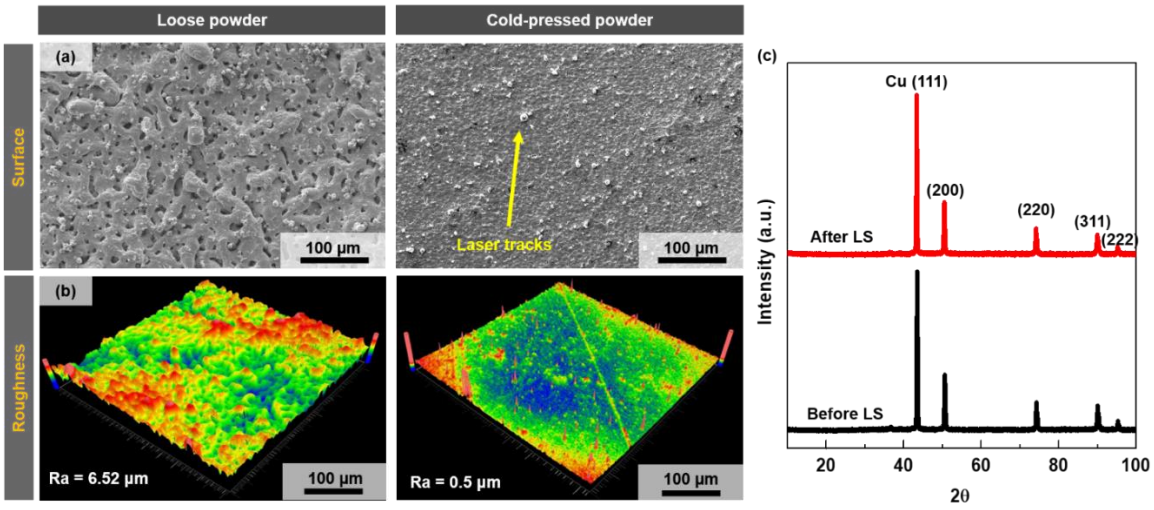

Figure 3.3-2 (a) SEM micrographs and **(b)** 3D surface mapping of Cu layer fabricated using SLS from loose and cold-pressed Cu powders, respectively **(c)** XRD patterns of the raw and sintered powders.

The surface roughness of the parts fabricated from the loose-powder bed and the cold-pressed was analyzed using a three-dimensional (3D) optical surface profiler. As shown in **Figure 3.3-2 (b)**, sintering of the loose-powder bed resulted in a rough surface containing a large quantity of voids and balling globules with a large average surface roughness value of 6.5 µm. In contrast, the surface of the part fabricated from the cold-pressed pellet has a smooth surface with no obvious voids. A significant decrease in the average surface roughness to 0.5 µm was identified. In addition, XRD was performed on the loose-powder

bed and on the parts fabricated from the cold-pressed pellet as shown in **Figure 3.3-2 (c)**. No change in phase and crystallographic orientations were observed.

Therefore, the average surface roughness of the final Cu parts was strongly affected by the cold-pressing step. Sintering is a diffusion mechanism driven by the reduction of the surface energy. Fick's and Jost's laws describe the diffusion mechanism mathematically and determine its strong dependence on the temperature as well as the material.[115,116] In solid diffusion, different diffusion paths occur at the same time, such as surface, phase boundaries, grain boundaries, and volume diffusion. The faster path is surface diffusion, which depends on the contacts among particles. Next, in order of decreasing speed, is phase boundaries diffusion, which varies depending on the number of phases. Then, grain boundaries diffusion, which is influenced by the grain sizes. Finally, volume diffusion, which is affected by the density of dislocations.[95,117] The contact between powder particles was enhanced by the cold pressing step, raising the surface diffusion during SLS and ultimately leading to easier neck formation for densification. Furthermore, it is well known that pressing of powder particles engenders dislocation formation, thus the cold-pressing treatment promoted volume diffusion as well.[118]

3.3.2 SLS of dense Cu part using cold-pressed powders

Although a fast diffusion by enhancing both surface and volume diffusions occurred during SLS of a cold-pressed pellet, solid diffusion remains a slow process and therefore not all pores were suppressed. To obtain a fully dense part with a density close to the theoretical limit, the sintering times need to be increased; and thus, the laser scan speed was varied from 125 to 25 µm/s. **Figure 3.3-3** shows the surface morphologies and the

cross-sectional micrographs of 50-μm-thick parts fabricated by SLS from cold-pressed Cu pellets at different scan speeds. As shown in **Figure 3.3-3 (a)**, smooth surfaces without balling globules were obtained for all cases and the number of pores decreased as the laser scan speed decreased. It was observed in **Figure 3.3-3 (b)** that homogenous sintering of the Cu powders was obtained throughout the whole thickness for each scan speed. Moreover, the cross-sectional micrographs, shown in **Figure 3.3-3 (c)**, revealed the consolidation behaviors at different scan speeds. At a scan speed of 125 μm/s, necks formed between Cu particles. By reducing the scan speed to 62 μm/s, the sintering of the powders was enhanced. At a scan speed of 25 μm/s, complete densification of the Cu powders was attained. The surface of the parts shows dimple-like features, which are a typical characteristic of ductile fracture.[106,119] As the scan speed decreased, the sintering time increased, which means more energy was delivered and absorbed by the powders and thus the atomic diffusion was promoted, which led to denser parts.[120]

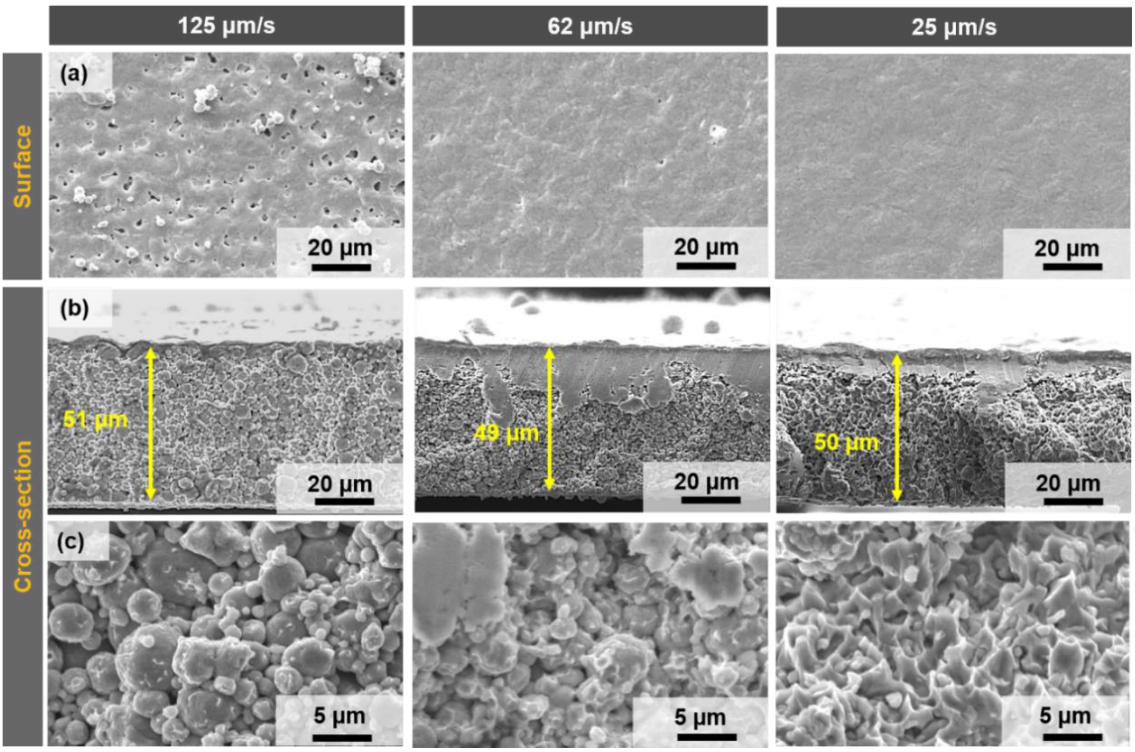

Figure 3.3-3 SEM micrographs of Cu sample surfaces fabricated by SLS at different scan speeds: **(a)** surface morphologies, **(b)** Cu part cross-sectional overviews, and **(c)** cross-sectional microstructures.

3.3.3 Conclusions

The effect of a cold-pressing step on the SLS of Cu powders is investigated. Due to better contacts among powder particles, the surface diffusion is promoted and powder ejection out of the laser tracks is eliminated during the SLS process of a cold-pressed powder pellet. It is demonstrated that cold-pressed powders, with optimized scan speed, allows fabrication of fully dense Cu parts with a low surface roughness. The whole sintering process is free of binders, which is promising to obtain comparable properties as Cu manufactured by conventional method while enabling complex structure designs without post-printing steps.

Nevertheless, to obtain dense Cu parts, the laser scan speed must be relatively low (25 μm/s). At a low speed, a long printing time is necessary to manufacture fully dense 3D parts. Thus, this method can only be applied on small objects where low surface roughness is required. For larger objects (i.e., heat sinks), another printing method is required. The next part will present an SLM process in which larger objects can be printed in a shorter time frame.

3.4 Selective laser melting (SLM) of pure copper

3.4.1 SLM parameter optimization

Reports on the 3D laser printing of pure Cu show that a high laser power is required to obtain dense Cu parts. The printing parameter windows reported are typically a laser power between 600 to 1000 W (λ = 1070 and 1080 nm, beam size = 40 to 80 μm), a scan speed between 200 to 1000 mm/s, a layer thickness between 0.03 to 0.05 mm, and a hatch distance from 0.05 to 0.12 mm.[83–85] Thus, the printing parameters are optimized in the range of the same parameters as found in the literature to achieve dense Cu parts with smooth surface finishes but by using a moderate laser power of 400 W. The hatch distance is adjusted from 0.08 to 0.12 mm at an increment of 0.01 mm. The scan speed increases from 200 to 600 mm/s with a 50 mm/s increment. The layer thickness is kept at 0.03 mm. First, the overall shapes of the printed parts is investigated and qualitatively categorized into three groups, which defines the process windows of printing pure Cu. **Figure 3.4-1 (a)** and **(b)** show a photo of the printed parts on the base plate and a 2D map depicting the quality of the parts at different scan speeds and hatch distances—cracked, high quality, and porous samples are represented by green squares, red circles, and blue triangles,

respectively. A low scan speed (200 to 350 mm/s) resulted in cracked samples for all hatch distances studied. With a low scan speed, the energy deposited greatly exceeded the amount required to melt the Cu powders. The high temperature of the molten pool generated a large thermal gradient in the solid Cu, which ultimately caused interlayer delamination and debonding from the build plate.[121–123] Note that, at a scan speed of 200 mm/s (**Figure 3.4-1 (a)**), the print was stopped because bending/debonding of Cu from the build plate caused severe damage to the powder recoater. Printing with a higher scan speed of 400 mm/s and a hatch distance of 0.12 mm produced smooth Cu parts without defects. Similar results were also obtained with scan speeds ranging from 450 to 500 mm/s and hatch distances from 0.08 to 0.09 mm (**Figure 3.4-1 (a)-(b**). Finally, scan speeds exceeding 500 mm/s yield rough and porous samples for the majority of the hatch distances investigated (**Figure 3.4-1 (a)-(b)**). When insufficient laser energy is applied partial melting and sintering of the powders occurs and subsequently resulting in pore generation.[124]

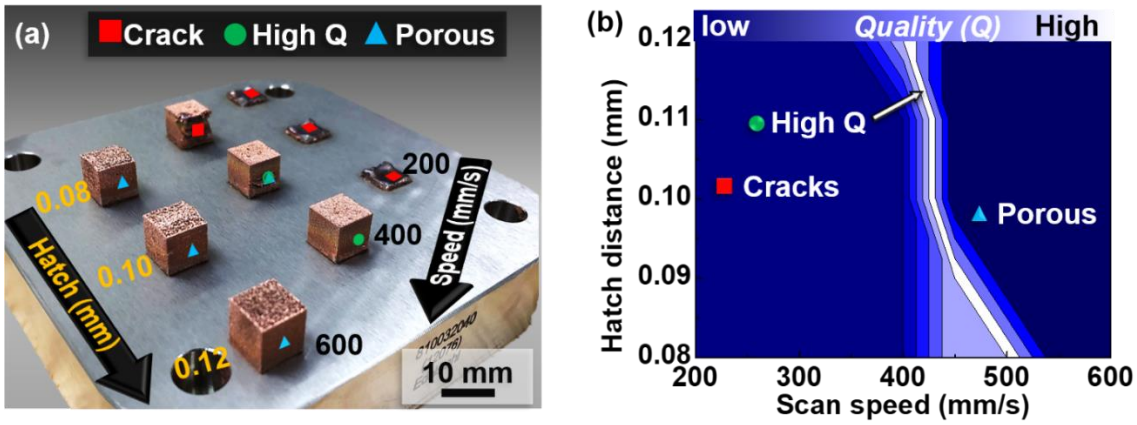

Figure 3.4-1 (a) Photo of printed Cu cubes with laser scan speeds from 200 – 600 m/s and hatch distances from 0.08 to 0.12 mm, respectively. **(b)** 2D map of the printing quality with respect to the scan speed and the hatch distance.

XRD was performed on the as-received Cu powders and the printed parts for crystalline and phase evaluation in **Figure 3.4-2**. The diffractions peaks at 2θ = 43, 50 and 74º and a small peak at 2θ = 36 º are attributed to (111), (200) and (220) planes of the face-centered Cu and the (-111) plane of Cu_2O.[125]

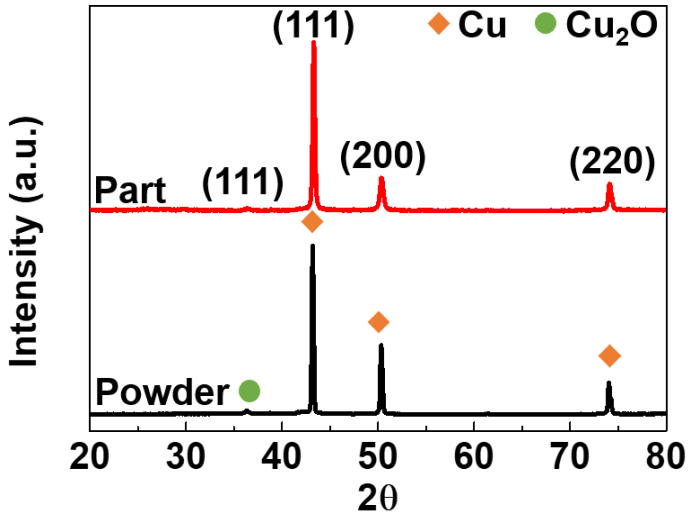

Figure 3.4-2 XRD diffractograms of the printed part (top) and Cu powders (bottom).

In addition to XRD diffractograms, energy dispersive X-Ray (EDX) was performed on the Cu powders and parts. **Figure 3.4-3 (a)** and **(b)** present the SEM micrographs of the Cu powders and polish Cu parts (printing parameters: power = 400 W, layer thickness = 0.03 mm, scan speed = 400 mm/s, and hatch distance = 0.12 mm), respectively. **Figure 3.4-3 (c)** and **(d)** show the EDX point spectra of the Cu powders and parts, respectively. **Figure 3.4-3 (e)** summarizes the EDX analysis where it can be observed that the powders present about 7.7 wt.% of oxygen while the Cu part shows an oxygen content of 2.4 wt.%. The XRD and EDX analyses prove that oxidation of Cu did not occur during the 3D printing step.

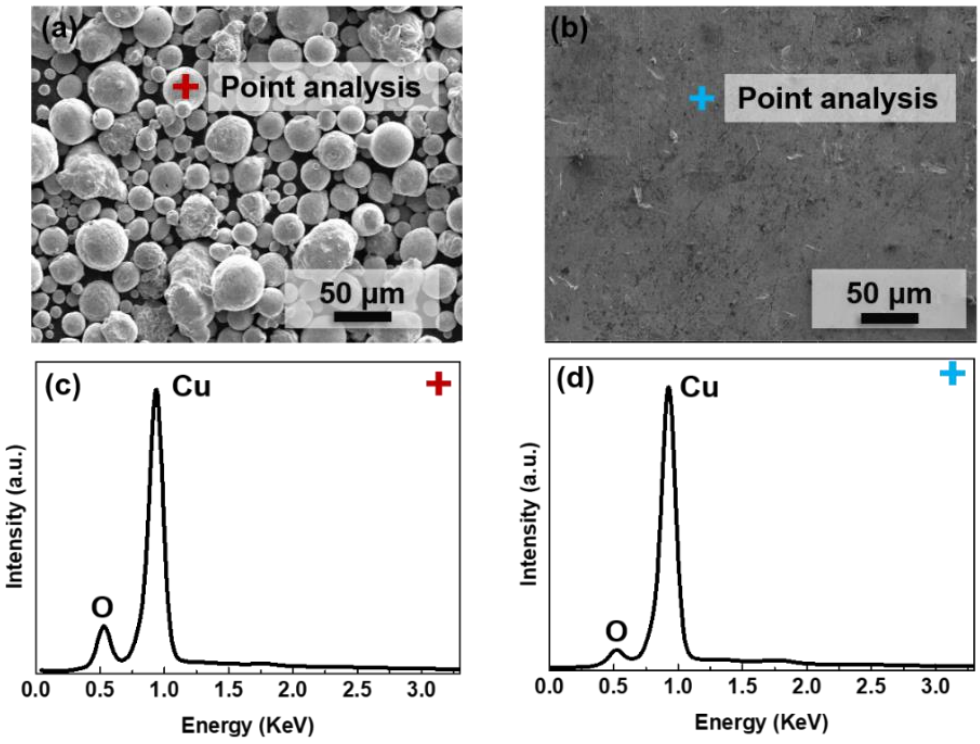

(e) Sample	Element	Weight %
Powder	O K	7.7
	Cu L	92.3
Printed Part	O K	2.4
	Cu L	97.6

Figure 3.4-3 (a) and **(b)** SEM micrographs of Cu powder and part, **(c)** and **(d)** EDX point spectra and **(e)** summarized EDX analyses.

Part density and surface finish are the essential attributes to evaluate when assessing the print quality and optimizing process parameters. The densities of the printed Cu parts are summarized in the 2D map as a function of the scan speed and the hatch distance in **Figure 3.4-4 (a)**. High-density parts were obtained within an extremely narrow processing window with a scanning speed of 400 mm/s and a hatch distance of 0.12 mm. A slight deviation either in the scan speed or hatch distance from the optimized processing window significantly decreased the density of the printed part from ~95% to 70%. The average

surface roughness (R_a) of the parts was measured using an optical profiler, with the results plotted in **Figure 3.4-4 (b)**. Using fast scan speeds (450 to 600 mm/s) for all hatch distances resulted in a large R_a (> 30 μm). Lower scan speeds led to a smaller R_a (< 18 μm). The R_a results at low and high scan speeds confirm the previous observations on the part quality (**Figure 3.4-1 (a)** and **(b)**). When the scan speed decreased, sufficient melting of the Cu powders occurred, leading to an adequate flow of molten metal, and thus, a low R_a.[126] The findings obtained by studying the part shape, density, and surface roughness, suggest that at a laser power of 400 W, a scan speed of 400 mm/s, and a hatch distance of 0.12 mm are the optimal parameters to print a crack-free Cu part with a density of 95% and a R_a of 18 μm.

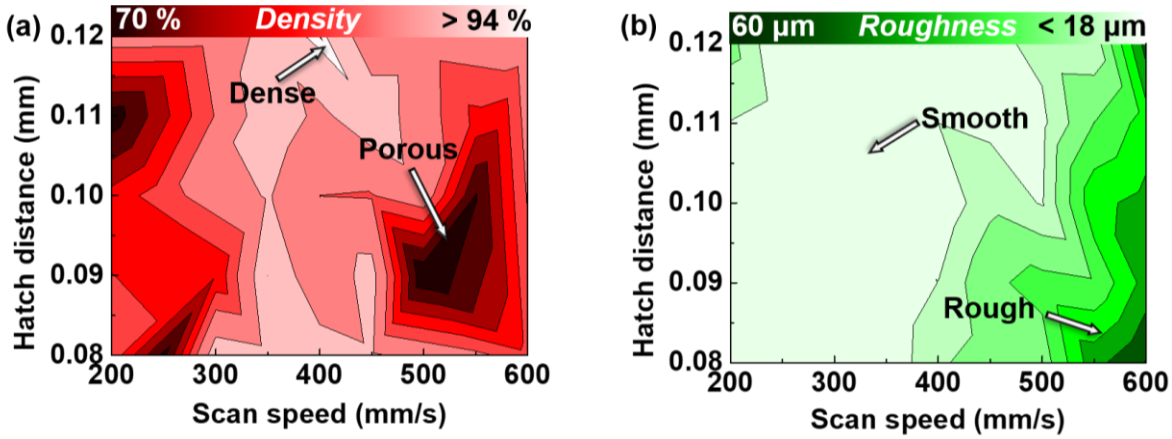

Figure 3.4-4 (a) 2D map of the part density, and **(b)** the average surface roughness as a function of the scan speed and the hatch distance.

To better understand how the printing parameters, influence the density, R_a, and the surface morphology of the printed parts was studied and associated with the molten metal stability. The laser-matter interactions induced the formation of a circular molten pool in several hundred microseconds.[127] Printing parameters, such as the scan speed and hatch

distance, influence the dynamic, temperature, shape, and stability of the molten pool as well as the surface finish and the part density.[84,128,129] At a slow laser scanning speed of 200 mm/s, bumps are formed on the surface, resulting in pores formation (**Figure 3.4-5 (a)** and **(b)**). A slow laser scanning speed generates a significant temperature gradient in the molten pool and induces a great difference in the surface tension between the edge and the center of the molten pool. As a result, the molten Cu tends to flow from the hot molten pool towards the colder edges of the pool, thus creating protrusion at the pool borders (**Figure 3.4-5 (c)).**[130] At 400 mm/s, the part shows a smooth and flat surface finish with minimal defects (**Figure 3.4-5 (d)** and **(e)**). At a moderate scan speed, the temperature of molten Cu is sufficiently high to achieve a desirable metal viscosity, resulting in a flat and stable molten pool, as illustrated in **Figure 3.4-5 (f)**. At 600 mm/s, the surface appears to be porous with the balling effect (**Figure 3.4-5 (g)** and **(h)**). The insufficient laser energy deposition that occurs at a fast scan speed leads to an unstable molten pool (i.e., fluctuation), with poorly melted powders and a slow molten metal flow, leading to the formation of large pores (> 80 μm) (**Figure 3.4-5 (i)** and **(f)**) and bumps on the surface (i.e., the balling effect).[131]

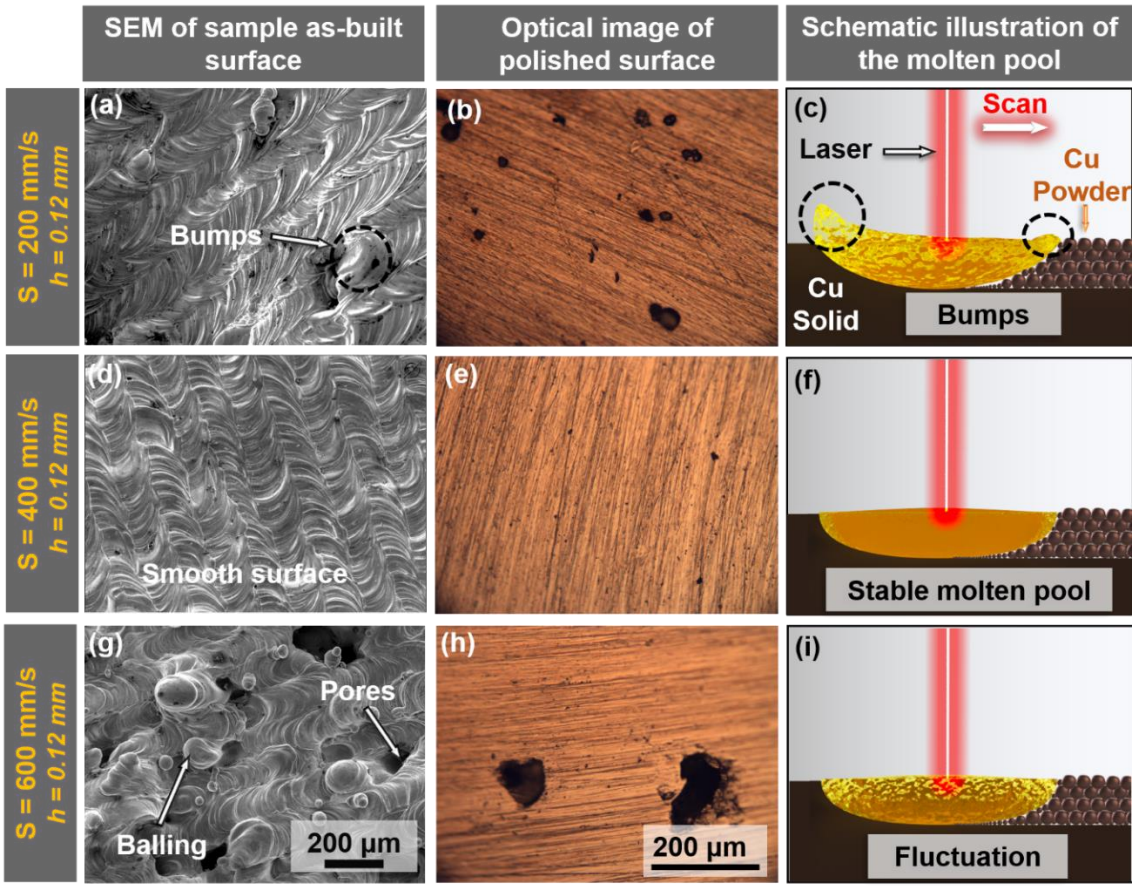

Figure 3.4-5 (a), **(d)**, and **(g)** SEM micrographs of as-printed surfaces and **(b)**, **(e)**, and **(h)** optical images of polished surfaces with scan speeds of 200, 400, and 600 mm/s, respectively, and **(c)**, **(f)**, and **(i)** schematic illustrations of the molten pool shapes at different laser scan speeds.

Producing high-density Cu parts with a moderate laser power is a critical advancement in additive manufacturing. Moderate powers prevent damage to the laser optics (the back reflection of the laser beam) and lower the energy consumption (60% less power compared to 1 KW laser).[132,133] One possible explanation of the successful additive manufacturing of dense Cu parts with a moderate power is associated with the laser beam. Jadlhav et al. reported that a low laser power led to porous Cu parts (84%).[85] Others reported that adding

oxide or carbon particles to the Cu parts enhanced the laser absorption, which should have decreased the laser power. Yet, high laser power was still required (> 500 W).[86,134] Several studies demonstrated that the wavelength, beam angle, size, and quality play vital roles in laser-matter interactions.[135–137] Naturally, the laser beam characteristics influence the power required to print Cu.

The SLM 125 3D printer is equipped with a 400 W single-mode CW fiber laser (IPG photonics, Yb:YAG, λ = 1070 nm). The laser beam has a stigmatic Gaussian profile, indicating a TEM_{00} mode, as shown in **Figure 3.4-6 (a)**. **Figure 3.4-6 (b)** lists the parameters of the laser beam and are conformed to the EN ISO 11146-2 measurement method. The beam quality is evaluated by the beam quality factor (BPP) and the effective beam quality factor (M^2). It is measured that the BPP has a value of 0.396 mm/rad and an M^2 of 1.16. The results imply an excellent beam quality when focused to a small spot with the conservation of the original output power.[138,139]

(a)

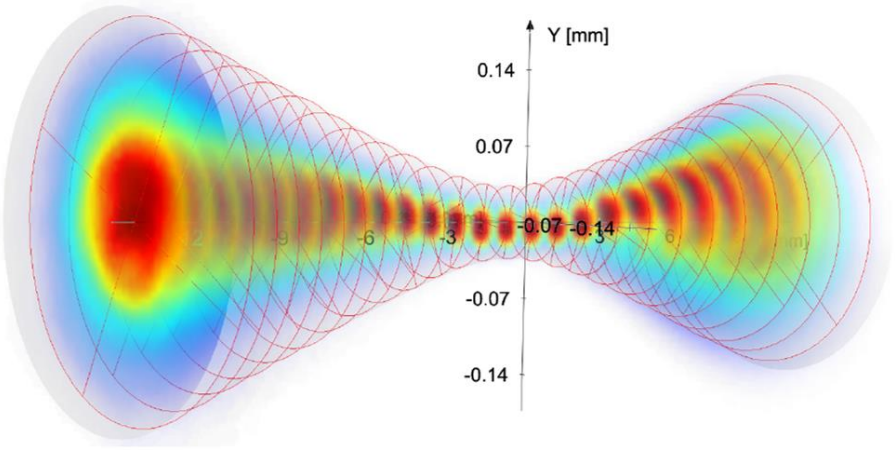

(b)

BPP	0.395(9) mm/mrad
M^2_{eff}	1.160(25)

Figure 3.4-6 (a) Laser beam profile, and **(b)** beam characteristics, measured inside the SLM 125's chamber.

3.4.2 3D printing of complex Cu heat sinks

The main advantage of the SLM is its ability to manufacture complex shapes that cannot be achieved by conventional machining. The ability to design thin and sophisticated structures has the potential to significantly enhance the functionality of current heat sinks to cool electronic devices. The full potential of the SLM method was investigated by fabricating different heat sink structures, as presented in **Figure 3.4-7.** The first heat sink is a commercial (COM) columnar type.

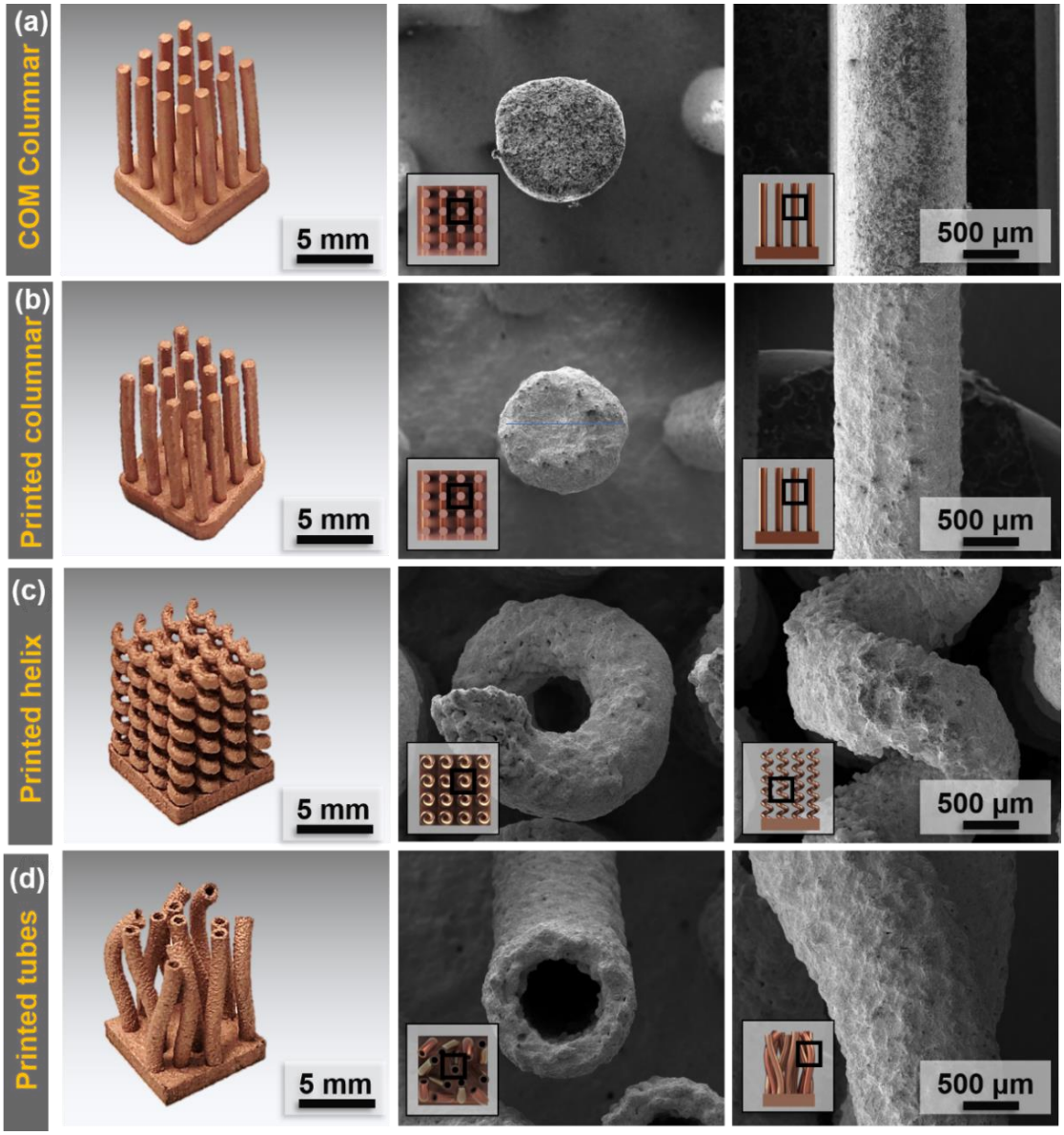

Figure 3.4-7 Top- and side-view optical and SEM micrographs of **(a)** a commercial (COM) columnar, **(b)** a printed columnar, **(c)** a printed helix, and **(d)** a printed bent-tube heat sinks.

Figure 3.4-7 (a) and **(b)** show optical and SEM micrographs of COM and printed heat sinks having the same morphology and appearance with a column height of 12 mm and a diameter of 1.2 mm, respectively. The second type of heat sinks is a helix structure with a height and diameter of 12 mm and 750 μm, respectively (**Figure 3.4-7 (c)**). The third type of heat sinks consist of hollow, bent tubes with a pore diameter of 1 mm and a wall thickness of 300 μm, as shown in **Figure 3.4-7 (d)**. The optimal printing parameters (scan = 400 mm/s, hatch = 0.12 mm) were applied for the fabrication of the complex structures with smooth, crack-free surfaces. It is worth mentioning that the printing of pure Cu shows a spatial resolution of a few hundred micrometers, which makes the SLM methods a desirable choice for the fabrication of complex components for thermal management.

3.4.3 Mechanical and thermal properties of printed heat sinks vs. a commercial one.

The physical properties of the columnar heat sink printed were measured and compared with the COM columnar heat sink and bulk Cu. Prior to the measurements, the printed and COM heat sinks were sandblasted to obtain a similar surface finish. The densities of the printed and COM heat sinks were 95% and 98%, respectively. Note that the other structures also had densities of approximately 95% (i.e., helix and bent tubes). **Figure 3.4-8 (a)** shows a schematic illustration of the sample preparation for the four-point probe and hardness measurements. The heat sink pillars were cut from the base plate for electrical conductivity measurements, while the base plate was used for hardness tests. **Figure 3.4-8 (b)** and **(c)** show the current/voltage (I/V) curves for the commercial (COM) and printed heat sinks, respectively. The resistance was calculated by linear regression of the I/V curves. As shown

in **Figure 3.4-8 (b)** and **(c)**, the resistances of the printed and COM heat sinks are 144 and 155 μΩ, respectively

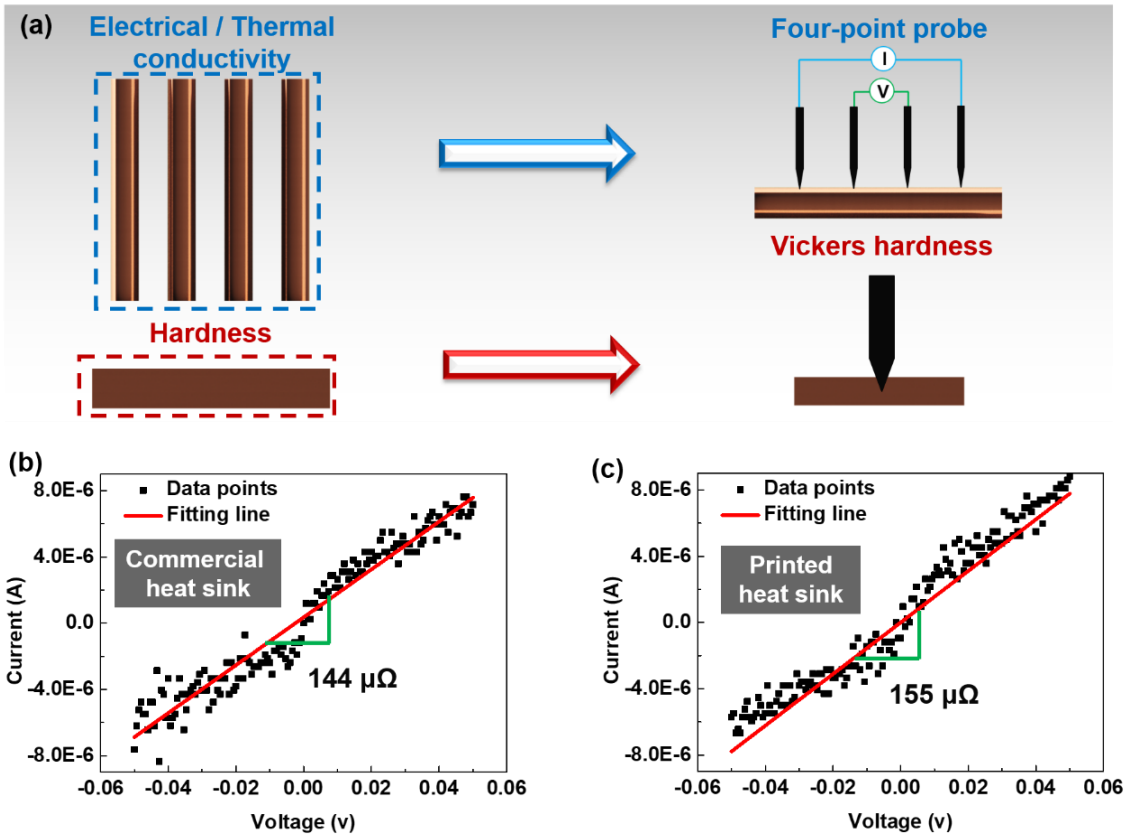

Figure 3.4-8 (a) Schematic illustration of the sample preparation for measurements of the physical properties; I/V curves of **(b)** commercial (COM) and **(c)** printed heat sinks.

The resistance of a single Cu pillar was obtained by linear regression of the I/V curve and converted into electrical conductivity using the following equation:[140]

$$\sigma = \frac{L}{A \times R}, \quad \textbf{(6)}$$

where σ is the electrical conductivity (S/m), L is the length of the pillar (m), A is the area cross-section (m^2), and R is the resistance (Ω). The results show that the printed and COM heat sinks have an electrical conductivity of 5.71×10^7 and 5.81×10^7 S/m corresponding to

98 % IACS (International Annealed Copper Standard) and 100 % IACS, respectively. The TC can be obtained from the electrical conductivity measurement for pure metals using the Wiedemann-Franz law:[141]

$$\frac{\kappa}{\sigma} = \mathrm{KL}, \quad \textbf{(7)}$$

where κ is the TC (W/m.K), K is the temperature (K), and L is a proportionality constant (2.2×10^{-8} WΩ/K^2). The TC of the COM and the printed heat sinks was 378 and 368 W/m.K, respectively. The TC of the commercial and printed heat sink measured in this study are comparable to the one measured by C. Vincent et al. on pure Cu prepared by a powder metallurgic route with similar density.[142] Note that the incertitude in the electrical conductivity measurements is derivate from the incertitude on the pillar dimensions measurement and the resistivity analysis.

The heat-sink base plate was used for the Vickers hardness tests using a Wilson Tukon™ 2500-3 with a load and dwell time of 0.5 kg and 10 s, respectively. The hardness was calculated using the following equation:

$$\mathrm{HV} \approx 1.891 \times \frac{\mathrm{F}}{\mathrm{d}^2}, \quad \textbf{(8)}$$

where F is the force of the intender in N, and d is the average length of the diagonal in mm. **Figure 3.4-9 (a)** shows the SEM micrographs of the indentation of the COM and printed heat sink bases. It can be seen that the diagonals of the COM heat sink are more significant than the printed one. The grain size was measured to understand the difference in the hardness between the COM and printed heat sinks (COM = 72 MPa and Printed = 108 MPa). For that, the heat-sink bases were etched in a solution composed of 23% HNO_3 and

77% H_2O for a time of 10 s for grains observation. **Figure 3.4-9 (b)** shows the SEM micrographs the COM and printed heat sinks after acid etching. It can be observed that the grain sizes of the COM and printed heat sinks are about ~30 and ~22 μm, respectively.

The porosity and microstructure (i.e., grain sizes) of the material affect the thermal and mechanical properties. Several studies demonstrated that the porosity mainly affects the thermal conductivity, while the microstructure alters the mechanical properties.[142–145] A smaller microstructure hardens the material, producing better mechanical properties.

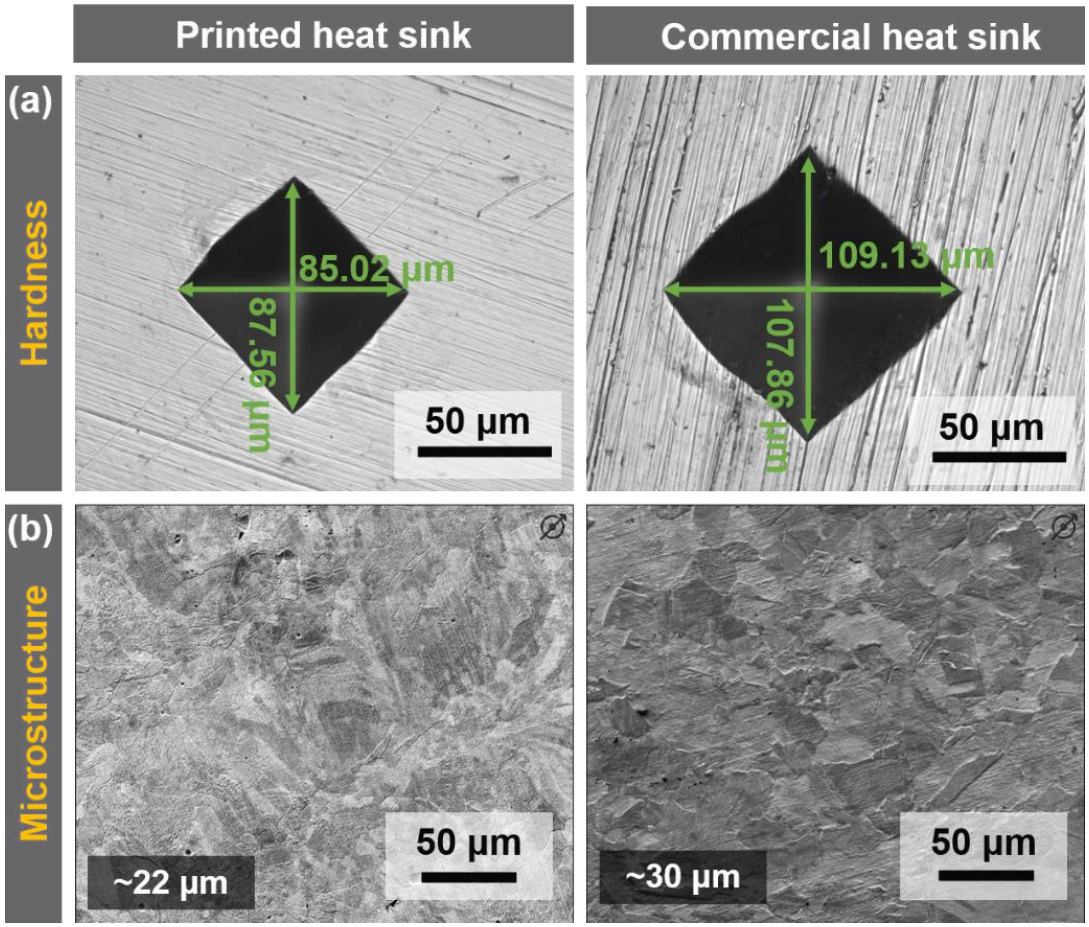

Figure 3.4-9 SEM micrographs of the base plates of the commercial (COM) and printed heat sinks after **(a)** Vickers hardness tests and **(b)** acid etching

Table 1 summarizes the mechanical properties, and electrical and thermal conductivities of the printed and commercial heat sinks and the values of the bulk Cu. It can be seen that the printed heat sink has similar properties to those obtained from the commercial heat sink and bulk Cu.[142,146,147] The high TC of the printed heat sink (i.e., 368 W/m.K) is encouraging. We will explore the heat dissipation of SLM-printed heat sinks that can outperform the COM ones.

Table 1. Physical properties of the printed and the commercial (COM) columnar heat sinks and bulk Cu made by powder metallurgy route.

Properties	Printed heat sink	COM heat sink	Bulk Cu [40-42]
Density (%)	95	98	100
Electrical conductivity (S/m)	$5.71 \pm 0.26 \times 10^7$	$5.81 \pm 0.17 \times 10^7$	5.97×10^7
IACS (%)	98 ± 4	100 ± 3	103
Thermal conductivity (W/m.K)	368 ± 17	378 ± 15	385
Hardness (MPa)	108 ± 4	72 ± 2	60 - 120

3.4.4 Heat dissipation performance of the printed heat sinks

The surface area is the main factor in thermal management. SLM has the ability to easily increase the specific surface areas through manufacturing thin features of complex shapes.[36,89] To demonstrate the benefit of additive manufacturing in thermal management, the heat dissipation performance of different structures printed was measured and compared to the COM heat sink. **Figure 3.4-10** shows the experimental set-up where the

heat sink was attached to a memory card chip placed on a hot plate heated to 100, 150, and 200 ºC, respectively. A fan was located 10 cm from the top of the heat sink to produce an airflow. The temperature of the electronic chip was measured using an IR camera about 0.5 m from the heat sink.

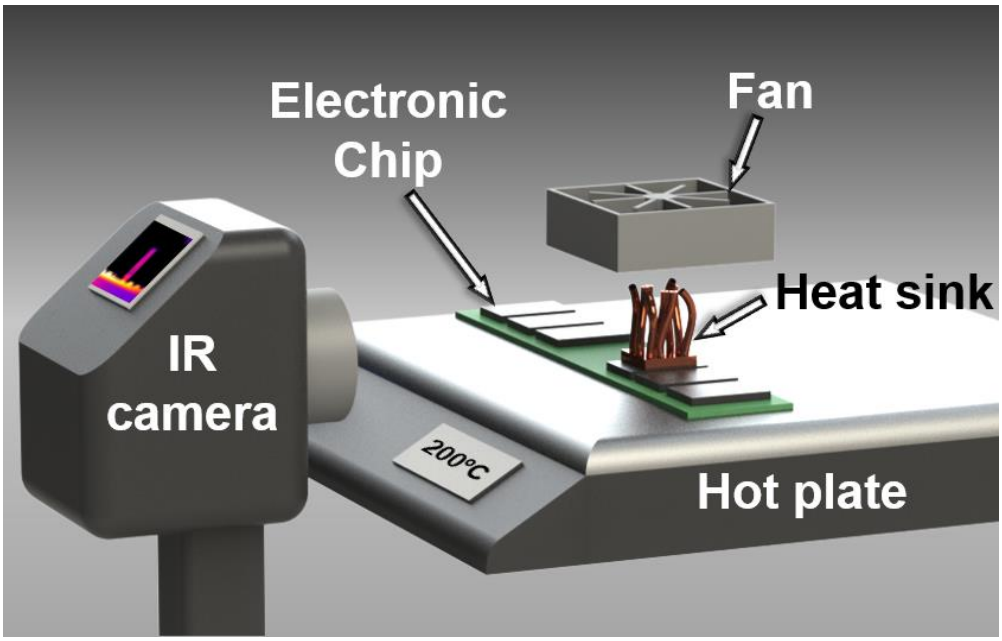

Figure 3.4-10 Schematic illustration of the experimental set-up to measure the heat dissipation performance of heat sinks.

The thermal performance of the different heat sink structures was measured for each structure after a chip being heated on a hot plate to 100, 150, and 200 ºC, respectively, for 5 min. As can be seen in **Figure 3.4-11 (a)** and **Figure 3.4-12 (a)**, at a temperature of 100 ºC, the temperature of the chip alone reaches a value of about 83 ºC. However, the temperature of the chip with the COM, printed, helix, and tubes heat sink structures is similar (IR images) and measured to be 66, 66, 67, and 66 ºC, respectively. However, when the hot plate temperature rises to 150 ºC, (**Figure 3.4-11 (b)** and **Figure 3.4-12 (b)**) a difference starts to appear among measured temperatures of the chip with the COM,

printed, helix and tubes heat sinks structures of 99, 99, 95, and 90 ºC, respectively. The temperature of the chip without a heat sink is about 123 ºC. At an even higher temperature (200 ºC), a significant difference between each structure can be seen. The chip temperatures with the COM, printed, helix, and bent heat sink structures are measured to be 130, 130, 123, and 115 ºC, respectively, in contrast to 166 ºC for the chip alone (**Figure 3.4-11 (c)** and **Figure 3.4-12 (c)**).

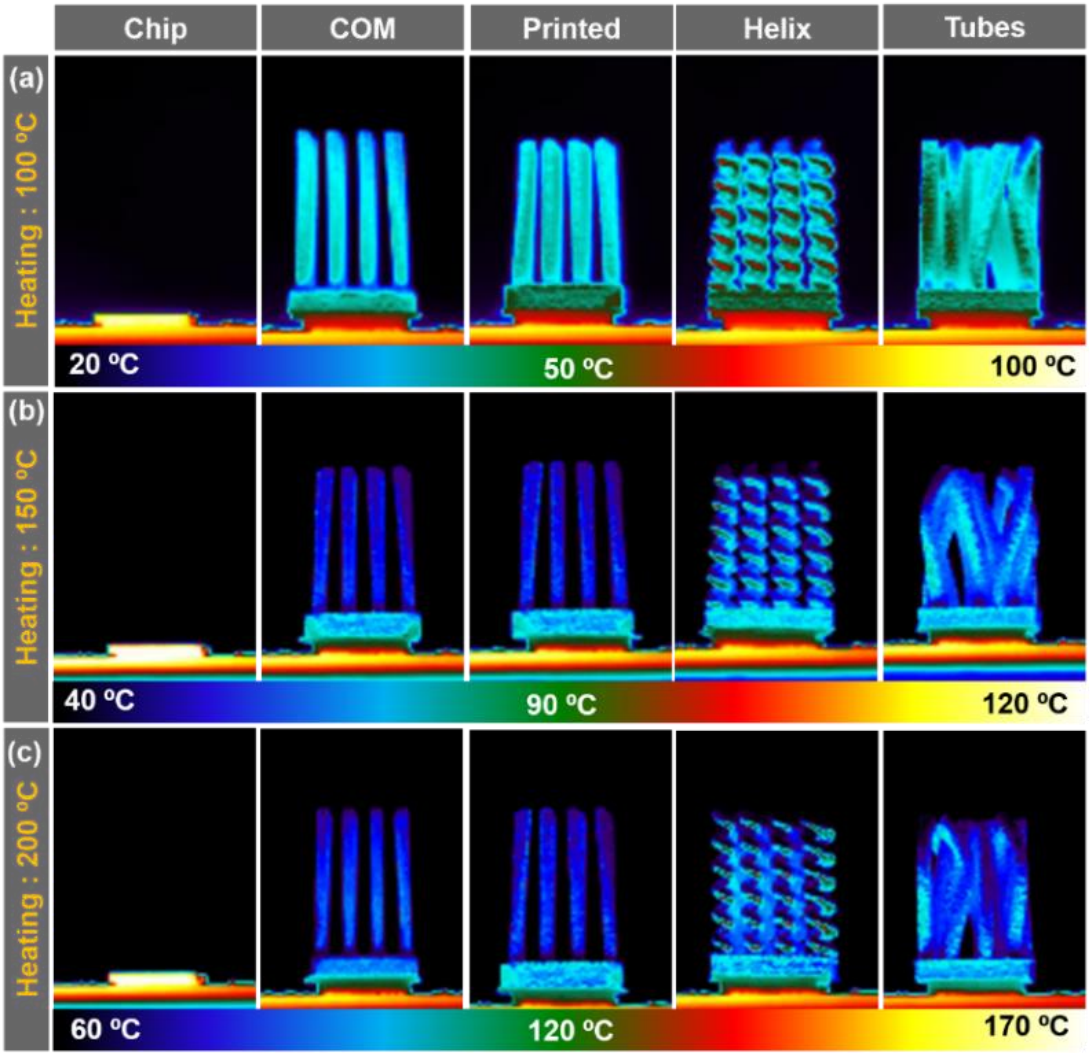

Figure 3.4-11 IR images of chip alone, and with COM, printed, helix, and tubes heat sinks heated at **(a)** 100, **(b)** 150, and **(c)** 200 ºC, respectively.

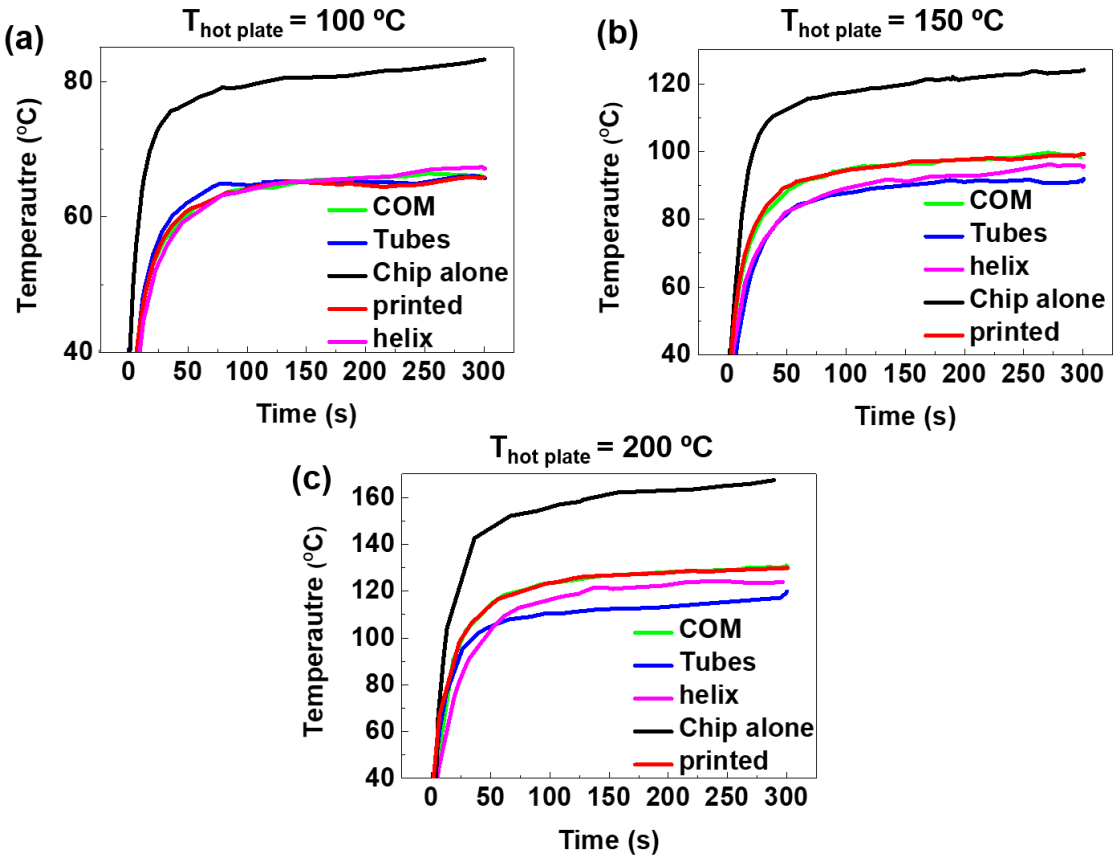

Figure 3.4-12 Chip temperature vs. time plots for different heat sink structures heated at **(a)** 100, **(b)** 150, and **(c)** 200 ºC, respectively.

The temperature of the chip alone was subtracted from the chip temperature with different heat sink structures (cooling effect). **Figure 3.4-13 (a)** shows the cooling effect as a function of the heating temperature. The different structures show similar cooling effects (-18 ºC) at 100 ºC. However, at 150 ºC, the different structures begin to show difference in the cooling effects, which become more pronounced when the heating temperature increases to 200 ºC. The printed and COM columnar structures have a similar cooling effect at about -36 ºC at 200 ºC. However, the helix and bent-tube heat sinks outperformed both types of columnar structures by reducing the chip temperature by -44 and -55 ºC, respectively. The superior cooling effect of the printed heat sinks is attributed

to their increased surface areas. As shown in **Figure 3.4-13 (b),** the bent-tube heat sink has the highest surface area of 600 mm^2/g, followed by the helix one with 390 mm^2/g, and the columnar heat sinks with 286 mm^2/g. In conclusion, using SLM to print intricately shaped heat sinks yielded dense and crack-free parts with large surface areas and excellent thermal properties. High dissipation performance is achieved with the SLM method and can produce heat-dissipating materials that exceed commercial ones.

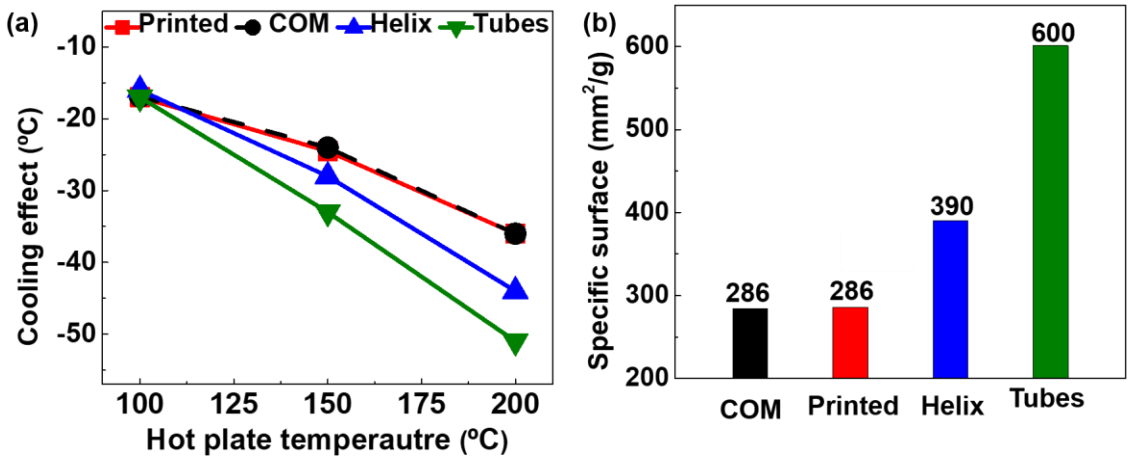

Figure 3.4-13 (a) Cooling effect (Cooling = $T_{chip} - T_{chip\ with\ heat\ sink}$) of different heat sinks as functions of the heating temperature and **(b)** specific surface area of heat sinks.

3.4.5 Conclusions

In this study, SLM with a moderate laser power (400 W) is successfully implemented to additively manufacturing complex-shaped crack-free functional Cu parts that have a density up to 95% and a surface roughness of 18 μm. A systematic investigation into the printing parameters is performed to optimize the printing quality and understand the part formation mechanism. It is found that the printing parameters play critical roles in

controlling the printing quality. Insufficient laser energy deposition leads to rough surface finish associated with bumps and pores, while excess energy deposition leads to destructive balling effects. The high-density achieved in this study is attributed to the high-quality laser beam, which allows to focus the beam with the conservation of the original output power.

Functional Cu heat sinks with various sophistic structural designs are fabricated using the optimized printing parameters. Their physical properties and thermal performance in cooling electronic chips are investigated. These printed Cu parts exhibit a thermal conductivity of 368 W/m.K, which is close to the bulk Cu fabricated using a powder metallurgy process (385 W/m.k).

The thermal performance of the printed Cu heat sinks is compared with commercially ones by studying their cooling dissipation efficiency of a hot electronic chip. The COM and the printed columnar heat sinks with the same dimension show similar cooling performances. However, the heat sinks printed with a helix structure and bent porous tubes outperform the thermal dissipation of the COM columnar structure by 45 % and is attributed to the significantly enhancement of surface areas.

4 Interphases for Copper Matrix Composite

4.1 Introduction

Metal matrix composites (MMCs) need robust interphases to enhance the transfer of properties between the matrix and the reinforcement and thus, tailor the overall properties of the resultant composites.[148] The formation of interphases is particularly crucial in composites comprised of chemically and thermomechanically dissimilar compositions.[149,150] Copper (Cu) reinforced carbon fibers (CFs), or diamond (D) are excellent examples of MMCs with weak interfacial bonding. These MMCs are of particular interest in thermal management, as next-generation heat sink materials.[151] Solid Cu alone is limited by fatigue failure due to stresses of thermal cyclicals. Adding carbon to reinforce Cu offers an advantage of combining the low CTE and high TC carbon (C) with the excellent TC of Cu (400 W/m.K). Nevertheless, a simple Cu/C composite suffers from poor Cu wettability with C due to the lack of chemical affinity.[152] The lack of affinity is more significant when the molten metal is in direct contact with the carbon reinforcement such as in laser-assisted AM.[109,153,154]

Extensive experimental and theoretical works have been devoted on the interphase engineering on C-reinforced Cu matrix composite.[155,156] One approach has been to alloy the metal with carbide-forming elements (e.g., titanium (Ti), zirconium (Zr), chromium (Cr), and boron (B)).[157–159] However, the properties are severely degraded due to inhomogeneous dispersion of the alloying elements at the interfaces.[160–162] The second approach of considerable interest is to coat the carbon reinforcement with carbides.[163,164] Titanium carbide (TiC) offers strong oxidation resistance, high mechanical strength, excellent chemical stability, and low density, making it a right candidate as the

interphase.[165] However, it has been reported that TiC does not wet thoroughly with molten Cu (contact angle >115°), resulting in poor Cu-TiC adhesion.[166]

Another concern to print Cu/C composites is the oxidation/degradation of the carbon reinforcement. Laser 3D printing involves high temperatures ($T_{m, Cu}$ = 1085 ºC) and laser matter interactions. Diamonds degrade into graphite at a temperature above 800 ºC, even in a vacuum. Thus, the D particles need to be protected from the molten metal and the laser radiation. Over the past decades, extensive research efforts were undertaken to develop effective oxidation barriers on C materials, such as oxides, nitrides, and carbides.[167–172] Among them, refractory carbides have the advantage of spontaneous reaction with C and being permeable to oxygen.[173,174] Substantial evidence suggests that materials coated in multiple carbide layers possess superior resistance to oxidation and thermal ablation as compared to traditional single-layer carbide coatings.[175,176,177] However, the production of multilayer coatings involves complex processes that often require pricey precursors to be decompose at elevated temperatures.[178–180] Developing a method straightforward for forming complex multilayer carbide coatings is thus challenging due to the covalent nature bonding of carbides materials, leading to high melting points.[181]

In this chapter, a graded Ti oxide–carbide (TiO_2-TiC) coating is developed on CFs and D particles to improve the wettability with molten Cu using a molten salt process. In addition, using the same method, an innovative single-step multilayer coating of refractory carbides is presented via an oscillatory reaction (**Figure 4.1-1**). This process provides a versatile and efficient way to produce transition metal carbides at relatively low temperatures in short time frames. The salt acts as a solvent to dissolve the metal powders

and, therefore, enhance the Ti mass transport to the CF surfaces.[182,183] The metal dissolution in the molten salt and mass transport are discussed.

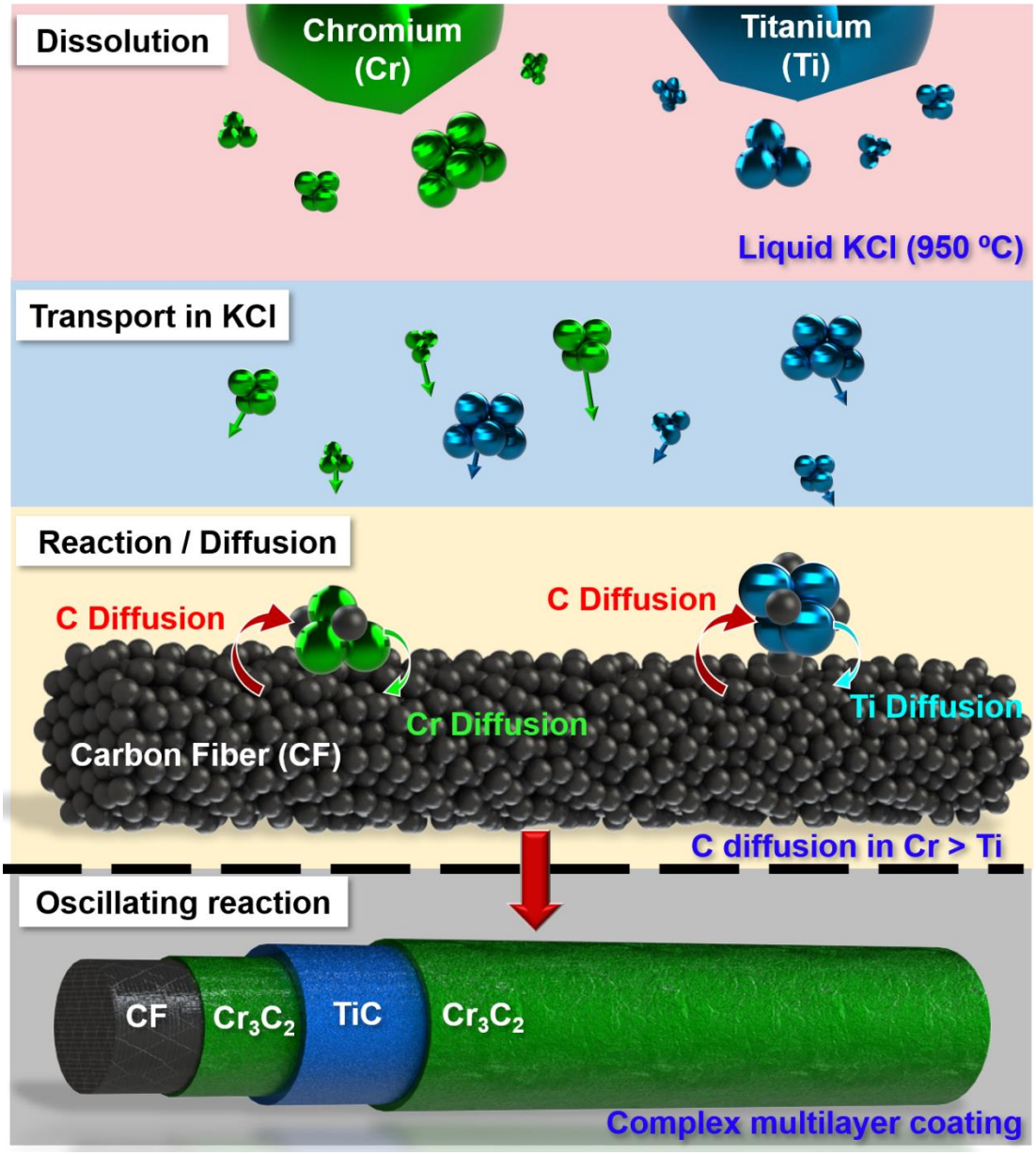

Figure 4.1-1 Schematic of a complex multilayer coating formed in a single-step, molten salt process.

4.2 Experimental set-up and procedures

4.2.1 Preparation of coatings

The synthesis of carbide coatings was carried out by a molten-salt process, illustrated schematically in

Figure 4.2-1. First, CFs (Mitsubishi Chemical DIALEAD™ K223HM) or D particles (Eastwind Diamond Abrasives, diameter = 105 μm) were mixed with a potassium chloride (KCl) (GPR Rectapur® 99%) salt and metallic Ti and/or Cr powder (Ti 99.5%, mean diameter 40 μm) at a molar ratio of KCl:CFs:Ti = 0.64:1:0.125, KCl:CFs:Cr:Ti = 0.64:1:0.06:0.06 or KCl:D:Ti = 0.64:1:0.04, respectively. The mixture was then placed in an alumina (Al_2O_3) crucible and heated in a tube oven filled with flowing argon (Ar) gas. The coating temperature varied from 800 to 950 °C for times of up to 5 h. These coating conditions were chosen based on the study by Lui et al..[184] After cooling down, the crucible was immersed in a boiling distilled water (~100 ºC) until the salt was fully dissolved. Finally, the coated C were filtered from the solution, flushed with deionized (DI) water, and air-dried in an oven at 60 ºC for 1 h. The filtration dissolution/filtering process was repeated three times.

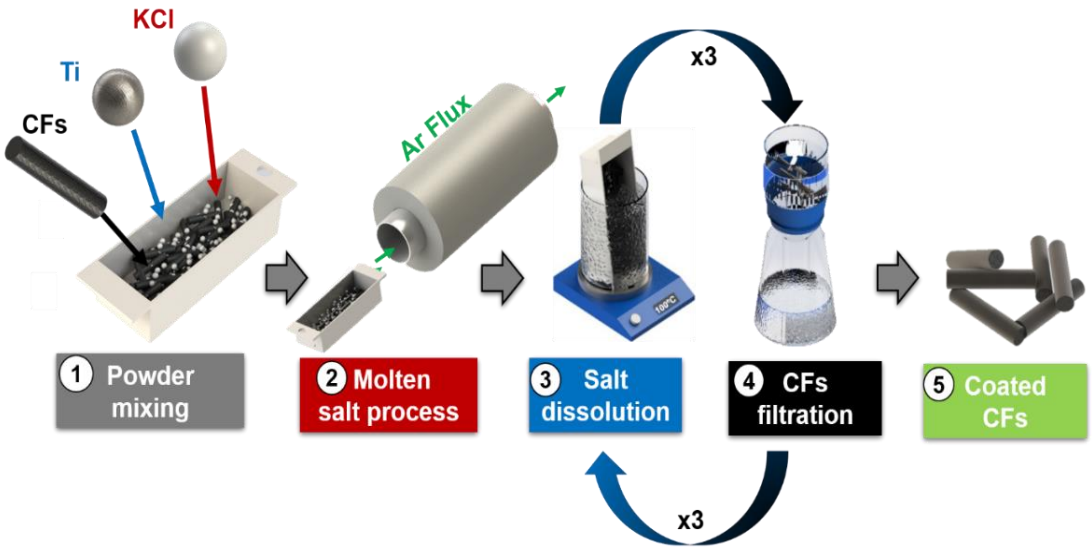

Figure 4.2-1 Illustration of the molten-salt process for preparing TiC-based coatings on CFs.

4.2.2 Wettability analysis

The wettability of molten Cu on the coated CFs was investigated using an approximate equal-molar mixture of 0.2 g (~0.017 mol) of coated CFs with 1.2 g (0.019 mol) of dendritic Cu powder (35 μm, ECKA Granules Germany CmbH). The mixture was placed in an Al_2O_3 crucible with a carbon paper liner to prevent reaction between the Cu powders and the crucible. The crucible was put into a tube oven filled with flowing argon gas and heated to 1200 ºC with a rate of 10 ºC/min. The crucible was held for 10 min and then cooled to room temperature at a rate of 15 ºC/min. Contact angles between the CFs and the Cu droplets were determined using scanning electron microscopy (SEM) and cross-sectional images of resin-encased and polished CFs.

4.2.3 Quenching tests

Rapid thermal quenching of the molten salt in the ambient air was used to terminate the coating process at intermediate stages. This enabled the study of the carbide formation, including metal dissolution, diffusion, and reaction with C. The quenching tests were performed by heating the powder mixture to 800 and 950 ºC for 0.5 and 5 h, respectively. The hot crucible was then rapidly quenched in the air at a cooling rate of about 500 ºC/min, resulting in KCl (m_p = 770 ºC) solidification in less than 20 s. A piece of the solidified KCl-CFs-Ti and KCl-CFs-Cr-Ti samples were embedded in a polyphenolic resin, and mechanically dry polished for SEM analyses.

4.2.4 The growth rates of the TiC and Cr_3C_2 layers

The diffusivity and associated activation energy were measured by mixing KCl, CFs, and Ti or Cr with molar ratio of KCl:CFs:Ti = 0.642:1:0.238 and KCl:CFs:Cr = 0.642:1:0.238, respectively. Both coating times and temperatures were varied between 1 to 5 h at processing temperatures of 800, 850, 900, and 950 ºC, respectively. After the reactions, the coated CFs were washed and dried as described earlier, before embedded in a polyphenolic resin and polished for SEM analyses.

4.2.5 Erosion/oxidation under an oxy-acetylene flame

A combustion torch with a 1.5 mm orifice was used to produce a combustion flame. The precursor gases were a mixture of 99.6% acetylene (C_2H_2) and 99.9% oxygen (O_2) with flow rates of 1780 and 1800 sccm (standard cubic centimeters per minute), respectively. Coated CFs were glued onto a tungsten carbide (WC) substrate containing 6% of cobalt

(Co) (dimensions: 12.5×12.5×1.6 mm^3). Samples were placed on a water-cooled brass stage 10 mm beneath the tip of the flame for 60 s. The temperature was evaluated by a noncontact pyrometer (OS3752, Omega Engineering, Inc.) and measured to be 1200 ºC.

4.2.6 Characterization methods

Morphological and microstructural characterization was performed using an SEM (VEGA II SBH, TESCAN). Crystal structures and chemical phases were identified by X-ray diffraction (XRD) (PANalytical X'pert PRO MPD, λ = 1.5405 Å). The stoichiometry of TiC_x was estimated by calculating the lattice parameters from the XRD diffractograms via the Le-Bail method [185] using the FullProf Suite. Auger electron spectroscopy (AES) (Auger VG Scientific Microlab 310F) and X-ray photoelectron spectroscopy (XPS, Thermo Electron K-alpha photoelectron spectrometer, Al Kα excitation) were used to determine the elemental and chemical compositions. The AES sputtering time was converted to a depth profile by measuring the layer removal depth using SEM. Grain morphology, orientation, and size were evaluated using electron backscatter diffraction (EBSD). The oxidation state and crystallinity of the coated CFs after being subjected to the oxy-acetylene flame were investigated using a micro-Raman spectrometer (inVia™, Renishaw). An Ar^+ ion laser with a wavelength of 514.5 nm and a power of 50 mW was used as the excitation source. The laser beam was focused using a 50× objective lens to approximately 5 μm.

4.3 Graded titanium oxide – carbide coatings on CFs.

4.3.1 Effect of temperature on TiC_x coating composition and morphology

The effects of the reaction temperature on the coating morphology and structure are shown in **Figure 4.3-1**. In this study, the reaction time was 5 h at temperatures ranging from 800 to 950 ºC. The SEM micrographs of the coatings display a drastic change in the morphology with different temperatures. Specifically, at 800 and 850 ºC, the surfaces appeared to be a porous collection of particle-like features with open, interconnected porosity of more than 50% (pore sizes ranging from 300 to 1000 nm). This suggests that the growth was from reactive sites on the C surface with little consolidation by surface-diffusion-driven sintering. Both Xiaoguang Liu et al. [184] and Qian Liu et al. [186] observed similar porous coatings formed by Ti reaction with C substrates at 750 ºC in a potassium chloride : lithium chloride (KCl:LiCl) salt and at 900 ºC in a lithium chloride : potassium chloride : potassium fluoride (LiCl:KCl:KF) salt, respectively.

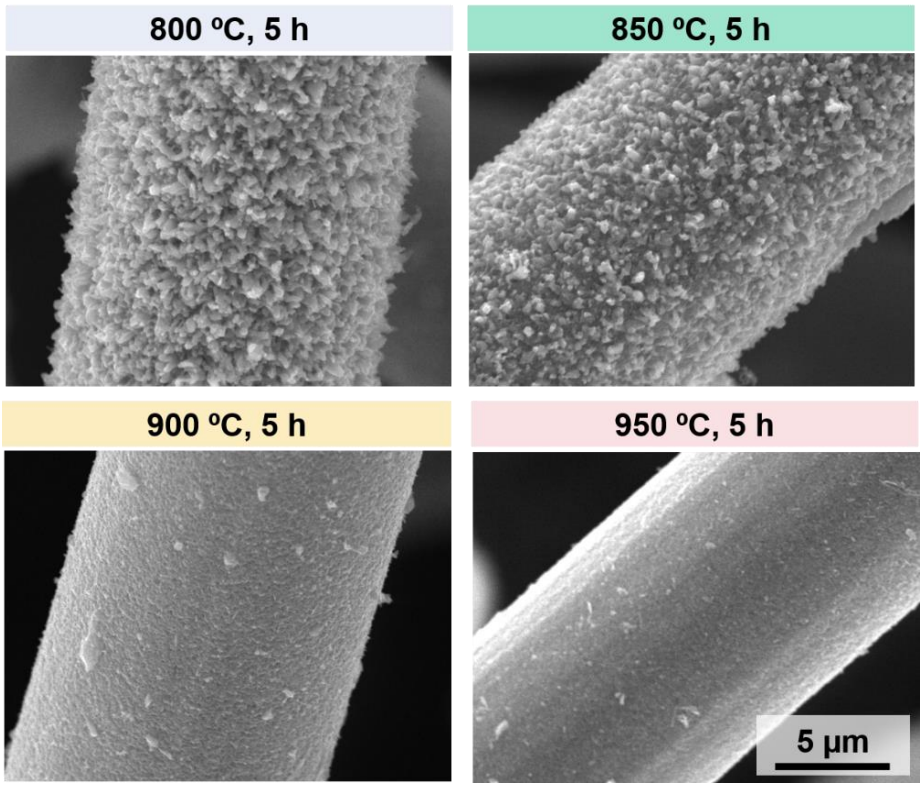

Figure 4.3-1 SEM micrographs of the Influence of the coating temperature, ranging from 800 to 950 ºC, on the layer morphology and composition

In contrast, coatings at 900 and 950 ºC have far fewer and smaller pores and appear almost fully consolidated. In these cases, the temperature is sufficiently high that localized differences in surface reactivity become less critical for determining the growth morphology. Moreover, the possibility of sintering driven by surface diffusion would be more significant. Both effects, individually or combined, could explain the dense coatings obtained at high temperatures. Others have also reported consolidated coatings at temperatures above 900 ºC in different salts.[164,187]

In addition to the surface morphology, XRD was performed at each processing temperature to quantify the product phase composition (**Figure 4.3-2**). It can be seen that for each temperature and a coating time of 5 h, diffraction peaks at 2θ = 35.9°, 41.7°, 60.5°,

72.4°, and 76.1º corresponded to the (111), (200), (220), (311), and (222) planes of a face-centered cubic (FCC) titanium carbide (TiC) phase. The strong and sharp (002) diffraction peak at 2θ = 26.4° is assimilated to CFs and confirmed its high degree of graphitic crystallinity.

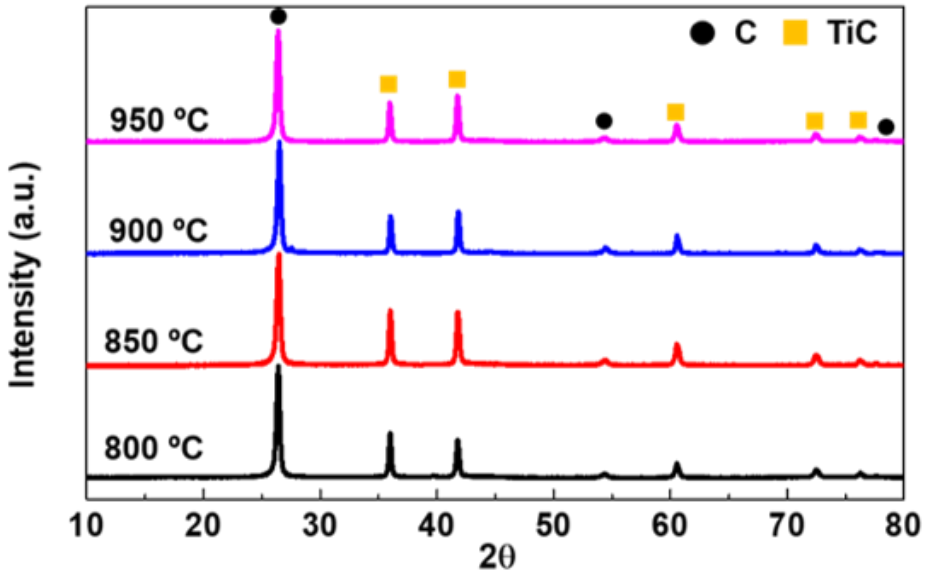

Figure 4.3-2 XRD diffractogram of the CFs coated with TiC_x at different temperatures and 5 h coating time.

SEM micrographs show that the diameters of the reacted fibers (i.e., core CFs plus coated layers) decreased as the temperature increased, as plotted in **Figure 4.3-3**. In other words, the growth of porous coatings at 800 and 850 ºC caused the resulting diameter to increase from ~11 (i.e., original CFs) to 13 µm (i.e., coated CFs). In contrast, the layer obtained at 950 ºC was almost fully dense and increased the diameter of the coated CFs by only ~0.5 µm from the original ones.

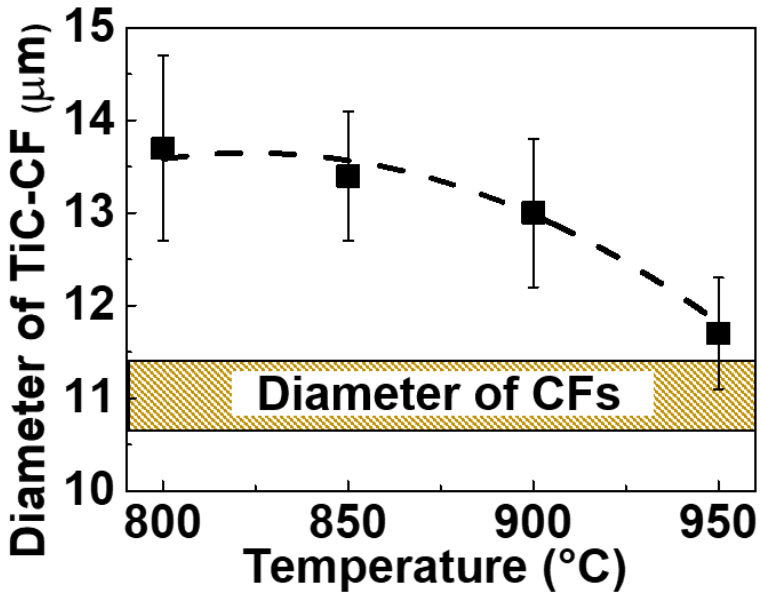

Figure 4.3-3 Influence of the coating temperature, ranging from 800 to 950 ºC, on the TiC_x-CF diameter.

The coating porosity was estimated from a mass balance of the reactants as follows:

$$xmole_{C\ reacted} = mole_{Ti\ reacted} = mole_{TiC\ formed}, \quad \textbf{(9)}$$

Thus, for a CF coated with TiC_x, the mole can be expressed as:

$$\frac{x2\pi L_F(R_0^2-R_c^2)\rho_c}{M_c} = \frac{2\pi L_F(R_{TiC}^2-R_c^2)\rho_c}{M_{Tic}}(\rho_{TiC}(1-\varphi)), \quad \textbf{(10)}$$

where x is the mole fraction of C in TiC_x product (0.93), L_F is the length of the fiber (around 200 μm), M_{TiCx} and M_C are the molecular weight of TiC_x and C respectively (59.9 and 12 mol/g), ρ_{TiCx} and ρ_C are C and TiC densities (1.68 and 4.93 g/cm^3), and φ is the coating porosity. The outer radius of the coated CF, the radius of the starting CF, and the CF core radius at the end of the reaction are R_{TiCx}, R_0, and R_C, respectively. After rearranging and combining the terms:

$$R_{TiC} = [k'(R_0^2 - R_C^2) + R_C^2]^{\frac{1}{2}}, \quad \textbf{(11)}$$

where

$$k' = \frac{xM_{TiC}}{M_C}\frac{\rho_C}{\rho_{TiC}\times(1-\varphi)}\,, \qquad \textbf{(12)}$$

Similarly, the radius of the unreacted CF is given by:

$$R_C = R_0(1 - xZ_{Ti/C})^{1/2}\,, \qquad \textbf{(13)}$$

where $Z_{Ti/C}$ is the mole ratio of Ti to C in the starting reactants. The reactant mole ratio ($Z_{Ti/C}$) used to prepare the coated CFs shown in **Figure 4.3-1** was Ti:C = 0.125. The fully dense (0% porosity) coating thickness was predicted to be 0.55 μm via the mass balance calculation, suggesting an outer fiber diameter of 11.45 μm. This is in reasonable agreement with the outer diameter of 11.6 μm observed for CFs reacted at 950 ºC (**Figure 4.3-1**) and supported the observations that the porosity was low (<10%). Similarly, the coating prepared at 800 ºC has a measured outer diameter of ~13.5 μm, suggesting a porosity of ~65%, again in agreement with the observations.

The relationships between the TiC_x lattice parameters and the coating temperature were determined from the XRD data using the Le-Bail method.[185] **Figure 4.3-4** represents the refinement results where the black, red, and blue lines correspond to the experimental, refined diffractogram, and residual intensities, respectively. The Bragg factor expresses the agreement between the calculated intensities and the measured ones (insert in **Figure 4.3-4**), which confirms an excellent agreement between the experimental and refined diffractograms.

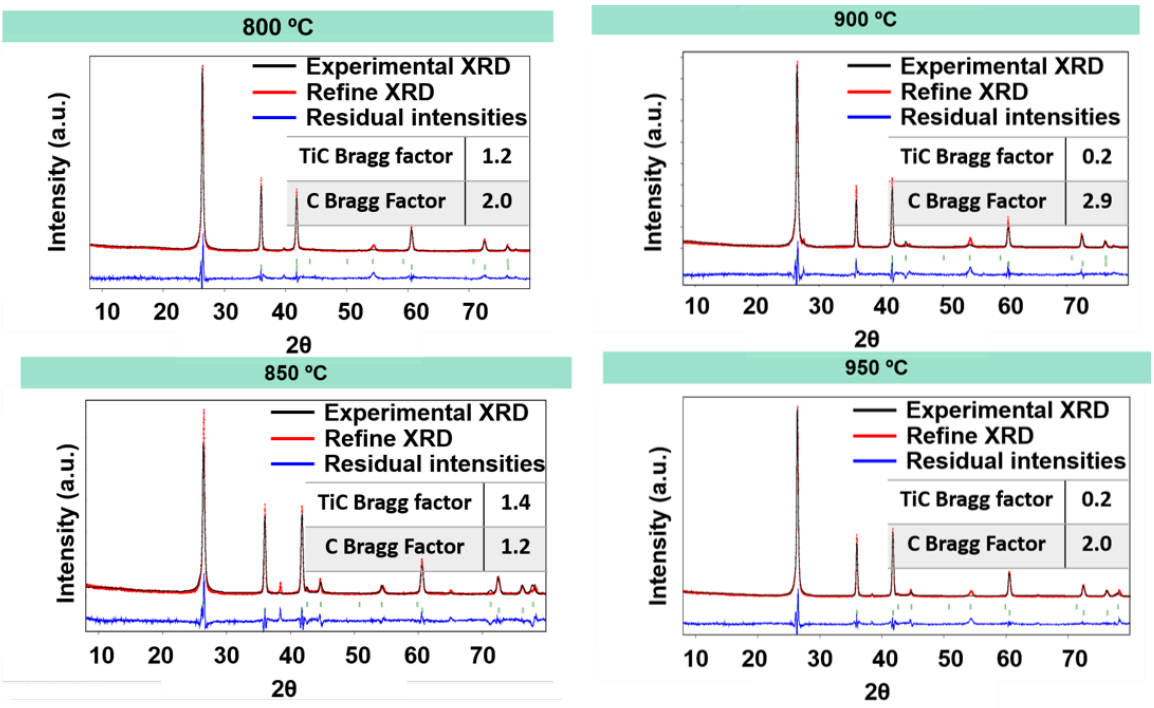

Figure 4.3-4 Le-Bail-structural refinement using FullProf Suite for XRD diffractograms of the CFs coated at different temperatures ranging from 800 to 950ºC, for a fixed time of 5 h, with a molar fraction of KCl:C:Ti = 0.64: 1: 0.125.

A correlation between the TiC_x lattice parameters and the chemical stoichiometry was then established to determine the change in the coating stoichiometry as a function of the temperature (**Figure 4.3-5**).[188–190] The results show, within the experimental errors, that the stoichiometry is ~$TiC_{0.73}$ for the product formed between 800 to 900 ºC. On the other hand, the coating produced at 950 ºC has a higher C content with a stoichiometry of ~$TiC_{0.93}$. One explanation for the change is that the Ti and C diffusivities were both greater at higher temperatures and thus tended to form a more reacted coating. This explanation is supported in part by the measurements of the self-diffusion coefficients of C and Ti in TiC as a function of the temperature,[191–193] as well as results from the process kinetics, described later in this chapter.

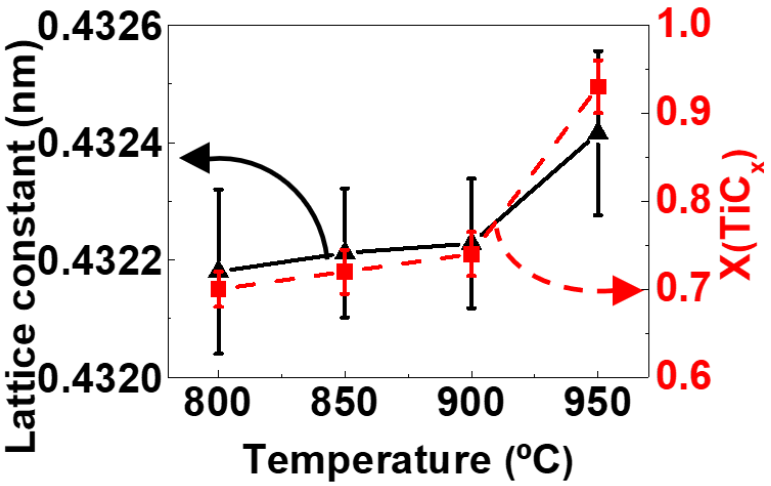

Figure 4.3-5 Influence of the coating temperature, ranging from 800 to 950 ºC, on the TiCx lattice constant and associated C/Ti atomic ratio vs. temperature.

4.3.2 Interphase elemental compositions (TiC_x vs. TiO_y-TiC_x)

In the previous section, it was shown that the salt-bath temperature influenced the morphology and stoichiometry of the TiC_x coatings. This section will describe how a combination of SEM, AES, and XPS were used to quantify the chemical compositions of the coated layers produced at the low (800 ºC) and high (950 ºC) temperatures. The AES compositional mapping in **Figure 4.3-6** shows the presence of not only TiC_x on the CF surfaces but also an outer layer of TiO_y. The elemental analyses at different depths of the coatings prepared at 800 ºC show a thin TiO_y outer layer that extends to ~20% of the coating thickness. Based on the results in **Figure 4.3-6 (a)** and **(c)**, the thickness of the coating at 800 ºC is about 1.2 µm, suggesting an partially oxidized outer layer of 250 nm. In contrast, the coatings prepared at 950 ºC were significantly denser with a thickness of ~0.30 µm (**Figure 4.3-6 (b)** and **(d)**) and a TiO_y outer layer of < 5 nm. In other words, the 950 ºC coating is essentially 100% TiC_x.

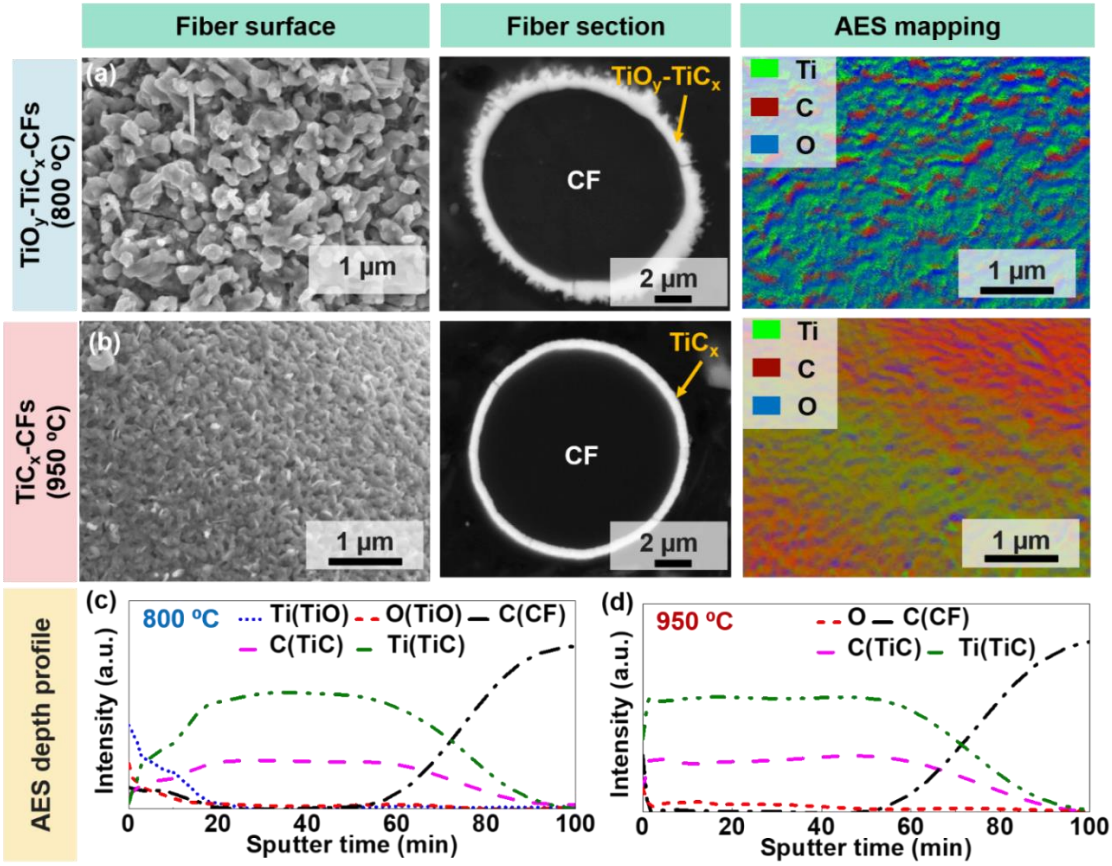

Figure 4.3-6 Surface morphology, cross-sectional and AES maps of the coated CFs prepared at **(a)** 800 and **(b)** 950 ºC, respectively; and AES depth profiles of the coated CFs prepared at **(c)** 800 and **(d)** 950 ºC, respectively.

Additionally, XPS was used to quantify the influence of the coating temperature on the graded oxide-carbide ratio. The C-C peaks observed at the binding energy (BE) of 284.6 eV in the C 1s spectra, originated from the unreacted CFs. The O 1s spectrum shows an O=C peak (BE ~530 eV) with an O-Ti shoulder (BE ~ 531 eV); and the Ti 2p spectra show two types of bonding configurations: Ti-C and Ti-O, respectively (**Figure 4.3-7**).

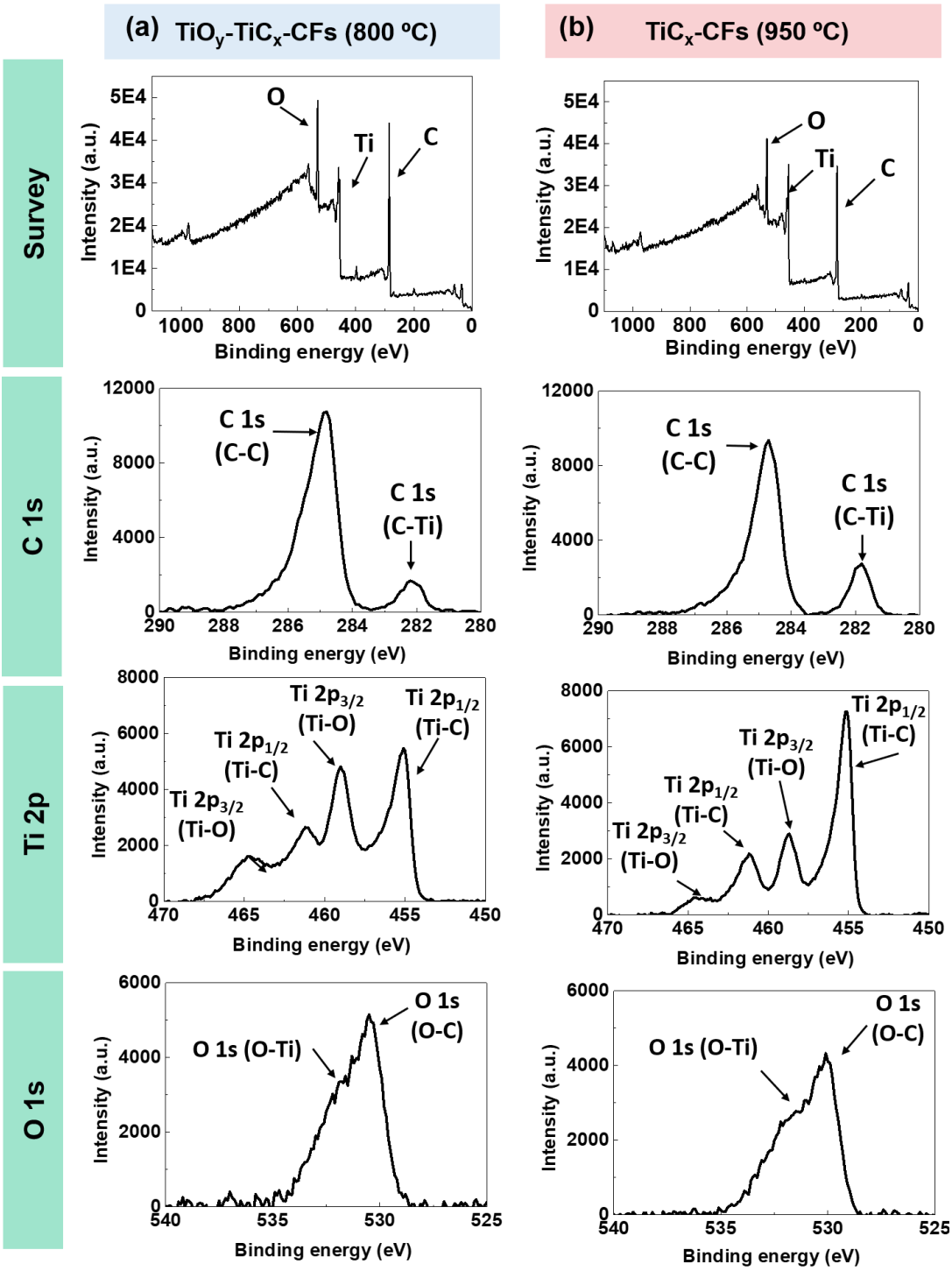

Figure 4.3-7 XPS survey and high-resolution spectra of the C 1s, Ti 2p, and O 1s peaks for **(a)** TiOy-TiCx and **(b)** TiCx CFs, respectively.

The spectra of C1s show a higher intensity of C-Ti for CFs with TiC_x than for CFs with TiO_y-TiC_x, suggesting a higher concentration of TiC on the surface where the same tendencies can be observed on the Ti 2p spectra. Moreover, it can be noticed that the intensity of the Ti-O peaks decreases when the coating temperature increases, suggesting a higher amount of Ti-O at a lower temperature accompanied by a lower concentration of Ti-C. Finally, on the O1s spectra, a higher intensity of O-Ti is observed for the CFs with TiO_y-TiC_x. Standard spectral analysis procedures were used to deconvolute the XPS Ti 2p spectra into contributions from TiC_x and TiO_y (**Table 4.3-1**). The results display the same trend as the AES results: the distributions of surface Ti bonded as Ti-C vs. Ti-O strongly depend on the coating temperature. The results demonstrate that ~50% of the surface Ti is bonded as TiO_y at 800 ºC but only ~10% at 950 ºC.

Table 4.3-1 XPS quantitative analyses using peak integration.

Sample	C_{tot} (at %)	C_{TiC_x} (at%)	Ti_{tot} (at %)	Ti_{TiO_y} (at %)	Ti_{TiO_y} (%)	Ti_{TiC_x} (%)
TiO_y-TiC_x-CFs (800 ºC)	70.8	7.3	14.6	7.3	50	50
TiC_x-CFs (950 ºC)	70.8	13.2	14.5	1.5	10.3	89.7

A possible explanation is that the TiO_y formed during the boiling-water (~100 ºC) dissolution of the KCl salt at the end of the process. Naturally, the effective oxidation depth (via both the AES and XPS) would be larger for the highly porous coatings obtained at 800 ºC, simply due to the enhanced water penetration. Also, the coatings obtained at 800 ºC have a more stoichiometrically Ti-rich layer ($TiC_{0.73}$, as described in the previous section), suggesting that more reactive, less -bonded Ti sites could be oxidized. In contrast, the

highly consolidated and essentially pure TiC_x coatings formed at 950 ºC (i.e., $TiC_{0.93}$) would allow much less water penetration and, thus, less oxidation.

4.3.3 Cu wettability and interphase surface energy

To understand the role of a graded TiO_y-TiC_x coating to tailor the interfacial bonding between Cu and C, we prepared two types of CFs coated with either a high or a low concentration of oxide content, respectively. The contact angles (wettability) of Cu on coated CFs prepared at 800 and 950 ºC were measured. The well-known Young-Dupre equation was used to estimate the adhesion energy:

$$E_{SL} = \gamma_{LV}(1 + cos\,\theta), \quad \textbf{(14)}$$

where E_{sl} is the energy (work) of adhesion ($mN.m^{-1}$), γ_{lv} is the liquid/vapor surface energy (tension) ($mN.m^{-1}$), which has been reported to be $\gamma_{Cu} = 1330 - 0.2\,(T - 1085)$ for Cu,[194] and θ is the equilibrium contact angle. The results show that Cu does not wet CFs (**Figure 4.3-8**).

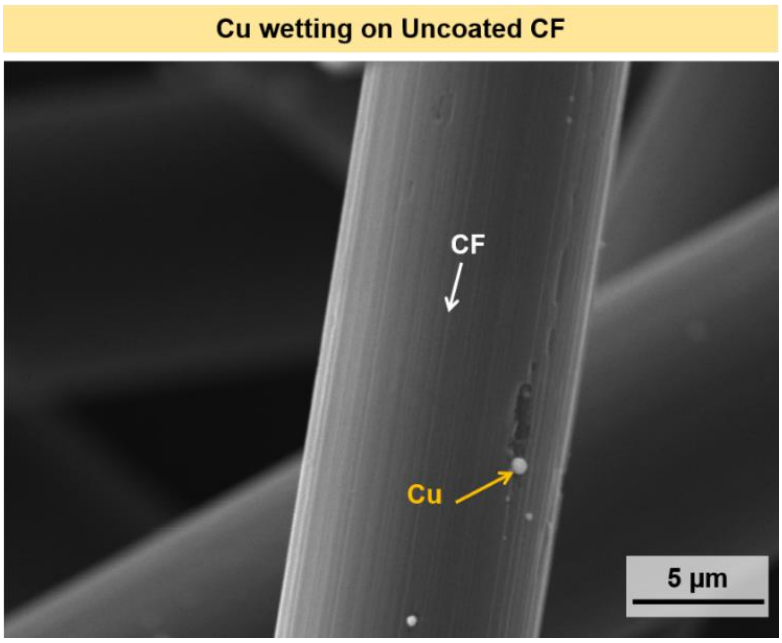

Figure 4.3-8 SEM micrographs of uncoated CFs after Cu wetting at 1200 ºC for 10 min.

This is in agreement with the prior work reporting a contact angle of 145º.[40] Creation of a TiC coating on CFs has shown to reduce the Cu contact angle to 115º,[195] but the coating is still non-wetting and is confirmed in this study for a coating prepared at 950 ºC (**Figure 4.3-9 (a)** and **(c)**). In contrast, the CFs coated at 800 ºC, with TiO_y surface layer (**Figure 4.3-9 (b)** and **(c)**), show a Cu wetting angle of ~80º (± 5º) and thus is a good wetting surface for Cu. In other words, there is sufficient oxide on the outer surface to increase the coating surface energy. For comparison, data reported for a Cu wetting angle of 80º on TiO is also included (**Figure 4.3-9 (c)**).[196]

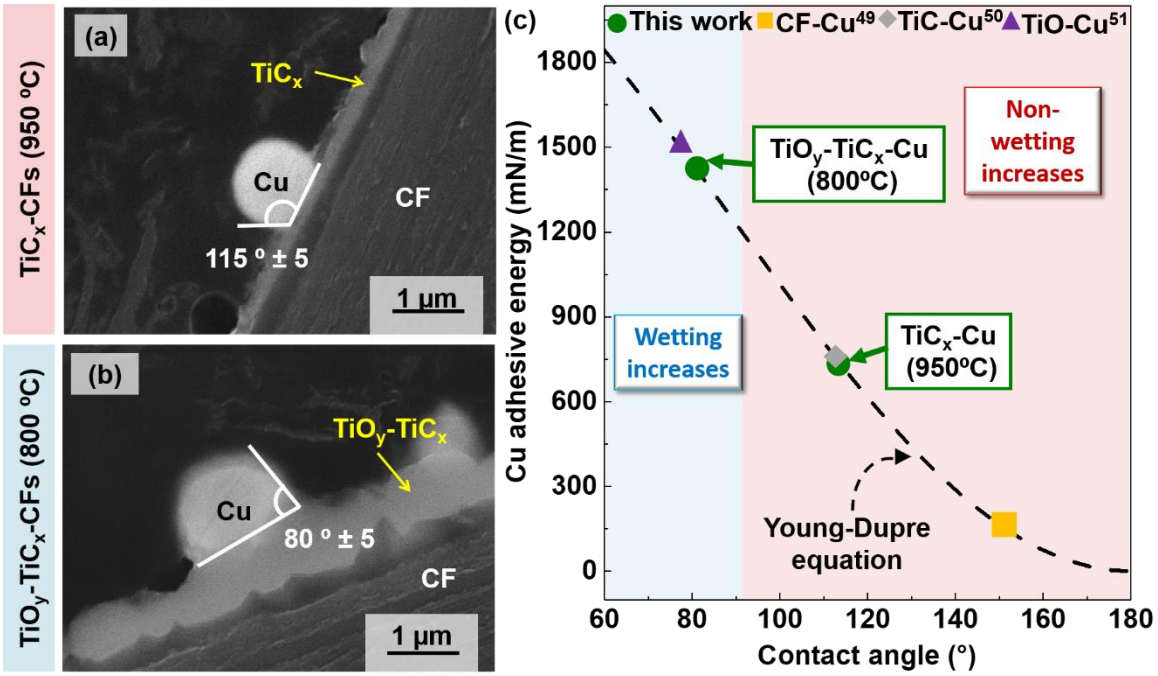

Figure 4.3-9 Cu contact angles measured on CFs coated with **(a)** TiCx and **(b)** TiOy-TiCx prepared at 800 and 950 °C, respectively. **(c)** Adhesive (wetting) energy vs. contact angle measured in this work (●) compared to values reported by others for Cu on CF (■),[40] TiC (♦),[195] and TiO (▲).[196]

The software imageJ was used to determine the surface coverage of Cu particles on coated CFs. First, the SEM micrographs presented in **Figure 4.3-10 (a)-(d))** were modified using the threshold tool to match the surface coverage of Cu and TiC layer. Once the threshold was well adjusted, the surface coverages were determined using the surface measuring tool. Finally, it is found that, in the cases of TiO_y-TiC_x and TiC_x CFs, 48% and 9% are covered by Cu and 52% and 91% by TiC, respectively. Thus, the surface coverage matches the results found by XPS (50% TiO_y for TiO_y-TiC_x CFs and 10% TiO_y for TiC_x CFs). The surface coverages by Cu droplets on the coated and bare CFs (**Figure 4.3-8**) were then compared with the fraction of TiO_y in the coatings (**Figure 4.3-10 (e)**).

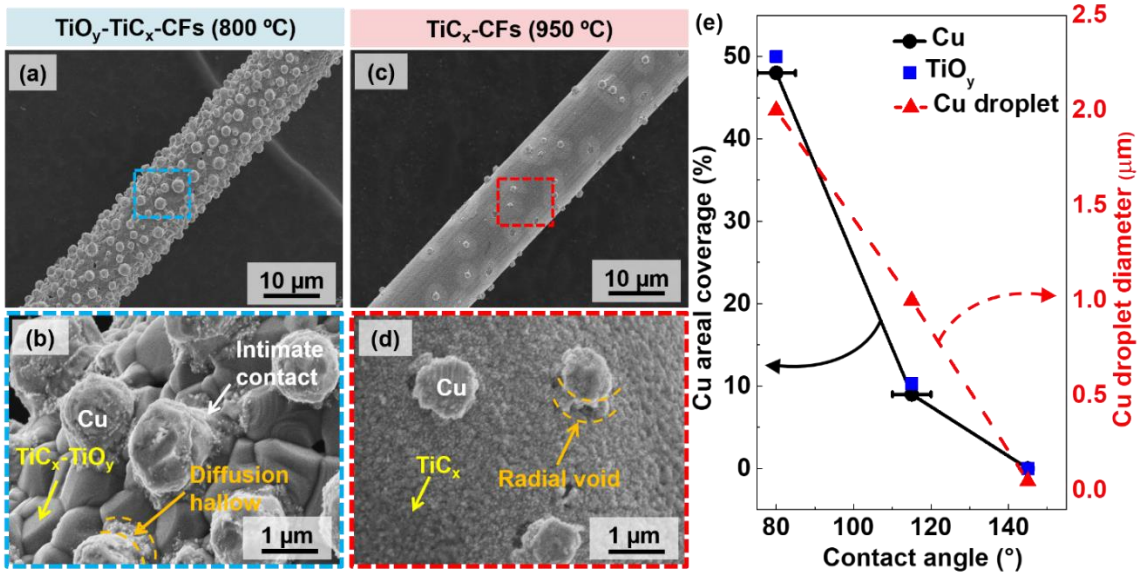

Figure 4.3-10 SEM micrographs showing the wetting behavior of Cu on the coated CFs prepared at **(a)**, **(b)** 800, and **(c)**, **(d)** 950 ℃. **(e)** Measured Cu area coverage with the equivalent TiOy content and droplet diameter as functions of the contact angle.

The Cu coverage is five-fold greater on the TiO_y-TiC_x CFs than on the TiC_x CFs. As expected, the Cu coverage of the bare (unreacted) CFs is negligible. The transition from low to high wettability correlates perfectly with the steady increase in the TiO_y content in the TiC_x coatings. The improved Cu wettability achieved with the graded TiO_y-TiC_x coatings developed in this work suggests a rather simple processing pathway for producing robust interphase in metal-carbon composites. The simplicity and cost-effectiveness of the molten-salt process have been extensively used to prepare a TiC interphase in Cu/C composites. Often high coating temperature is employed, resulting in the formation of a pure TiC layer.[163,186] As demonstrated previously, TiC is known as a non-wetting material on molten Cu with a contact angle of 115 º. The development of a tailored TiO_y-TiC_x coating enables the formation of strong interphase between Cu and C in comparison with a pure TiC layer. The strong interfacial bonding observed in this work between the graded

TiO_y-TiC_x layer and Cu could enhance the interaction between molten Cu and coated-C during the composite fabrication via laser-assisted AM which will be the focus of the next chapter.[153,154]

4.3.4 The kinetic analysis of the coating formation process

To further characterize the TiC_x growth process, we rapidly quenched the molten salt at intermediate stages to "freeze" the state of the reactions. Specifically, we are interested in examining the intermediate states of the molten salt, CFs, interphase, and Ti reactant particles. The growth process is governed by three main steps: 1) oxidation-driven dissolution of Ti particles into the salt (Ti^o to Ti^{n+}),[197,198] 2) diffusion mass transport of Ti^{n+} to the outer surface of the CFs or the TiC_x-CF interphase, and 3) Ti and C mass transport through the TiC_x interphase layer and reaction (**Figure 4.3-12**).

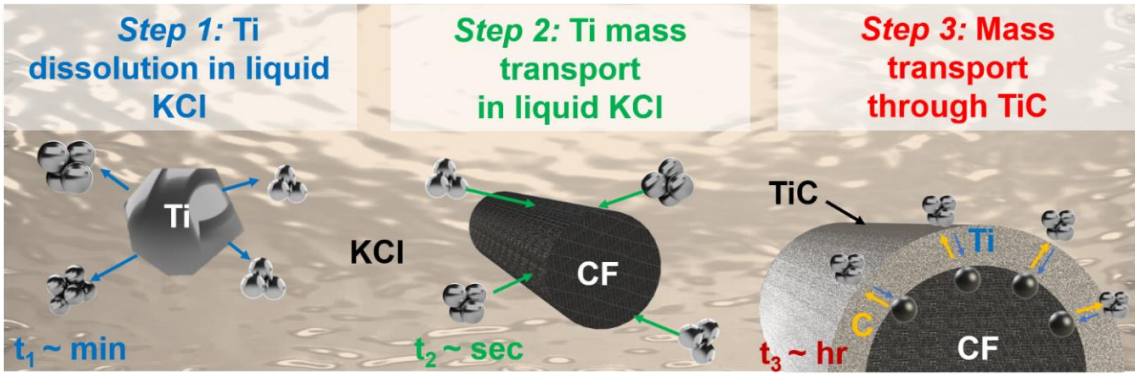

Figure 4.3-11 Schematic of the 3 main steps of the molten-salt coating process.

Regarding Ti dissolution (step 1), we were able to observe the intermediate state of Ti particles in the sample that was heated at 800 ºC for 0.5 h and then quenched. The results show that the original 40 µm Ti particles were not only dissolved but also disintegrated into small sub-particles (presumably individual Ti grains) that undergo further and more

rapid dissolution due to a greater surface- -to-volume ratio (**Figure 4.3-12 (a)**). The dissolution time of a Ti particle in an infinite KCl melt can be estimated as follows:[199]

$$t_d \sim \frac{\frac{\rho_{Ti}}{M_{Ti}} \times r_{0\,Ti}^{x}}{2D_{Ti^{n+}} \times \Delta C_{Ti}}, \quad \textbf{(15)}$$

where ρ_{Ti} is the density (4.59 g/cm^3), M_{Ti} is the molar weight (47.9 g/mol), R_{0Ti} is the radius of Ti particles (20.10^{-6} cm), D_{Ti}^{n+} is the diffusion coefficient for Ti^{n+} in molten KCl. The diffusion coefficient can be estimated from the viscosity (η) by the well-known Stokes-Einstein equation:

$$D \sim \frac{kt}{6\pi\eta r_h}, \quad \textbf{(16)}$$

where r_h is the effective hydrodynamic radius of the Ti^{n+} and k is Boltzmann's constant. The reported viscosity of molten KCl at 800 ºC is quite low (~1.2 mPa-s).[200] Thus, assuming an effective Ti^{n+} radius of ~0.1 nm that yields a diffusion coefficient of 8.10^{-6} cm^2/s. Finally, $\Delta C_{Ti} = C_{sat} - C_b$ where C_{sat} is the concentration of Ti^{n+} at saturation and C_b in the liquid KCl. We are interested in estimating the time to dissolve a Ti particle in the early stage of the process. Thus $C_b = 0$ and the following simplification can be made:

$$\Delta C_{Ti} = C_{Sat}, \quad \textbf{(17)}$$

Sekimoto et al. reported the saturation concentration of Ti^{2+} and Ti^{3+} in KCl-NaCl at 740 ºC are of about 1.10^{-3} to 1 mol/l.[197] By using the lowest Ti^{n+} concentration, the result shows the dissolution time is concise and of about 4 min.

The rate of diffusion mass transport of Ti^{n+} to the outer CFs or TiC_x-CF interphase surface (step 2) is controlled by the viscosity of the KCl and the mean distance between

the Ti^{o} particles and the CFs. Assuming a statistical average distribution of particles, the mean interparticle distance is, conservatively, smaller than 100 μm. The approximate time for Ti^{n+} to diffuse this distance can be estimated from:

$$t_d \sim \frac{\langle x \rangle^2}{2D_{Ti^{n+}}}, \quad \textbf{(18)}$$

Eq **(18)** gives an estimated time of t_d < 10 s to diffuse the 100 μm (mean Ti^0 - CF interparticle distance). The conclusion from the simple analysis above is that both the particle dissolution (step 1) and Ti^{n+} diffusion mass transport (step 2) are fast. Thus, the process step governing the rate of TiC_x coatings formation is step 3, the diffusion and mass transport of C. Semi-qualitative analyses of XRD peaks intensities of coated CFs were used to follow the reaction versus time at temperatures of 800 and 950 ºC as presented in **Figure 4.3-12 (b)** and **(c),** respectively. The integrated XRD peak intensities at 800 ºC show significant formation of TiC_x even after 0.5 h (**Figure 4.3-12 (d)**). Moreover, the amount of TiC continuously increases with time as Ti decreases. After 3 h of reaction, the Ti is only present in trace amounts, and none is observed after 5 h. At 950 ºC, complete Ti dissolution occurs essentially only after 0.5 h as evidenced by the lack of a Ti XRD peak and the high TiC_x signal. Also, the TiC peak intensity is essentially constant from 0.5 h to 5h within the XRD analysis error limits. These results agree with our calculations for the rapid dissolution and diffusion of Ti particles in molten KCl.

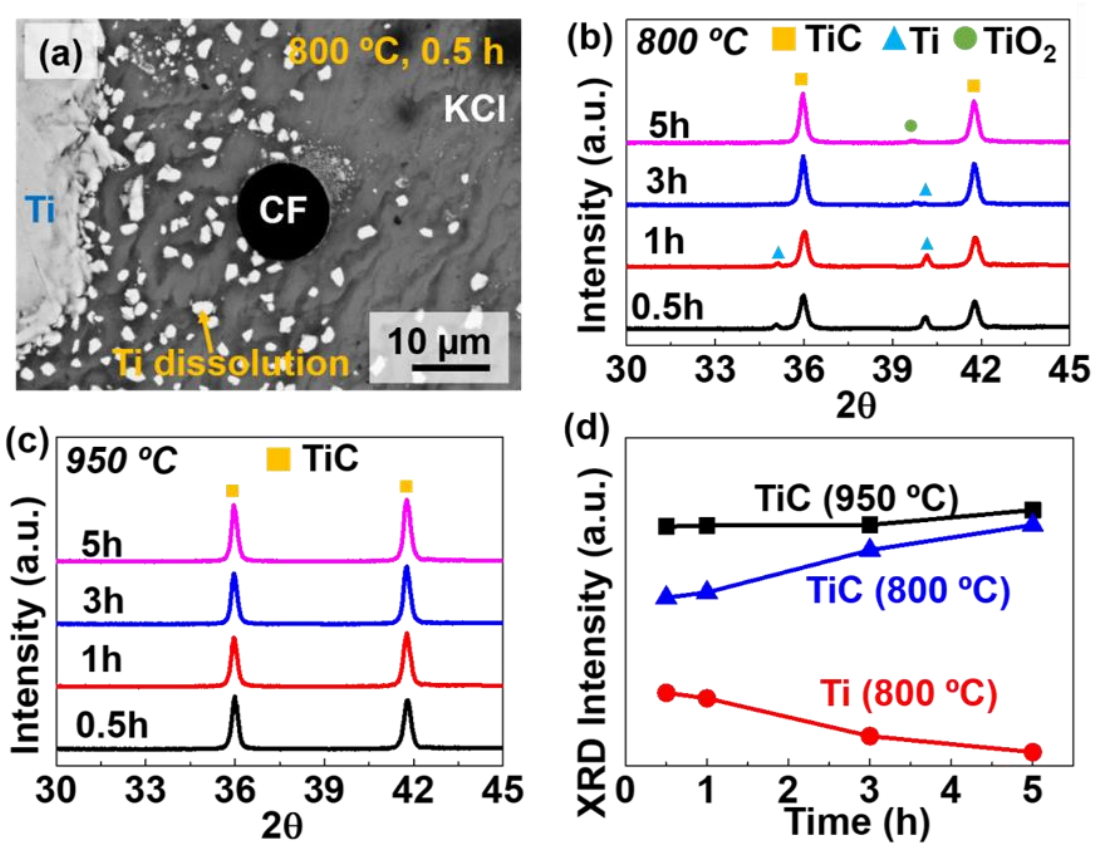

Figure 4.3-12 (a) SEM micrographs of rapidly quenched salt at 800 after 0.5 h, XRD diffractograms of washed CFs for coating times ranging from 0.5 to 5 h for **(b)** 800 and **(c)** 950 ºC, **(d)** XRD peak intensities as functions of the coating time.

To find more insight into step 3; Ti and C mass transport through the TiC_x layer, the growth kinetics of the coatings were investigated. To calculate these parameters, the variation of the coating thickness with the coating time was monitored up to 5 h between 800 and 950 °C. As shown in the cross-sectional SEM micrographs of the as-prepared coatings (**Figure 4.3-13)**, the coating thickness increases as the coating time and temperature increase.

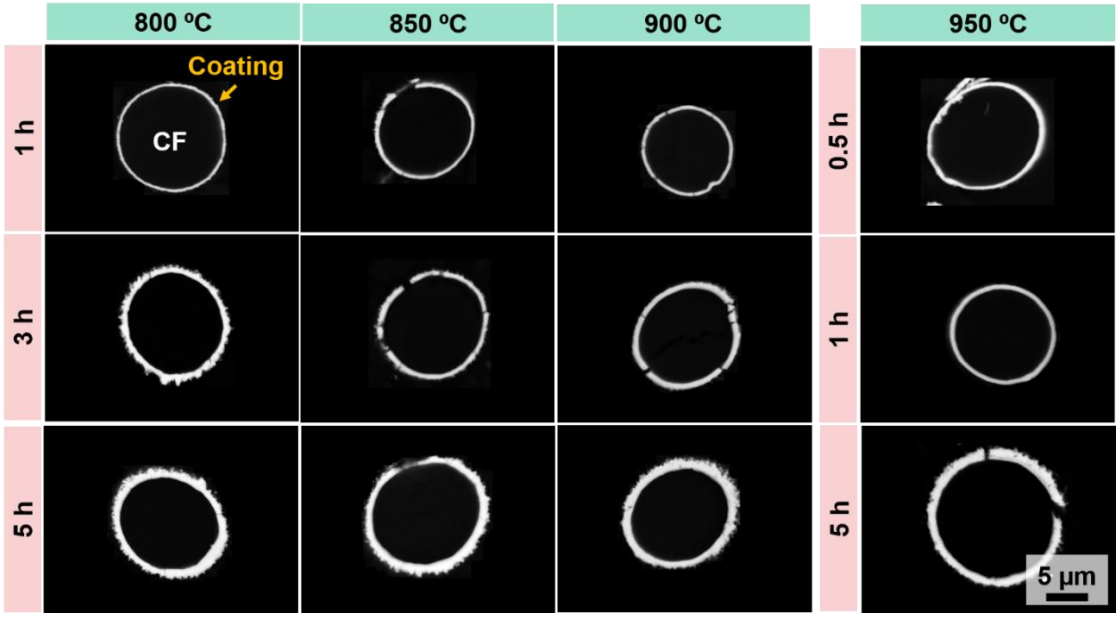

Figure 4.3-13 SEM micrographs of the cross-sectional views of the CFs coated at different temperatures and times used to determine the diffusion coefficient and activation energy.

According to classical kinetic theory, the coating thickness can be described as a function of the square root of the coating time using the following equation:[201,202]

$$x = \sqrt{D_{eff} T}\,, \tag{19}$$

where x is the carbide coating thickness (cm), t is the coating time (s), and D_{eff} is the effective diffusivity through the TiC_x layer (cm^2/s). As shown in **Figure 4.3-14 (a)**, the coating thickness (x) shows a linear increase with the square root of the coating time. The diffusivity, D_{eff}, can be retrieved from the slope of the curve. The value increases with the coating temperature ranging from 3.8×10^{-13} to 1.3×10^{-12} cm^2/s. These values, agree reasonably with values report by Koichiro Koyama et al. for the diffusion of C in TiC

containing a small amount of oxygen and over a temperature range similar to that used in this work.[203]

The effective diffusivity is expected to show an Arrhenius temperature dependence by an activation energy:[204,205]

$$D_{eff} = D_0 \, e^{\frac{-Q_{eff}}{RT}}, \quad \textbf{(20)}$$

where D_0 is the pre-exponential factor, Q_{eff} is the activation energy (J/mol) governing the process and R is the gas constant (J/mol.K). The effective process activation energy was determined to be ~88 KJ/mol by linear regression to the data in **Figure 4.3-14 (b)**. As might be expected, the activation energy is lower than the one reported by Knuth Albertsen et al. for grain boundary diffusion of C in bulk TiC below 1100 ºC (174 kJ/mol).[206] This could be due to the enhancement of the grain boundary diffusion due to the difference in microstructures between bulk and coated TiC.[206,207]

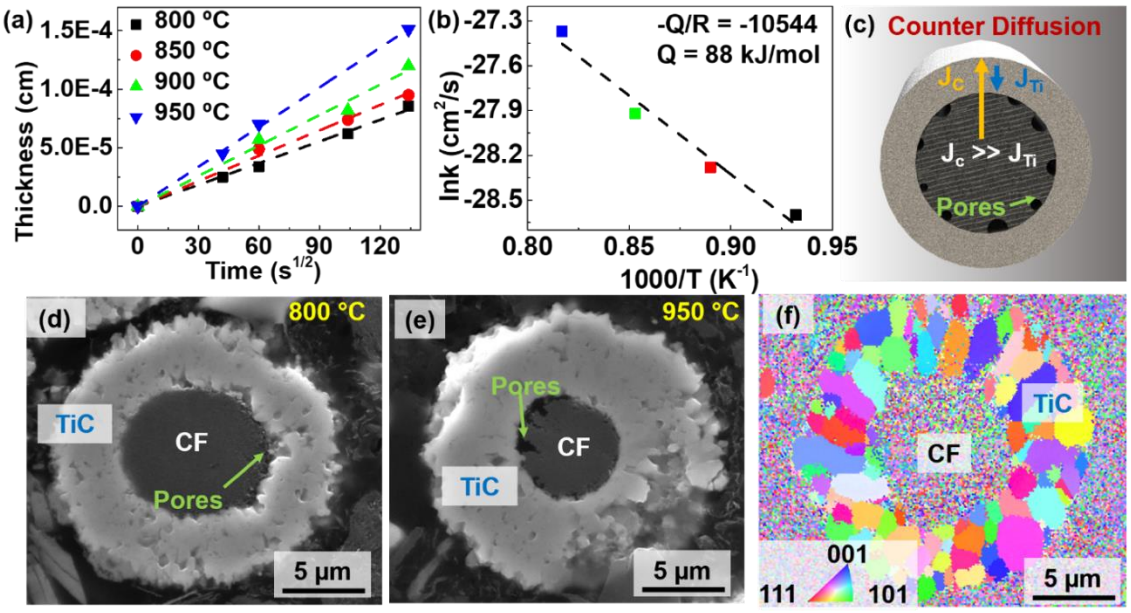

Figure 4.3-14 (a) Plots of the coating thickness as functions of the square root of time for different coating temperatures; **(b)** Arrhenius plot of D_{eff} as a function of the coating temperature; **(c)** a schematic of the counter-diffusion; cross-sectional view of coated CFs prepared at **(d)** 800 and **(e)** 950 °C, **(f)** EBSD mapping of the cross-section of a TiC-covered CF showing the distribution of grain orientations.

To better understand the diffusion mechanism behind the coating process, we coated CFs for 7 h at 800 and 950 ºC, respectively, with an equimolar mixture of Ti and C and examined the coating and the reaction interphase in greater details (**Figure 4.3-14 (d)** and **(e)**). Our data show evidence of the Kirkendall effect (**Figure 4.3-14 (c)**). Here the Kirkendall effect related to the rapid counter diffusion of C that ultimately generates voids at unreacted carbon interfaces.[208] The diffusion rates of C in TiC have been reported to be several order of magnitude faster than Ti in bulk TiC.[193] Consequently, the more rapid diffusion of C than that of Ti would be expected to generate Kirkendall like voids at the

reaction interface. Moreover, higher void generation was observed at 950 ºC than 800 ºC. This suggests that the C diffusion rate increases with the temperature.[191,193]

EBSD analysis was performed on the TiC_x coating obtained at 950 ºC (**Figure 4.3-14 (f))** and showed a polycrystalline columnar structure with an average grain size close to 1 µm. The grains arrange in a conformal structure. The grain boundaries are aligned along the radial direction. These grain boundaries may serve as an easy diffusion path for C and thus enhance the C diffusion rate at higher temperatures.

4.3.5 Graded TiO_2 – TiC coatings on diamond particles

In the previous part, we studied the impact of molten-salt-bath temperature on the TiC coatings on CFs. It was demonstrated that a low bath temperature at 800 ºC resulted in the formation of a TiO_2-TiC layer. Compared to a TiC coating on CFs, the TiO_2-TiC surfaces facilitated the adhesion of Cu particles on CFs. In this part, we performed a similar study to reveal the influence of molten-salt-bath temperature on the coatings on diamonds. **Figure 4.3-15 (a)** shows that the as-received D powder has an average diameter of 50 µm and smooth surfaces. After the TiC coating, the octahedron shape of the D particles is maintained (**Figure 4.3-15 (b)**); however, the surface morphology of the coating changes with the salt-bath temperature. As shown in **Figure 4.3-15 (c)** to **Figure 4.3-15 (f),** as the coating temperature increases, the surface becomes smoother. According to our understanding from previous studies, the surface roughness is closely related to the abundance of TiO_2 humps on top of the TiC coatings.

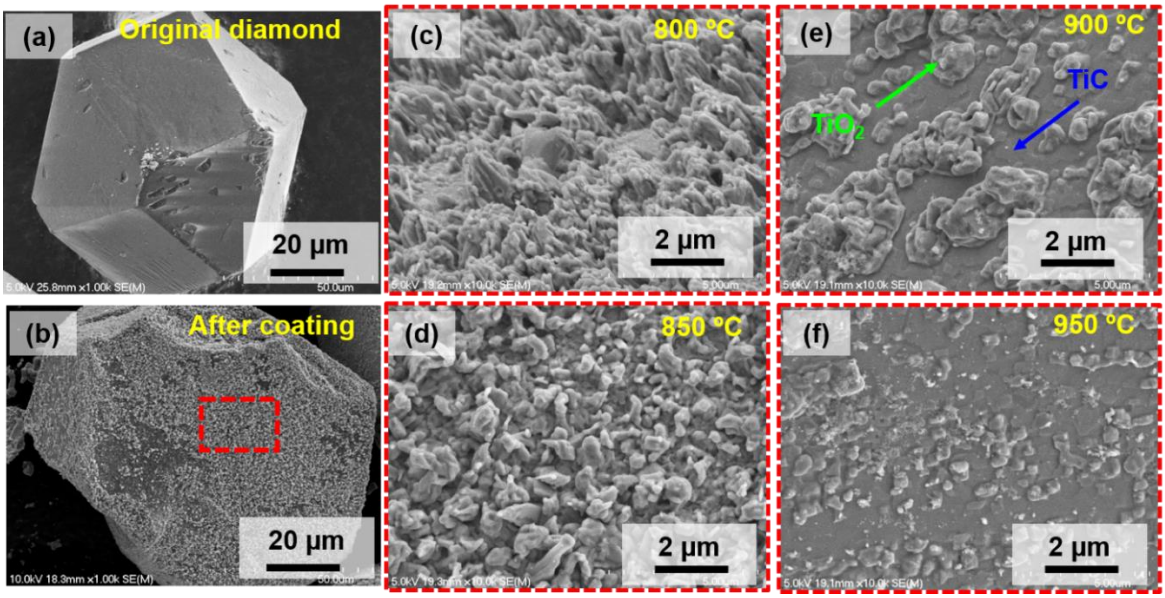

Figure 4.3-15 SEM micrographs of **(a)** an as-received D particle, **(b)** a D particle with TiO_2/TiC coating; high magnification SEM micrographs of D surface coated at **(c)** 800, **(d)** 850, **(e)** 900, and **(f)** 950 ºC, respectively.

The surface roughness of the coated diamonds was measured by an optical surface profiler. **Figure 4.3-16 (a)** to **(d)** shows 3D surface profiles of the coatings at salt-bath temperatures ranging from 800 to 950 ºC. It is noticed that the surface becomes smoother as the salt-bath temperature increases (**Figure 4.3-16 (e)**), which agrees with the SEM observations (**Figure 4.3-15**). The average surface roughness (R_a) vs. the salt-bath temperature is plotted in **Figure 4.3-16 (e)** and shows a sharp drop of R_a from 2.25 to 0.5 μm as the salt-bath temperature increases from 800 to 950 ºC.

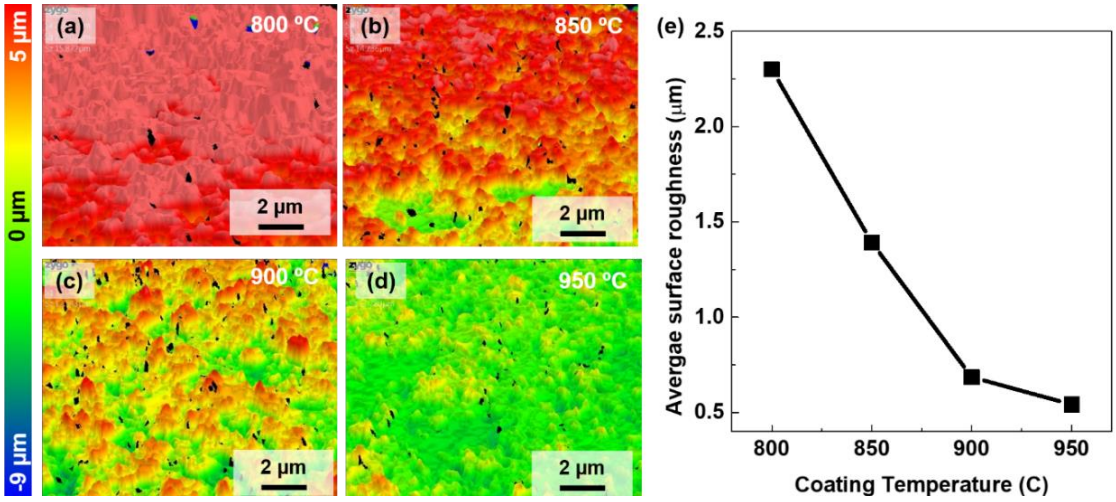

Figure 4.3-16 Surface analysis of diamond coated with TiO_2-TiC at **(a)** 800, **(b)** 850**, (c)** 900, and **(d)** 950 ºC; **(e)** the curve for the average surface roughness vs. the salt-bath temperature.

The chemical composition of the TiO_2-TiC coating was analyzed by Raman spectroscopy. Both TiO_2 and TiC have strong Raman signatures at 147 cm^{-1} and 262, 418, and 602 cm^{-1}, respectively, as can be seen in **Figure 4.3-17** [209,210].

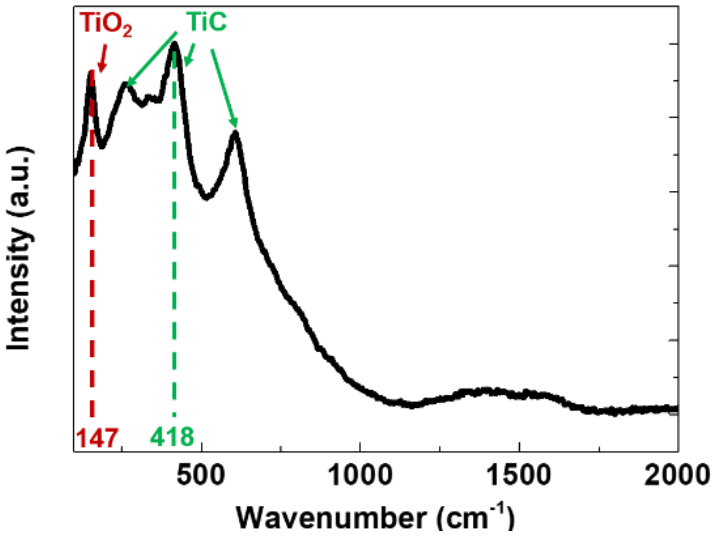

Figure 4.3-17 A typical Raman spectrum of TiO_2-TiC coating.

Raman mapping of the coating layer in term of their signature Raman band intensity (**Figure 4.3-18**) was performed to find the distribution of TiO_2 and TiC in the coatings using the peaks at 147 and 418 cm^{-1}, respectively. TiO_2 and TiC are represented by red and green colors, respectively. It is noticed that as the coating temperature increases, the TiO_2 fraction decreases while the TiC fraction increases.

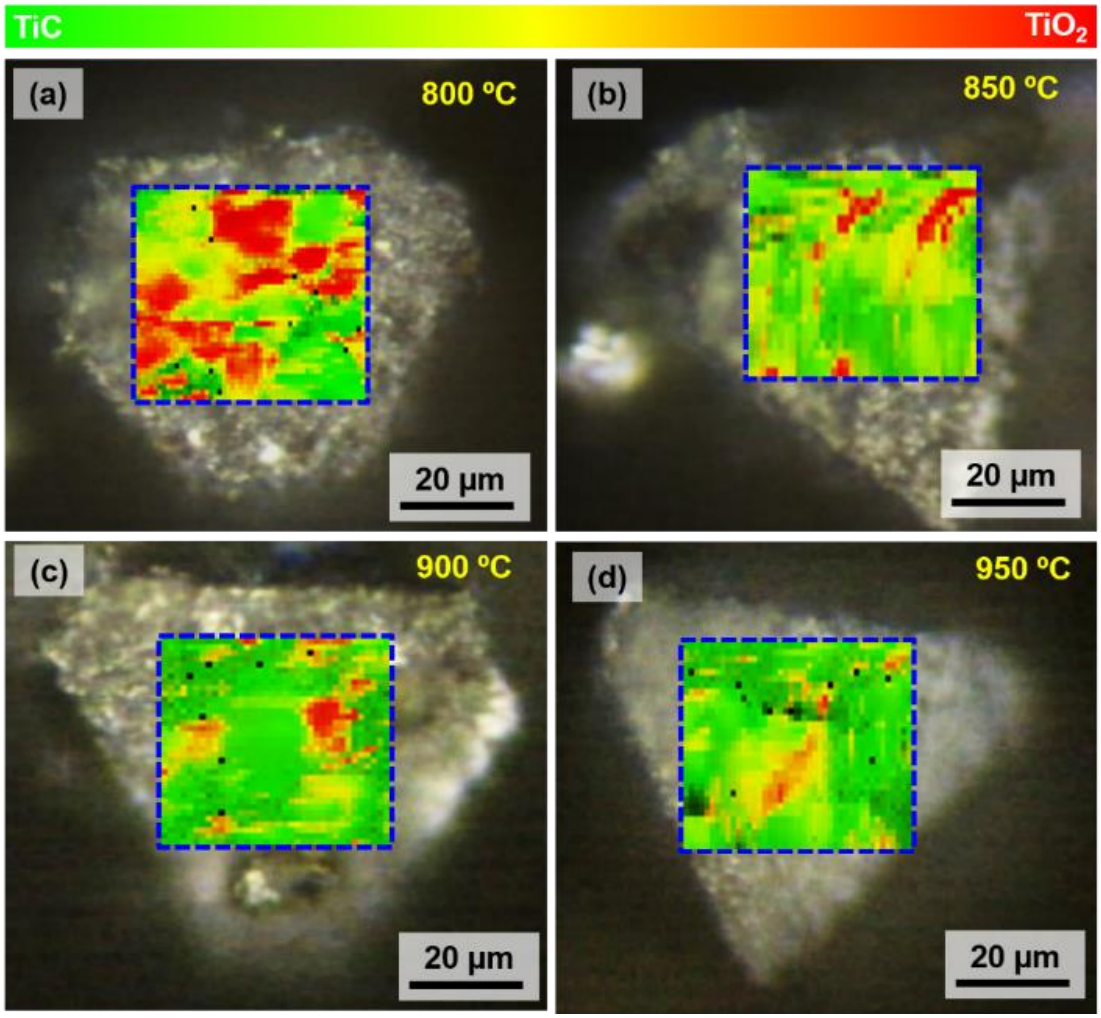

Figure 4.3-18 Raman mapping of diamond coated with TiO_2-TiC at **(a)** 800, **(b)** 850, **(c)** 900, and **(d)** 950 ºC, respectively. The red and green color represent TiO_2 and TiC, respectively.

4.3.6 Conclusions

In summary, tailored TiO_y-TiC_x coatings are synthesized on CFs. The TiO_y formation is observed after the dissolution of the molten salt in boiling water and is assumed to be the result of oxidation of reactive Ti sites near the exterior coated surfaces. The oxide-rich carbide coating shows significantly improved wettability with molten Cu compared to the carbide-rich layers. Notably, the Cu wetting angle for the TiO_y-TiC_x-CF samples prepared at 800 ºC is ~80º ± 5º with a Cu surface coverage of ~50% versus ~115º and ~ 10% for those of the TiC_x-CF samples prepare at 950 ºC. CFs alone show mostly no Cu coverage.

By varying the reaction temperature (800 to 950 ºC) and time (1 to 5 h) and using rapid thermal quenching, the formation mechanism is investigated. The results indicate a three-step process: 1) a short induction period controlled by rapid Ti dissolution in the molten salt, 2) rapid Ti mass transport in the molten salt and fast reaction at the CF surfaces, and 3) mass transport through the coating layer that is controlled by a competition of Ti and C diffusions.

Finally, the graded TiO_2-TiC layers developed on CFs are applied on D particles. It is shown that similar results are obtained. A TiO_2 layer forms on the D surfaces. The concentration of Ti oxide is found to be related to the coating temperature. A lower coating temperature leads to a lower diffusion of the reactant resulting in a partial oxidize coating. The Ti-based coating will be used later in the laser 3D printing of Cu/D composite materials.

4.4 Multilayer coatings of refractory carbide in a molten salt

4.4.1 Single-step coating of multilayer carbides in a molten salt

Creating a multilayer carbide coating could efficiently and effectively protect carbon materials under extreme environment (i.e., laser 3D printing). For that, the multilayer coating process necessitates a salt media which can dissolve several metallic powders; in our case Cr and Ti powders. The literature shows that a eutectic salt composed of sodium chloride and potassium chloride (NaCl:KCl) is suitable to coat carbon materials with Cr_3C_2 while KCl allows the formation of TiC layers on the CFs.[184,211] Therefore, KCl appears to be an excellent candidate as a reaction media to synthesize both TiC and Cr_3C_2 layers on CFs. To confirm the formation of these carbides, the CFs were coated using KCl at a time and temperature of 5 h and 950 ºC, respectively. After coating and washing away the salt, the CFs were analyzed by SEM using the back-scattered electron (BSE) mode to enhance the contrast between the CFs and the layers coated (Cr_3C_2 appears to be brighter than TiC which is brighter than C).[212] **Figure 4.4-1 (a)** shows the CFs coated using M = Ti, M = Cr, and M = Ti + Cr, revealing homogenous layers on all CFs throughout the anisotropic structure. The thicknesses of the 3 layers were similar, about 700 nm (**Figure 4.4-1 (a)**). However, the coating obtained by a Ti and Cr powder mixture consisted of two layers of contrast, suggesting the formation of two phases, as illustrated in **Figure 4.4-1 (b)**.

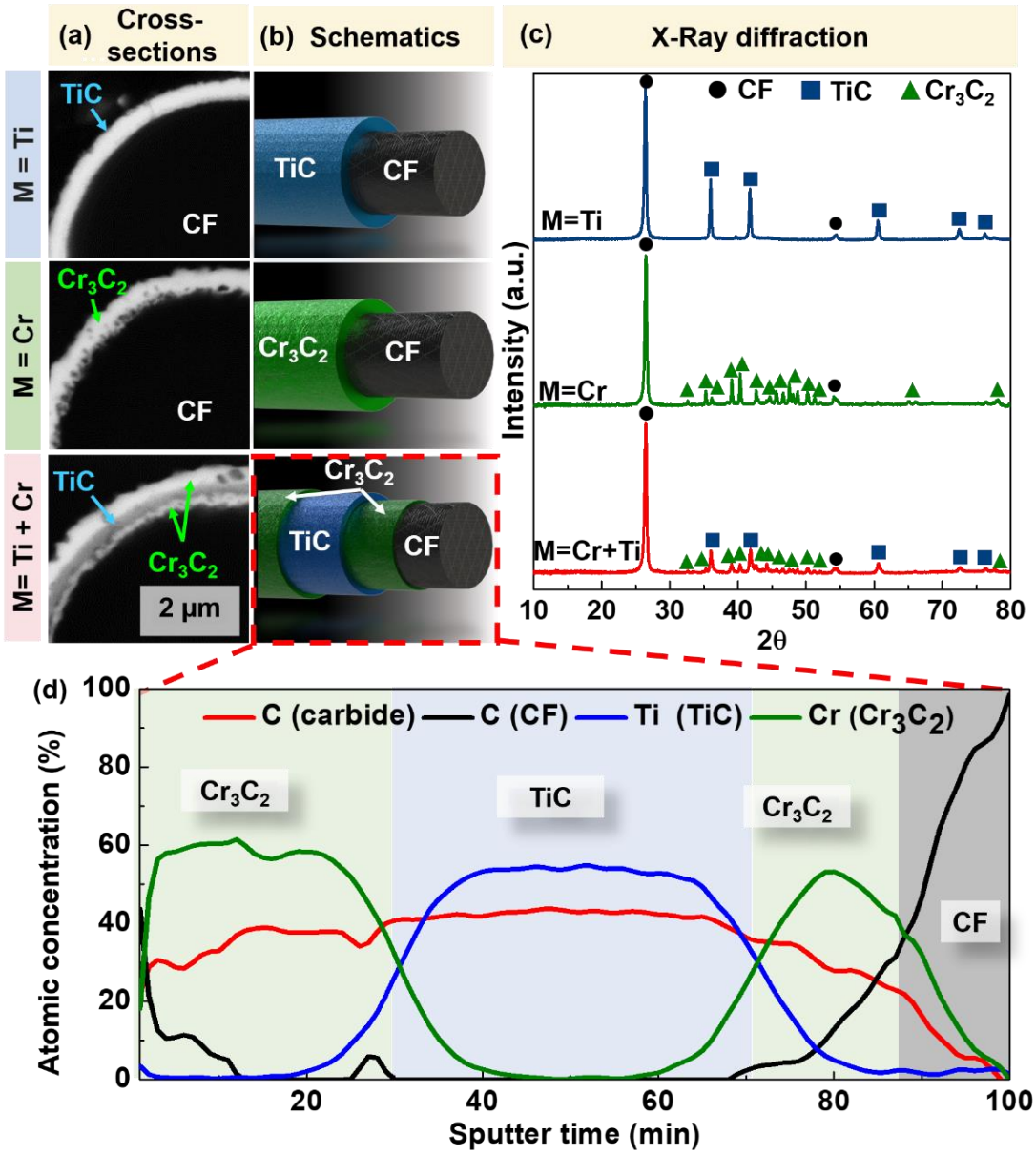

Figure 4.4-1 SEM micrographs of coatings on CFs with M = Ti, Cr, and Ti + Cr. **(a)** cross-sectional views, **(b)** schematic illustrations of the coatings with M = Ti, Cr, and Cr + Ti, and **(c)** XRD diffraction patterns of TiC, Cr_3C_2, and TiC + Cr_3C_2 coatings, and (**d)** AES depth profiles of the CFs coated in a Ti + Cr salt solution.

XRD was performed, as shown in **Figure 4.4-1 (c)** to confirm the formation of single carbide coatings (M = Ti, M = Cr) and to identify the crystalline phases of the multilayer

coating (M = Ti + Cr). When M = Ti or M = Cr, the diffractograms show peaks matching TiC, Cr_3C_2, and the CFs, respectively. In contrast, when M = Ti + Cr, the diffractograms displayed peaks attributed to both the Cr_3C_2 and TiC phases, indicating the formation of a multilayer carbide coating.

Nonetheless, Cr carbides have a non-negligible solubility in TiC at high temperatures (> 1300 ºC), which could contaminate the TiC layer and change its mechanical properties and oxidation resistance.[213–215] AES depth profiling was performed to analyze the chemical compositions of the multilayer coating. The creation of three distinct layers composed of 1) Cr_3C_2, 2) TiC, and 3) Cr_3C_2 layers were confirmed (**Figure 4.4-1 (d)**). In addition, no trace of Cr was detected in the TiC layer, and vice versa, which suggests no diffusion of Cr in TiC occurred at a coating temperature of 950 ºC. These results indicate that the formation of complex multilayer carbide coatings can be achieved using a single-step, molten-salt process at a low temperature (950 ºC).

4.4.2 Oscillatory reaction in a molten salt

The liquid salts containing a mixture of Ti + Cr and CFs were frozen at different coating steps using an air quenched method to understand how the layer sequence is formed in the molten KCl.

Figure 4.4-2 (a) shows the SEM micrographs of the salt quenched in the early stage of the coating at 950 ºC. Within a few seconds, submicrometer particles of Ti and Cr were observed, suggesting their dissolution in the molten salt. An XRD analysis of the coated fibers (**Figure 4.4-3**) showed that the peaks corresponded to both Cr_3C_2 and TiC phases,

indicating that the salt bath significantly reduced the reaction time similar to an analysis reported by Tohru Arai et al. for Cr carbides.[216]

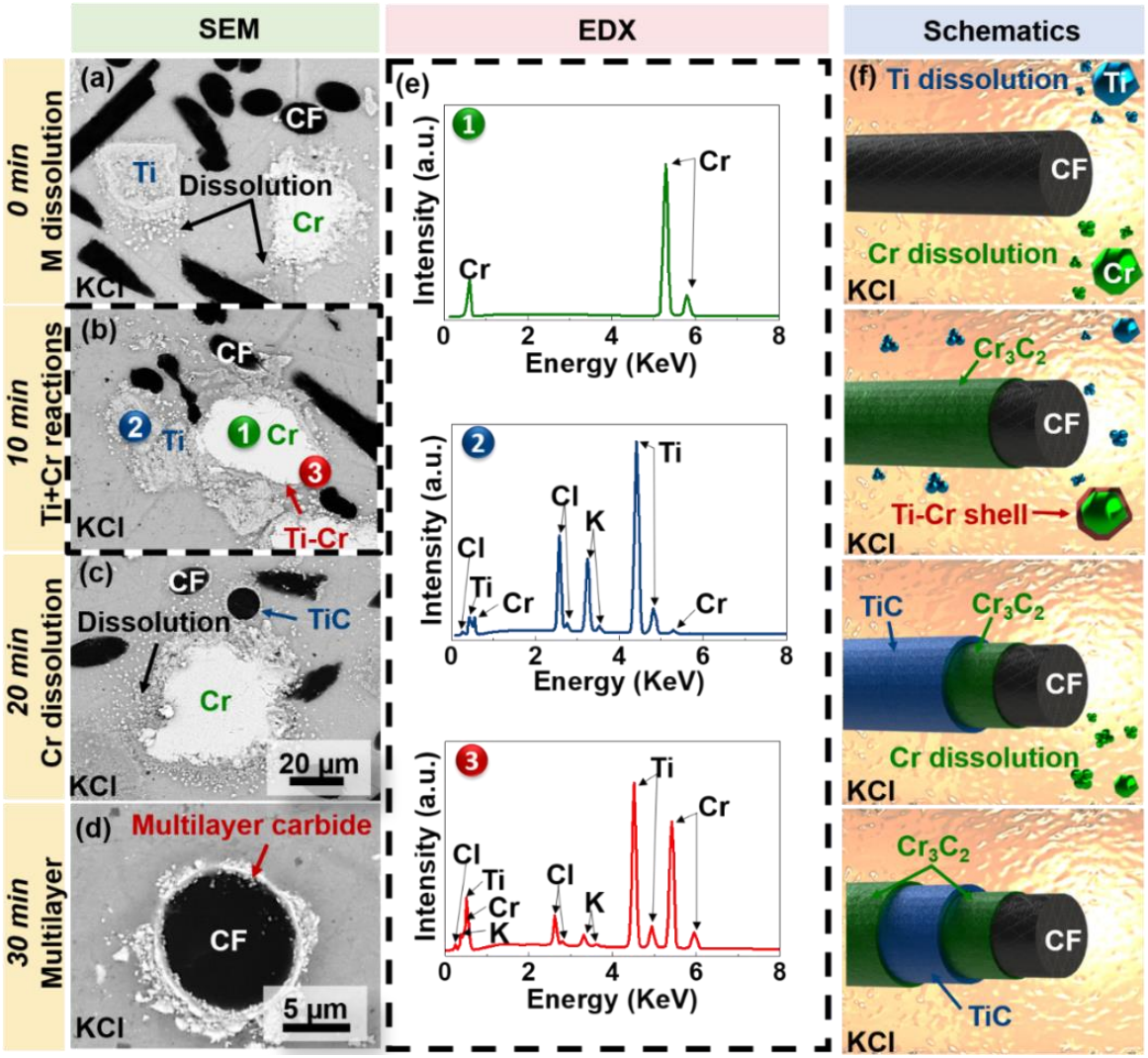

Figure 4.4-2 The steps to form the multilayer coating: **(a)-(d)** SEM micrographs after salt quenching at different times of 0, 10, 20, and 30 min, **(e)** EDX analysis of the salt quenched at 10 min, and **(f)** schematic illustration of the coating steps.

After 10 min, the number of Ti particles decreased as they transformed into TiC, while a shell surrounded the Cr particles (**Figure 4.4-2 (b)**). Three positions were analyzed by energy-dispersive X-ray spectroscopy (EDX) to define the chemical compositions of the

shells encapsulating the Cr particles: 1) the Cr particle, 2) the Ti particle, and 3) the envelope, as presented in **Figure 4.4-2 (e)**. The EDX spectrum of Point 1 shows the peaks corresponding to Cr. The analysis of Point 2 identifies the presence of Ti and a small amount of Cr. Finally, point 3 indicates the presence of both Ti and Cr with a composition of about 45 at.% Ti and 55 at. %Cr. These findings suggest that while Ti reacts with the CFs to form TiC, it simultaneously reacts with Cr to form a Ti-Cr shell around the Cr particles. Additionally, the binary phase diagram of the Ti-Cr system demonstrated that two phases could be obtained for a molar fraction of 0.55 Cr and 0.45 Ti. Temperatures below 1272 ºC yield both Cr_2Ti and Ti phases, while temperatures above 1272 ºC stimulate the formation of a Ti-Cr solid solution.[217] The XRD diffractogram obtained 10 min after coating (**Figure 4.4-3)** shows peaks corresponding to Ti and Cr metals and oxides (due to the air quenching), but no trace level of Cr_2Ti is observed. Moreover, reaction via the molten salt lowers the synthesis temperature and thus, a coating temperature of 950 ºC could suffice to form a Ti–Cr solid solution. **Figure 4.4-2 (c)** shows the salt mixture quenched after 20 min. At this point, the Ti particles and the shells around the Cr particles were no longer observable, suggesting their complete reaction. After 30 min, Cr powders dissolved in the salt, forming the outer Cr_3C_2 layer (**Figure 4.4-2(d)**).

The previous observations show an oscillatory reaction behavior in the molten salt, leading to the formation of a complex multilayer coating. Especially, in the early stages of the coating process, Ti and Cr saturated the liquid salt and the first Cr_3C_2 layer forms. Next, the TiC layer nucleated on the CFs and Ti surrounds the Cr particles, preventing further Cr dissolution. After the completion of the TiC layer, Cr dissolved in the salt reacted with the CFs, creating the final Cr_3C_2 layer, as illustrated in **Figure 4.4-2 (f)**.

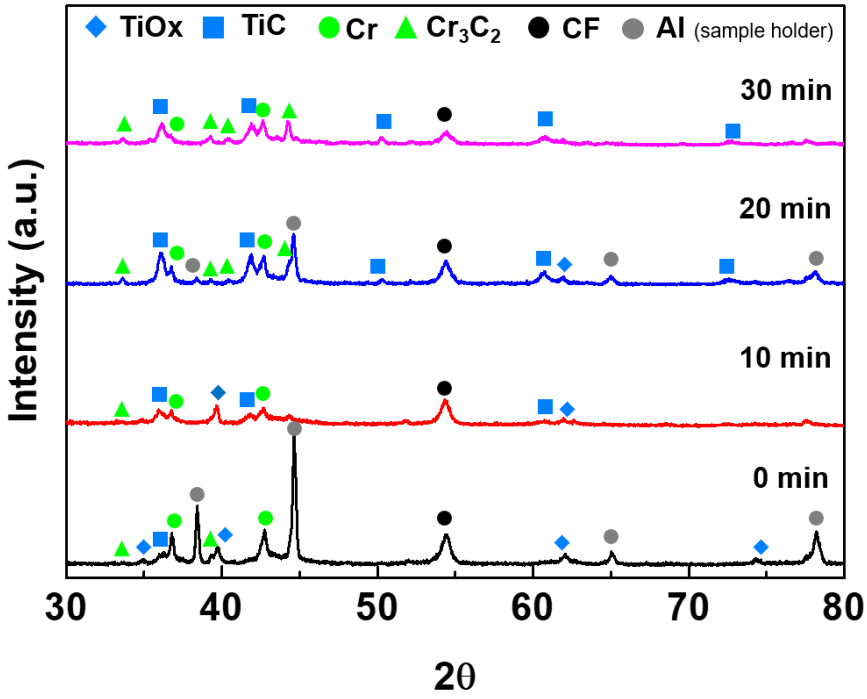

Figure 4.4-3 XRD diffractogram of the quenched CFs after salt dissolution for different coating times between 0 and 30 min.

4.4.3 The kinetic analysis of the multilayer coating

To clarify the formation of the first Cr_3C_2 layer during the early stage of the coating, the kinetic growth of single carbides (M= Ti, M = Cr) was studied independently at different temperatures and times ranging from 800 to 950 ºC and 1 to 5 h, respectively, as shown in **Figure 4.3-13** and **Figure 4.4-4.**

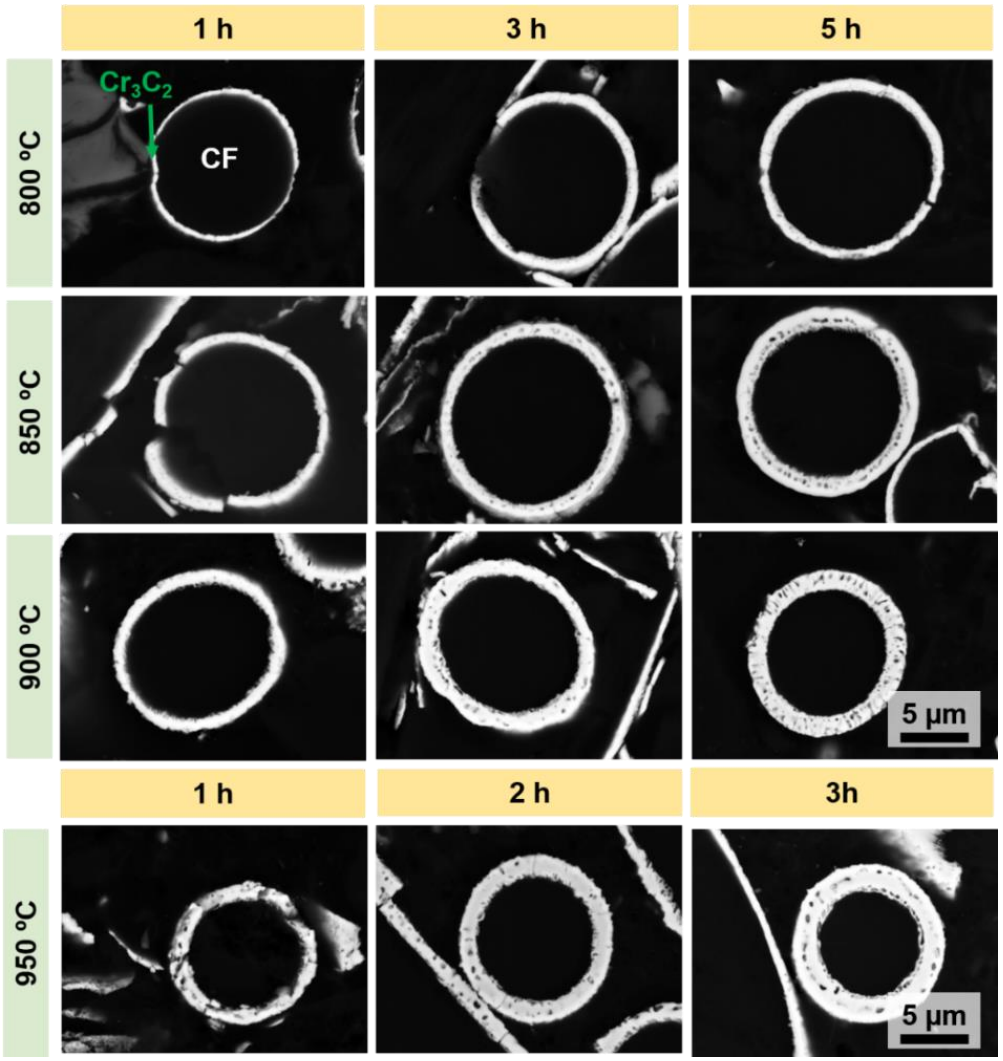

Figure 4.4-4 BSE-mode SEM cross-sectional views of CFs coated with Cr_3C_2 for 1 to 5 h at 800, 850, 900, and 950 ºC for different times between 1 and 3 h.

The measured D_{eff} for TiC and Cr_3C_2 vs. the coating temperature are plotted in **Figure 4.4-5 (a).** The kinetic analysis shows that at 950 ºC, D_{eff} is equal to 1.3×10^{-12} and 4.4×10^{-12} cm^2/s for TiC and Cr_3C_2, respectively. Both values agree well with C diffusion in TiC and Cr_2C_3 reported by both D.D Himbeault et al. and Koichiro Koyama et al..[203,207] The fact that C diffuses three times faster in Cr_3C_2 at 950 ºC than in TiC could explain why Cr_3C_2 formed first, as illustrated in **Figure 4.4-5(b)**.

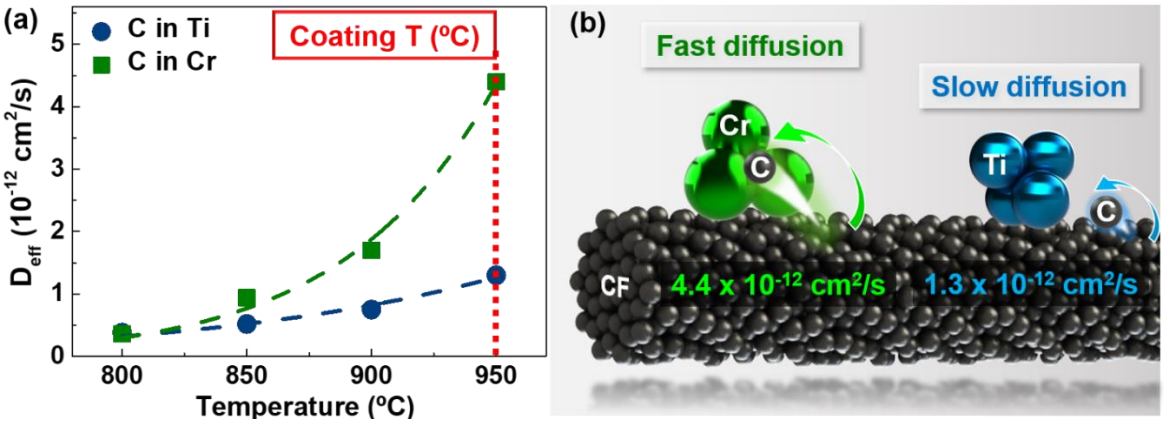

Figure 4.4-5 (a) C diffusion coefficients in both Ti and Cr as functions of the coating temperature, **(b)** schematic illustration of the C diffusion.

Additionally, the counter diffusion of C in Ti and Cr carbides is qualitatively explained based on the Kirkendall-induced porosity.[218] Once pore formation occurred, the surface diffusion became the predominant driving force and led to channel formation, as illustrated in **Figure 4.4-6 (a)**.[208] Both TiC and Cr_3C_2 layers were grown with an equimolar mixture of metals and carbon for 7 h at 950 ºC to obtain a thick layer. **Figure 4.4-6 (b)** depicts the formation of pores at the TiC-CF interphase with a remaining CF diameter of 7 µm (~ 11 µm initially). In contrast, channels formed near the interface between the Cr_3C_2 layer and the CF surfaces, with its diameter reduced to 5 µm (**Figure 4.4-6 (c)**). These findings imply that C has faster reaction and diffusion in Cr_3C_2 produced by molten salt than in TiC, which supports the kinetic analyses carried out in this study.

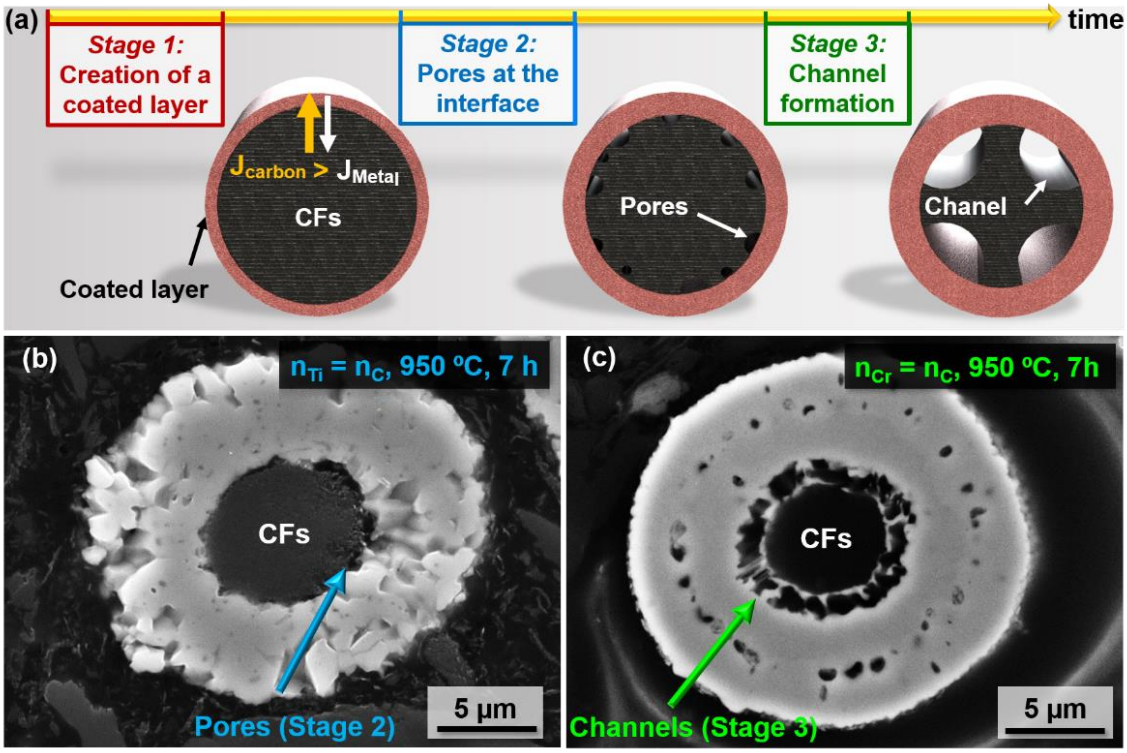

Figure 4.4-6 (a) schematic illustration of the Kirkendall effect and coatings at 950 ºC for 7 h with $n_M = n_C$ for **(b)** M = Ti and **(c)** M = Cr.

4.4.4 Extreme temperature resistance of the multilayer-coated CFs

A multilayer coating containing both TiC and Cr_3C_2 carbides should act as effective protective barriers for the CFs due to the high strength and excellent wear resistance of TiC, combined with the superior oxidation and corrosion resistance of Cr_3C_2.[219] An oxy-acetylene flame was used for high-temperature oxidation tests because chemical erosion happens at high temperatures, requiring excellent wear resistance, chemical stability, and low oxidation.[220] To demonstrate the advantage of multilayer (Cr_3C_2-TiC-Cr_3C_2) over single carbide coatings (TiC and Cr_3C_2), coated CFs were glued onto a WC substrate and subjected to the flame at 10 mm from the inner cone (~ 1200 ºC) for 60 s, as illustrated in **Figure 4.4-7 (a)**. Prior to the oxidation test, the surface of the TiC layer (M = Ti) appeared

smooth. After the oxidation, particle-like features appeared on the surface of the TiC layer, indicating TiC oxidation (**Figure 4.4-7 (b)**).

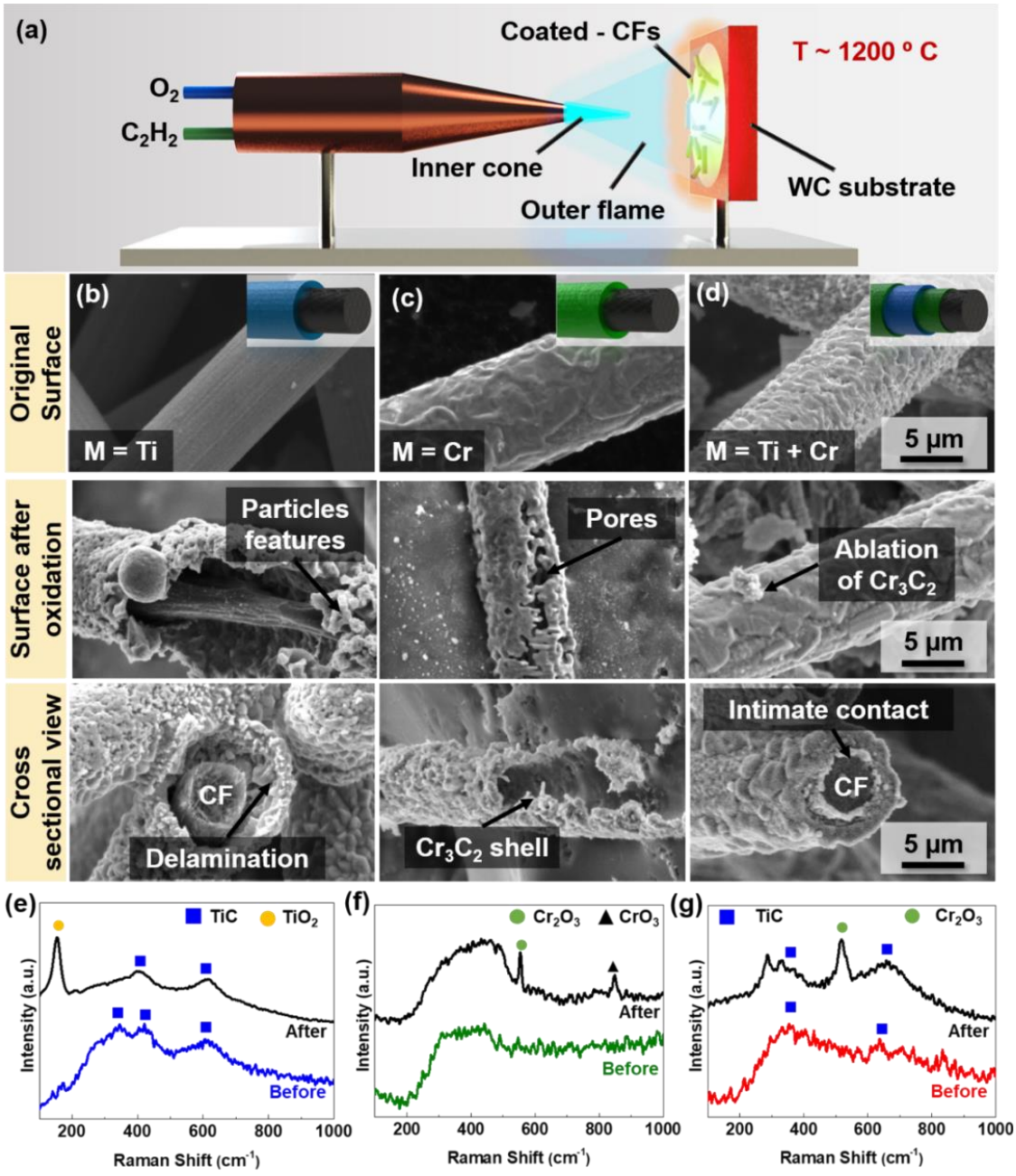

Figure 4.4-7 SEM micrographs before and after testing for CFs with **(a)** TiC, **(b)** Cr_3C_2, and **(c)** Cr_3C_2/TiC/Cr_3C_2 coatings. **(d)** Schematic illustration of the high temperature gas

erosion. Raman spectra before and after the oxidation test for **(e)** M = Ti, **(f)** M = Cr and **(g)** M = Ti + Cr.

To investigate the oxidation of the TiC layer, Raman spectroscopy was performed and confirmed the presence of a strong, sharp peak attributed to TiO_2 (**Figure 4.4-7 (e)**). Moreover, the cross-sections of the coated CFs showed that the CFs were not completely vaporized but delaminated at the interfaces between the TiC layers and the CFs. In contrast, the initially smooth surface of the Cr_3C_2 layer (M = Cr), obtained after the salt step, became porous. Additionally, there was no more trace of CFs in the cross-sectional view, indicating that the oxidation of Cr_3C_2 occurred, as shown in **Figure 4.4-7 (c)** and **Figure 4.4-7 (f)**. Finally, when M = Cr + Ti, the Cr_3C_2 layer was partially eroded after oxidation (**Figure 4.4-7 (d)** and **Figure 4.4-7 (g)**). However, the TiC layer underneath remained intact. The CFs remained unchanged with an intimate CF-coating interface, as shown in the cross-sectional view. These results indicate that the outer Cr_3C_2 layer served as a sacrificial layer that protected the TiC from oxidation, and then the TiC layer and the inner Cr_3C_2 layer protected the CFs from the extreme environment.

Therefore, the single-layer coating of TiC or Cr_3C_2 is not suitable as oxidation barrier coating on CFs. Delamination and pores were observed on coatings resulting in the partial or total oxidation of the CFs. Nevertheless, when TiC and Cr_3C_2 were combined as a multilayer coating, an intimate CF-coating interface is observed. In addition, the fiber's graphitization was estimated based on the D-band (~1350 cm^{-1}; related to defects and disorder in the carbon structure) and G-band (~1580 cm^{-1}, results from ordered graphitic structure) ratio (I_D/I_G) (**Figure 4.4-8**).[221] It is found that I_D/I_G is of about ~ 0.90 for the original and after the flame exposure CFs. Hence, the high graphite crystallinity was

conserved and demonstrates the effectiveness of the multilayer coatings as a protection barrier for carbon materials.

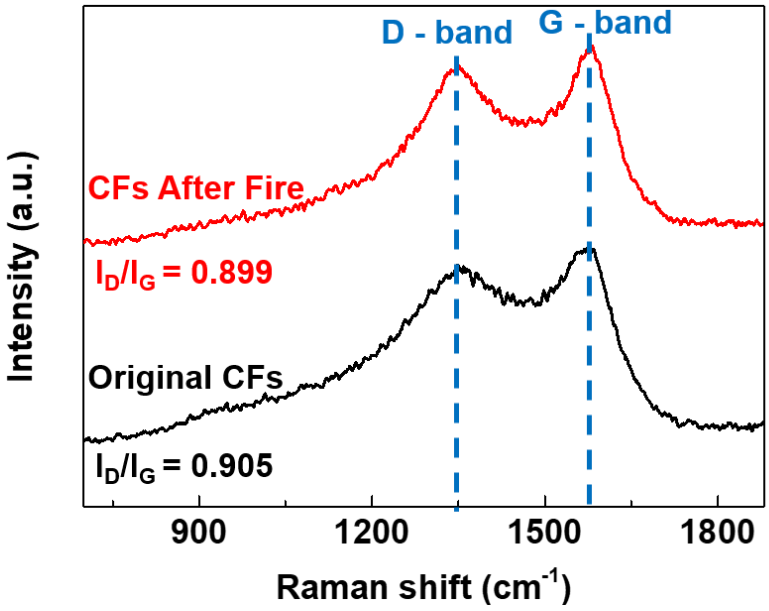

Figure 4.4-8 Raman spectra of original CFs and multilayer-coated CFs after the flame exposure.

4.4.5 Conclusions

In summary, a molten-salt coating process is investigated using Ti, Cr, and Ti + Cr to produce homogenous coatings of single and multilayer carbides on CFs at a relatively low temperature (950 ºC). The microstructural characterization of the complex multilayer carbides shows a three-layered coating composed, starting from the CFs, of an inner Cr_3C_2 layer, followed by a TiC layer, and an outer Cr_3C_2 layer. The study confirms the advantage of the molten-salt process as a single-step, cost-effective coating method for synthesizing multilayer carbides on CFs.

Furthermore, analyses of the coating process show an oscillatory reaction mechanism of forming the multilayer carbide coating. In the early stage of the process, the liquid salt is saturated with Ti and Cr, which react with the CFs to form carbide layers. Subsequently, Ti began reacting with Cr particles to form a shell, which prevents further Cr dissolution. Once a complete TiC layer formed, Cr is free to dissolve inside the liquid salt and react with the CFs to create the final Cr_3C_2 layer. Additionally, the kinetic growth of TiC and Cr_3C_2 show that the Cr_3C_2 layer grew twice as fast as the TiC layer, implying a faster reaction/diffusion of C species in Cr. Thus, the inner Cr_3C_2 layer resulted from a kinetic regime at a high temperature (950 ºC).

Finally, the advantages of the multilayer over a single carbide coating are demonstrated by high-temperature oxidation under an oxy-acetylene torch. The multilayer coatings composed of TiC and Cr_3C_2 combined the physical properties of both materials to create an efficient and effective barrier layer for CFs in harsh environments.

5 Additive Manufacturing of Cu / D Composite Materials

5.1 Introduction

The manufacturing of materials with high thermal conductivity (TC) and intricate shapes is crucial for the development of highly efficient heat-exchanging components for microelectronic industries.[35,36] Creating a composite material consisting of two highly thermal conductive elements, such as Copper (Cu) and Diamond (D), may fulfill these unmet needs.[37] However, the lack of chemical affinity between Cu and D and the difficulty of machining D-based materials presents significant challenges.[38,39] Extensive research has been devoted to achieving highly thermally conductive metal matrix composites (MMCs) by promoting the interfacial bonding between Cu and D.[222,223] Common interphases are composed of carbide elements and have demonstrated enhanced thermal properties compare to pure Cu.[163,224–226] However, conventional manufacturing methods, such as high-pressure sintering, spark plasma sintering, or infiltration, suffer several limitations when sophisticated geometries are required.

The recent development of laser 3D printing has attracted much attention due to the ability to design complex shapes and has exhibited impressive results on metals and alloys.[82,93,109,111,112] Over the past decades, different approaches were undertaken to laser 3D print MMCs via selective laser melting (SLM). The first approach lies in simply mixing the reinforcement and metal powders. However, the large size of the reinforcement modifies the molten pool dynamic and rheology, leading to the fabrication of porous parts.[227–229] The second approach involves the creation of a composite powder containing the metal matrix and the reinforcement to form a homogenous mixture at the microscale.[230–233] This method allows to 3D print dense MMCs with mechanical properties

comparable to ones obtained via conventional method. Yet, only nanocomposites can be manufactured and, thus, cannot be generalized for micro-reinforced MMCs. The third approach consists in the in-situ formation of the reinforcement.[234–237] This technic enables obtaining dense MMCs with micro-size reinforcement, but a limited number of reinforcements can be formed during SLM. Although numerous attempts to laser 3D print MMCs, to our best knowledge, additive manufacturing (AM) of Cu/D composites remains less explored.

In this chapter, the feasibility of laser 3D printing of Cu/D composite materials is investigated via laser directed energy deposition (LDED) as illustrated in **Figure 5.1-1 (a)**. The printing parameters are optimized to obtain a dense material. Also, the TC of the printed composite as well as the quality of the D after the process are studied. Later, the fabrication of complex Cu/D composite 3D structures is studied via SLM (**Figure 5.1-1 (c)**). It is shown that the presence of D affects the molten pool dynamics. Different printing strategies are employed to overcome this issue. Finally, highly complex designs are printed which have potential used in thermal management applications.

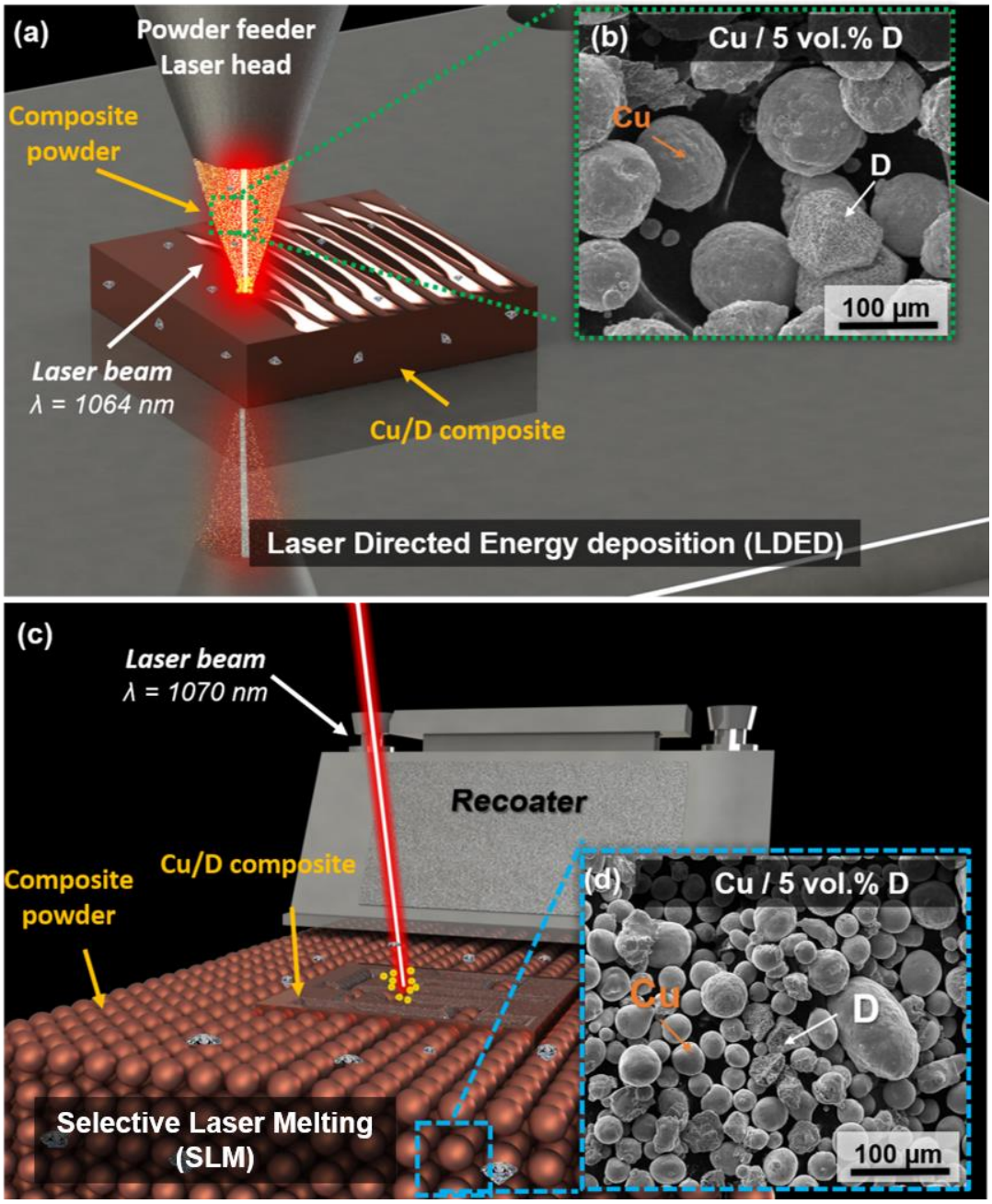

Figure 5.1-1 (a) schematic illustration of the laser directed energy deposition system (LDED), **(b)** SEM micrographs of Cu+D powders used in the LDED, **(c)** schematic illustration of the SLM technology, **(d)** SEM micrographs of Cu+D powders used in the SLM.

5.2 Experimental set-up and procedures

5.2.1 Laser directed energy deposition (LDED)

D powders with a mean diameter of 105 μm (Eastwind Diamond Abrasives) were coated with a graded TiO_2-TiC layer using a molten-salt process. A 5 vol.% of coated D was mixed with spherical Cu powder with a mean diameter of 93 μm (99.5% US Research Nanomaterials, Inc.) as shown in **Figure 5.1-1 (b)**. AM was performed using an Optomec, Inc., LENS® 3D Hybrid Machine Tool System (Optomec, Inc. LENS MR-7). The laser power (λ = 1064 nm, gaussian profile, continuous wave, max. power : 2 KW, spot diameter : 600 μm) and scan speed were varied between 700 and 1000 W, 4.25 and 21.2 mm/s, and the layer thickness and hatch distance were kept constant to 0.2 and 0.3 mm, respectively. The printing chamber was filled with argon (99.9%, Matheson) to prevent oxidation of the Cu and D powders. The printing parameters are summarized in **Figure 5.2-1**.

(a)

Parameters	Values
Spot Size	600 μm
Laser Power	700 to 1000 W
Scan Speed	8.5 to 21.7 mm/s
Hatch Distance	0.3 mm
Layer Thickness	0.2 mm
Part Size	5x5x5 mm^3

(b)

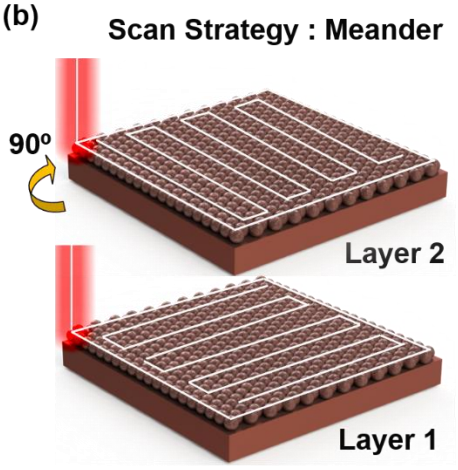

Figure 5.2-1 (a) Table of printing parameters and **(b)** schematic illustration of the meander scan strategy.

The energy density (J/mm^3) was calculated with the following equation:

$$E = \frac{P}{LT \times h \times s} \quad \textbf{(21)}$$

Where P is the laser power (W), LT is the layer thickness (mm), h is the hatch distance (mm), and s is the scan speed (mm/s). The crystalline phases and chemical structures of the coated D were analyzed both by X-ray diffraction and micro-Raman spectroscopy. The volume percentage of D in the printed composites was estimated by image analyses using ImageJ. The density of the printed samples was measured using the Archimedes method. The microstructures of the parts printed were characterized using a scanning electron microscope (SEM) and a high-resolution transmission electron microscope (HRTEM, FEI Tecnai Osiris™, 200 kV). The periodic photothermal radiometry (PPTR) [238] was used to measure the thermal diffusivity (TD) of a printed Cu/D composite material as schematically illustrated in **Figure 5.2-2**. The setup is equipped with an Nd:YAG laser (Coherent MATRIX Q-switched diode-pumped laser, λ = 1064 nm) that delivers a 40 ns pulse duration each period T_R with a maximum power of 10 W. The laser beam (diameter 0.55 mm) was directly focused on the sample; an infrared (IR) detector (Teledyne Judson Technologies J15D12) was used to monitor the temperature change at the rear face of the sample. The method consists of heating the front face of the sample with a pulsed laser and to measure the related temperature increase on the opposite face using a fast (10 MHz) IR detector. The heat transfer is thus 1D with the spatial resolution is the bulk material. The material isotropy was considered. The measurement has been performed along with the two directions of the sample and no difference was noticed, applying that the building direction does not affect the thermal conductivity. Comparable TC was measured with a 2% deviation range. Also, a photodiode was set to trigger the acquisition after each laser

pulse. An averaging process was performed over the period of repetition that allows to increase the signal-to-noise ratio of the response by the detector. The TD of the sample is identified by minimizing the gap between the experimental response and the theoretical one calculated using an analytical solution of the heat transfer within the material. The minimization is achieved by implementing a nonlinear least square algorithm (the Levenberg-Marquardt technique).

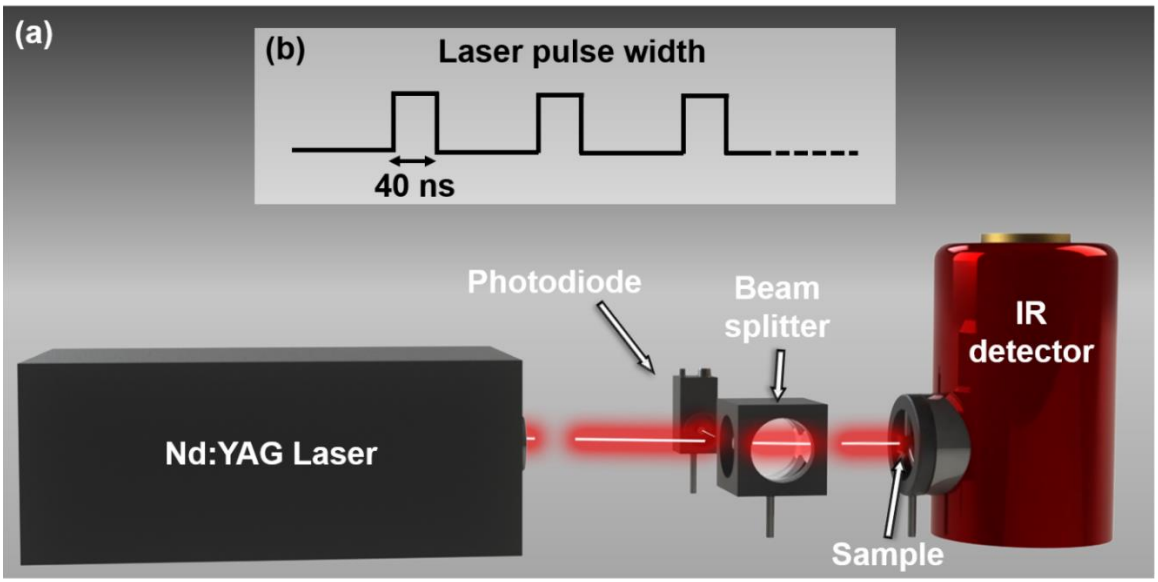

Figure 5.2-2 (a) Schematic illustration of the laser-flash setup for TC measurement and **(b)** illustration of the laser pulse width.

The TD was converted into TC using the following equation:

$$k(T) = a(T) \times C_p(T) \times \rho(T), \quad \textbf{(22)}$$

where k is the TC (W/m.K), a is the TD (mm^2/s), ρ is the density (g/cm^3), and C_p is the heat capacity of the sample (J/Kg.K). The C_p was calculater using the rule of mixture using the following value : D = 630 J/Kg.K, TiC = 190 J/Kg.K and Cu = 392 J/Kg.K.[239]

5.2.2 Selective laser melting (SLM)

Coated-D particles (Eastwind Diamond Abrasives, 25 µm) were mixed with spherical metallic Cu powders (US Nano, Cu 99.5%, mean diameter 45 µm) at a volume percentage of 5% (**Figure 5.1-1 (d)**). The SLM was carried out using the SLM®125 3D printer from SLM Solutions as described in Chapter 3. A stipe laser scan strategy was used for all prints. The laser power and layer thickness were kept constant throughout the study to 400 W and 0.03 mm, respectively. First, a single melting strategy was investigated for a scan speed and hatch ranging from 100 to 600 mm/s and 0.03 to 0.2 mm, respectively. The single melting consists of shining the laser once on each layer, as illustrated in **Figure 5.2-3 (a)**. Next, a recoating and a remelting strategy were employed at scan speeds and hatch distances ranging from 200 to 450 mm/s and 0.6 to 0.12 mm. The remelting strategy involves shinning the laser twice on the same layer, as shown in **Figure 5.2-3 (b)**. The recoating implies repassing the recoater on the same layer and shining the laser a second time, as illustrated in **Figure 5.2-3 (c).** The structures designed using SolidWork® were uploaded to the Magics® software for parameters assignment and print job creations. Then, the parts were printed on a stainless-steel building plate (stainless steel, 123 × 123 × 25 mm^3). The SLM was monitored using a layer control system (LCS) installed in SLM®125 printer.

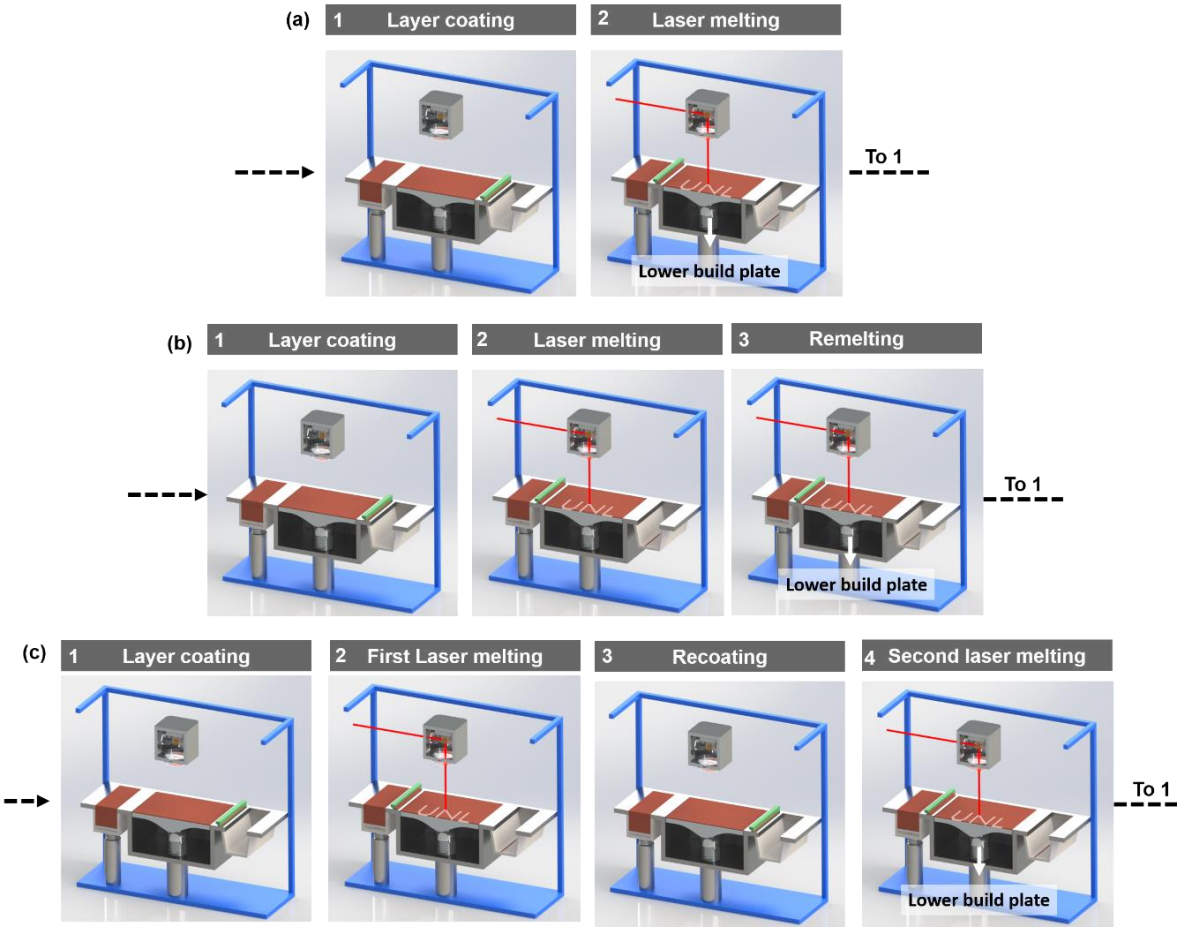

Figure 5.2-3 Schematic illustration of **(a)** single melting, **(b)** remelting, and **(c)** recoating printing strategies.

5.3 Laser directed energy deposition of Cu/D composite materials

5.3.1 Optimization of the printing parameters

The realization of dense Cu/D composites with high TC requires the formation of an interphase between the Cu and D because of their chemical incompatibility.[39,211] In Chapter 4, a Titanium (Ti)-based coating on carbon fibers, via a molten salt process, has demonstrated an enhanced wettability of molten Cu on a graded TiO_2-TiC layer compared to a pure TiC layer. The same process has been applied to the D particles.[240]

Coated D particles were then mixed with Cu powder **Figure 5.1-1 (b)**). The printing parameters were explored to form a dense Cu/D composite material. It was observed that scan speeds between 8.7 and 21.7 mm/s and laser powers between 700 and 1000 W, mainly resulted in parts with large numbers of printing defects on the surfaces (i.e., pores, balling) (**Figure 5.3-1 (a)** and **(d)**). The poor surface finish has arisen because the Cu powder was insufficiently melted which inhibits its ability to fuse completely.[126] Nevertheless, a narrow processing window was identified for obtaining parts with minimized printing defects: a scan speed of 12.7 mm/s and laser powers ranging from 900 to 925 W (**Figure 5.3-1 (b)** and **(d)**). At a low scan speed (4.3 mm/s) and high laser powers (800 to 1000 W), the printed parts exhibit a spherical shape, not a designed cubic shape (**Figure 5.3-1 (c)** and **(d)**). Slow scan speeds and high laser powers enlarge the molten pool size, which increases the powder track height and width. As a result, the original cube deforms into a spherical shape.[241]

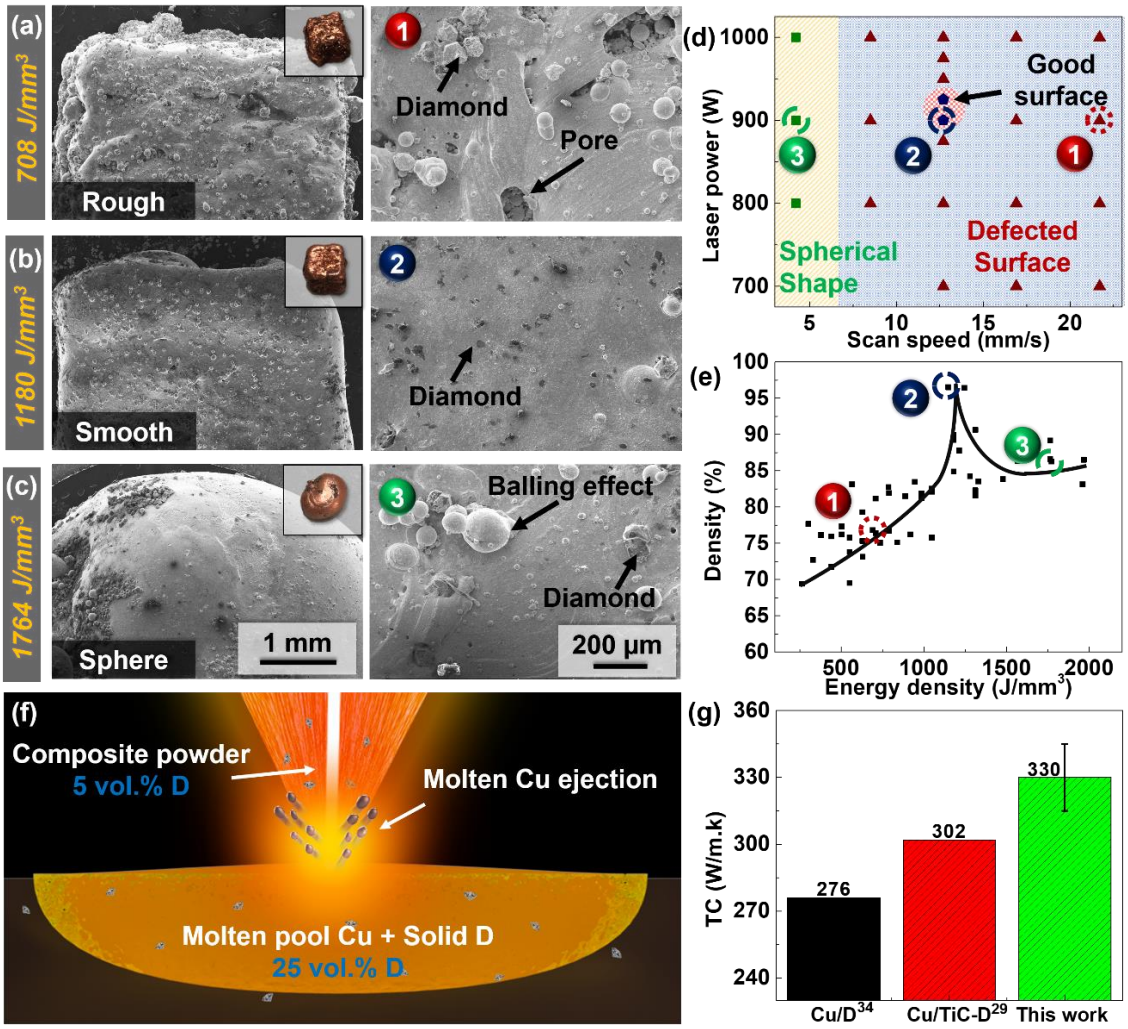

Figure 5.3-1 SEM micrographs of Cu/D composite surfaces printed at an energy density of **(a)** 708, **(b)** 1180, and **(c)** 1764 J/mm^3; **(d)** qualitative quality of Cu/D vs. printing parameters; **(e)** sample density vs. laser energy density; **(f)** illustration of particle ejection during LDED; and **(g)** TC of Cu/D composites with no interphase [242], a TiC interphase [239], and a graded TiO_2-TiC interphase.

The D volume percentage in the Cu/coated-D composite printed was measured to be about 25 vol.%. compared to 5 vol.% in the powder feeding. A significant increase in the D volume percentage was found in the printed composites. One possible explanation is that

during the laser-matter interaction, Cu particles were ejected or evaporated (T_m = 1080 ºC) from the molten pool, leading to an increased concentration of coated-D in the final composites (**Figure 5.3-1 (f)**). **Figure 5.3-1 (e)** shows the relationship between the sample density and energy density.[85] It is noted that an energy density of about 1250 J/mm^3 (i.e., Power = 950 W, scan = 12.7, hatch = 0.3 mm, and layer = 0.2 mm), yields a relative density of 96% with a TC of about 330 W/m.K for a Cu/D composed of 25 vol.% of D. The TC of the Cu/TiO_2-TiC-D (330 W/mK) in this work is 10% and 20% higher than the TC reported for Cu/D (276 W/mK)[242] and Cu/TiC-D (302 W/mK)[239], respectively for the same D volume fraction (**Figure 5.3-1 (f)**).

5.3.2 Interfacial characterization of Cu and coated-D

The interfacial bonding between the matrix and the reinforcement is one of the main concerns to obtain dense and high-TC composites. **Figure 5.3-2 (c)** shows a cross-sectional micrograph of the interface between Cu and D, where the coated-D was previously embedded in the Cu matrix (**Figure 5.3-2 (a)** and **(b))**. As shown in the SEM micrographs, an intimate contact between the Cu matrix and the coated-D particle was found. The HRTEM micrographs at the Cu-TiO_2 and TiO_2-TiC interfaces demonstrate a smooth transition between layers with no pores, confirming a chemical bonding (**Figure 5.3-2 (d)** and **(e))**. Additionally, HRTEM of the Cu, TiO_2, and TiC layers in **Figure 5.3-2 (f)–(h)** shows the crystalline structures of the (111) Cu, (101) TiO_2 and (111) TiC planes with interlayer distances of 0.21, 0.35, and 0.25 nm, respectively.[243,244]

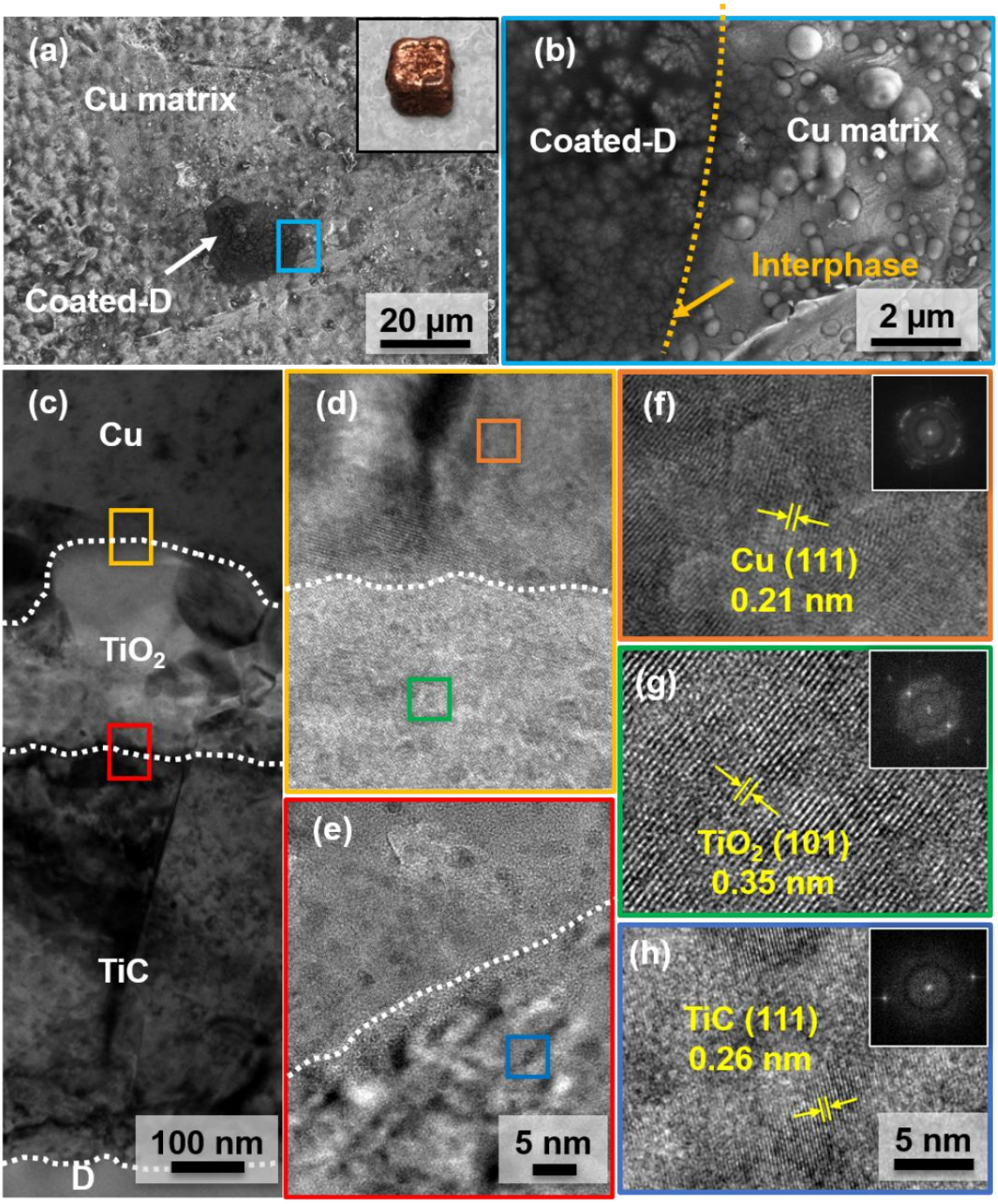

Figure 5.3-2 (a)–(b) SEM micrographs of the Cu/D surface. TEM micrographs of **(c)** cross-sectional view of Cu-(TiO_2-TiC)-D, **(d)** Cu-TiO_2 interface, and **(e)** TiO_2-TiC interface. **(f)–(h)** HRTEM micrographs of Cu, TiO_2, and TiC, respectively.

5.3.3 Diamond quality through the printing process

The D quality is a crucial point to study the feasibility to laser 3D printing of Cu/D composites due to the potential D graphitization during the printing process. The D quality was evaluated after being immersed in a salt bath (coating process) and exposed to a high-power laser (printing process) as shown in **Figure 5.3-3 (a) – (c)**.

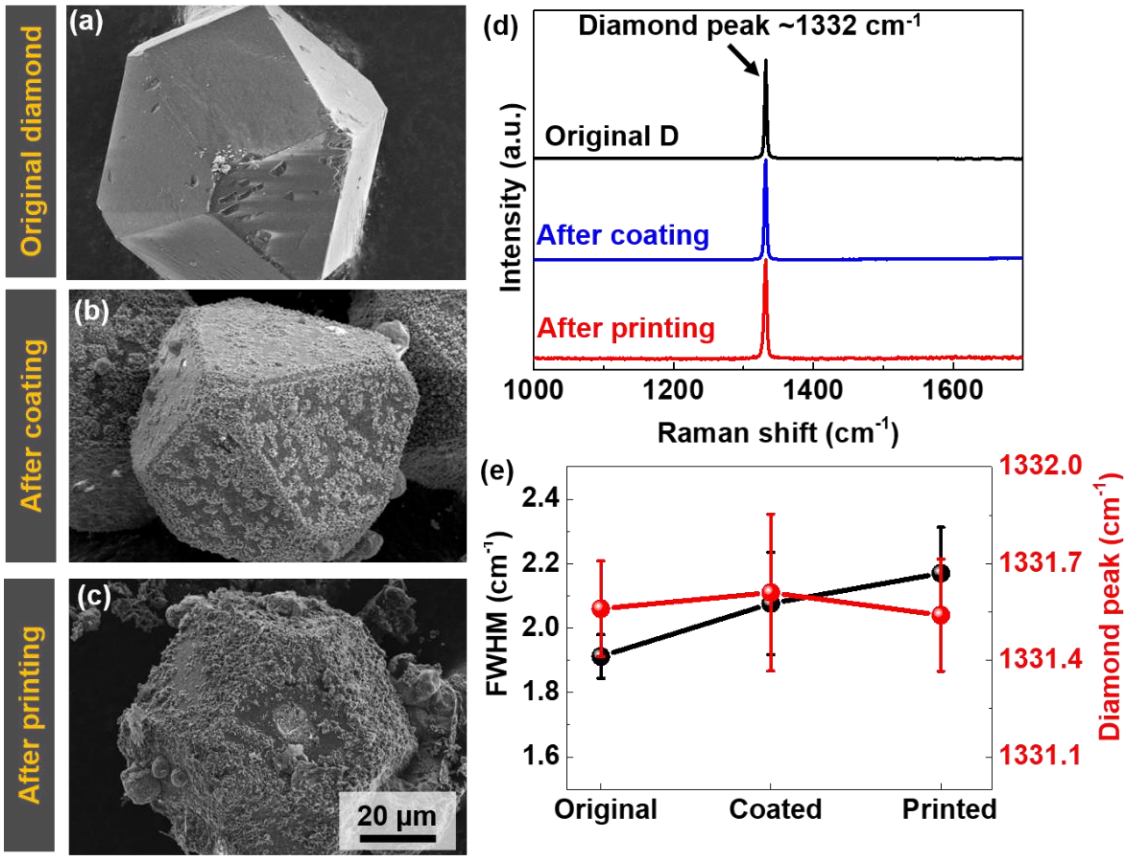

Figure 5.3-3 SEM micrographs of D particles at different stages of **(a)** as received, **(b)** after salt coating, and **(c)** after laser printing. **(d)** Raman spectra of an as-received D particle and D particles after salt coating and laser printing, and **(e)** FWHM and position of the diamond peaks measured from the D particles as-received, after salt coating, and after laser printing.

The as-received D powder showed a sharp peak around 1331.5 cm^{-1}, with a full width at half maximum (FWHM) of 1.9 cm^{-1}, confirming its high degree of crystallinity (**Figure 5.3-3 (d)** and **(e)**).[245,246] D particles were recollected and reevaluated after the salt coating and printing processes. As shown in **Figure 5.3-3 (d)** and **(e)**, the processed D particles still exhibit a sharp D peak, suggesting no graphitization occurred during the high-temperature coating and printing processes. The D peak position and FWHM values retrieved from the Raman spectra show no obvious peak broadening, confirming the multi-step processing does not degrade the crystallinity of the D particles.

5.3.4 Conclusion

This work demonstrates the feasibility of additive manufacturing using Cu/D composites. An energy density of about 1250 J/mm^3 is necessary to make dense composite materials with a limited amount of printing defects and high TC (330 W/m.K). The introduction of the Ti-based coating on the D particles before printing enables the formation of a chemical bonding between the matrix Cu and reinforcement D, facilitating the printing of dense Cu/D composites. In addition, the quality of the post-printing D is found to be close to the original one, making the process suitable for manufacturing high-TC materials. However, LDED leads to the formation of coarse cubes and may not be suitable to fabricate intricated heat sink designs.

5.4 Selective laser melting (SLM) of Cu/D composite materials

5.4.1 SLM of Cu/D via a single laser melting strategy

As shown previously, the manufacturing of Cu/coated-D composites via LDED exhibits a chemical bonding between the Cu matrix, the (Ti)-based interphase, and the D particles leading to the fabrication of highly thermally conductive MMCs.[247] Nevertheless, as mentioned in Chapter 2, the LDED is a technology used to print large objects or repair parts. Thus, the fabrication of Cu/D composite material is then studied via SLM. Note that, a similar coating as shown in the previous part was realized here on D particles, as presented in **Figure 5.1-1 (d).**

Recall that, in Chapter 3, a dense Cu parts were printed via SLM with a laser power (P), layer thickness (LT), scan speed (s), and hatch distance (h) of 400 W, 0.03 mm, 400 mm/s, and 0.12 mm, respectively. Also, Y. Ma et al. studied the SLM of $Al_{12}Si$/D composites and found that the energy density necessaries to manufacture MMCs must be higher than that for the puremetal.[228] Therefore, to optimize the print, the following parameters were investigated on Cu and D powders: printing strategy: single melting; s = 100 mm/s to 600 mm/s; and h = 0.03 to 0.20 mm. The laser power and layer thickness are fixed to 400 W and 0.03 mm, respectively, for all experiments. **Figure 5.4-1 (a)** to **(c)** show the SEM micrographs of printed Cu/D composites with a low, moderate, and high energy densities of 333, 533, and 1333 J/mm^3, respectively. The surface of all samples appears porous, with pore/cavity sizes ranging from 100 to 500 μm. The density of the samples increases from 67% to 90% when the energy density increases (**Figure 5.4-1 (d)**). Previous reports demonstrated that an higher energy density (i.e., lower scan speed and hatch distance) enhances the molten metal flow and the wettability with the previously melted layers,

resulting in a denser materials.[248,249] In addition, the energy required to 3D print Cu/D composites appears more substantial than that for pure Cu, where an energy density of 275 J/mm^3 led to a dense material (95%). One explanation is that the presence of solid coated-D particles into the molten Cu increases its viscosity and limits its ability to flow and fuse.[228,231] Also, Cu is known to have a high optical reflection in the near-infrared domain (i.e., λ = 1070 nm).[87,109] When setting an energy density above 1000 J/mm^3 (i.e., low scan speed < 200 mm/s), important back-refection into the laser occurred (>10 W), which triggered the laser back-reflection security and make it shut down automatically. Consequently, a lower scan speed limit of 200 mm/s must be fixed to prevent damage to the laser optics and to the laser itself. Therefore, the maximum density which can be reached using a single melting is about 88%.

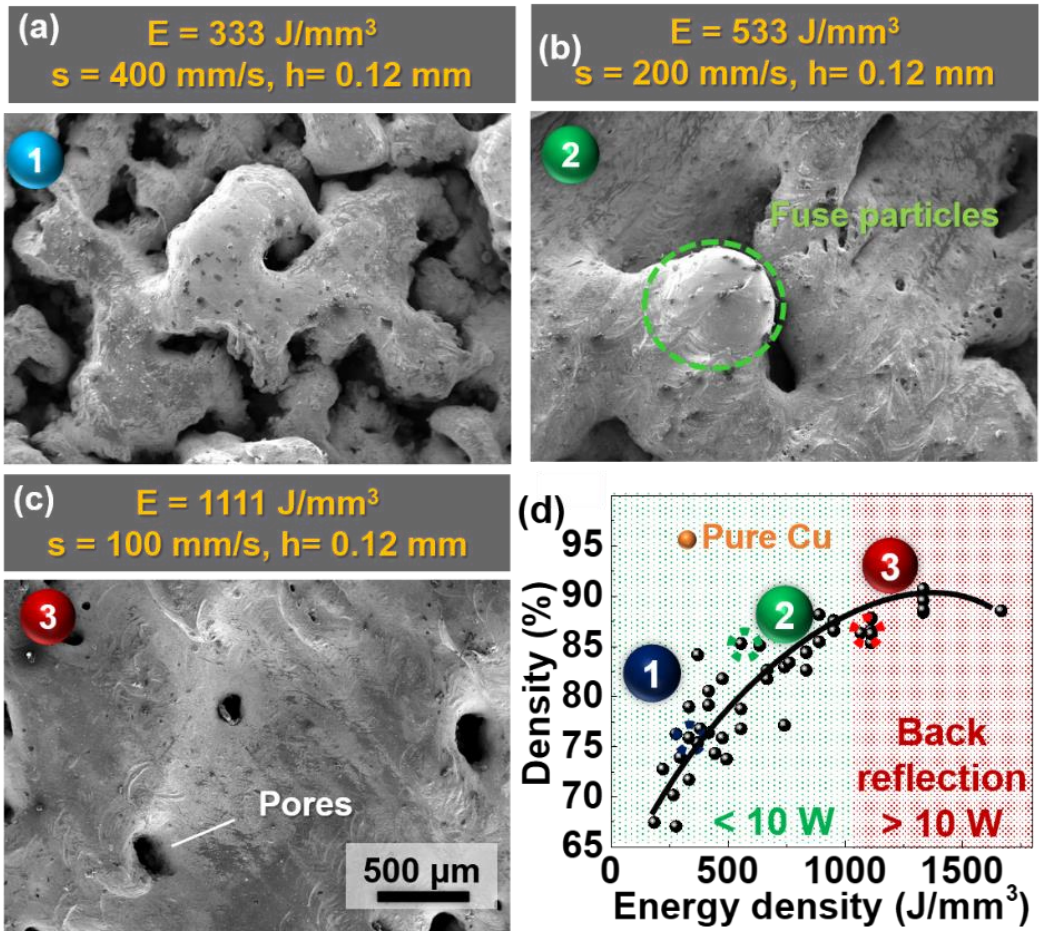

Figure 5.4-1 SEM micrographs of Cu/D surface printed with energy densities of **(a)** 333, **(b)** 533, and **(c)** 1111 J/mm^3 and **(d)** Cu/D density vs. energy density.

The low density observed when employing a single melting on Cu and coated-D powders can be related to the spatter ejections during the SLM. Observations of the outgoing MMC printing shows a significant number of particle ejection and a dense metal vapor compared to the situation of pure Cu (**Figure 5.4-2 (a)** and **(b)**), for the same process parameters (P = 400 W, s= 400 mm/s, h= 0.12 mm, and LT = 0.03 mm).

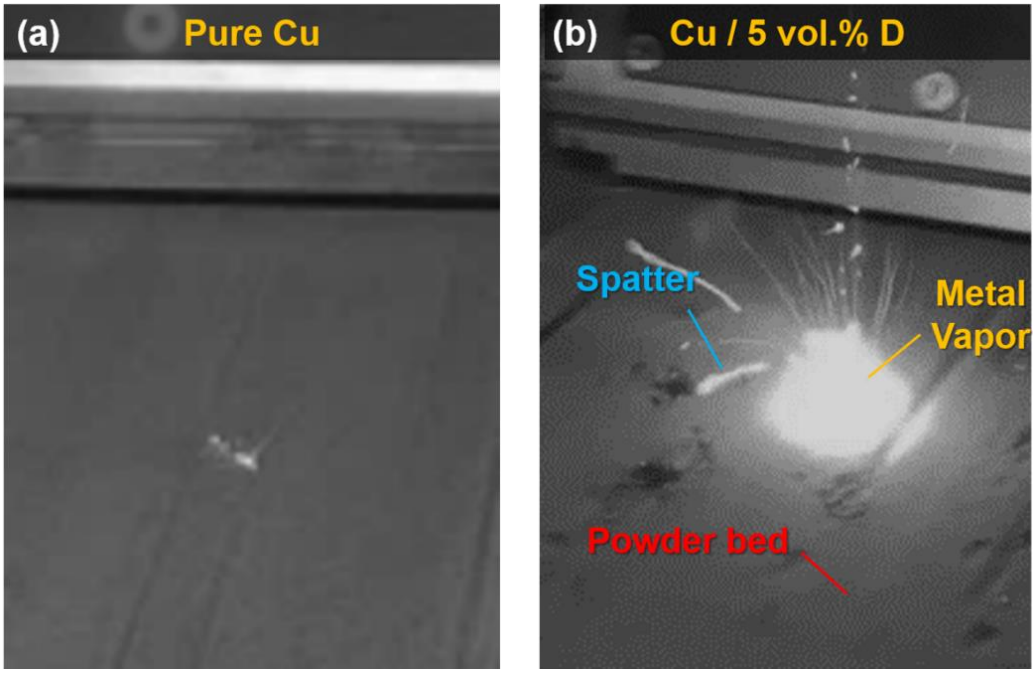

Figure 5.4-2 Optical photograph of the laser shining on **(a)** Cu and **(b)** Cu/D powder beds for the same printing parameters (P = 400 W, s = 400 mm/s, h = 0.10 mm, and LT = 0.03 mm).

These observations imply that the coated-D particles have a major effect on the pool dynamics. Two types of spatter particles are categorized in SLM.[59] During the laser-matter interaction, a spheroidal molten pool is created within a few microseconds.[127] Quickly, a metal vapor appears above the molten pool, inducing a recoil pressure on the pool surface. Meanwhile, inside the liquid, a thermal gradient rapidly emerges, which inducing a flow of the molten metal from the hot area to the coldest one, known as the Marangoni effect. Both effects represent the cause of particle ejection, called recoil-induced ejection, as illustrated in **Figure 5.4-3**.[129,250] In the meantime, a denudation zone is created on the sides of the molten track where powders can be swept under the flow of the metal vapor and the gas shield, named entrainment particles. In this scenario, the particles can be "cold" if there

is no interaction with the laser beam or "hot" if they intercept with it (**Figure 5.4-3**).[58] Naturally, the presence of solid coated-D particles in the pool changes the molten pool rheology, surface tension, and the metal vapor density, which explain the important particle ejections as compared to a pure Cu powder bed.

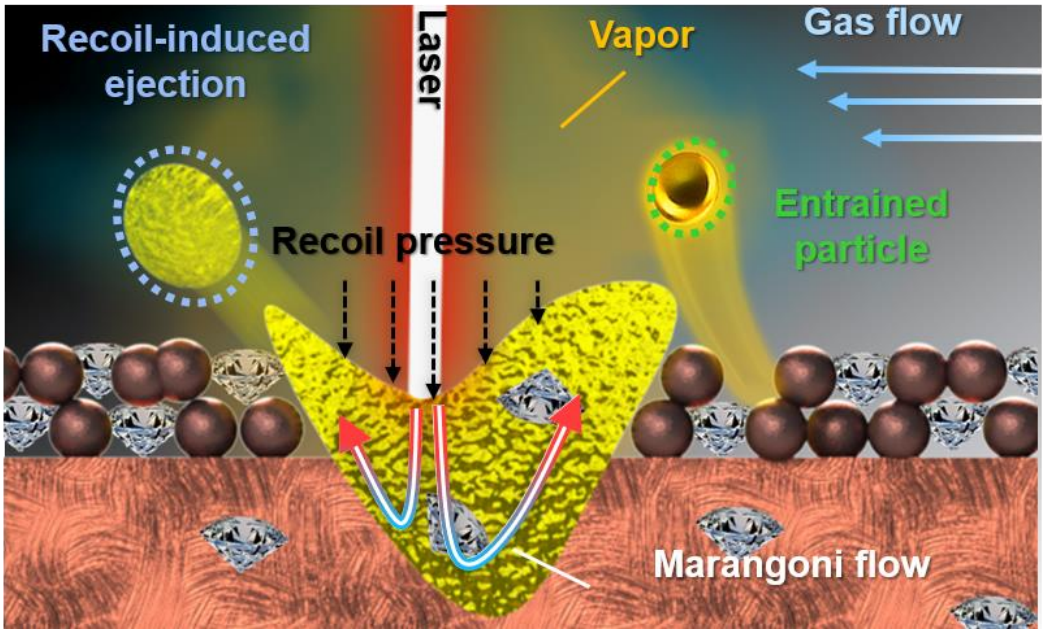

Figure 5.4-3 Schematic illustration of spatter ejection in SLM.

Furthermore, spatter particles affect the quality of the printed parts. These particles fall back into the powder bed after cooling down. Later, during the deposition of a subsequent layer, they partially fuse with the solid material which leads to the formation of bumps, pores, and cavities. Moreover, if spatter particles or the part roughness is higher than the layer thickness, damage of the recoater blade occurs, and uneven powder distribution arises.[57] Several studies showed that the laser power and the scan speed are major parameters that affect the number and size of spatters at constant layer thickness, pressure and gas flow.[129,251] It is commonly accepted that a faster laser scan speed lowers the molten pool temperature, vapor pressure and decreases the denudation zone, thus limits the spatter

ejection. Nevertheless, as shown before, a rapid scan speed leads to an insufficient flowing and fusing of the powders; thus, porous materials are formed. Hence, the conventional SLM (i.e., single melting) of Cu/D composites raises several issues. First, the high back reflection of Cu in the near-IR domain limits the laser scan speed to a minimum of 200 mm/s. On the other hand, the presence of coated-D particles in the powder bed perturbs the molten Cu dynamics, generating spatter ejections and leads to the porous parts during SLM.

5.4.2 Powder-bed quality for different printing strategies

The successful manufacturing of a micro-reinforced MMCs requires to limit or suppress the spatter ejections. For that, two different printing strategies were introduced in the SLM and their effect on the spatter ejection were monitored and compared with the single melting situation using the layer control system (LCS). Note that the LCS images allow observing only significant particles that represent a small amount of the spatter ejection. Only large particles are considered here, as they are most likely to influence the printing quality. **Figure 5.4-4 (a)** shows the pictures of the powder bed after the coating of a new layer and at different stages of the printing for a single melting (i.e., layer 10, 60, 110, and final part). As can be seen, at the beginning of the print (layer 10 ~ 300 μm), the powder bed is flat, uniform, without defect. Next, when the number of layers increases (layer 60 ~ 1200 μm), white and large particles appear on the surface. Later, they disappear (layer 110 ~ 3300 μm), and the printed part emerges at the powder bed surface, witnessing its high surface roughness. The fading away of the large particles after 110 layers is due to their incorporation into the printed part, causing the roughness of the parts and their absorption inside the bed. Sonny Ly et al. reported that the size of the recoil-induced particle ejection (i.e., molten pool) are often a few times larger than the raw powders, while entrainment

particles are about the size of the bed powders.[58] Recall that the metal vapor was found to be more critical for a Cu/D powder bed than the Cu one for the same printing parameters. Hence, it is reasonable to assume that these particles originate from an instability of the molten pool due to an increase in the recoil pressure.

Consequently, a recoating strategy was implanted during the SLM to improve the density and part quality, which consists of adding more powder to the current layer by repassing the recoater and shinning the laser for the second time (**Figure 5.2-3 (c))**. As can be seen in **Figure 5.4-4 (b)**, the same tendency as a single melting situation can be observed. The bed is uniform at the beginning of the print, then spatter appears when the LPBD goes on, with the only difference that the number of particles is more important. The recoating permits to fill some pores by redepositing powders and shining the laser a second time. However, a larger amount of powder is deposited on each layer conducing to increase the number of spatter ejection. Finally, the part shows an improved surface, but the pores remain. A third strategy was tested, which involves shining the laser beam on the same layer twice, known as re-melting (**Figure 5.2-3 (b)**). **Figure 5.4-4 (c)** shows the LCS photographs for the remelting strategy and shows that the large spatter particles have almost vanished during the SLM, leading to the laser 3D printing of smooth and dense composite structures.

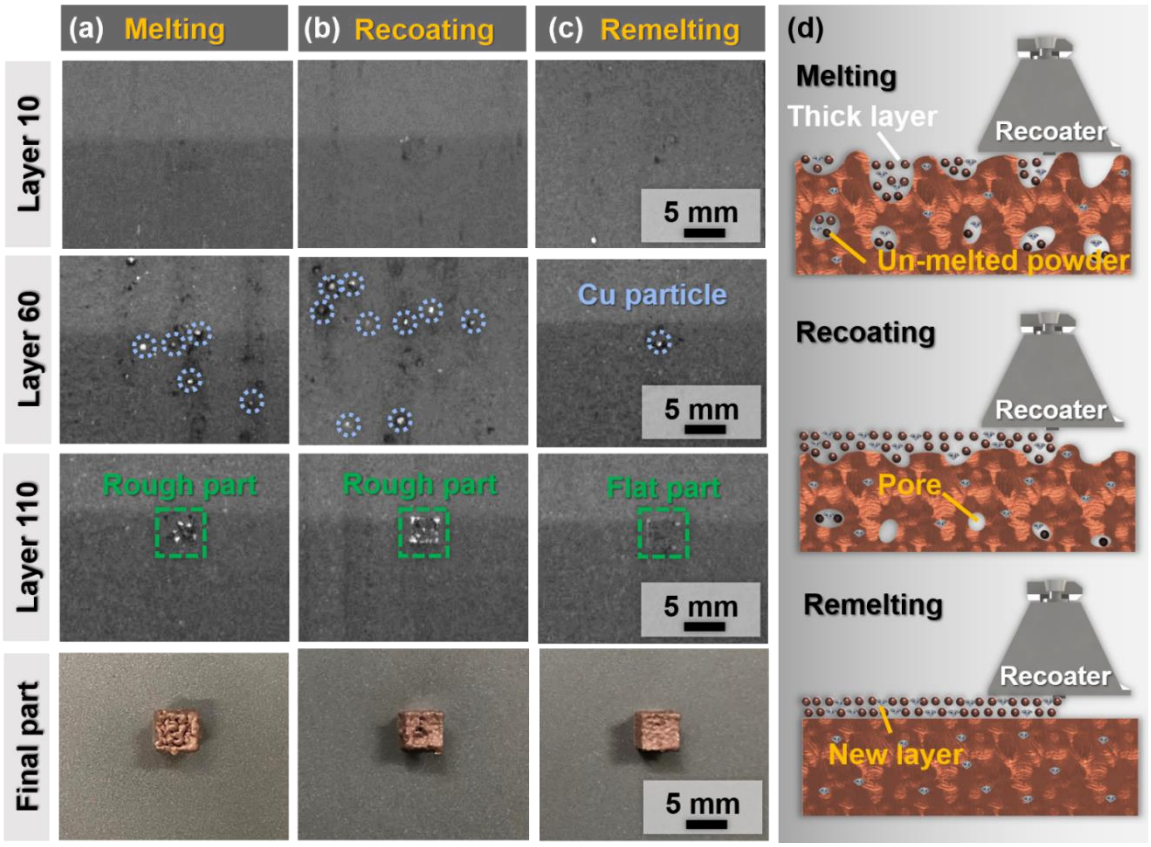

Figure 5.4-4 Pictures of the powder bed after the coating of a new layer using the **(a)** melting, **(b)** recoating, and **(c)** re-melting strategies, and **(d)** schematic illustration of the layer coating for the different printing strategies. The printing parameters are fixed to s = 250 mm/s, h = 0.1 mm, P = 400 W, and LT = 0.03 mm.

The single melting and recoating strategies led to pronounced spatter ejection and hence resulting in rough surfaces, as observed in **Figure 5.4-4 (a)** and **(b)**. As discussed previously, splash particles cause defects and roughness on the printed parts. Due to the layer upon layer nature of the SLM, after a certain number of deposited layers, the density of the spatter particles on the bed increases, which then fuses with the composite creating bumps, pores, and cavity. Chunlei Qiu et al. demonstrated that the layer thickness is a vital parameter in the spatter phenomena.[60] They showed that when the layer thickness increases

from 20 to 100 μm, the spatter and metal vapor increased. They also reported the formation of large pores, discontinuous laser tracks, and cavities on the sample surfaces. Besides, an important surface roughness creates a beam offset and disable its ability to efficiently melt defects during the printing of the next layer.[252–254] Naturally, the cavities, pores, and bumps observed on the surface of the printed Cu/D composite materials alter the layer thickness which affect the pool dynamics and, thus, promoting spatter ejection as schematically illustrated in **Figure 5.4-4(d)**. Also, the high surface roughness noted on the samples inhibits the laser to accurately melt defects. Both effects combined or separately can explain the formation of the porous materials. On the contrary, the remelting strategy led almost no large spatter and to a smooth and dense Cu/D surface. Several studies demonstrated that a remelting of each layer allows suppressing printing defects, fills pores, and smoothens the surface.[255–257] Therefore, the remelting strategy reduces the spatter ejection by flattening the layers' surfaces ((**Figure 5.4-4 (d)**).

5.4.3 Quality and density of printed composite with different printing strategies

Study of the composite qualities associated with different printing strategies was carried out for scan speeds and hatch distances ranging from 200 to 450 mm/s and 0.06 to 0.12 mm, respectively. Photographs of the printed samples can be seen in **Figure 5.4-5 (a)-(c)**.

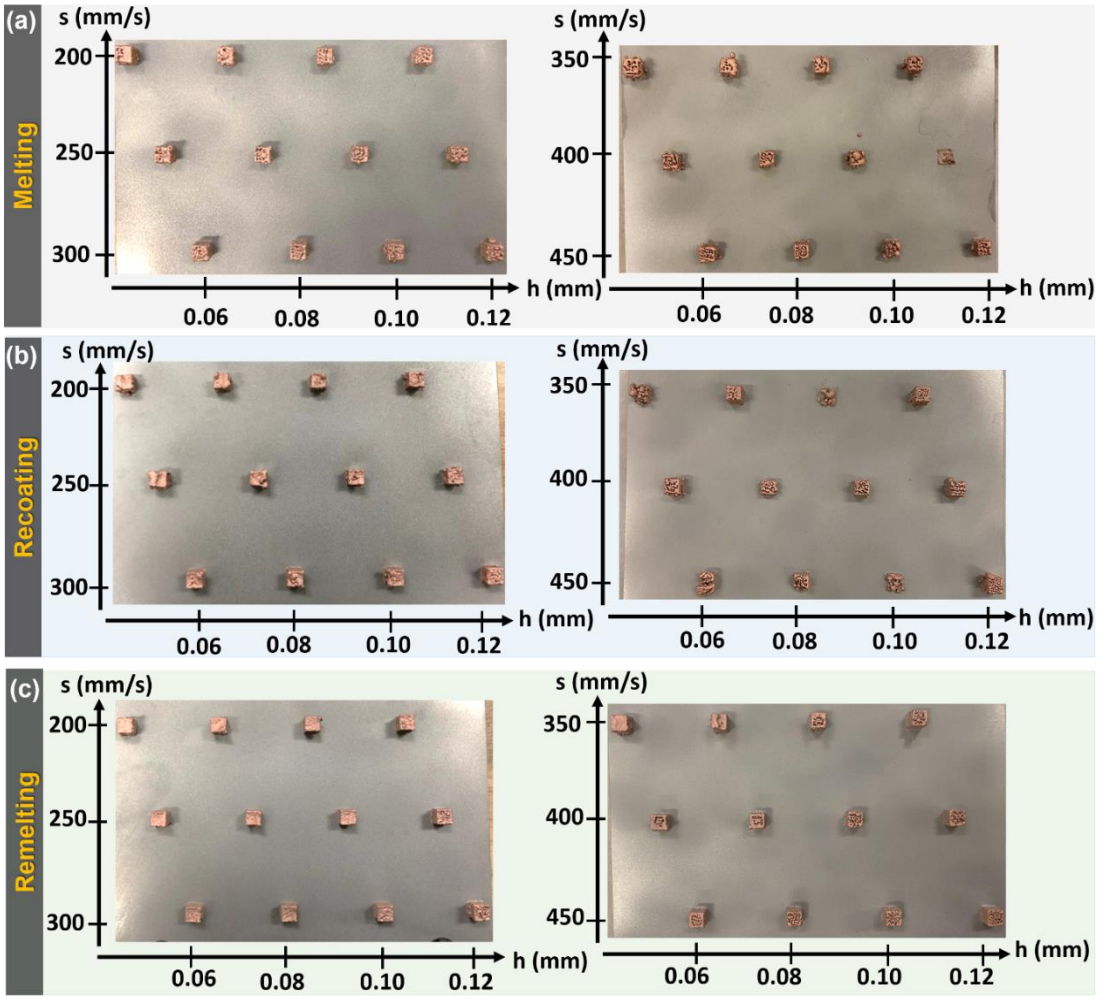

Figure 5.4-5 Photographs of Cu/D composite materials printed with scan speeds and hatch distances between 200 to 400 mm/s and 0.06 to 0.12 mm for **(a)** melting, **(b)** recoating, and **(c)** remelting strategies.

The samples were categorized into three groups – porous, dense, and crack represented by black, blue, and red circles, respectively (**Figure 5.4-6(d)**). As mentioned previously, a single melting leads to essential porous parts (**Figure 5.4-6 (a)**). For the recoating strategy, composites show porous surfaces for fast scan speeds and large hatch distances. However, samples crack at slow speeds and small hatch distances (**Figure 5.4-6 (b)**). The cracks arise due to the apparition of a critical thermal gradient between the bottom and top of the sample at a high energy density.[123] The same tendency was observed when the remelting strategy was used to print Cu/D composite material, but a small process window was found for scan speeds of 200, 250, 300, and 350 mm/s with hatch distances of 0.12, 0.1, 0.08, and 0.06 mm, respectively (**Figure 5.4-6 (c)**). **Figure 5.4-6 (e)** shows the Cu/D composite density as a function of the energy density. As can be noted,densities of MMCs fabricated using a remelting strategy show the highest one, with 96% at an energy density range between 500 to 700 J/mm^3. Next, Cu/D composites prepared with the recoating strategy show a lower density of 92%, followed by the single melting approach (90%) in the same process window. In addition, **Figure 5.4-6 (f)** reveals the density of the Cu/D composites printed at a fixed hatch distance and different printing strategies and scan speeds. As can be noted, the density of the sample decreases with faster scan speed, essential due to the insufficient flow and fusing of Cu. These observations imply that the scan speed needs to be sufficiently slow to have a sufficient flow of the molten metal but must be faster or equal to 200 mm/s to avoid critical back reflection.

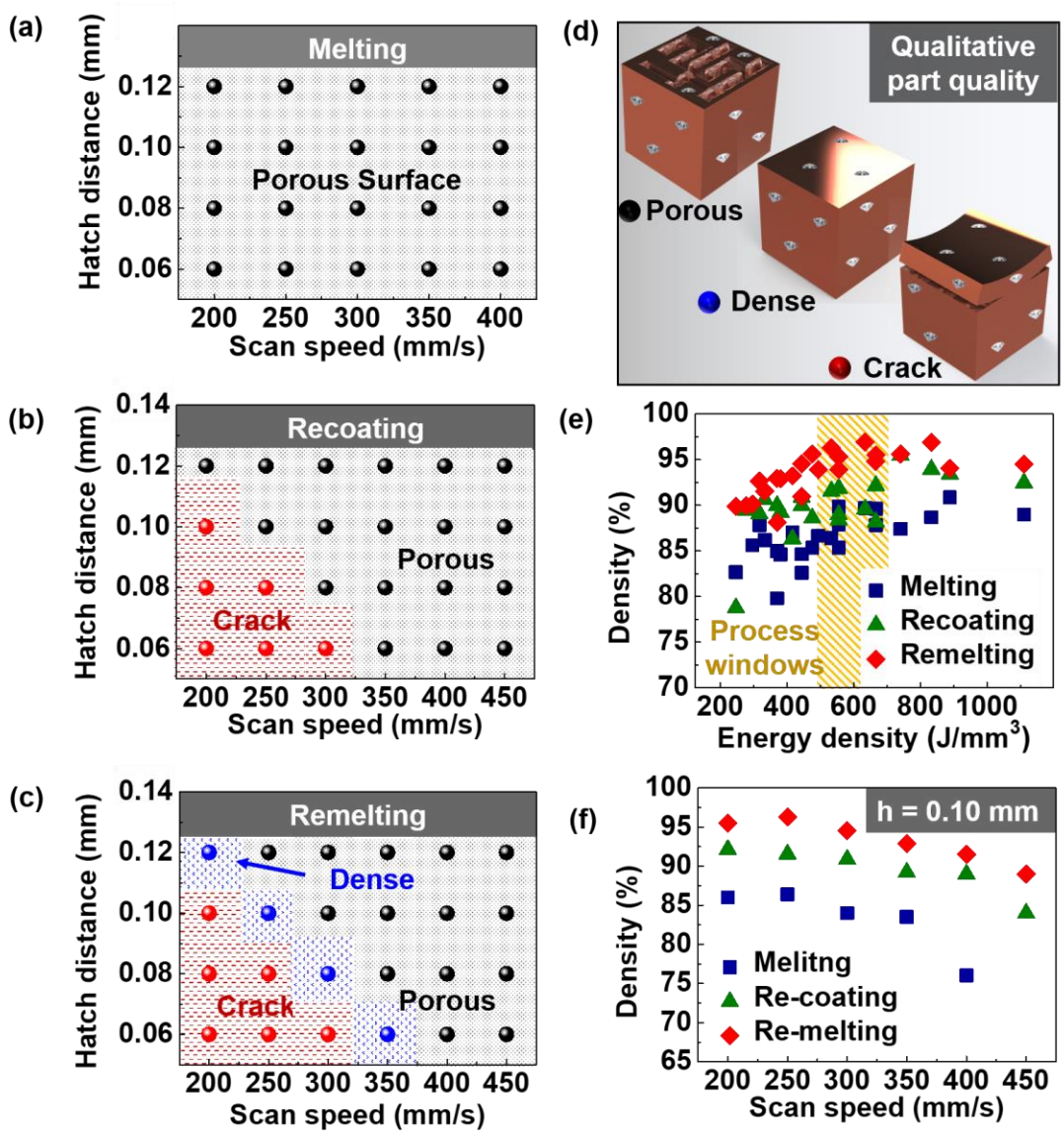

Figure 5.4-6 2D map of the part quality as functions of the laser scan speed and hatch distance using the **(a)** melting, **(b**) recoating, and **(c)** re-melting strategies. **(d)** Schematic illustration of part quality **(e)** part density vs. energy density, and **(f)** Cu/D density as a function of the scan speed (with h = 0.10 mm).

5.4.4 Microstructures of Cu/D composites printed with different strategies

The influence of spatter on the layer-upon-layer manufacturing of MMCs was then correlated to the sample densities by observing their cross-sectional and surface microstructures. All samples were manufactured with a constant scan speed and hatch of 250 mm/s and 0.1 mm, respectively (**Figure 5.4-7 (a)**). **Figure 5.4-7 (b)** shows the bottom, top cross-section, and surface of the Cu/D composite printed with a single melting strategy. Note that the section was polished and slightly etched to reveal particle inclusion inside the composite. The sample printed with a unique fusion shows pores, cavities, partially fuse inclusions, and "balls". The presence of these printing defects was expected, considering the previous observations. Undoubtedly, the addition of new layers on highly defected Cu/D layers leads to uneven powder dispersion. Hence the defects remained during the printing, contributing to the formation of the low-density materials. **Figure 5.4-7 (c)** shows the microstructure of the sample printed using the recoating strategy. The bottom part of the sample is denser compared to the single-melting approach, but the inclusion remains. As mentioned previously, the recoating approach allows filling the pores and cavities during the SLM by adding a new powder layer and shining the laser the second time. Nevertheless, spatter ejection continues, adding up defects to the composite material. Thus, a partially dense sample was obtained, as shown on the SEM micrographs. **Figure 5.4-7 (d)** displays the microstructure of the sample printed using the remelting strategy. The bottom of the sample appears to be dense, with only a few inclusions. The bottom of the sample with no defect leads to the formation of a dense composite during the layer-upon-

layer process. These observations confirm the advantages of using the remelting printing strategy to manufacture dense micro-reinforced MMCs.

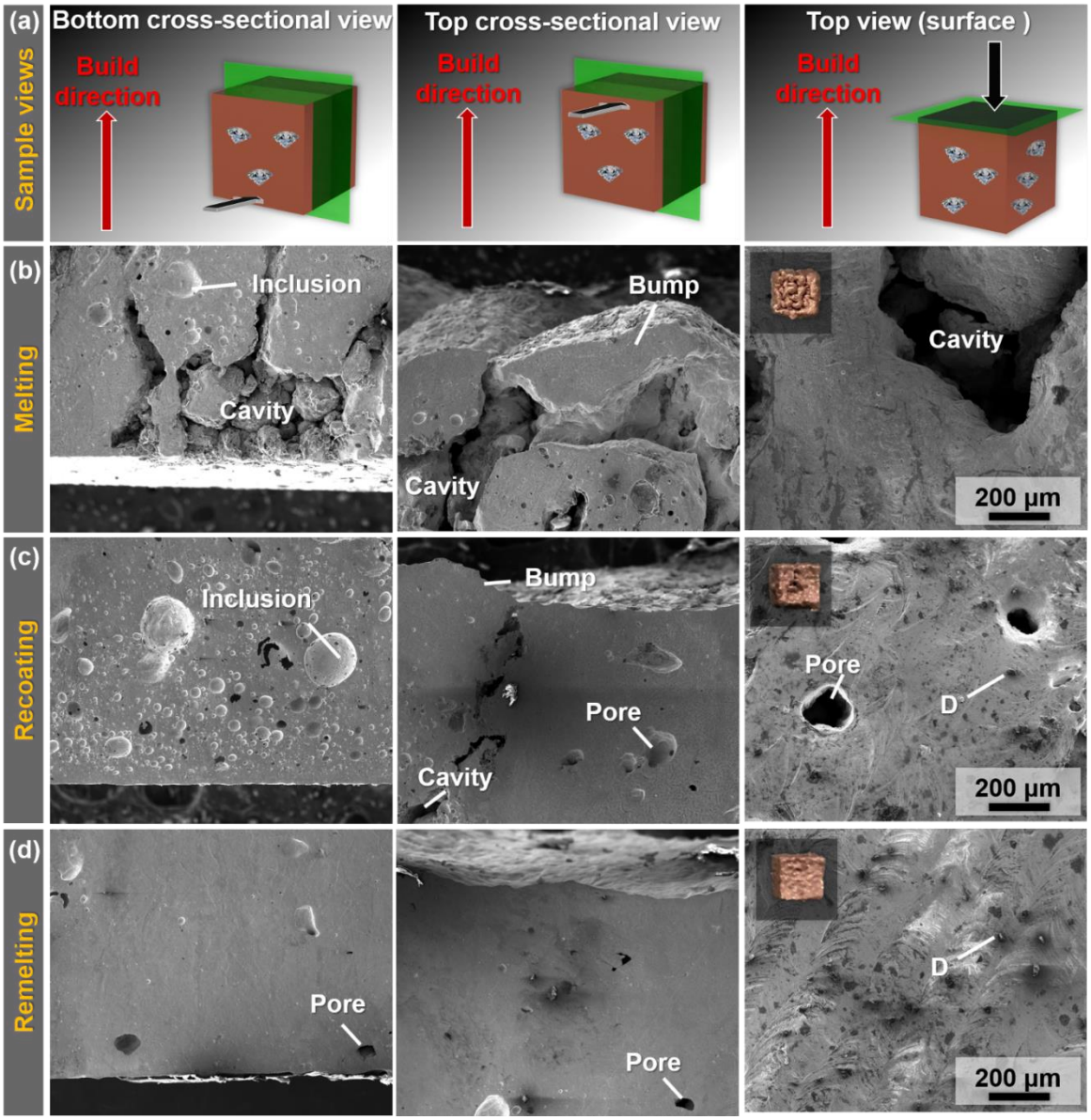

Figure 5.4-7 (a) Schematic illustrations of the analyzed views of the CU/D composite, and SEM micrographs of the printed part using a scan speed of 250 mm/s and a hatch distance of 0.10 mm using he **(b)** single-melting **(b**) recoating, and **(c)** remelting strategies.

5.4.5 3D printing of complex Cu/D structures

Cu/D composite materials are commonly referred as the next generation of thermal management materials to be utilized as heat sinks and base plates (**Figure 5.4-8 (a)**). Heat sinks require high surface areas to enhance the heat dissipation, hence intricated designs. However, these intricated designs are difficult to achieve on D-based materials.[36] On the other hand, Cu has a high density (8.93 g/cm^3) withstand their applications compared to Al (2.7 g/cm^3), which is widely used in thermal applications. Nevertheless, SLM has the ability to fabricate efficient and lightweight Cu/D heat dissipators by forming intricate and porous designs. Therefore, different complex structures were printed, using the optimized parameters developed in the previous parts (i.e., remelting s = 250 mm/s, h = 0.1 mm), which have prospective uses in heat dissipation. First, a diamond lattice structure was printed, as shown in **Figure 5.4-8 (b).** The SEM micrographs show the sophisticated and thin features (400 μm) of the D-structures printed. The thermal performance of a D-structure made of Al alloys was previously reported by M. Wong et al..[80] They showed that the heat dissipation of a D-structure is 60% more efficient than an array heat sink while being lightweight and strong.[258,259] Hence, D-structure made of Cu/D composite is likely to show excellent heat dissipation performance when used as a heat sink. In addition, three honeycomb structures were additively manufactured with filling percentages ranging from 40 to 60% (**Figure 5.4-8 (c)**) Honeycombs are a well-established structure as effective and lightweight heat dissipators.[260,261] Combining this shape with the excellent thermal properties of Cu/D materials could improve the thermal performance of base plates by increasing the surface areas and lowering their weights. In summary, the introduction of the SLM method to manufacture Cu/D composite materials has immense potential to

produce thermally efficient designs and surpass the thermal properties of available heat dissipators components.

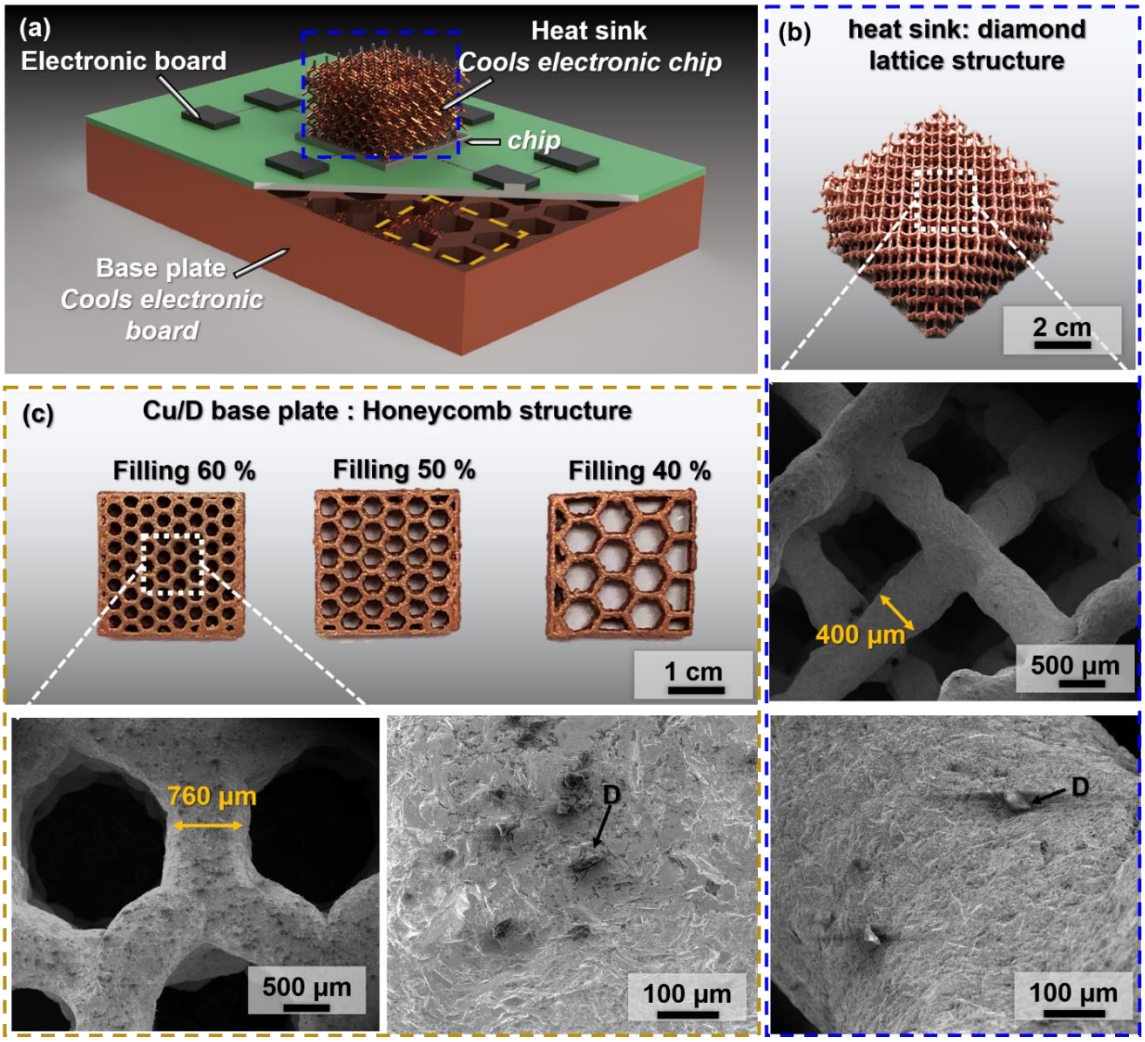

Figure 5.4-8 (a) Schematic illustration of Cu/D composites for microelectronic applications, **(b)** picture and SEM micrographs of a heat sink with diamond lattice structure, and **(c)** picture and SEM micrographs of the honeycomb structures.

5.4.6 Conclusion

In this part, the effects of the single melting, recoating, and remelting printing strategies are systematically compared in terms of powder bed quality, part density, and microstructure of the Cu/D composites laser 3D print. It is shown that the presence of coated-D influences the molten pool dynamics during the SLM, generating a large amount of spatter ejections. The spatters are assumed to be originated from the recoil-induce spatter due to the high metal vapor above the pool when D are introduced in the powder mixtures. Later it is shown that the spatter perturbed the powder bed homogeneity and resulted in the formation of porous composite materials. Besides, the low laser absorption of Cu causes significant back reflection, and limits the laser scan speed to a minimum of 200 mm/s. Later, to obtain dense composite material, both the recoating and remelting strategies are introduced during the SLM. It is shown the only the remelting approach reduces the spatter ejection by suppressing the printing defects and thus dense Cu/D composites (~96%) are manufactured with scan speeds of 200, 250, 300 and 350 mm/s and hatch distances of 0.12, 0.10, 0.08 and 0.06 mm, respectively.

Finally, complex 3D structures are printed for thermal management applications. Honeycombs of Cu/D with different fillings and D-structures are successfully manufactured using the remelting strategy with a scan speed of 250 mm/s and hatch of 0.10 mm. The introduction of the remelting in the SLM has promising prospective to laser 3D print a large variety of MMCs and thus remodel their applications via the development of intricated designs.

6 Diamond coating by chemical vapor deposition assisted ultraviolet lasers

6.1 Introduction

Diamond (D) has been referred as “the ultimate engineering material” for a wide range of applications which are attributed to its exceptional thermal, optical, mechanical, and electronic properties.[262] Chemical vapor deposition (CVD) of diamonds at low pressure has been extensively studied over the past decades due to its numerous advantages, including low cost, high growth rate, and high diamond quality.[263,264] All CVD methods, including plasma, hot-filament, and combustion-flame CVD, involve a number of chemical reactions of hydrocarbon precursors near thermal equilibrium,[265–268] where a lack of selectivity among different reaction channels take place, towards products or desired products.

With the significant advances in laser technology, lasers provide a unique means for efficient dissociation of precursors or radicals by exciting specific transitions (electronic, vibrational, rotational) in reactant molecules, enabling reaction control to some extent.[269–271] Laser chemistry has long been explored as a means of seeking chemical control of molecular reactions.[272–276] Zare and et al. demonstrated vibrational control of an isotopic variant of water, HOD, to influence outcome through selective bond cleavage with wavelength-matched infrared (IR) laser irradiation.[277] Ding et al. showed that ultraviolet (UV) photolysis of glyoxal, $(CHO)_2$, proceeded through different pathways depending on the photolysis wavelength, subsequently leading to different products.[278] Laser-assisted CVD (LCVD) opens up new possibilities in thin-film deposition and enables one to study new reaction pathways.

In this chapter, a UV-laser-assisted CVD is developed to grow D films. First, the effects of UV lasers on the combustion fame chemistry, film growth rate, and D quality are investigated. With a better understanding of the phenomena occurring during the UV-laser-assisted CVD of D, the effects of laser irradiation with the UV wavelengths are studied. D films are prepared with excitation by KrF (λ = 248 nm) and an ArF (λ = 193 nm) lasers (**Figure 6.1-1**).

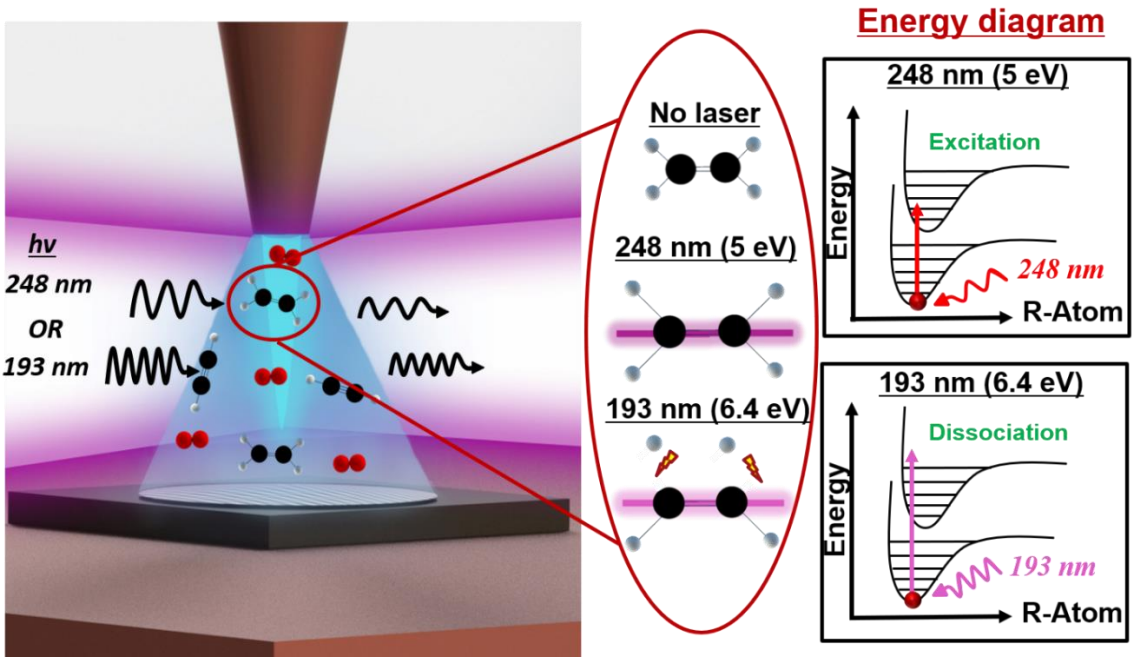

Figure 6.1-1 Schematic illustration of the UV-laser-assisted combustion CVD setup and light-molecule interaction mechanisms of UV laser irradiations at different wavelengths.

6.2 Experimental set-up and procedures

6.2.1 Growth of diamond films

A schematic diagram of the UV-laser-assisted combustion D CVD experiment setup is shown in **Figure 6.2-1**. A combustion torch with a 1.5 mm orifice tip was used to produce the flames. The precursor gases were a mixture of ethylene (C_2H_4, 99.999%), acetylene (C_2H_2, 99.6%), and oxygen (O_2, 99.996%) with a volume ratio of 1:1:2. A krypton fluoride (KrF) excimer laser (Lambda Physik®, COMPex® 205, 248 nm, 20 ns) and an argon fluoride (ArF) excimer laser (Lambda Physik®, COMPex® 205, 193 nm, 15 ns) were directed perpendicularly through the combustion flames and parallel to the substrate to excite the combustion species. A UV convex lens with a focal length of 25 mm was used to focus the laser beam from its original size of ~ 20×10 mm^2 to ~ 2×1 mm^2, which was sufficient to cover the whole primary flame. A power meter was placed in the UV laser path next to the combustion flame to measure the laser power. The laser fluence was calculated by dividing the laser pulse energy by the beam spot size. D growth was performed with UV laser irradiation of the combustion flame by tuning the laser fluence from 600 to 1400 mJ/cm^2 and from 10 to 25 mJ/cm^2 for the 248 and 193 nm lasers, respectively. A tungsten carbide (WC) substrate with a Co composition of 6% and a dimension of 12.5×12.5×1.6 mm^3 was placed on a water-cooled brass plate that was mounted on an X-Y-Z stage. The distance between the substrate surface and the primary flame tip was kept around 0.5 mm in all experiments. The substrate temperature during the deposition was maintained at 770 ~ 780 ℃ and monitored by a noncontact pyrometer (OS3752, Omega Engineering, Inc.). For the investigation of the growth rate and film

quality, the deposition time was varied to obtain a similar film thickness, ~10 mm, for comparison purposes. For the D nucleation study, the deposition time was 10 min.

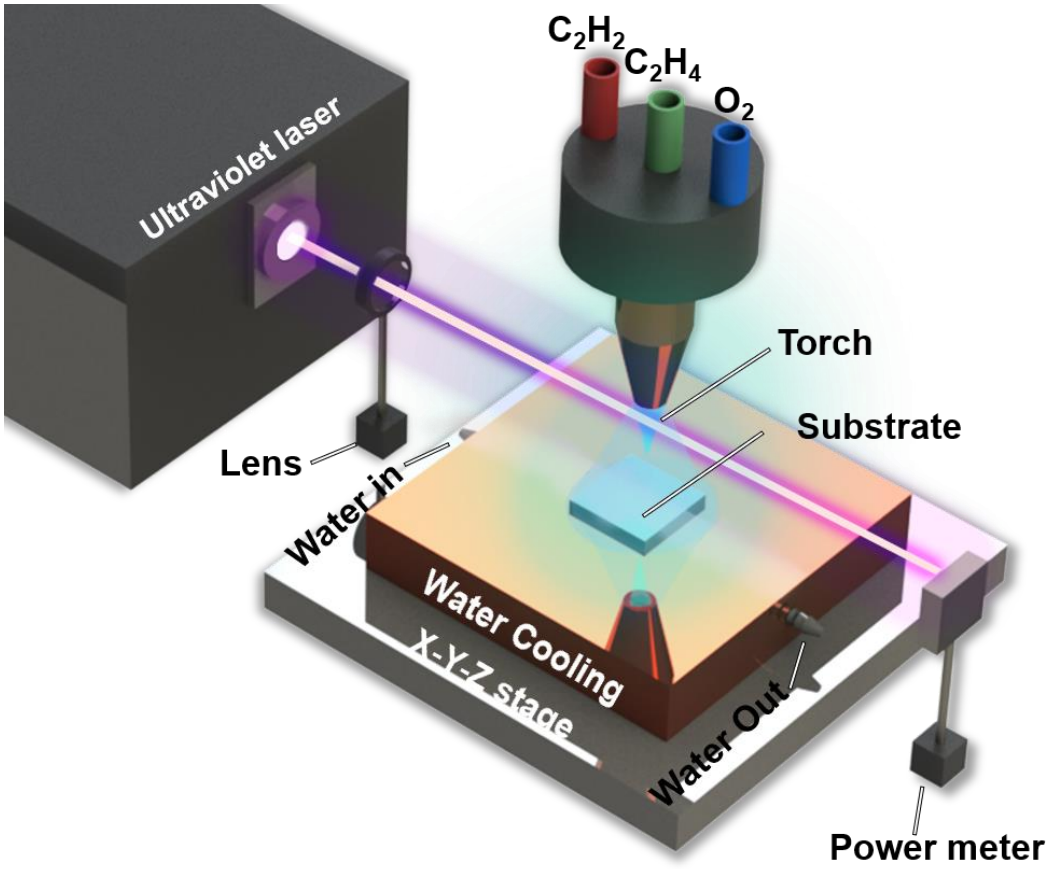

Figure 6.2-1 Schematic illustration of the diamond-assisted UV laser setup

6.2.2 Gas phase investigation of the combustion flame under UV laser irradiation

A Schematic illustration of the optical emission spectroscopy (OES) and light induce fluorescence (LIF) measurement setup to fully characterize flame species both at the excited and ground states, respectively, is shown in **Figure 6.2-2**. For OES measurements, a KrF excimer laser with a wavelength of 248 nm and a repetition rate of 10 Hz was used for irradiating the flames. The laser fluence was tuned from 600 to 900 mJ/cm^2 and from

10 to 25 mJ/cm^2 for the 248 and 193 nm lasers, respectively. The laser beam was focused to a spot size of 4 mm × 8 mm on the sample surface by Lens 1 (f_1 = 20 cm) to fully cover the primary inner flame. Lens 3 (f_3 = 10 cm) was used to collect and couple the emission from excited molecules into a spectrometer (Andor Technology, Shamrock 505i, intensified charge-coupled device (ICCD) DT-334T, 3 gratings: 150, 600, 2400 l/mm, range: 190-800 nm) for measurements. The laser and the ICCD of the spectrometer were synchronized using a digital delay generator (Stanford Research System DG 535, 5 ps delay resolution). The following parameters were used for OES spectroscopy and flame image measurement with KrF and ArF UV lasers irradiation at different laser fluences: ICCD gate delay = 0 ms, ICCD gate width = 10 ms, and laser frequency = 35 Hz. Wide-range spectra for identification of chemical species were collected with a horizontal slit width of 50 μm centered at the primary flame using a grating of 150 lines/mm while the high-resolution narrow-range spectra for rotational temperature calculation were collected using a grating of 2400 lines/mm. The horizontal slit width was set to 2500 μm for taking flame images. The flame images were proportional to the real flames in size. All spectra and images were measured for 500 pulses to reduce the standard deviation. A background spectrum was taken before the collections of the emission spectra and subtracted from all spectra captured.

For LIF measurements, a wavelength-tunable optical parametric oscillator (OPO) laser (OPOTEK Inc., VIBRANT™ 355 LD, 5 ns, 0.22–2.4 μm) was slightly defocused on the flame by Lens 2 (f_2 = 10 cm) to a spot size of 5 mm in diameter. The probe laser wavelength was tuned to selectively excite the electronic transition system of intermediate species (C_2, CH, and OH) presenting in the diamond-forming flames. The probe laser energy was 5

mJ/pulse for resonance fluorescence excitation at different wavelengths. The interpulse delay time between the UV KrF laser pulse and the probe OPO laser pulse was controlled by the digital delay generator (Stanford Research Systems DG535, 5 ps delay resolution). The light-collecting lenses were in plane while vertical to the probe laser beam. The ICCD detector was synchronized with the probe laser on time. The following parameters were used for the LIF measurements: the interpulse delay time between the KrF UV laser and the OPO laser = 50 ns, ICCD gate delay = 0 ns, ICCD gate width = 5 ns, and laser frequency = 10 Hz. The LIF spectra were collected with a horizontal slit width of 50 μm centered at the primary flame using a grating of 600 lines/mm. All spectra were measured for 500 pulses to reduce the standard deviation. Background subtraction was applied to all measurements to eliminate the remaining natural emission of the flame and possible non-resonant fluorescence.

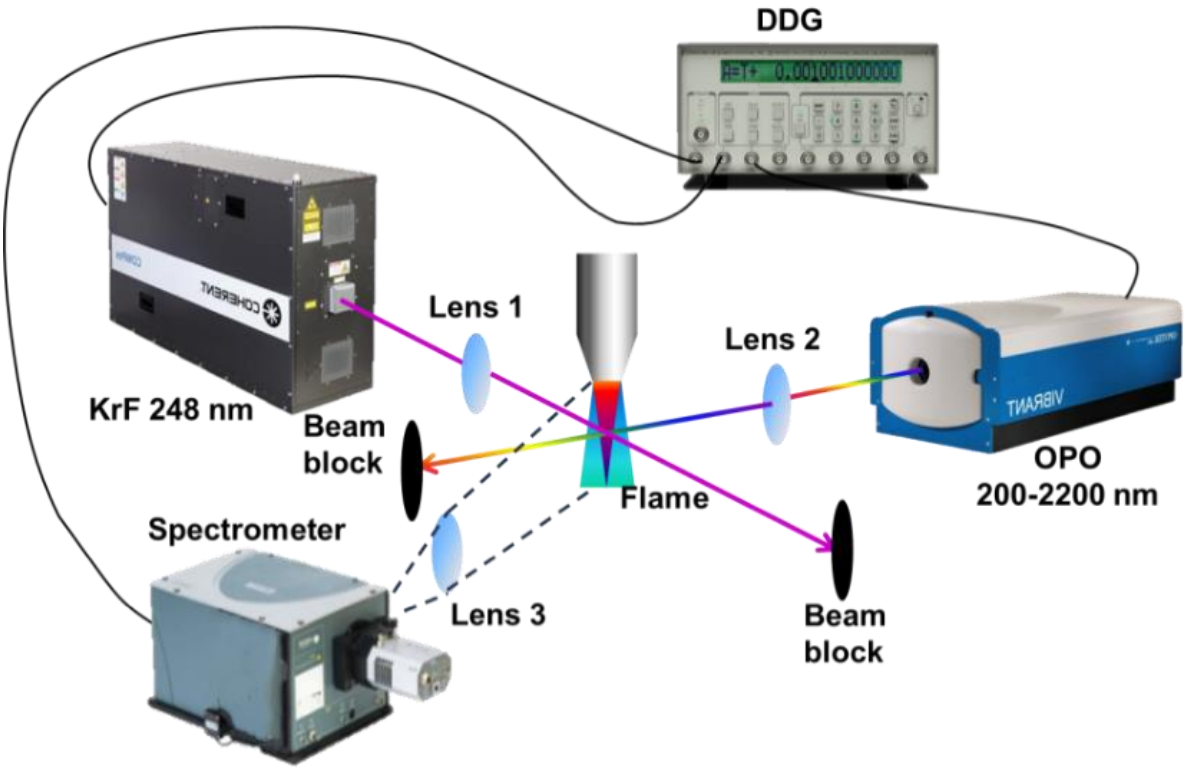

Figure 6.2-2 Schematic diagram of the experimental system used for optical emission spectroscopy (OES) and laser-induced fluorescence (LIF) to characterize the species in the combustion flame under UV laser irradiation.

6.2.3 Diamond film characterizations

Surface morphologies and cross-sectional microstructures of the diamond films were characterized using SEM. The growth rate was calculated by dividing the film thickness by the deposition time. D quality was evaluated using a micro-Raman spectrometer. TEM was performed to study the growth transition zone at the film-substrate interface.

6.3 UV laser-assisted (KrF, λ = 248 nm) combustion synthesis of diamond films

6.3.1 Effects of UV laser irradiation on the flame chemistry

Material synthesis arises from chemical processes occurring in the gas phase.[279] Examination of the gas phase variation under UV irradiation is, therefore, critical to determine its role in the growth process. As one of the most-used techniques for detecting excited species in a reaction system, OES of the diamond-forming flames under different laser irradiation conditions was studied. **Figure 6.3-1 (a)** illustrates the acquisition time and sequences between the KrF UV laser and the intensified charge-coupled device (ICCD) gate of the spectrometer. The emission peaks from three mains species were detected in the spectra (**Figure 6.3-1 (b**) C_2: $X'^3P_u \leftarrow A^3P_g$ (Dv = -1, 0, 1, 2), 2) CH: $A^2\Delta \leftarrow X^2P$ (Dv = 0), and 3) OH: $A^2\Sigma^+ \leftarrow X^2P$ (Dv = 0). All emission peaks of the species increase as the laser fluence increases.

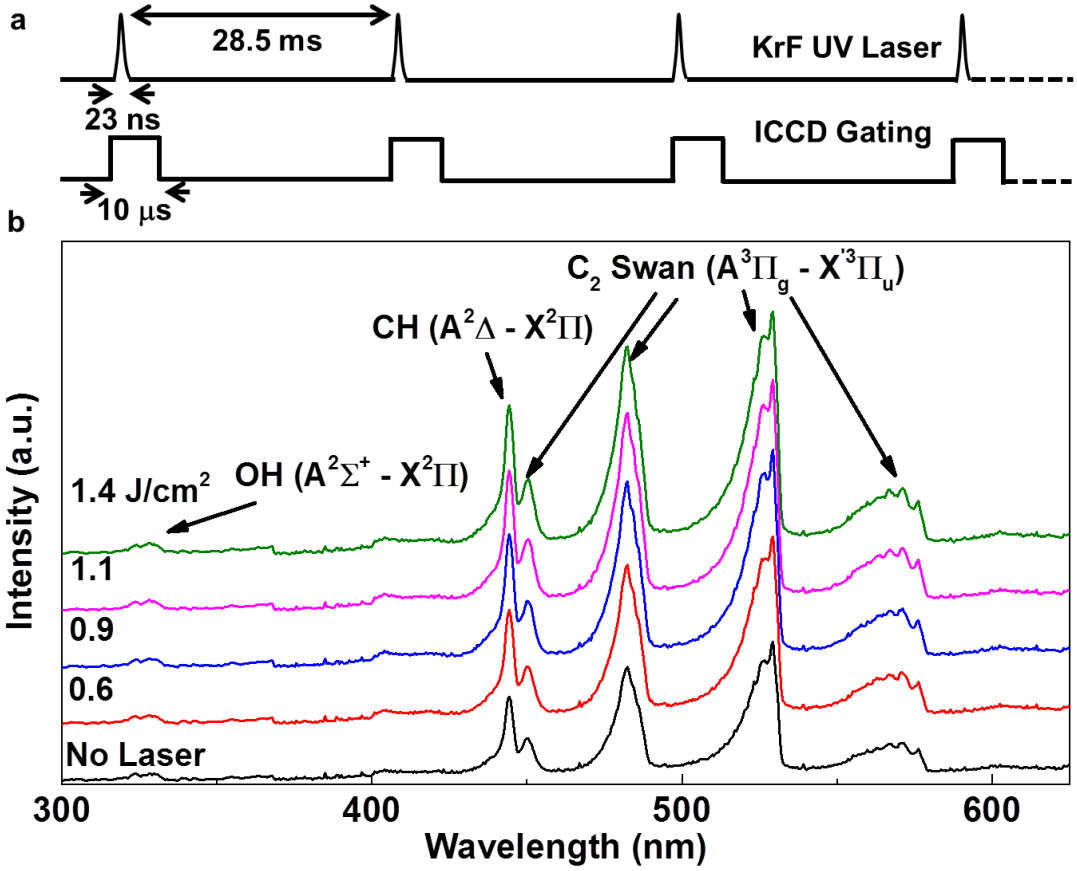

Figure 6.3-1. (a) The time relationship between the synchronized ICCD gate of the spectrometer and the KrF laser pulses for OES measurements. **(b)** Optical emission spectra of the combustion flames without and with UV laser irradiation at different fluences at 35 Hz.

However, it is difficult to determine two-dimensional (2D) distributions of the species using spectroscopic diagnostics with point measurements.[280,281] 2D natural emission flame images under different UV laser irradiation conditions provide more insight into the radical distributions within the flame, as shown in **Figure 6.3-2**. The false colors were used to indicate the emission intensities, representing the abundance of the excited species. It was noted that the total emission from the flame became brighter as the laser fluence increased.

Three filters were placed in the optical path to measure the 2D emission images created by the emission band from each excited species: diatomic carbon (C_2), methylidyne radical (CH), and hydroxyl radical (OH). Upon inspection of the images, it is clear that UV laser irradiation effectively induces generation of all three excited species, following the same trend in the spectra. It is noted that the increment of OH is concentrated in the center of the flame, while C_2 and CH are more significant at the flame edges.

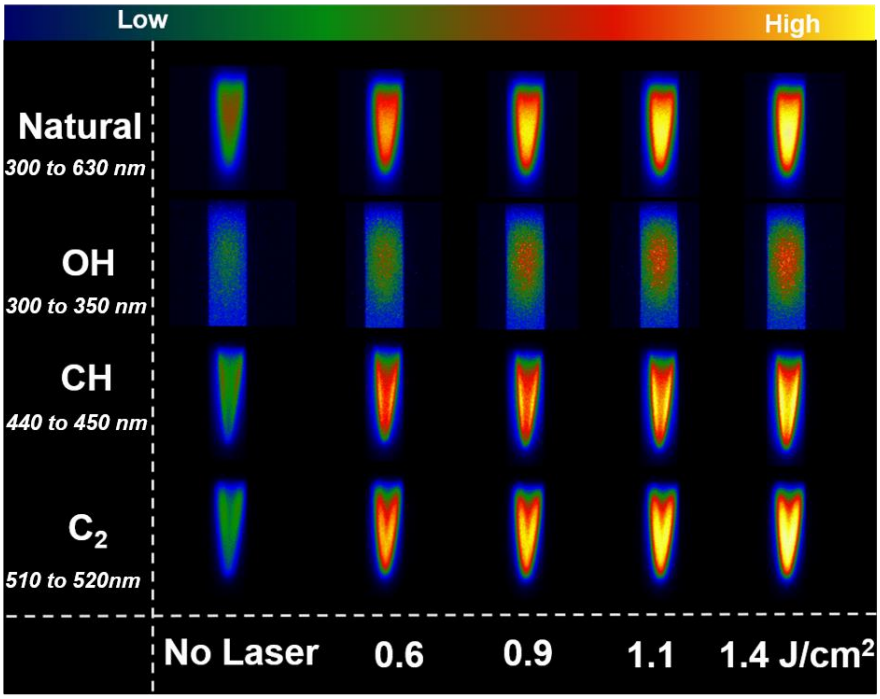

Figure 6.3-2 Flame images without and with UV laser irradiation at different laser fluences with different filters inserted to show the individual species.

A limitation of OES is that it only probes excited-state species, which are usually not sufficient in the overall chemistry because their number densities are several orders of magnitude smaller than those at the ground states. LIF is often the technique of choice to selectively and unambiguously detect ground-state species by its excitation spectrum. The

LIF signal is directly proportional to the density of the probed ground-state species under investigation.

The acquisition time sequences among the KrF excimer laser, the OPO laser, and the ICCD gating of the spectrometer for LIF measurements are illustrated in **Figure 6.3-3 (a)**. **Figure 6.3-3 (b)-(d)** show the electronic transition diagrams, OES spectra, and LIF spectra of C_2, CH, and OH. The OES spectra in **Figure 6.3-3 (b)** show that the emission intensity in the C_2 swan band, A^3P_g - X'^3P (Dv = 0), is the strongest at 516.5 nm (A-X (0,0)). The electronic transition diagram in **Figure 6.3-3 (b)** shows the exciting of C_2 radicals through the X'^3P (v"=0) → A^3P_g (v'=1) transition by the OPO laser at a wavelength of 473.7 nm. When the excited C_2 radicals relaxed back to the lower state through the A^3P_g (v'=1) → X'^3P (v"=1) transition, detection of photons is allowed with a wavelength of 512.9 nm, as indicated in **Figure 6.3-3 (b)**. Significant enhancement of the peak intensity at 512.9 nm was observed in the LIF spectra, confirming the effective resonant excitations of the ground-state C_2 species by OPO laser probing. **Figure 6.3-3 (c)** shows CH was excited through the X^2P (v"=0) → B^2S^- (v'=0) transition at 388.9 nm. Because the B^2S^- state and the A^2D state crossed each other, strong collisional redistribution between these two states took place. The fluorescence from the A^2D (v'=0) → X^2P (v"=0) transition was observed around 431.4 nm. Significant enhancement of the peak intensity at 431.4 nm was observed in the LIF spectra, confirming the effective excitations of the ground-state CH species by the OPO laser probing. **Figure 6.3-3 (d)** presents the LIF detection of OH was carried out by excitation of the X^2P (v"=0) → A^2S^+ (v'=0) transition at 307.8 nm. Detection of fluorescence around 343-348 nm (A^2S^+ (v'=0) → X^2P (v"=1)) was observed. Quantitative analysis of the LIF signals was impeded by quenching the fluorescence due to inelastic

collision of the excited molecules. Certainly, collisional quenching cannot be neglected in flames at the atmospheric pressure. This quenching depends strongly on the pressure, temperature, and collision partners, which are different in different regions of the flame. The LIF results were, therefore, interpreted in a more qualitative way. The LIF signals at 512.9, 431.4, and 347.2 nm in **Figure 6.3-3 (b)-(d)** were integrated to represent the abundance of the ground-state C_2, CH, and OH species in the flame, respectively.

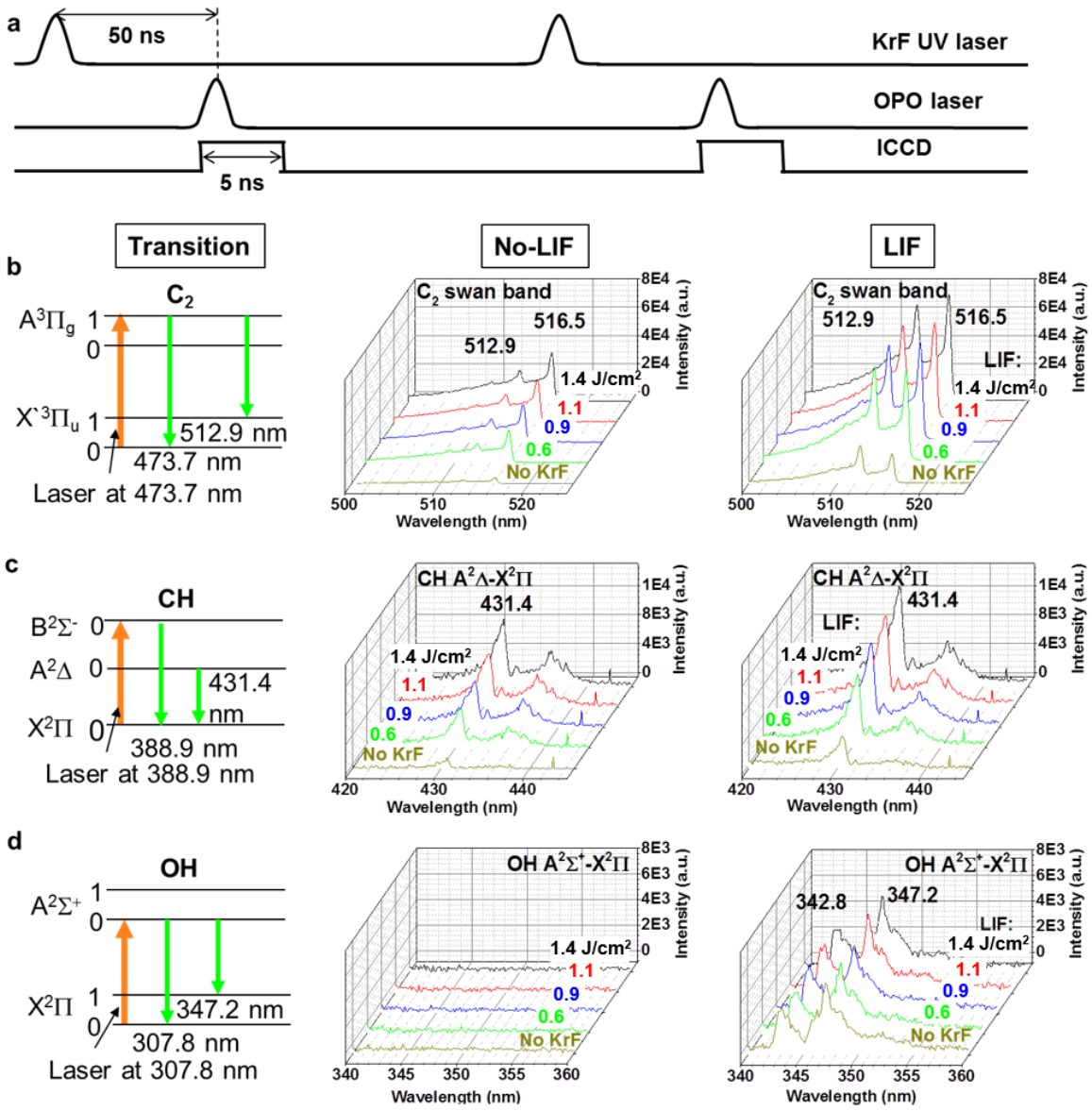

Figure 6.3-3 The time relationship among the synchronized ICCD gating of the spectrometer, the KrF excimer laser, and the OPO laser for the LIF measurements. Electronic transition diagrams, OES and LIF signals of **(b)** C_2, **(c)** CH, and **(d)** OH with and without UV laser irradiation at different KrF excimer laser fluences.

Integrated intensities of OES peaks and LIF signals of C_2, CH, and OH were plotted as a function of the laser fluence in **Figure 6.3-4 (a) and (b)**. Compared with the values

without KrF excimer laser irradiation, significant increases in the integrated peak intensities for both excited and ground-state species (C_2, CH, OH) were observed with the Kr excimer laser irradiation, suggesting more excited and ground-state species were generated with the KrF excimer laser irradiation. However, the increment of integrated peak intensities slowed down as the laser fluence increased from 0.6 to 1.4 J/cm^2.

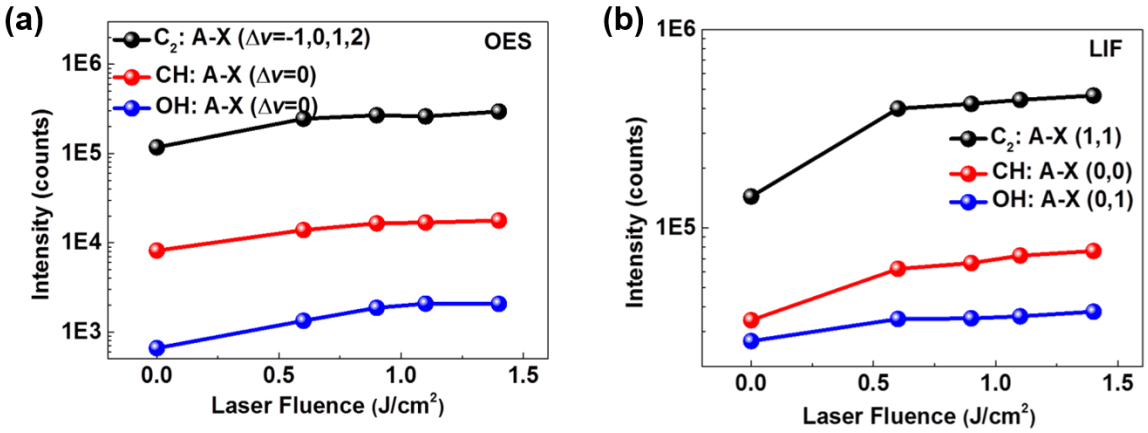

Figure 6.3-4 Integrated intensities of **(a)** OES peaks and **(c)** LIF signals of C_2, CH, and OH plotted as a function of the laser fluence.

Obvious increments in the concentrations of both excited and ground-state C_2, CH, and OH species were observed in the excimer-laser-irradiated flames. These species are all considered to be critical for diamond formation.[266,282–285] To determine how these species were generated, the flame temperature, T_{flame}, was analyzed at different laser fluences. Due to a strong coupling between the translational and rotational energy states, the flame temperature can be approximated by the rotational temperature derived from the emission intensities of the high-resolution rotational lines of CH using the Boltzmann plot (**Figure 6.3-5 (a)**).[286,287] The Boltzmann plots were derived from the spectra using the following equation:

$$\ln\left(\frac{I\lambda^4}{S_{J'J''}}\right) = -\frac{1}{T_f}\frac{E_{J'}}{k} + \ln C, \quad \textbf{(23)}$$

where I is the relative emission intensity of a rotational line obtained from the experimental spectrum; C is a proportionality constant that is the same for all rotational transitions within a band; $S_{J'J''}$ is the rotational intensity factor, l is the wavelength of the emitted spectral line, $E_{J'}$ is the rotational energy of the initial level, k is the Boltzmann constant, and T_r is the rotational temperature. **Figure 6.3-5 (b)** shows the Boltzmann plots of $\ln(I\lambda^4/S_{J'J''})$ versus $E_{j'}/k_B$, in which the slopes correspond to $1/T_r$.

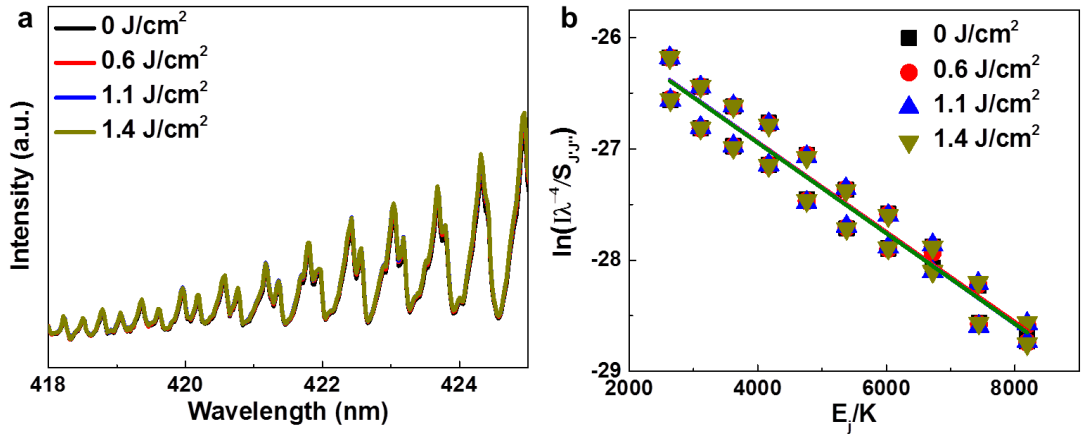

Figure 6.3-5 (a) High-resolution optical emission spectra of the rotational R-branch structure of the CH emission band at different laser fluences; **(b)** Boltzmann plots derived from the optical emission spectra

As shown in **Figure 6.3-6,** the flame temperature was found to be almost constant with respect to the laser fluence, suggesting that the excimer-laser-induced generation of both excited and ground-state species (C_2, CH, and OH) was attributed to nonthermal processes: electronic excitation and direct photolytic processes.

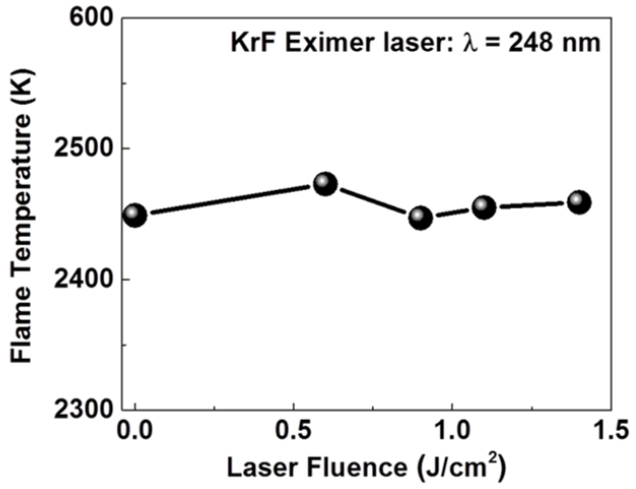

Figure 6.3-6 Flame temperature as a function of the KrF excimer laser fluence.

The constant flame temperature suggests that UV photochemistry is a "cold" process, contributing little to the gas-phase temperature variation. As illustrated in **Figure 6.3-7**, UV photons absorbed by the molecules can directly excite electronic transitions to the states where dissociation is ready to occur when the photon energy, hv, exceeds the bond dissociation energy, D_0[6]. The large photon energy of the KrF excimer laser, 5 eV, is sufficiently high to induce both electronic excitations of CH, OH, and C_2 and direct photolysis of CH and OH whose bond dissociation energies are lower than the excimer laser photon energy (**Figure 6.3-7**). Based on the comparison of the LIF and OES signals, it was found that both electronic excitation and photolysis occurred in the flame with the KrF excimer laser irradiation.

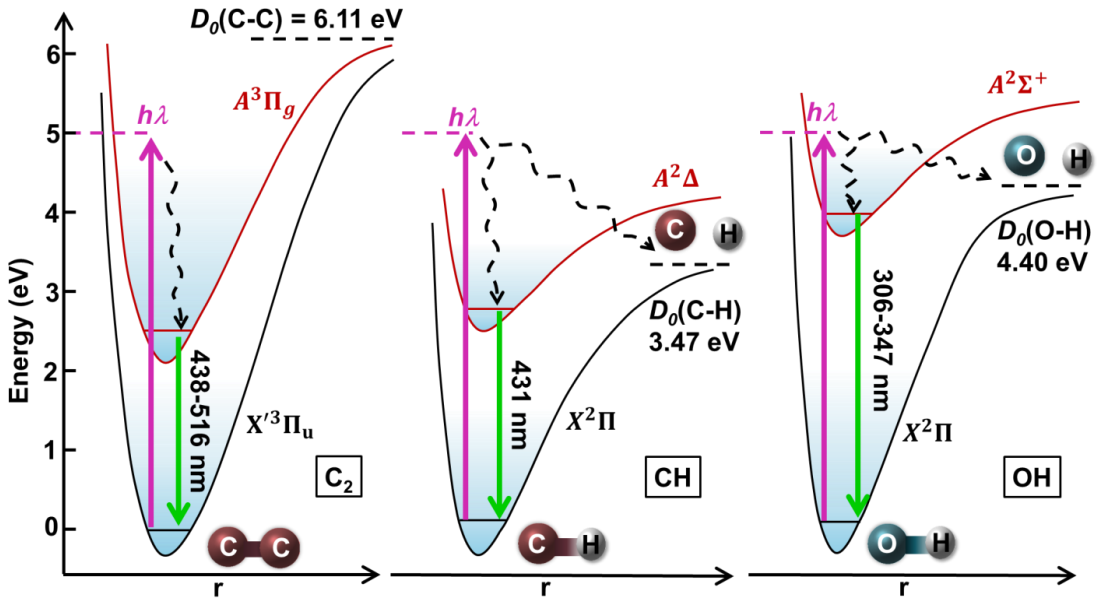

Figure 6.3-7 Diagram of transition processes of reactive radicles, C_2, CH and OH, under the KrF excimer laser excitations.

Besides the three emissive species which are detectable using both OES and LIF, there are also a large number of other non-emissive hydrocarbons existing in the flame, including CH_3 (D_0 = 4.69 eV), C_2H_4 (D_0 = 4.81 eV), etc., whose bonding energies are lower than the photon energy of the KrF excimer laser.[288] Photolysis of C_2H_2 and more than 20 organic molecules by either 193 or 248 nm laser have also been reported.[273,275] The higher the laser fluence is, the larger the photon flux would be, leading to the generation of more reactive species. The electronically excited reactive species are generated from the direct UV photolysis in a "nonthermal" fashion.

6.3.2 Effect of KrF (λ = 248 nm) excimer laser irradiation on diamond growth rate and quality

Based on the understanding of the flame gas phase variation with the KrF excimer laser irradiation, we prepared diamond films under KrF excimer laser irradiation at a fixed laser frequency of 35 Hz with laser fluences tuned from 0.6 to 1.4 J/cm^2 to study the influence of the KrF excimer laser irradiation on the diamond growth. The surface morphologies of the diamond films deposited at different laser fluences, from 0.6 to 1.4 J/cm^2, are shown in **Figure 6.3-8 (a)**. The diamond film deposited without KrF excimer laser irradiation consisted of randomly oriented grains with an average size of 2 μm. The average diamond grain size increase as the laser fluence increases, reaching a value of 5 μm at a laser fluence of 1.4 J/cm^2.

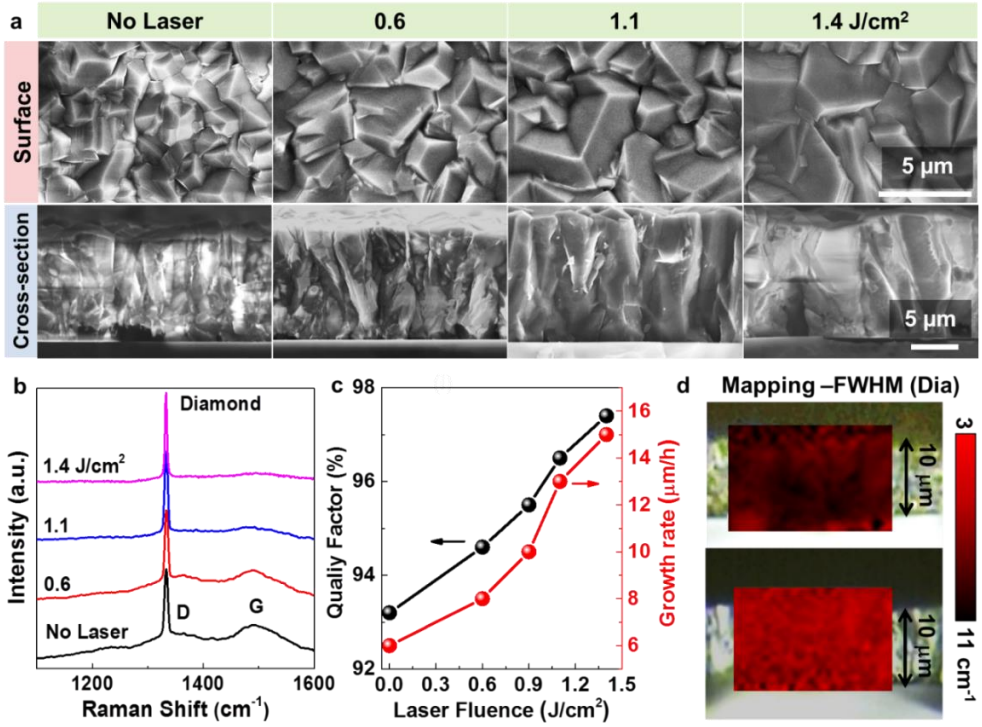

Figure 6.3-8 (a) SEM micrographs of surface and cross-sectional morphologies of the D films deposited without and with KrF excimer laser irradiation at different laser fluences

and 35 Hz. **(b)** Raman spectra of corresponding D films. **(c)** The growth rate and the film quality factor as functions of the laser fluence. **(d)** Raman mapping of the D peak full width half maximum (FWHM)of the D films prepared (top) without and (bottom) with KrF excimer laser irradiation at 1.4 J/cm^2.

CVD diamond grows in a columnar structure with a grain size that is initially very small and then increases through the film thickness.[289] To determine how KrF excimer laser irradiation affects the grain size evolution, the cross-sectional microstructures of the films were evaluated. As shown in **Figure 6.3-8 (a)**, large, uniform grains were obtained with KrF excimer laser irradiation. The lateral grain size increased as the laser fluence increased. The fast-lateral grain size evolution suggests that the D crystal growth under KrF excimer laser irradiation experienced less secondary nucleation, which is known to impede expanded growth of a single grain. Secondary nucleation is believed to arise from amorphous graphitic carbon accumulation that alters the initial crystal growth direction and subsequently induces secondary nucleation.[290] Apparently, the significantly enlarged lateral grain sizes indicate that KrF excimer laser irradiation greatly suppresses the amorphous graphitic carbon formation during the diamond growth.

The D film quality was evaluated using Raman spectroscopy. A sharp diamond peak around 1332 cm^{-1} was observed in all spectra, as shown in **Figure 6.3-8 (b)**. The D-band at 1370 cm^{-1} and the G-band centered at 1500 cm^{-1} represent disordered carbon and graphitic carbon content in the film, respectively.[291] The D peak became sharper and higher as the laser fluence increased, suggesting higher D quality and pure D phase obtained with KrF excimer laser irradiation. A quality factor, $Q_i = I_D / (I_D + I_{a\text{-}C}/ 233)$, was derived from the Raman spectra, with I_D and $I_{a\text{-}C}$ being the integrated intensities of the D peak and the

sum of the integrated intensities of the non-D carbon bands, respectively [292]. The D quality factor exhibites a nearly linear increase with respect to the laser fluence, reaching a value of 97.4% at a laser fluence of 1.4 J/cm^2, 4.2% higher than the film prepared without KrF excimer laser irradiation (**Figure 6.3-8 (c)**). The growth rate, R, shows a linear increase with respect to the laser fluence in **Figure 6.3-8 (c)**, reaching a value of 15 μm/hr at 1.4 J/cm^2, more than twice that obtained without KrF excimer laser irradiation. The enhanced growth rate and the improved quality suggest the positive role of UV laser irradiation in promoting D growth.

Raman mapping based on full width at half maximum (FWHM) of the D Raman peak was performed to evaluate the cross-sectional grain crystal quality and uniformity. As shown in **Figure 6.3-8 (d)**, the cross-section of the D film prepared with KrF excimer laser irradiation at 1.4 J/cm^2 is more uniform than that prepared without laser irradiation, exhibiting an average FWHM value of 5.7 cm^{-1}, which was 3.1 cm^{-1} narrower than that prepared without a KrF excimer laser irradation. A uniformly promoted D quality was thus confirmed through the film thickness with KrF excimer laser irradiation.

The morphology and quality characterization of the D films suggested that KrF excimer laser irradiation affected the D growth process in a way that suppresses graphitic carbon formation and favors the D growth. The nucleation stage is the most sensitive to amorphous graphitic carbon accumulation because D nucleates from spontaneous precipitation of a pure sp^3 C cluster from the amorphous graphitic C matrix that forms during the incubation stage.[293,294] To confirm the suppressing effects of KrF excimer laser irradiation on amorphous graphitic C accumulation, the D nucleation process was further investigated by in situ monitoring of the field-enhanced thermionic emission current[294] and preparing D

films for a short time, (i.e., 10 min). The current measurement setup and the thermionic current evolution as a function of the deposition time are illustrated in **Figure 6.3-9 (a)**. A power supply was connected to the flame torch and the brass sample holder. The bias voltage on the substrates was -5 V with respect to the flame torch. The current between the WC substrate and the torch was measured using a nanoampere meter during the diamond growth. **Figure 6.3-9 (b)** shows the thermionic current-deposition time curves without and with KrF excimer laser irradiation at different fluences. The zero-emission current period between 0 to 300 s (the flat segment of the curve) indicates a diamond-free surface, representing an incubation period. From 300 to 600 s, the thermionic current increased from 13 to 27 μA due to newly nucleated diamond particles and increased surface coverage, representing a nucleation period. At 600 s, the thermionic current was close to the maximum, about 28 μA. From 600 to 800 s, the thermionic current remained stable and continuous films form. As shown in **Figure 6.3-9 (b)**, the nucleation time is significantly shortened as the KrF excimer laser fluence increased.

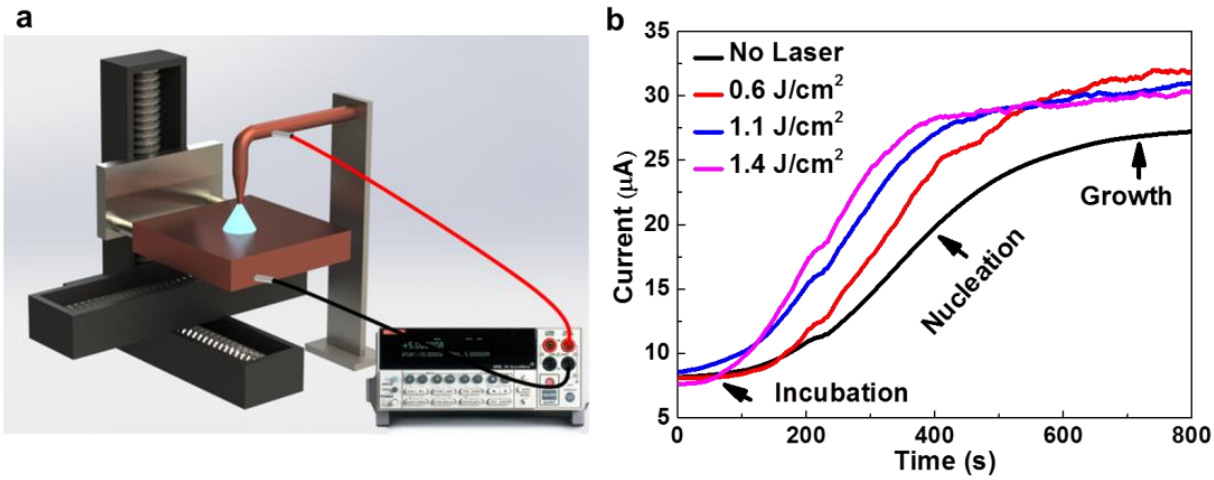

Figure 6.3-9 (a) Schematic illustration of in situ field-enhanced thermionic current measurement setup. **(b)** Thermionic current-deposition time curves without and with KrF excimer laser irradiation at different fluences.

The surface morphologies of the 10 min D films prepared at different laser fluences are shown in **Figure 6.3-10 (a).** Cauliflower-like nano-D films were obtained without laser irradiation while KrF excimer laser irradiation transformed the nano-D feature to a larger faceted microcrystal structure. The cauliflower-like grains formed under a condition where continuous growth of an initial-formed crystalline nuclei was severely disturbed by the secondary nucleation process due to the amorphous graphitic C accumulation. As shown in the Raman spectra (**Figure 6.3-10 (b)**), the 10-min D film prepared without laser irradiation exhibited a typical nano-D feature. The Raman peaks appearing at around 1150 (ν_1) and 1480 cm^{-1} (ν_3) are related with the trans-polyacetylene phase present at the grain boundaries as the grain size reached nanometer scale, representing a signature of nano-D.[33] These two peaks became weakened, and the D peak rose up as the laser fluence increased.

At a laser fluence of 1.4 J/cm^2, the ν_1 and ν_3 peaks were difficult to observe; and a micro-D Raman feature was exhibited.

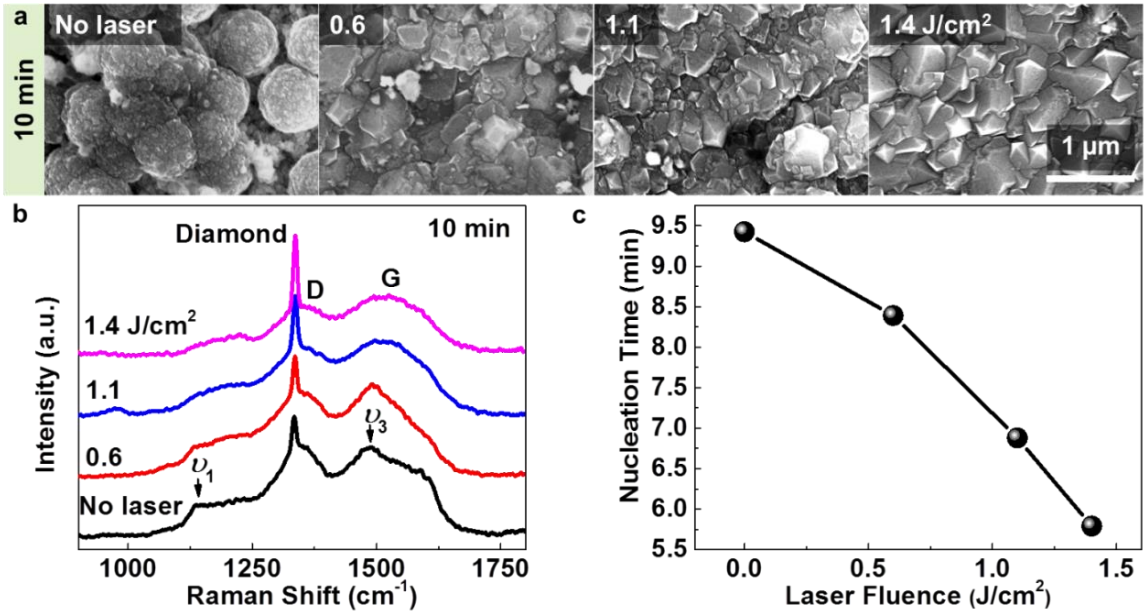

Figure 6.3-10 **(a)** SEM micrographs of D film surface morphologies prepared without and with KrF excimer laser irradiation at different laser fluences and 35 Hz for 10 min. **(b)** Raman spectra of the corresponding D films. **(c)** The nucleation time plotted as a function of the laser fluence.

As shown in **Figure 6.3-10 (c)**, the nucleation period was obviously shortened from 9.5 to 5.5 min as the laser fluence increased. D nuclei grow through transformation of amorphous C to D at the amorphous matrix-D interface. This transformation is governed by a kinetic balance of the etching and the growth of graphitic C and D.[36] The longer the nucleation process, the thicker the amorphous C transition layer that forms at the initial stage. The significantly shortened nucleation process confirmed that the KrF excimer laser irradiation affects the D growth process by quickly balancing the kinetic competition process in a way favoring D nucleation and suppressing amorphous graphitic C co-

deposition. The significantly shortened nucleation time and the morphology/Raman characterization of the 10 min D films suggest that KrF excimer laser irradiation facilitates the nucleation process to quickly complete, accompanied by greatly suppressed non-D C accumulation.

Figure 6.3-11 (a) shows a TEM micrograph of the cross-section of a 389 nm thick D film on WC prepared with KrF excimer laser irradiation at 1.4 J/cm^2. A thin platinum (Pt) layer was deposited on the D film to protect it from ion beam damage during the sample preparation process. A high resolution TEM (HRTEM) micrograph (**Figure 6.3-11 (b)**) of the D crystal region marked by a blue square, in **Figure 6.3-11 (a)**, clearly shows continuous D {111} planes, confirming the good D grain quality. D has an interplane d_{111} value of 2.06 Å. A distance of 10 planes were measured for accurate d value evaluation of the diamond {111} planes and measured to be 0.207 nm, which matches the theoretical value. The corresponding Fast Fourier Transform (FFT) pattern shows D (440) spots, suggesting the beam direction was <110>.

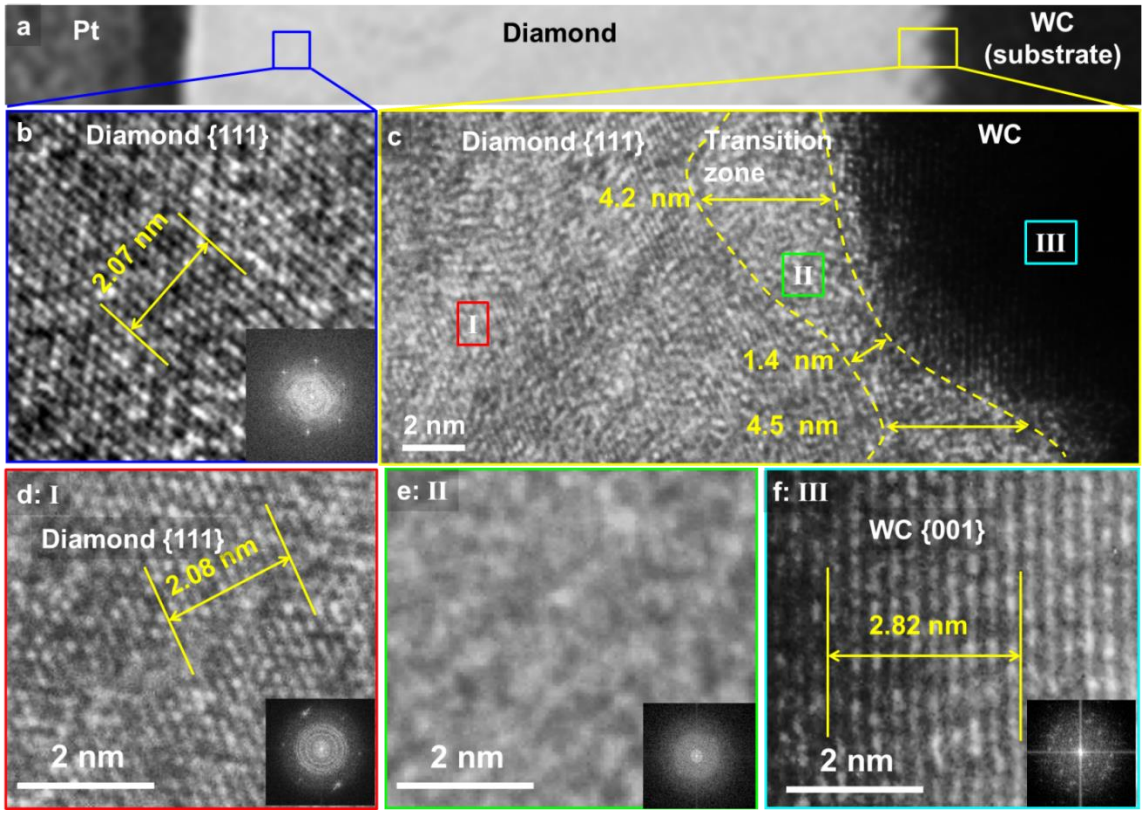

Figure 6.3-11 (a) A TEM micrograph of a 389 nm thick D film on a WC substrate prepared with KrF excimer laser irradiation at 1.4 J/cm^2. HRTEM micrograph of **(b)** the D crystal region with its FFT pattern and **(c)** the film-substrate interface as marked by a blue square and a yellow rectangle in **(a)**, respectively. Atomic-resolution TEM micrographs of the regions **(d)** I, **(e)** II, and **(f)** III marked in **(c)** with their corresponding FFT patterns, representing D, transition zone, and WC, respectively.

To further confirm that the nucleation time is greatly shortened and the amorphous C transition layer is suppressed with KrF excimer laser irradiation, HRTEM was performed to reveal the film-substrate interface in **Figure 6.3-11 (c)**. No sharp interface was identified because the WC substrate was not atomically flat and has nanoscale roughness. WC has a theoretical d_{001} value of 2.82 Å. Based on the atomic-resolution HRTEM micrographs

(**Figure 6.3-11 (d)-(f)**) of different zones and their FFT patterns, shown in the insets, it is easy to differentiate them based on the d value evaluation.

Additionally, TEM micrograph of a D film prepared without KrF excimer laser irradiation is shown in **Figure 6.3-12 (a)**. A 756 nm thick graphitic C transition zone was identified between the D crystal zone and the WC substrate. The Raman spectrum of this transition zone in the inset of **Figure 6.3-12 (a)** exhibits a typical polycrystalline graphitic C Raman feature. A HRTEM micrograph (**Figure 6.3-12 (b)**) of the D crystal region marked by a green rectangle in **Figure 6.3-12 (a)** shows fringes from the D {111} planes with some particle inclusions, which can be assigned to a graphitic C quantum dots with {1120} planes according to the d value measurement. A HRTEM micrograph of the transition zone in **Figure 6.3-12 (c)** shows graphitic C particles embedded in an amorphous matrix, matching the Raman features.

Such a narrow transition zone was comparable to the D films on WC prepared using microwave-enhanced and hot-filament CVD, as reported,[295,296] which are known to produce better quality D films than combustion CVD. The narrow transition zone observed with KrF excimer laser irradiation confirms again that KrF excimer laser irradiation improves the diamond growth process by suppressing the non-D carbon formation.

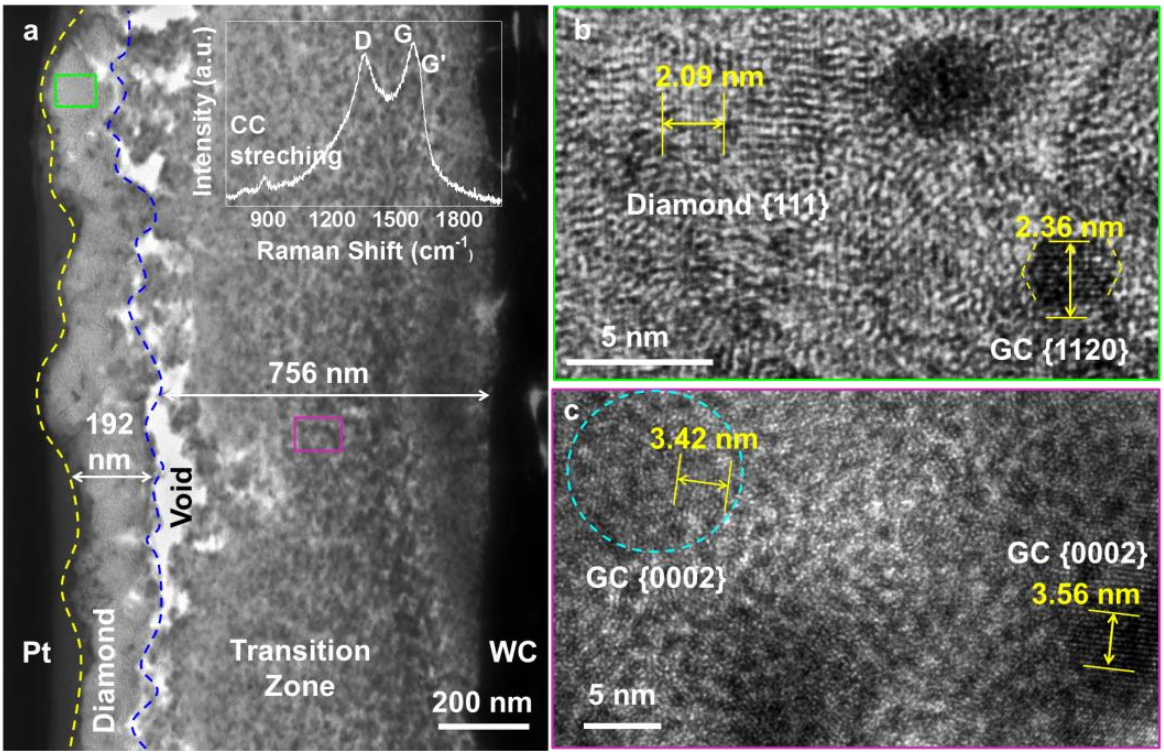

Figure 6.3-12 (a) A TEM micrograph of a D film sample prepared without KrF excimer laser irradiation, and HRTEM micrographs of **(b)** the D crystal region and **(c)** the graphitic C transition zone as marked by green and purple rectangles, respectively. The inset of **(a)** is the Raman spectrum of the sample.

The observation of fast lateral grain size involution and the significantly shortened nucleation time can be explained by the observation of gas phase variation in the flame. We found a pronounced increase of OH- abundance in the center region of the flame. OH-radical plays a critical role in combustion synthesis of D by etching the surface-bond hydrogen and stabilizing the sp^3 hybridized surface C bonds.[273,274] Its increment explains why the graphitic C accumulation was greatly suppressed with KrF excimer laser irradiation. Furthermore, another possible contribution to the significantly promoted diamond growth is the increased atomic H concentration due to promoted H-abstraction

processes with KrF excimer laser photolysis. The photo-induced dissociation of hydrocarbons preferentially occurs at C-H bonds through H-abstraction processes rather than at C-C bonds.[297] The primary processes of 193 nm UV photolysis of C_2H_2 are:

$$C_2H_2 \rightarrow C_2H + H, \quad \textbf{(24)}$$

$$C_2H_2 \rightarrow C_2 + H_2.^{298} \quad \textbf{(25)}$$

The primary processes of 147 nm UV photolysis of C_2H_4 are:

$$C_2H_4 \rightarrow C_2H_2 + H_2, \quad \textbf{(26)}$$

$$C_2H_4 \rightarrow C_2H_2 + 2H.^{299} \quad \textbf{(27)}$$

The reactions of atomic H not only control the gas-phase chemistry but also determine the availability of reactive sites upon the sites. D growth from oxyacetylene flame proceeds through two critical surface reactions: 1. addition of reactive hydrocarbon radicals on the active surface sites; 2. H-abstraction from the hydrocarbon radicals to make more reactive sites to accept hydrocarbons and stable sp^3 hybridized carbon bonds.[289] The promoted H-abstraction processes with KrF excimer laser photolysis of hydrocarbons thus could play a dominant factor in promoting diamond growth. However, more detailed study is required to confirm this hypothesis because the KrF excimer laser used in this study has a wavelength of 248 nm, longer than those used in the reported photochemistry study of C_2H_2 and C_2H_4, making the photo-induced H abstraction rate much smaller. [298,299]

6.3.3 Conclusions

The influence of UV-laser-induced photolysis in D growth is investigated. OES and LIF of the flame indicated that the UV-laser-induced photolysis produced large quantities of reactive radicals in the flame, contributing directly to the promotion of D growth. Investigation of the nucleation process suggests that the KrF excimer laser irradiation modifies the diamond growth in a way favoring diamond formation and suppressing nondiamond C accumulation, leading to an enhanced diamond deposition rate and improved diamond quality. The transition layer is reduced from 700 nm without laser to 5 nm with UV laser irradiation. The discovery of the laser photochemistry advantages in diamond growth is of great significance for extensive improvement in the synthesis of a broad range of technically important materials.

6.4 Effect of UV laser wavelength (KrF, λ = 248 nm vs. ArF λ = 193 nm) on the diamond growth

6.4.1 Effect of UV wavelength on D growth rate and quality

To identify how UV laser irradiation at different wavelengths affects D growth, D films were prepared under ArF and KrF excimer laser irradiations at 193 and 248 nm, respectively. **Figure 6.4-1** shows the SEM micrographs of the surface morphologies of the D films after 1 h of deposition.

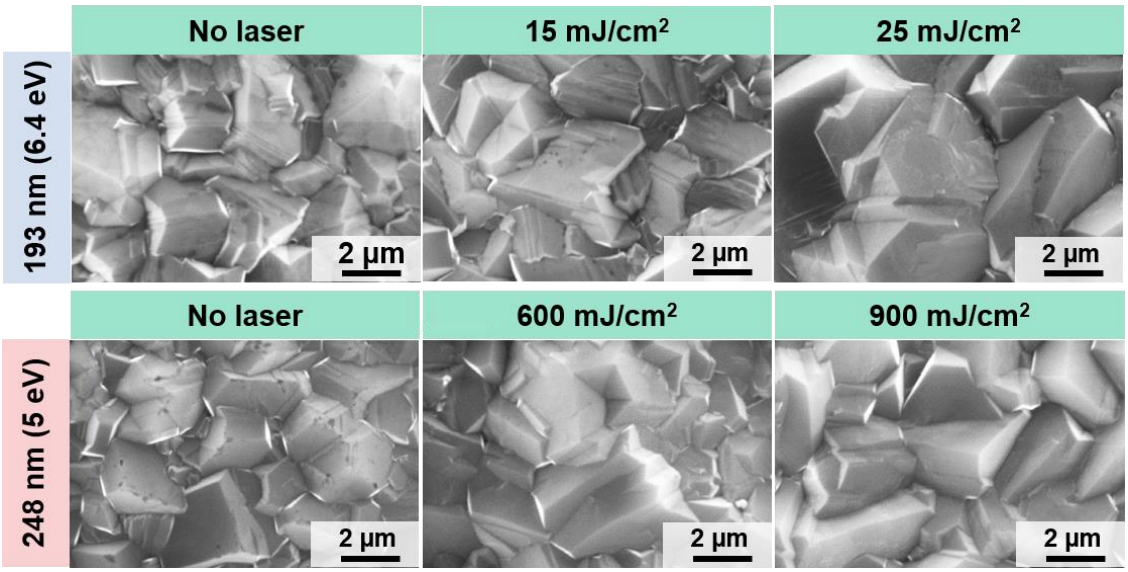

Figure 6.4-1 SEM micrographs of surface morphologies of the D films prepared for 1 h deposition under 193 and 248 nm laser irradiations at different laser fluences.

The D film deposited without laser irradiation consisted of randomly oriented diamond crystals with an average size of 2.5 µm. It was noticed that UV laser irradiations do not change the D grain shape but resulted in an obvious increase in the grain size. The average D grain size increased with respect to the laser fluence at both wavelengths, 193 and 248 nm, reaching 5 µm at a laser fluence of 25 mJ/cm^2 for the 193 nm laser and 3.5 µm at a laser fluence of 900 mJ/cm^2 for the 248 nm laser, respectively.

The thickness profiles of the D films are shown in **Figure 6.4-2**, and the deposition rate was plotted as a function of the laser fluence and is shown in **Figure 6.4-3**.

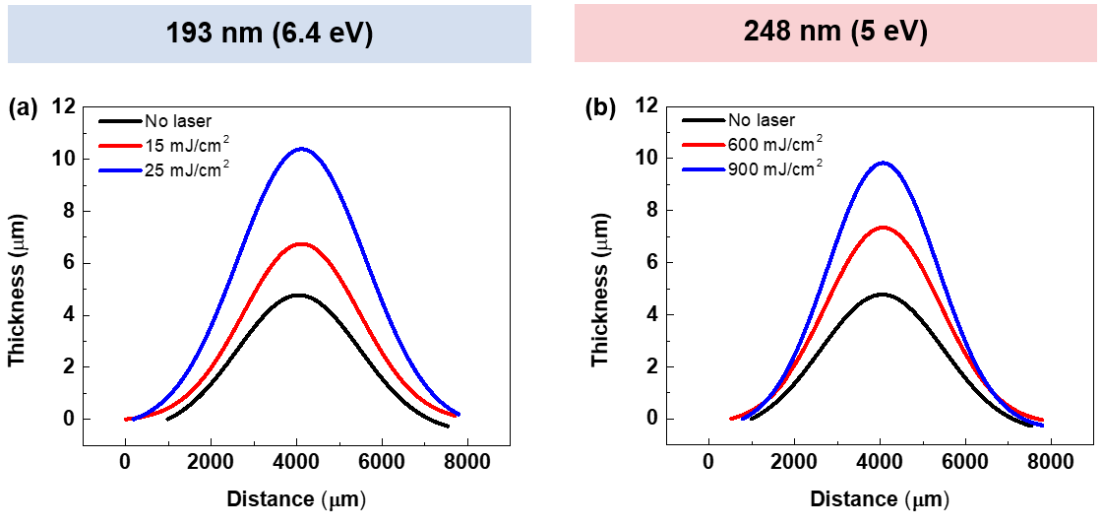

Figure 6.4-2 Thickness profiles of D films prepared at different laser fluences at a UV wavelength of **(a)** 193 and **(b)** 248 nm.

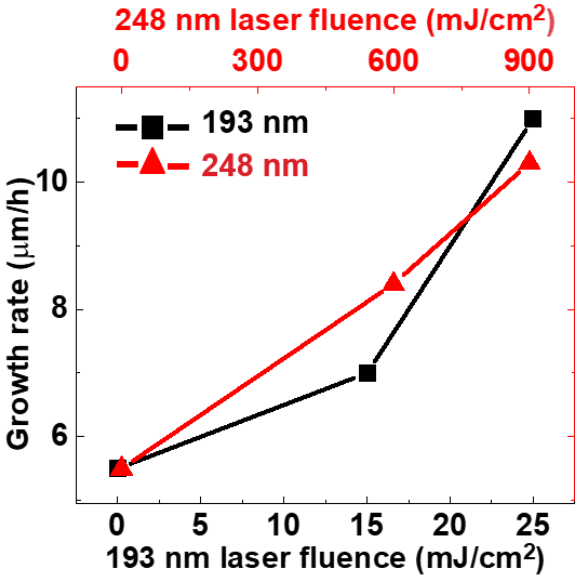

Figure 6.4-3 Growth rates of the D films prepared for 1 h deposition under 193 and 248 nm laser irradiations at different laser fluences.

The D film prepared without UV laser irradiation had a deposition rate of 5 μm/h. With UV laser irradiations, the deposition rates increased to 11 μm/h at a laser fluence of 25 mJ/cm^2 for the 193 nm laser and 10.3 μm/h at a laser fluence of 900 mJ/cm^2 for the 248 nm laser. In addition, the D film quality was evaluated by Raman spectroscopy. All Raman

spectra were constituted with a diamond peak at 1332 cm^{-1} and two bands at 1370 (D-band) and 1500 cm^{-1} (G-band), which represent graphitic C, as shown in **Figure 6.4-4 (a)** and **(b)**.

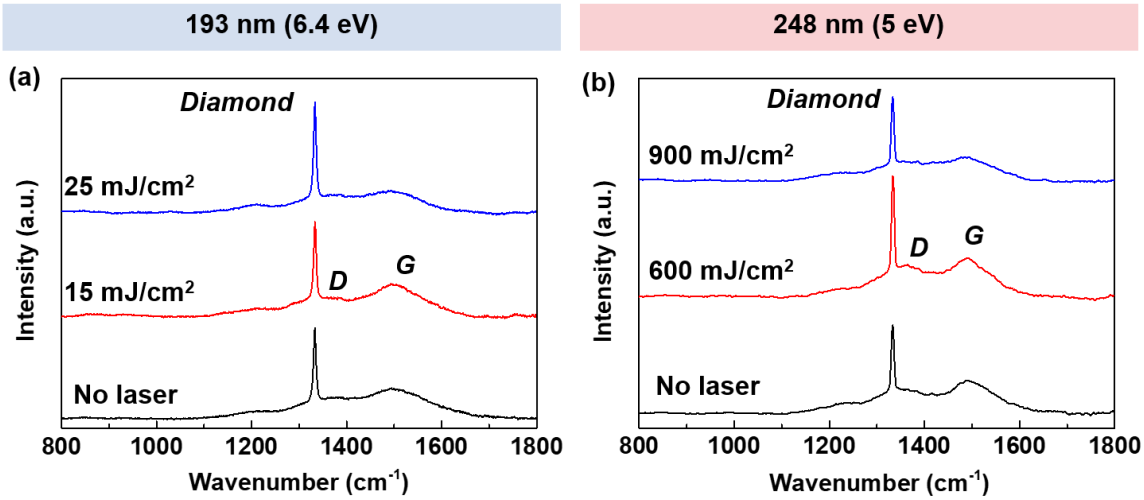

Figure 6.4-4 Raman spectra of the D films prepared with 193 or 248 nm laser irradiations at different fluences

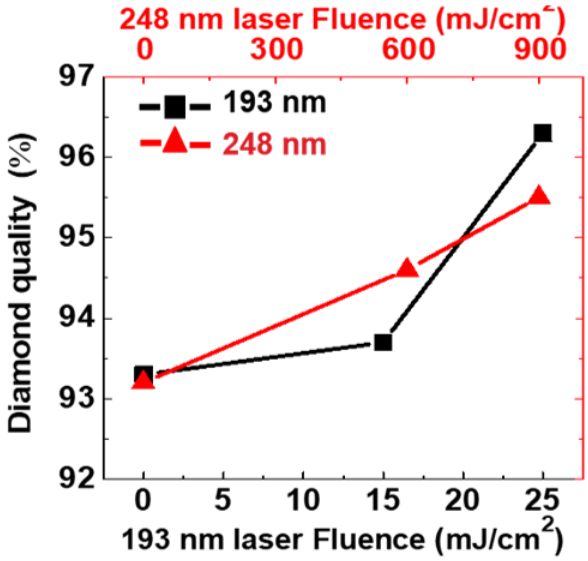

Figure 6.4-5 D quality factors of the diamond films plotted as functions of the laser fluence: black solid squares and red solid triangles are for the 193 and 248 nm lasers, respectively.

The D quality was evaluated from the Raman spectra by calculating the quality factor.[292] **Figure 6.4-5** shows the quality factors plotted as functions of the laser fluence for the 193 and the 248 nm lasers. The diamond quality factor increased with respect to the laser fluence. The quality factor was 93.2% without laser irradiation and reached 96.5% and 95.5% with UV laser irradiations at a laser fluence of 25 mJ/cm^2 for the 193 nm laser and at a laser fluence of 900 mJ/cm^2 for the 248 nm laser, respectively.

It is worthy to note that the laser fluence has a linear influence on the growth rate and D quality at 248 nm, but a super-linear influence at 193 nm. Moreover, a larger grain size, a higher deposition rate, and a higher D quality factor were obtained with UV laser irradiation at 193 nm than those obtained at 248 nm, although the laser fluence of the 193 nm laser was one order of magnitude lower than that of the 248 nm laser. The results suggest the advantage of a short laser wavelength from the irradiating laser source in promoting the diamond growth.

During the CVD process, D films grew with a columnar microstructure where the lateral grain size increased as the film became thicker as explain before.[289] To further understand the effects of UV laser wavelength on the lateral grain evolution, the cross-sectional microstructures of the D films were studied using SEM and are shown in **Figure 6.4-6**. The UV laser in both cases induce a faster lateral grain size evolution which can be attributed to the suppression of secondary nucleation sites in the early stage of the D deposition.

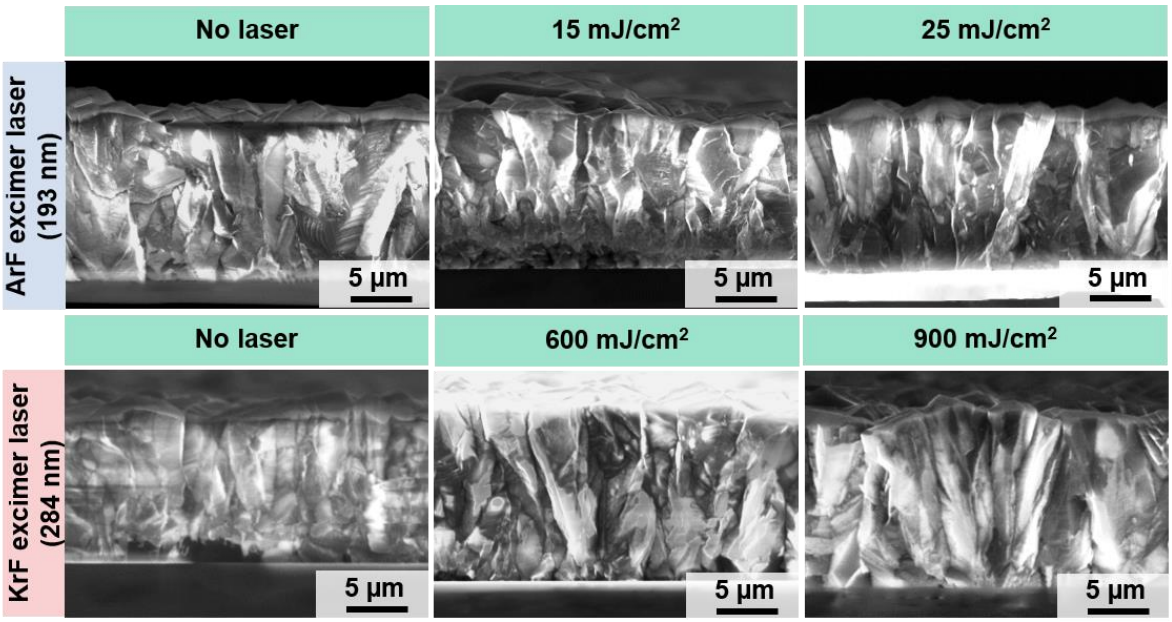

Figure 6.4-6 Cross-sectional SEM micrographs of the D films obtained for a similar thickness under 193 and 248 nm laser irradiations

The fast-lateral grain size evolution indicates that the UV laser irradiation effectively suppressed secondary nucleation, which is known to impede the expanded growth of D grains. The faster lateral grain size evolution observed in the D films prepared with UV lasers irradiations indicate that non-D C formation was suppressed more efficiently.

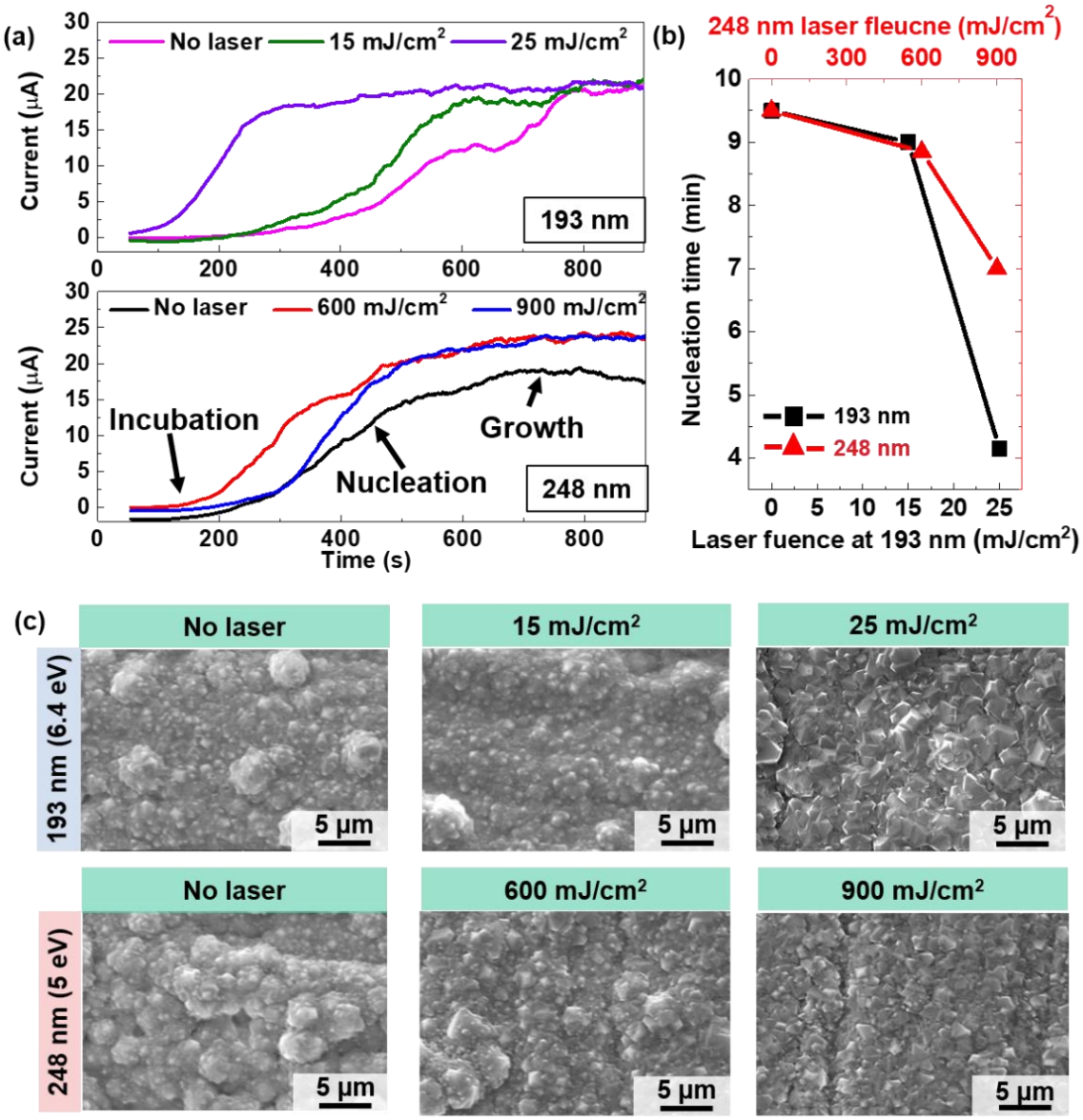

Figure 6.4-7 (a) nucleation times as functions of UV laser wavelengths and fluences, and **(b)** D quality plotted as functions of laser fluence at 193 and 248 nm, **(c)** SEM micrographs of surface morphologies of the 10-min D films prepared without and with UV laser irradiation at different laser fluences at laser wavelengths, 193 and 248 nm.

Suppression of non-D C formation by UV laser irradiation is indicated based on the study of lateral grain size evolution through D film thickness. To further confirm the suppression effects of non-D C formation by UV laser irradiation, the D nucleation was monitored by

in situ measurement of the field-enhanced thermionic current during D growth under UV laser irradiations at 193 and 248 nm. Three distinct regions were identified as the incubation, nucleation, and growth stages from the thermionic emission current curves, as shown in **Figure 6.4-7 (a)**. The nucleation time was retrieved and plotted as functions of the laser fluences for the 193 nm and 248 nm laser irradiations in **Figure 6.4-7 (b)**. Compared with a long nucleation time of 9.5 min without laser irradiation, UV laser radiations reduced the nucleation time to 4.2 and 7.0 min for the 193 nm and 248 nm lasers, respectively, as shown in **Figure 6.4-7 (b)**. Similar to the variation trend of growth rate and D quality, the nucleation time decreased linearly with respect to the laser fluence at 248 nm, but exhibited a super-linear relation at 193 nm, which suggests that lasers with a shorter wavelength influence the D growth more efficiently.

A much shorter nucleation time with 193 nm laser irradiation compared to 248 nm laser irradiation suggests that the 193 nm laser irradiation affects the D growth in the initial nucleation and, in a more efficient way, suppresses non-D C formation. To confirm the suppressing effects of UV laser irradiation on amorphous graphitic C accumulation, the D nucleation process was further investigated by preparing D films for a short time, i.e., 10 min. The surface morphologies of the 10-min D films prepared at 193 and 248 nm are shown in **Figure 6.4-7 (c)**. Nanocrystalline D films were obtained without laser irradiation while UV laser irradiation transformed the nano-D feature to a larger faceted microcrystal structure. The influence was more significant in the D films prepared at 193 nm.

6.4.2 Influence of UV wavelength on the flame chemistry

An increase in the deposition rate, improvement in diamond quality, fast lateral grain size evolution, and significantly reduced nucleation time with the UV laser irradiation of the D-forming combustion flame have been understood in the D growth process. Irradiation at the short wavelength of 193 nm was found to affect the D growth process in a more pronounced way. Material synthesis by CVD is highly sensitive to the gas phase chemistry change.[300,301] To reveal the effects of UV laser irradiation on D growth, the flame chemistry was studied under laser irradiations both at 193 and 248 nm using OES. As shown in **Figure 6.3-1 (a)**, the ICCD gate time of the spectrometer and the laser pulses were synchronized to acquire OES signals at the beginning of each laser pulse with a 0 μs gate delay for a gate width of 10 μs. Three species were identified in the OES spectra (**Figure 6.4-8**): diatomic carbon (C_2), methylidyne radical (CH), and hydroxyl radical (OH).[266] It was found that the emission intensities of all species increased with respect to the increase in the laser fluence.

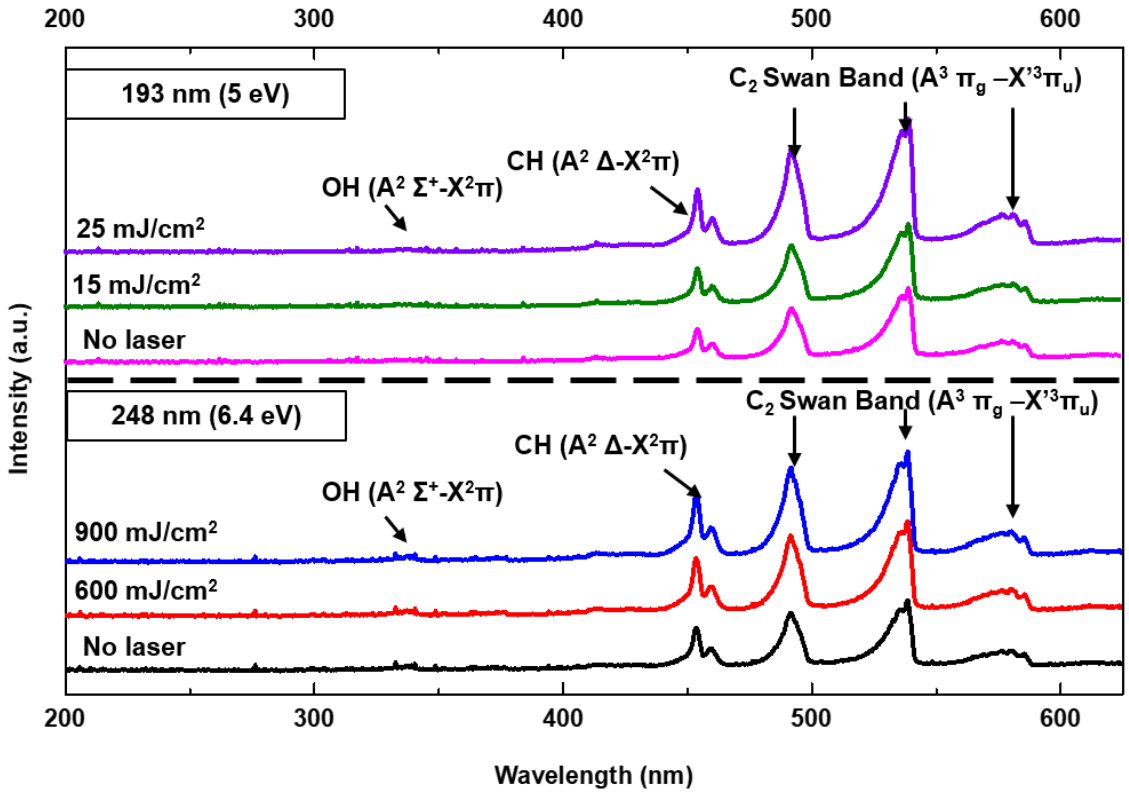

Figure 6.4-8 OES spectra of the combustion flame under 193 or 248 nm laser irradiations at different fluences.

To visualize the two-dimensional (2D) distribution of the excited species within the flame, images were collected with and without the UV laser irradiations at 193 and 248 nm, as shown in **Figure 6.4-9**. The flame under the UV laser irradiation was much brighter than the flame without laser irradiation. The brightness increased as the laser fluence increased, suggesting that more species were generated with the laser excitation. Three band-pass filters were placed in the optical path to distinguish the emission bands of the following individual excited species: C_2, CH, and OH. More enhanced emission intensities were identified with the 193 nm laser irradiation than those with the 248 nm irradiation, suggesting an increase in the amounts of all observed emissive species. It is worth mentioning that the laser fluence of the 193 nm laser is about 40 times lower than that of

the 248 nm laser. The larger the laser fluence is, the higher the photo flux is, which means that the UV-laser-induced yield of the excited species per photon was much higher with the 193 nm laser irradiation than the 248 nm laser irradiation.

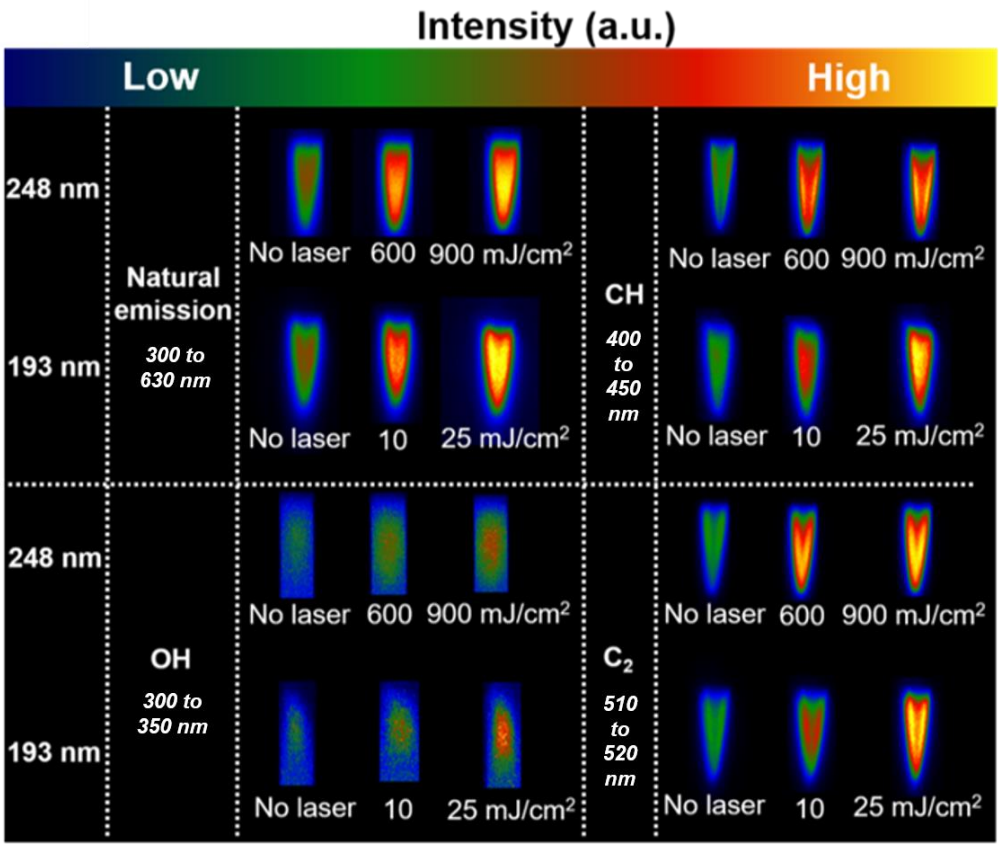

Figure 6.4-9 Flame images with and without the filters under different laser irradiation conditions.

Optical images show an increase in the OH, CH, and C_2 abundance with UV laser irradiations. All three species were reported to positively influence the diamond growth. The OH radical functions as carbon etchant by etching the surface-bond hydrogen and stabilizing the sp^3 hybridized surface carbon bonds.[302] The CH radical was also believed to be helpful in D growth.[303] The addition of a C_2 to a hydrogen-terminated diamond (110) surface is energetically favorable and makes the growth of the existing crystal proceeds

readily.[284,285] The increments of all three radicals explain why both growth rate and crystal quality were improved in the UV-laser-assisted combustion synthesis of diamond. To determine how the species were generated by UV laser irradiations, the flame temperatures were estimated for both laser wavelengths at different fluences. Due to a strong coupling between the translational and rotational energy states of the molecules, the flame temperature was approximated by the rotational temperature derived from high-resolution rotational line emission intensities of CH using the Boltzmann plot (**Figure 6.4-10 (a)-(d)**).[287]

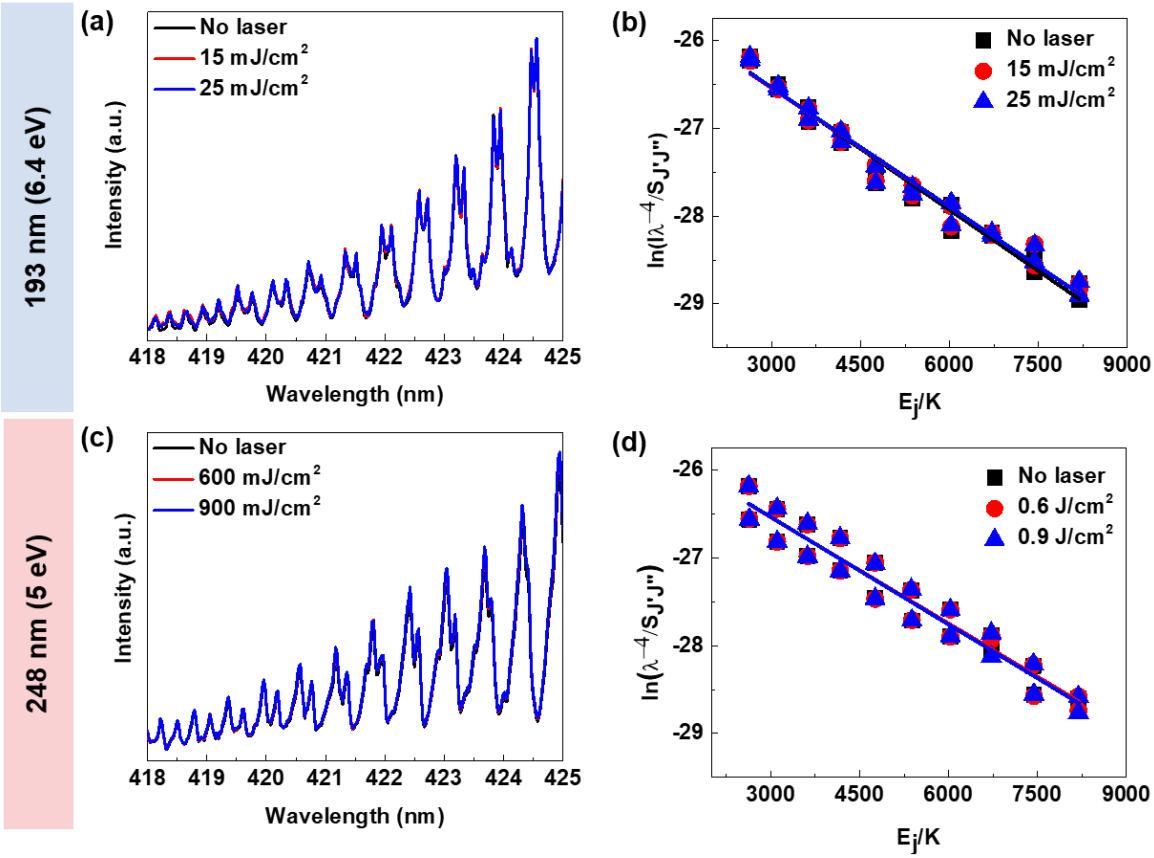

Figure 6.4-10 High-resolution optical emission spectra of the rotational R-branch of the CH and Boltzmann plots derived for flame temperature estimation of the combustion

flame under **(a)** and **(b)** 193 or **(c)** and **(d)** 248 nm laser irradiations at different laser fluences.

The flame temperatures with the UV laser irradiations at 193 (black square curve) and 248 nm (red triangle curve) were plotted as functions of the laser fluence, respectively, as shown in **Figure 6.4-11**. The flame temperatures fluctuated around 2450 K with an error of ± 40 K, showing weak dependence upon the laser fluence and wavelength. The fact that UV laser irradiation does not elevate the flame temperature suggests that the UV-laser-induced generation of the excited species is nonthermal.

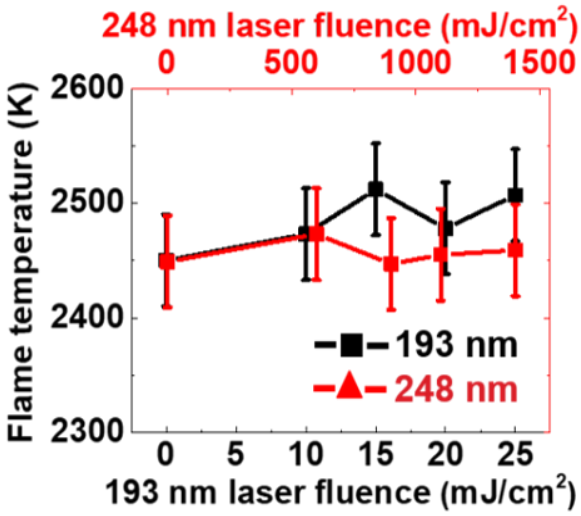

Figure 6.4-11 Flame temperatures as functions of the laser fluence.

The 2D flame images provide a general overview of specie distribution and their abundance. To qualitatively compare the effects of the UV laser irradiations at 193 and 248 nm on the change in species abundance, emission peak intensities assigned to each species were integrated and plotted as functions of the laser fluence, as seen in **Figure 6.4-12 (a)-(c)**. Although accompanied by large error bars due to the low peak intensity of OH, increases of OH with respect to the laser fluence at both 193 and 248 nm were observed.

Interestingly, it was found that the increasing curves of CH and C_2, with respect to the laser fluence at 248 nm, were well fitted linearly, while they were exponentially fitted in the case of laser fluence at 193 nm. Different fitting trends imply different mechanisms governing the photo-induced generation of the species at 193 and 248 nm. As mentioned previously, the laser fluence of the 193 nm laser was 40 times less than that of the 248 nm laser. By retrieving the slopes of the integrated intensity curves with respect to the laser fluence, it is found that 193 nm laser irradiation leads to approximately a two orders of magnitude higher increment rate of integrated peak intensity for all species, as shown in **Figure 6.4-12 (d)**, confirming that the 193 nm laser is much more efficient in changing the flame chemistry than the 248 nm laser.

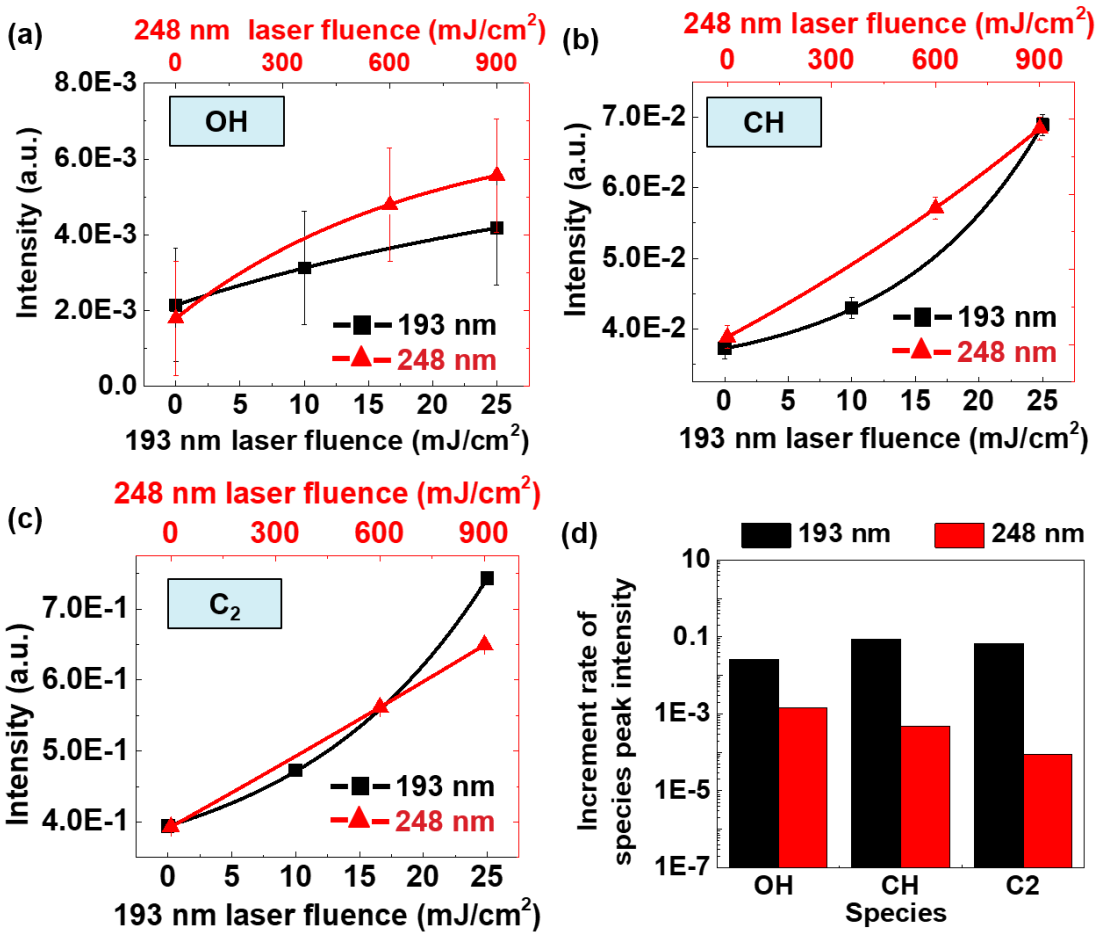

Figure 6.4-12 Integrated intensities of emission peaks assigned to distinct species, **(a)** OH, **(b)** CH, and **(c)** C_2, plotted as functions of the laser fluences at 193 and 248 nm, respectively, **(d)** slopes retrieved from the peak integration curves for the 193 nm and 248 nm lasers.

Chemical changes occur when the molecules are raised to an excited state possessing more than sufficient energy to break the weakest bond in the molecules. Electronic excitations or direct photolysis of simple molecules occur by absorbing photons in the UV regions, in which the primary products are generally in either electronically excited molecules or their dissociation products, i.e., reactive species. The photochemical process can be very specific, depending on the region of absorption. The advantages of a short laser wavelength, 193 nm, in modifying the flame chemistry over a wavelength of 248 nm have been identified, indicating that high photon energy is more efficient in photo-dissociations of hydrocarbons in the combustion flames. To determine the photodissociation pathways of the two hydrocarbon precursors, C_2H_2 and C_2H_4, upon absorbing photons with different photon energies, their energies and photochemical behaviors were carefully examined. The C-H bonding energy of C_2H_2 and C_2H_4 was 5.38 and 4.81 eV, respectively. The 193 nm photodissociation of C_2H_2 and C_2H_4 was extensively studied.[304–306] The 193 nm photodissociation of C_2H_2 proceeded through two steps, as illustrated in **Figure 6.4-13 (a)**. By absorbing one 193 nm photon, a C_2H_2 molecule was excited to the ^1A_u trans-bent excited state following by the primary dissociation process:[306]

$$C_2H_2 \rightarrow C_2H + H, \qquad \textbf{(28)}$$

The early emission studies by McDonald, Baronavski, and Donnelly showed that at high laser intensities,[307] two-photon photodissociation channels open up and proceed via sequential elimination of H atoms:

$$C_2H \rightarrow C_2 + H, \quad \textbf{(29)}$$

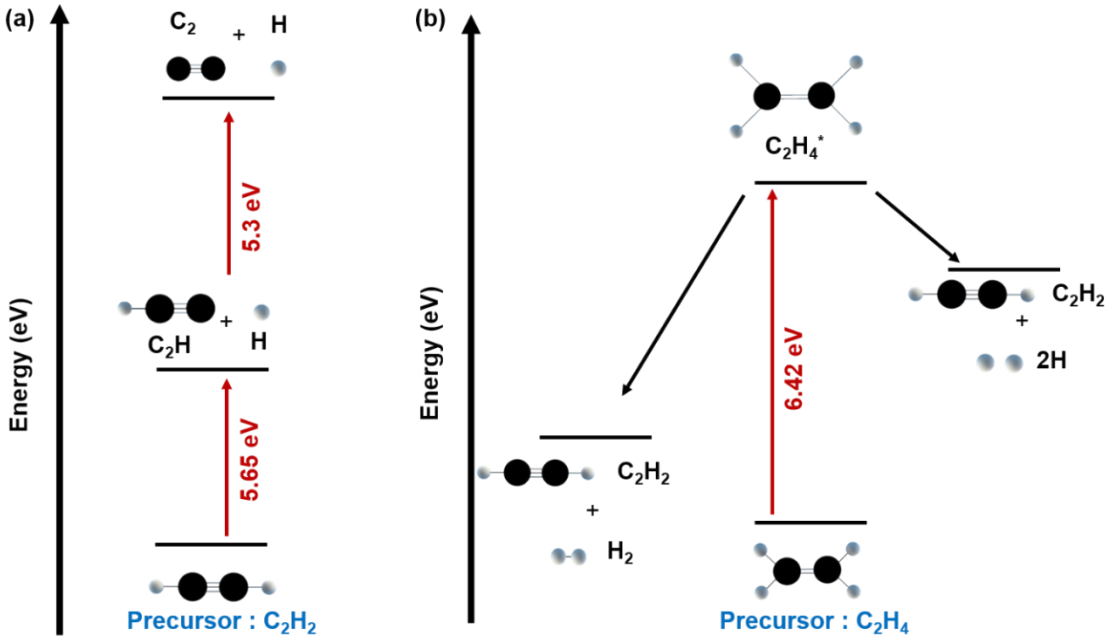

Figure 6.4-13 Possible photolysis mechanisms of hydrocarbon precursors: **(a)** C_2H_2, and **(b)** C_2H_4. [304–306]

Emissions from both C_2 (swan band) and CH (A-X) were detected in their experiments.[308] These studies well support the observation of UV-laser-induced generation of a large quantity of C_2 and CH in our OES study.[305,306,309,310] The 193 nm photodissociation of C_2H_4 has also been well characterized.[311] Ethylene molecules can be electronically excited by absorbing a 193 nm photon. The decay of excited C_2H_4* decomposes the molecule into acetylene and either hydrogen or dihydrogen atoms, as illustrated in **Figure 6.4-13 (b)**.[311] Apparently, the 193 nm photons possess sufficient

energy leading to direct photodissociation of both C_2H_2 and C_2H_4 via either one-photon or two-photon processes. Photolysis rate, the number of times a photodissociation occurs per photon absorbed, is highly wavelength dependent. The shorter the wavelength of the radiation is , the high photolysis rate would be obtained. Although C_2H_4 has a C-H bond energy which is around 0.2 eV below the 248 nm photon energy, the photolysis rate is much lower than that at 193 nm, of which the photon energy is around 1.5 eV higher than the C-H bond energy. Compared with 193 nm laser irradiation, direct photodissociation of either C_2H_2 or C_2H_4 by absorbing the 248 nm photon is difficult and must proceed through a two-photon process, which requires high laser intensity. This explains why, although the output fluence of the 193 nm laser was one order of magnitude lower than that of the 248 nm laser, the 193 nm laser irradiation of the combustion flame led to a more pronounced enhancement in diamond growth and a more significant increase in the generation of key radicals.

6.4.3 Conclusions

The effects on diamond growth through UV laser irradiation of the D-forming combustion flame at different laser wavelengths is studied. The 193 nm laser irradiation is found to be more efficient in enhancing D growth and modifying the flame chemistry than the 248 nm laser irradiation. Similar D growth enhancement is obtained with laser irradiations at both 193 and 248 nm, although the laser fluence of the 193 nm laser is one order of magnitude lower than that of the 248 nm laser. Investigation of the lateral grain size evolution and the D nucleation process suggest that the secondary nucleation is significantly suppressed by the UV irradiation to the flame at 193 nm. A higher increment rate of reactive species under the 193 nm laser irradiation is identified by analyzing the

flame chemistry using OES. The more pronounced effects of the 193 nm irradiation can be attributed to the high photonic energy which leads to the direct photodissociation of hydrocarbon precursors.

7 Summary and Outlook

7.1 Summary

The objectives of the research presented herein were to additively manufacture intricate Cu/D composite materials designed for heat sinks and achieve fast, high-quality deposition of D films to be used as heat spreaders. Several challenges were addressed to fulfill the above objectives, such as the difficulty of 3D laser printing of Cu/D composite materials, the lack of chemical affinity between both Cu and D components, and the low D film quality obtained using combustion flame.

The research first focused on the 3D laser printing of pure Cu. The SLS of dense, smooth, and crack-free Cu structures was demonstrated using a low-power green laser (5 W, λ = 532 nm) by compacting the powder. Cold pressing the Cu powder enhanced the sintering process and limited the formation of printing defects during SLS. Then, SLM of pure Cu was investigated using a NIR laser (400 W, λ = 1070 nm). After optimizing the printing parameters, it was demonstrated that laser power, scan speed, hatch distance, and layer thicknesses of 400 W, 400 mm/s, 0.12 mm, and 0.03 mm, respectively, led to the manufacturing of dense and crack-free Cu parts (95%). The measured properties of a simple printed heat sink were equivalent to a commercial one having the same geometry with an electrical and thermal conductivity of 98% and 100% IACS and 368 and 378 W/m.K, respectively. The advantages of SLM over conventional manufacturing methods

were demonstrated by 3D printing of highly complex Cu heat sinks. The heat dissipation of intricate printed heat sinks allowed the cooling performance to be enhanced by 45% compared to commercial ones.

The research then focused on addressing the lack of affinity between Cu and D, which required the formation of a coating on the D reinforcement. For that, a graded TiO_2-TiC coating was produced via the molten salt process on C fibers. It was shown that the coating temperature influenced the chemical composite of the Ti-based layer. A deposition temperature of 800 ºC led to a fifty-fifty concentration of TiO_2 and TiC, while a temperature of 950 ºC facilitated the formation of a pure carbide coating. Studies of the coating steps showed that the reaction was limited by C diffusion. Thus, at a low coating temperature, the diffusion was slower, enabling the formation of a graded coating. Finally, it was demonstrated that a graded Ti-based coating enhanced the wettability with molten Cu (80º) compared to a pure TiC (115º) coating and the C substrate (145º). Moreover, the same process was extended to D particles and similar results were found. Later, using the molten-salt process, a sophisticated multilayer coating was achieved on CFs, enabling them to withstand harsh environments. The synthesis of advanced coatings resulted from the oscillating reaction of metals in the molten salt driven by a kinetic control.

The additive manufacturing using 5 vol.% of coated D with Ti-based interphase and Cu powder was evaluated via LDED. It was shown that an energy density of about 1200 J/mm^3 allowed the manufacturing of dense Cu/D composites (96%) with a high TC of 330 W/m.K. The coated D concentration increased during the process to 25 vol.%, probably due to the metal evaporation and spatter ejection. The studies of the interface between Cu-TiO_2-TiC-D showed a chemical bonding, demonstrating the advantages of the Ti-based interphase in

3D laser printing of dense and high TC Cu/D composites. Also, the D crystallinity was found to be unchanged after the molten-salt coating and printing processes. Next, the SLM of Cu/D composite materials was investigated with a powder mixture of 5 vol.% of coated D and 95 vol.% of Cu. The introduction of D particles altered the dynamics of the Cu molten pool, leading to significant spatter ejection and metal evaporation compared to the SLM of pure Cu. The density of the composite materials was measured to be about 90%, indicating that the single melting printing strategy was not suitable to print micro-reinforced MMCs. Therefore, recoating and remelting approaches were implemented during the SLM process. It was shown that the remelting allowed elimination of the spatter ejection by smoothing the printing layers. Hence, the remelting allowed 3D laser printing of dense Cu/D composite (96%). Intricate designs made of Cu/D composites and thin, sophisticated features were printed.

Finally, the laser-assisted combustion flame of diamond film was demonstrated using KrF and ArF excimer lasers to improve the D growth rate and quality. It was shown that the KrF excimer laser with a wavelength of $\lambda = 248$ nm altered the flame chemistry and promoted the concentration of D-forming reactive species. The high photon energy provided by the excimer lasers effectively suppressed non-D carbon during growth. The transition zone between the tungsten carbide (WC) substrates and D films was reduced to 5 nm with excimer laser irradiation compared to 700 nm without laser irradiation. The reduction of the transition zone was related to a shorter incubation and nucleation period induced by laser irradiation. In addition, shining the excimer laser into the combustion flame enhanced the D quality by 6% and increased the growth rate by about three times. Next, the effect of the excimer laser wavelength on the flame chemistry and D growth was

studied. It was found that the laser wavelength was critical to the growth of high-quality D. A lower UV wavelength enhanced D growth and quality due to a higher photon energy, thereby promoting the photolysis of reactive species in the combustion flame.

7.2 Future work

In this work, the 3D laser printing of Cu/D composites was investigated, the first report on these materials. Several challenges were addressed to achieve this goal. Nevertheless, this research must move forward to provide more significant results.

The thermal properties and heat dissipation performance of the Cu/D structures printed should be the focus of future work. Next, only a low concentration of D particles was introduced in the Cu matrix (i.e., 5 vol.%). It is thus essential to increase the D concentration gradually and to investigate the effect of D concentration on the printing parameters and thermal characteristics. This study could result in the ability to anticipate the printing parameters and thus easily produce tailored TC and CTE of Cu/D materials. Also, each fabrication method has its own limitations on the reinforcement concentration. It is crucial to know and understand the limitations of 3D laser printing in the manufacturing of Cu/D composite materials.

Another study which is vital to the development of 3D laser printing of Cu/D is to understand the role of the interphase (i.e., coating of D particles) on the wettability, consolidation, and final properties of the composites. For example, in Chapter 3, a multilayer coating was demonstrated, which had a Cr_3C_2 layer on the outside. This carbide is known to possess an enhanced wettability with molten Cu compared to Ti-based

interphase. Thus, it will be interesting to study the effect of different coated D particles on the evolution of the printing parameters, densification, and final properties.

Also, in this work, the D is coated before printing, thus adding a step to the process. The in-situ formation of interphase could allow Cu/D composite to be 3D laser printed more efficiently and cost-effectively. For that, a low melting point, carbide-forming metal can be added to the powder mixture, such as Al. The short melting time provided by the SLM process may limit the reaction between Cu and Al while enabling the formation of an Al carbide interphase on the D particles.

Finally, the TC of the D film grown with and without a laser must be measured to confirm the advantage of laser-assisted CVD for producing a diamond film heat spreader. In summary, the work presented in this dissertation establishes a baseline for future development of 3D laser printing of highly conductive MMCs and heat spreaders for thermal management applications.

REFERENCE

1. World Energy Outlook – Topics. *IEA* https://www.iea.org/topics/world-energy-outlook.
2. Ferain, I., Colinge, C. A. & Colinge, J.-P. Multigate transistors as the future of classical metal–oxide–semiconductor field-effect transistors. *Nature* **479**, 310–316 (2011).
3. Tong, X. C. *Advanced Materials for Thermal Management of Electronic Packaging*. (Springer Science & Business Media, 2011).
4. Sabryz, M. M., Atienzaz, D. & Coskuny, A. K. Thermal analysis and active cooling management for 3D MPSoCs. in *2011 IEEE International Symposium of Circuits and Systems (ISCAS)* 2237–2240 (2011). doi:10.1109/ISCAS.2011.5938046.
5. Moore, G. E. Cramming more components onto integrated circuits, Reprinted from Electronics, volume 38, number 8, April 19, 1965, pp.114 ff. *IEEE Solid-State Circuits Newsletter* (2006) doi:10.1109/n-ssc.2006.4785860.
6. 2015: Moore's "Law" prevails for 50 years | The Storage Engine | Computer History Museum. https://www.computerhistory.org/storageengine/moore-s-law-prevails-for-50-years/.
7. Anandan, S. S. & Ramalingam, V. Thermal management of electronics: A review of literature. *Thermal Science* **12**, 5–26 (2008).
8. Ellsworth, M. J. Chip power density and module cooling technology projections for the current decade. in *The Ninth Intersociety Conference on Thermal and Thermomechanical Phenomena In Electronic Systems (IEEE Cat. No.04CH37543)* vol. 2 707-708 Vol.2 (2004).
9. Huque, M. A. *et al.* Silicon-on-insulator based high-temperature electronics for automotive applications. in *2008 IEEE International Symposium on Industrial Electronics* 2538–2543 (2008). doi:10.1109/ISIE.2008.4677170.
10. Guillemet, T. Diamond-based heat spreaders for power electronic packaging applications. (2013).
11. Azina, C. Diamond-based multimaterials for thermal management applications. *ETD collection for University of Nebraska - Lincoln* 1–236 (2017).
12. Geffroy, P.-M., Mathias, J.-D. & Silvain, J.-F. Heat Sink Material Selection in Electronic Devices by Computational Approach. *Advanced Engineering Materials* **10**, 400–405 (2008).
13. Lee, S. Optimum design and selection of heat sinks. *IEEE Transactions on Components, Packaging, and Manufacturing Technology: Part A* **18**, 812–817 (1995).
14. Silvain, J.-F., Heintz, J.-M., Veillere, A., Constantin, L. & Lu, Y. A review of processing of Cu/C base plate composites for interfacial control and improved properties. *Int. J. Extrem. Manuf.* (2019) doi:10.1088/2631-7990/ab61c5.
15. Asmussen, J. & Reinhard, D. *Diamond Films Handbook*. (CRC Press, 2002).
16. Fan, L. Diamond film deposition using laser-assisted combustion flames. *ETD collection for University of Nebraska - Lincoln* 1–179 (2014).
17. Luedtke, A. Thermal Management Materials for High-Performance Applications. *Advanced Engineering Materials* **6**, 142–144 (2004).
18. Silvain, J.-F., Heintz, J.-M., Veillere, A., Constantin, L. & Lu, Y. F. A review of processing of Cu/C base plate composites for interfacial control and improved properties. *Int. J. Extrem. Manuf.* **2**, 012002 (2020).

19. Silvain, J.-F., Heintz, J.-M., Guillemet, T. & Lu, Y. Role of metal/matrix ,interfaces in the thermal management of metal-carbon composites. *ICALEO* **2012**, 1130–1137 (2012).
20. Asmussen, J. & Reinhard, D. *Diamond Films Handbook*. (CRC Press, 2002).
21. Sung, J. Graphite → diamond transition under high pressure: A kinetics approach. *Journal of Materials Science* **35**, 6041–6054 (2000).
22. Matsumoto, S., Sato, Y., Tsutsumi, M. & Setaka, N. Growth of diamond particles from methane-hydrogen gas. *J Mater Sci* **17**, 3106–3112 (1982).
23. Angus, J. C., Will, H. A. & Stanko, W. S. Growth of Diamond Seed Crystals by Vapor Deposition. *Journal of Applied Physics* **39**, 2915–2922 (1968).
24. Fan, L.-S. *et al.* Ultraviolet laser photolysis of hydrocarbons for nondiamond carbon suppression in chemical vapor deposition of diamond films. *Light Sci Appl* **7**, 17177–17177 (2018).
25. Murakawa, M., Takeuchi, S. & Hirose, Y. Diamond coating of a long substrate by use of a combustion flame. *Surface and Coatings Technology* **39–40**, 235–240 (1989).
26. Xie, Z. Q. *et al.* Resonant excitation of ethylene molecules in the combustion flame CVD of diamond using a wavelength tunable CO2 laser. in *Laser-based Micro- and Nanopackaging and Assembly IV* vol. 7585 758509 (International Society for Optics and Photonics, 2010).
27. Xie, Z. Q. *et al.* Control of crystallographic orientation in diamond synthesis through laser resonant vibrational excitation of precursor molecules. *Sci Rep* **4**, 1–7 (2014).
28. Fan, L. S. *et al.* Influence of Laser Vibrational Excitations of Ethylene Molecules in Laser-Assisted Combustion Diamond Synthesis. *MRS Online Proceedings Library Archive* **1734**, (2015).
29. Fan, L. S. *et al.* Mass spectrometric investigation of the roles of several chemical intermediates in diamond synthesis. *RSC Adv.* **5**, 4822–4830 (2014).
30. Azina, C. Diamond-based multimaterials for thermal management applications. *ETD collection for University of Nebraska - Lincoln* 1–236 (2017).
31. Takabatake, N., Kobayashi, T., Sekine, D. & Izumi, T. Thermal characterization of CVD diamond film by photoacoustic method. *Applied Surface Science* **159–160**, 594–598 (2000).
32. Ho, H. P., Lo, K. C., Tjong, S. C. & Lee, S. T. Measurement of thermal conductivity in diamond films using a simple scanning thermocouple technique. *Diamond and Related Materials* **9**, 1312–1319 (2000).
33. Wolter, S. D. *et al.* Thermal conductivity of epitaxially textured diamond films. *Diamond and Related Materials* **12**, 61–64 (2003).
34. Anthony, T. R., Fleischer, J. L., Olson, J. R. & Cahill, D. G. The thermal conductivity of isotopically enriched polycrystalline diamond films. *Journal of Applied Physics* **69**, 8122–8125 (1991).
35. Vasiliev, L. L. Heat pipes in modern heat exchangers. *Applied Thermal Engineering* **25**, 1–19 (2005).
36. Neugebauer, R., Müller, B., Gebauer, M. & Töppel, T. Additive manufacturing boosts efficiency of heat transfer components. *Assembly Automation* (2011) doi:10.1108/01445151111172925.

37. Qu, X., Zhang, L., Wu, M. & Ren, S. Review of metal matrix composites with high thermal conductivity for thermal management applications. *Progress in Natural Science: Materials International* **21**, 189–197 (2011).
38. López, G. A. & Mittemeijer, E. J. The solubility of C in solid Cu. *Scripta Materialia* **51**, 1–5 (2004).
39. Silvain, J.-F., Veillère, A. & Lu, Y. Copper-Carbon and Aluminum-Carbon Composites Fabricated by Powder Metallurgy Processes. *J. Phys.: Conf. Ser.* **525**, 012015 (2014).
40. Kong, B., Ru, J., Zhang, H. & Fan, T. Enhanced wetting and properties of carbon/carbon-Cu composites with Cr 3 C 2 coatings by Cr-solution immersion method. *Journal of Materials Science & Technology* **34**, 458–465 (2018).
41. Schubert, Th., Trindade, B., Weißgärber, T. & Kieback, B. Interfacial design of Cu-based composites prepared by powder metallurgy for heat sink applications. *Materials Science and Engineering: A* **475**, 39–44 (2008).
42. Tao, J., Zhu, X., Tian, W., Yang, P. & Yang, H. Properties and microstructure of Cu/diamond composites prepared by spark plasma sintering method. *Transactions of Nonferrous Metals Society of China* **24**, 3210–3214 (2014).
43. Mortimer, D. A. & Nicholas, M. The wetting of carbon by copper and copper alloys. *J Mater Sci* **5**, 149–155 (1970).
44. Veillère, A. *et al.* Relationship between interphase chemistry and mechanical properties at the scale of micron in Cu–Cr/CF composite. *Acta Materialia* **59**, 1445–1455 (2011).
45. Chung, C.-Y., Chu, C.-H., Lee, M.-T., Lin, C.-M. & Lin, S.-J. Effect of Titanium Addition on the Thermal Properties of Diamond/Cu-Ti Composites Fabricated by Pressureless Liquid-Phase Sintering Technique. *The Scientific World Journal* vol. 2014 e713537 https://www.hindawi.com/journals/tswj/2014/713537/ (2014).
46. Liu, Q. *et al.* Fabrication and thermal conductivity of copper matrix composites reinforced with Mo2C or TiC coated graphite fibers. *Materials Research Bulletin* **48**, 4811–4817 (2013).
47. Li, J., Zhang, H., Zhang, Y., Che, Z. & Wang, X. Microstructure and thermal conductivity of Cu/diamond composites with Ti-coated diamond particles produced by gas pressure infiltration. *Journal of Alloys and Compounds* **647**, 941–946 (2015).
48. Kang, Q. *et al.* Preparation of copper–diamond composites with chromium carbide coatings on diamond particles for heat sink applications. *Applied Thermal Engineering* **60**, 423–429 (2013).
49. Information, R. B. *New Scientist*. (Reed Business Information, 1974).
50. Sames, W. J., List, F. A., Pannala, S., Dehoff, R. R. & Babu, S. S. The metallurgy and processing science of metal additive manufacturing. *International Materials Reviews* **61**, 315–360 (2016).
51. Kruth, J., Mercelis, P., Van Vaerenbergh, J., Froyen, L. & Rombouts, M. Binding mechanisms in selective laser sintering and selective laser melting. *Rapid Prototyping Journal* **11**, 26–36 (2005).
52. Tolochko, N. K. *et al.* Balling processes during selective laser treatment of powders. *Rapid Prototyping Journal* **10**, 78–87 (2004).
53. Kingery, W. D. Densification during Sintering in the Presence of a Liquid Phase. I. Theory. *Journal of Applied Physics* **30**, 301–306 (1959).

54. Li, R., Shi, Y., Liu, J., Xie, Z. & Wang, Z. Selective laser melting W–10 wt.% Cu composite powders. *Int J Adv Manuf Technol* **48**, 597–605 (2010).
55. Anestiev, L. A. & Froyen, L. Model of the primary rearrangement processes at liquid phase sintering and selective laser sintering due to biparticle interactions. *Journal of Applied Physics* **86**, 4008–4017 (1999).
56. Yap, C. Y. *et al.* Review of selective laser melting: Materials and applications. *Applied Physics Reviews* **2**, 041101 (2015).
57. Wang, D. *et al.* Mechanisms and characteristics of spatter generation in SLM processing and its effect on the properties. *Materials & Design* **117**, 121–130 (2017).
58. Ly, S., Rubenchik, A. M., Khairallah, S. A., Guss, G. & Matthews, M. J. Metal vapor micro-jet controls material redistribution in laser powder bed fusion additive manufacturing. *Sci Rep* **7**, 1–12 (2017).
59. Matthews, M. J. *et al.* Denudation of metal powder layers in laser powder bed fusion processes. *Acta Materialia* **114**, 33–42 (2016).
60. Qiu, C. *et al.* On the role of melt flow into the surface structure and porosity development during selective laser melting. *Acta Materialia* **96**, 72–79 (2015).
61. Brown, M. S. & Arnold, C. B. Fundamentals of Laser-Material Interaction and Application to Multiscale Surface Modification. in *Laser Precision Microfabrication* (eds. Sugioka, K., Meunier, M. & Piqué, A.) 91–120 (Springer, 2010). doi:10.1007/978-3-642-10523-4_4.
62. Ali, H., Ghadbeigi, H. & Mumtaz, K. Effect of scanning strategies on residual stress and mechanical properties of Selective Laser Melted Ti6Al4V. *Materials Science and Engineering: A* **712**, 175–187 (2018).
63. King, W. E. *et al.* Observation of keyhole-mode laser melting in laser powder-bed fusion additive manufacturing. *Journal of Materials Processing Technology* **214**, 2915–2925 (2014).
64. Carter, L. N., Attallah, M. M. & Reed, R. C. Laser Powder Bed Fabrication of Nickel-Base Superalloys: Influence of Parameters; Characterisation, Quantification and Mitigation of Cracking. *Superalloys* (2012) doi:10.1002/9781118516430.ch64.
65. Kruth, J. P. *et al.* Selective laser melting of iron-based powder. *Journal of Materials Processing Technology* **149**, 616–622 (2004).
66. Herzog, D., Seyda, V., Wycisk, E. & Emmelmann, C. Additive manufacturing of metals. *Acta Materialia* **117**, 371–392 (2016).
67. Thompson, S. M., Bian, L., Shamsaei, N. & Yadollahi, A. An overview of Direct Laser Deposition for additive manufacturing; Part I: Transport phenomena, modeling and diagnostics. *Additive Manufacturing* **8**, 36–62 (2015).
68. Agarwala, M., Bourell, D., Beaman, J., Marcus, H. & Barlow, J. Direct selective laser sintering of metals. *Rapid Prototyping Journal* **1**, 26–36 (1995).
69. Gu, D. & Shen, Y. Effects of processing parameters on consolidation and microstructure of W–Cu components by DMLS. *Journal of Alloys and Compounds* **473**, 107–115 (2009).
70. Das, S., Beama, J. J., Wohlert, M. & Bourell, D. L. Direct laser freeform fabrication of high performance metal components. *Rapid Prototyping Journal* **4**, 112–117 (1998).
71. Chichkov, B. N., Momma, C., Nolte, S., von Alvensleben, F. & Tünnermann, A. Femtosecond, picosecond and nanosecond laser ablation of solids. *Appl. Phys. A* **63**, 109–115 (1996).

72. Tolochko, N. K. *et al.* Absorptance of powder materials suitable for laser sintering. *Rapid Prototyping Journal* **6**, 155–161 (2000).
73. Hojjatzadeh, S. M. H. *et al.* Pore elimination mechanisms during 3D printing of metals. *Nat Commun* **10**, 1–8 (2019).
74. Leary, M. *et al.* Selective laser melting (SLM) of AlSi12Mg lattice structures. *Materials & Design* **98**, 344–357 (2016).
75. Li, S. J. *et al.* Influence of cell shape on mechanical properties of Ti–6Al–4V meshes fabricated by electron beam melting method. *Acta Biomaterialia* **10**, 4537–4547 (2014).
76. Wang, D., Yang, Y., Liu, R., Xiao, D. & Sun, J. Study on the designing rules and processability of porous structure based on selective laser melting (SLM). *Journal of Materials Processing Technology* **213**, 1734–1742 (2013).
77. Wong, K. K. & Leong, K. C. Saturated pool boiling enhancement using porous lattice structures produced by Selective Laser Melting. *International Journal of Heat and Mass Transfer* **121**, 46–63 (2018).
78. Jafari, D. & Wits, W. W. The utilization of selective laser melting technology on heat transfer devices for thermal energy conversion applications: A review. *Renewable and Sustainable Energy Reviews* **91**, 420–442 (2018).
79. Wong, M., Owen, I., Sutcliffe, C. J. & Puri, A. Convective heat transfer and pressure losses across novel heat sinks fabricated by Selective Laser Melting. *International Journal of Heat and Mass Transfer* **52**, 281–288 (2009).
80. Wong, M., Owen, I. & Sutcliffe, C. J. Pressure Loss and Heat Transfer Through Heat Sinks Produced by Selective Laser Melting. *Heat Transfer Engineering* **30**, 1068–1076 (2009).
81. Ho, J. Y., Wong, K. K., Leong, K. C. & Wong, T. N. Convective heat transfer performance of airfoil heat sinks fabricated by selective laser melting. *International Journal of Thermal Sciences* **114**, 213–228 (2017).
82. Tran, T. Q. *et al.* 3D Printing of Highly Pure Copper. *Metals* **9**, 756 (2019).
83. Colopi, M., Caprio, L., Demir, A. G. & Previtali, B. Selective laser melting of pure Cu with a 1 kW single mode fiber laser. *Procedia CIRP* **74**, 59–63 (2018).
84. Ikeshoji, T.-T., Nakamura, K., Yonehara, M., Imai, K. & Kyogoku, H. Selective Laser Melting of Pure Copper. *JOM* **70**, 396–400 (2018).
85. Jadhav, S. D. *et al.* Influence of selective laser melting process parameters on texture evolution in pure copper. *Journal of Materials Processing Technology* **270**, 47–58 (2019).
86. Jadhav, S. D. *et al.* Influence of Carbon Nanoparticle Addition (and Impurities) on Selective Laser Melting of Pure Copper. *Materials* **12**, 2469 (2019).
87. Hess, A., Schuster, R., Heider, A., Weber, R. & Graf, T. Continuous Wave Laser Welding of Copper with Combined Beams at Wavelengths of 1030nm and of 515nm. *Physics Procedia* **12**, 88–94 (2011).
88. Silbernagel, C. *et al.* Electrical resistivity of pure copper processed by medium-powered laser powder bed fusion additive manufacturing for use in electromagnetic applications. *Additive Manufacturing* **29**, 100831 (2019).
89. Singer, F., Deisenroth, D. C., Hymas, D. M. & Ohadi, M. M. Additively manufactured copper components and composite structures for thermal management applications. in *2017 16th IEEE Intersociety Conference on Thermal and Thermomechanical*

Phenomena in Electronic Systems (ITherm) 174–183 (2017). doi:10.1109/ITHERM.2017.7992469.
90. Körner, C. Additive manufacturing of metallic components by selective electron beam melting — a review. *International Materials Reviews* **61**, 361–377 (2016).
91. Lee, J. & Mudawar, I. Two-phase flow in high-heat-flux micro-channel heat sink for refrigeration cooling applications: Part I—pressure drop characteristics. *International Journal of Heat and Mass Transfer* **48**, 928–940 (2005).
92. Zhang, H., Chen, L., Liu, Y. & Li, Y. Experimental study on heat transfer performance of lotus-type porous copper heat sink. *International Journal of Heat and Mass Transfer* **56**, 172–180 (2013).
93. Frazier, W. E. Metal Additive Manufacturing: A Review. *J. of Materi Eng and Perform* **23**, 1917–1928 (2014).
94. Ramirez, D. A. *et al.* Open-cellular copper structures fabricated by additive manufacturing using electron beam melting. *Materials Science and Engineering: A* **528**, 5379–5386 (2011).
95. Exner, H. E. & Arzt, E. Sintering Processes. in *Sintering Key Papers* 157–184 (Springer, Dordrecht, 1990). doi:10.1007/978-94-009-0741-6_10.
96. Alexander, B. H. & Balluffi, R. W. The mechanism of sintering of copper. *Acta Metallurgica* **5**, 666–677 (1957).
97. Johnson, D. L. Solid-State Sintering. in *Ultrafine-Grain Ceramics* 173–183 (Springer, Boston, MA, 1970). doi:10.1007/978-1-4684-2643-4_9.
98. Agarwala, M., Bourell, D., Beaman, J., Marcus, H. & Barlow, J. Direct selective laser sintering of metals. *Rapid Prototyping Journal* **1**, 26–36 (1995).
99. Tang, Y. *et al.* Direct laser sintering of a copper-based alloy for creating three-dimensional metal parts. *Journal of Materials Processing Technology* **140**, 368–372 (2003).
100. Kruth, J.-P., Mercelis, P., Vaerenbergh, J. V., Froyen, L. & Rombouts, M. Binding mechanisms in selective laser sintering and selective laser melting. *Rapid Prototyping Journal* **11**, 26–36 (2005).
101. Niu, H. J. & Chang, I. T. H. Liquid phase sintering of M3/2 high speed steel by selective laser sintering. *Scripta Materialia* **39**, 67–72 (1998).
102. Lü, L., Fuh, J. & Wong, Y.-S. *Laser-Induced Materials and Processes for Rapid Prototyping*. (Springer US, 2001).
103. Zhu, H. H., Lu, L. & Fuh, J. Y. H. Influence of binder's liquid volume fraction on direct laser sintering of metallic powder. *Materials Science and Engineering: A* **371**, 170–177 (2004).
104. Popovich, A. *et al.* Microstructure and mechanical properties of additive manufactured copper alloy. *Materials Letters* **179**, 38–41 (2016).
105. Gu, D. & Shen, Y. WC–Co particulate reinforcing Cu matrix composites produced by direct laser sintering. *Materials Letters* **60**, 3664–3668 (2006).
106. Ren, L. *et al.* A novel coping metal material CoCrCu alloy fabricated by selective laser melting with antimicrobial and antibiofilm properties. *Mater Sci Eng C Mater Biol Appl* **67**, 461–467 (2016).
107. Zhu, H. H., Lu, L. & Fuh, J. Y. H. Influence of binder's liquid volume fraction on direct laser sintering of metallic powder. *Materials Science and Engineering: A* **371**, 170–177 (2004).

108. Silbernagel, C. *et al.* Electrical resistivity of pure copper processed by medium-powered laser powder bed fusion additive manufacturing for use in electromagnetic applications. *Additive Manufacturing* **29**, 100831 (2019).
109. Constantin, L. *et al.* Laser sintering of cold-pressed Cu powder without binder use. *Materialia* **3**, 178–181 (2018).
110. Zhang, S. *et al.* Microstructure and properties of high strength and high conductivity Cu-Cr alloy components fabricated by high power selective laser melting. *Materials Letters* **237**, 306–309 (2019).
111. Zhang, S., Zhu, H., Hu, Z., Zeng, X. & Zhong, F. Selective Laser Melting of Cu10Zn alloy powder using high laser power. *Powder Technology* **342**, 613–620 (2019).
112. Sabelle, M., Walczak, M. & Ramos-Grez, J. Scanning pattern angle effect on the resulting properties of selective laser sintered monolayers of Cu-Sn-Ni powder. *Optics and Lasers in Engineering* **100**, 1–8 (2018).
113. Zhou, X., Liu, X., Zhang, D., Shen, Z. & Liu, W. Balling phenomena in selective laser melted tungsten. *Journal of Materials Processing Technology* **222**, 33–42 (2015).
114. Shen, Y. F., Gu, D. D. & Pan, Y. F. Balling Process in Selective Laser Sintering 316 Stainless Steel Powder. *Key Engineering Materials* **315–316**, 357–360 (2006).
115. Jost, W. *Diffusion in solids, liquids, gases: W. Jost.* (Academic Press, 1960).
116. Fick, D. A. V. On liquid diffusion. *The London, Edinburgh, and Dublin Philosophical Magazine and Journal of Science* **10**, 30–39 (1855).
117. Kühl, C. H. & Straße, N. Free Sintering or Hot Pressing. *Diamond tool consulting* 1–8 (2013).
118. Eksi, A. & Kulekci, M. K. Hardness and Densification Behaviour of Copper and Bronze Powders Compacted with Uniaxial Die and Cold Isostatic Pressing Processes. *Metalurgija* **43**, 129–134 (2004).
119. Zhang, H., Zhu, H., Qi, T., Hu, Z. & Zeng, X. Selective laser melting of high strength Al–Cu–Mg alloys: Processing, microstructure and mechanical properties. *Materials Science and Engineering: A* **656**, 47–54 (2016).
120. German, R. M. Chapter Seven - Thermodynamic and Kinetic Treatments. in *Sintering: from Empirical Observations to Scientific Principles* 183–226 (Butterworth-Heinemann, 2014). doi:10.1016/B978-0-12-401682-8.00007-0.
121. Olakanmi, E. O., Cochrane, R. F. & Dalgarno, K. W. A review on selective laser sintering/melting (SLS/SLM) of aluminium alloy powders: Processing, microstructure, and properties. *Progress in Materials Science* **74**, 401–477 (2015).
122. Kruth, J.-P., Levy, G., Klocke, F. & Childs, T. H. C. Consolidation phenomena in laser and powder-bed based layered manufacturing. *CIRP Annals* **56**, 730–759 (2007).
123. Zaeh, M. F. & Branner, G. Investigations on residual stresses and deformations in selective laser melting. *Prod. Eng. Res. Devel.* **4**, 35–45 (2010).
124. Mingchuan, Y. *et al.* Synthesis of W--20%Cu Nanocomposite Powders. *Acta Metall* **40**, 639 (2004).
125. Raffi, M. *et al.* Investigations into the antibacterial behavior of copper nanoparticles against Escherichia coli. *Ann Microbiol* **60**, 75–80 (2010).
126. Maamoun, A. H., Xue, Y. F., Elbestawi, M. A. & Veldhuis, S. C. Effect of Selective Laser Melting Process Parameters on the Quality of Al Alloy Parts: Powder

Characterization, Density, Surface Roughness, and Dimensional Accuracy. *Materials (Basel)* **11**, (2018).
127. Gusarov, A. V., Yadroitsev, I., Bertrand, P. & Smurov, I. Model of Radiation and Heat Transfer in Laser-Powder Interaction Zone at Selective Laser Melting. *J. Heat Transfer* **131**, (2009).
128. Dai, D. & Gu, D. Tailoring surface quality through mass and momentum transfer modeling using a volume of fluid method in selective laser melting of TiC/AlSi10Mg powder. *International Journal of Machine Tools and Manufacture* **88**, 95–107 (2015).
129. Yin, J. *et al.* High-power laser-matter interaction during laser powder bed fusion. *Additive Manufacturing* **29**, 100778 (2019).
130. Xiao, B. & Zhang, Y. Marangoni and Buoyancy Effects on Direct Metal Laser Sintering with a Moving Laser Beam. *Numerical Heat Transfer, Part A: Applications* **51**, 715–733 (2007).
131. Wang, L., Wang, S. & Wu, J. Experimental investigation on densification behavior and surface roughness of AlSi10Mg powders produced by selective laser melting. *Optics & Laser Technology* **96**, 88–96 (2017).
132. Ytterbium Multi-mode CW Lasers, Up to 2.5 kW | IPG Photonics. https://www.ipgphotonics.com/en/products/lasers/mid-power-cw-fiber-lasers/1-micron/ylm-mm-and-ylr-mm#[ylm-mm-200-400-w].
133. Ytterbium Multi-mode CW Lasers, Up to 2.5 kW | IPG Photonics. https://www.ipgphotonics.com/en/products/lasers/mid-power-cw-fiber-lasers/1-micron/ylm-mm-and-ylr-mm#[ylr-mm-wc-1000-2000-w].
134. Jadhav, S. D., Vleugels, J., Kruth, J.-P., Humbeeck, J. V. & Vanmeensel, K. Mechanical and electrical properties of selective laser-melted parts produced from surface-oxidized copper powder. *Material Design & Processing Communications* **0**, e94.
135. Brown, M. S. & Arnold, C. B. Fundamentals of Laser-Material Interaction and Application to Multiscale Surface Modification. in *Laser Precision Microfabrication* (eds. Sugioka, K., Meunier, M. & Piqué, A.) 91–120 (Springer Berlin Heidelberg, 2010). doi:10.1007/978-3-642-10523-4_4.
136. Bean, G. E., Witkin, D. B., McLouth, T. D., Patel, D. N. & Zaldivar, R. J. Effect of laser focus shift on surface quality and density of Inconel 718 parts produced via selective laser melting. *Additive Manufacturing* **22**, 207–215 (2018).
137. Rodrigues, G. C., Vorkov, V. & Duflou, J. R. Optimal laser beam configurations for laser cutting of metal sheets. *Procedia CIRP* **74**, 714–718 (2018).
138. Siegman, A. E. Defining, measuring, and optimizing laser beam quality. in *Laser Resonators and Coherent Optics: Modeling, Technology, and Applications* vol. 1868 2–12 (International Society for Optics and Photonics, 1993).
139. Luo, X., Chen, P. & Wang, Y. Power content M2-values smaller than one. *Appl. Phys. B* **98**, 181 (2009).
140. Lu, Y., Santino, L. M., Acharya, S., Anandarajah, H. & D'Arcy, J. M. Studying Electrical Conductivity Using a 3D Printed Four-Point Probe Station. *J. Chem. Educ.* **94**, 950–955 (2017).
141. *Theoretical Solid State Physics*. (Courier Corporation, 1985).

142. Vincent, C., Silvain, J. F., Heintz, J. M. & Chandra, N. Effect of porosity on the thermal conductivity of copper processed by powder metallurgy. *Journal of Physics and Chemistry of Solids* **73**, 499–504 (2012).
143. Ramirez, D. A. *et al.* Novel precipitate–microstructural architecture developed in the fabrication of solid copper components by additive manufacturing using electron beam melting. *Acta Materialia* **59**, 4088–4099 (2011).
144. Botcharova, E., Freudenberger, J. & Schultz, L. Mechanical and electrical properties of mechanically alloyed nanocrystalline Cu–Nb alloys. *Acta Materialia* **54**, 3333–3341 (2006).
145. Gendelman, O. V., Shapiro, M., Estrin, Y., Hellmig, R. J. & Lekhtmakher, S. Grain size distribution and heat conductivity of copper processed by equal channel angular pressing. *Materials Science and Engineering: A* **434**, 88–94 (2006).
146. Matula, R. A. Electrical resistivity of copper, gold, palladium, and silver. *Journal of Physical and Chemical Reference Data* **8**, 1147–1298 (1979).
147. Yu, J., Wang, G. & Rong, Y. Experimental Study on the Surface Integrity and Chip Formation in the Micro Cutting Process. *Procedia Manufacturing* **1**, 655–662 (2015).
148. Hasan, M., Zhao, J. & Jiang, Z. Micromanufacturing of composite materials: a review. *Int. J. Extrem. Manuf.* **1**, 012004 (2019).
149. Sun, S. J. & Zhang, M. D. Interface characteristics and mechanical properties of carbon fibre reinforced copper composites. *Journal of Materials Science* **26**, 5762–5766 (1991).
150. Koráb, J., Štefánik, P., Kavecký, Š., Šebo, P. & Korb, G. Thermal conductivity of unidirectional copper matrix carbon fibre composites. *Composites Part A: Applied Science and Manufacturing* **33**, 577–581 (2002).
151. Buchgraber, W., Korb, G., Schubert, T. & Kempf, B. Carbon Fibre Reinforced Copper Matrix Composites: Production Routes and Functional Properties. in *Microstructural Investigation and Analysis* 150–155 (Wiley-VCH Verlag GmbH & Co. KGaA, 2006). doi:10.1002/3527606165.ch22.
152. Silvain, J.-F., Veillère, A. & Lu, Y. Copper-Carbon and Aluminum-Carbon Composites Fabricated by Powder Metallurgy Processes. *Journal of Physics: Conference Series* **525**, 012015 (2014).
153. Hidalgo-Manrique, P. *et al.* Copper/graphene composites: a review. *J Mater Sci* **54**, 12236–12289 (2019).
154. Spierings, A. B., Leinenbach, C., Kenel, C. & Wegener, K. Processing of metal-diamond-composites using selective laser melting. *Rapid Prototyping Journal* (2015) doi:10.1108/RPJ-11-2014-0156.
155. Yoshida, K. & Morigami, H. Thermal properties of diamond/copper composite material. *Microelectronics Reliability* **44**, 303–308 (2004).
156. Xia, L., Jia, B., Zeng, J. & Xu, J. Wear and mechanical properties of carbon fiber reinforced copper alloy composites. *Materials Characterization* **60**, 363–369 (2009).
157. Kang, Q. *et al.* Preparation of copper–diamond composites with chromium carbide coatings on diamond particles for heat sink applications. *Applied Thermal Engineering* **60**, 423–429 (2013).
158. Rambo, C. R., Travitzky, N. & Greil, P. Conductive TiC/Ti–Cu/C composites fabricated by Ti–Cu alloy reactive infiltration into 3D-printed carbon performs. *Journal of Composite Materials* **49**, 1971–1976 (2015).

159. QU, X., ZHANG, L., WU, M. & REN, S. Review of metal matrix composites with high thermal conductivity for thermal management applications. *Progress in Natural Science: Materials International* **21**, 189–197 (2011).
160. Chu, K., Jia, C., Guo, H. & Li, W. Microstructure and thermal conductivity of Cu–B/diamond composites. *Journal of Composite Materials* **47**, 2945–2953 (2013).
161. Schubert, Th., Trindade, B., Weißgärber, T. & Kieback, B. Interfacial design of Cu-based composites prepared by powder metallurgy for heat sink applications. *Materials Science and Engineering: A* **475**, 39–44 (2008).
162. Chu, K., Jia, C., Guo, H. & Li, W. On the thermal conductivity of Cu–Zr/diamond composites. *Materials & Design* **45**, 36–42 (2013).
163. Zhang, Y., Zhang, H. L., Wu, J. H. & Wang, X. T. Enhanced thermal conductivity in copper matrix composites reinforced with titanium-coated diamond particles. *Scripta Materialia* **65**, 1097–1100 (2011).
164. Dong, Z. J. *et al.* Fabrication and oxidation resistance of titanium carbide-coated carbon fibres by reacting titanium hydride with carbon fibres in molten salts. *Thin Solid Films* **517**, 3248–3252 (2009).
165. Pierson, H. O. *Handbook of refractory carbides and nitrides : properties, characteristics, processing, and applications*. (Noyes Publications, 1996).
166. Mortimer, D. A. & Nicholas, M. The wetting of carbon and carbides by copper alloys. *Journal of Materials Science* **8**, 640–648 (1973).
167. Lee, Y.-J. Formation of silicon carbide on carbon fibers by carbothermal reduction of silica. *Diamond and Related Materials* **13**, 383–388 (2004).
168. Abdel Gawad, O., Abou Tabl, M. H., Abdel Hamid, Z. & Mostafa, S. F. Electroplating of chromium and Cr-carbide coating for carbon fiber. *Surface and Coatings Technology* **201**, 1357–1362 (2006).
169. Hackl, G., Gerhard, H. & Popovska, N. Coating of carbon short fibers with thin ceramic layers by chemical vapor deposition. *Thin Solid Films* **513**, 217–222 (2006).
170. Popovska, N. *et al.* Chemical vapor deposition of titanium nitride on carbon fibres as a protective layer in metal matrix composites. *Materials & Design* **18**, 239–242 (1997).
171. Landry, C. C. & Barron, A. R. MOCVD of alumina-silica oxidation resistant coatings on carbon fibers. *Carbon* **33**, 381–387 (1995).
172. Brown, M., Hayes, P. & Prangnell, P. Characterisation of thin silica films deposited on carbon fibre by an atmospheric pressure non-equilibrium plasma (APNEP). *Composites Part A: Applied Science and Manufacturing* **33**, 1403–1408 (2002).
173. Ledain, O. *et al.* Reactive Chemical Vapour Deposition of Titanium Carbide from H2-TiCl4 Gas Mixture on Pyrocarbon: A Comprehensive Study. *Physics Procedia* **46**, 79–87 (2013).
174. Zhang, Y., Li, H., Li, K., Fei, J. & Zeng, X. C/SiC/Si-Mo-Cr multilayer coating for carbon/carbon composites for oxidation protection. *New Carbon Materials* **27**, 105–109 (2012).
175. Baklanova, N. I. *et al.* Protective ceramic multilayer coatings for carbon fibers. *Surface and Coatings Technology* **201**, 2313–2319 (2006).
176. Piquero, T., Vincent, H., Vincent, C. & Bouix, J. Influence of carbide coatings on the oxidation behavior of carbon fibers. *Carbon* **33**, 455–467 (1995).

177. Liu, Q. *et al.* Laser ablation behaviors of SiC–ZrC coated carbon/carbon composites. *Surface and Coatings Technology* **205**, 4299–4303 (2011).
178. Choy, K. L. Chemical vapour deposition of coatings. *Progress in Materials Science* **48**, 57–170 (2003).
179. Stowell, W. R. Ion-plated titanium carbide coatings. *Thin Solid Films* **22**, 111–120 (1974).
180. Ledermann, N., Baborowski, J., Muralt, P., Xantopoulos, N. & Tellenbach, J.-M. Sputtered silicon carbide thin films as protective coating for MEMS applications. *Surface and Coatings Technology* **125**, 246–250 (2000).
181. Dash, A., Vaßen, R., Guillon, O. & Gonzalez-Julian, J. Molten salt shielded synthesis of oxidation prone materials in air. *Nat. Mater.* **18**, 465–470 (2019).
182. Li, X. *et al.* Low-Temperature Preparation of Single Crystal Titanium Carbide Nanofibers in Molten Salts. *Crystal Growth & Design* **11**, 3122–3129 (2011).
183. Kimura, T. Molten Salt Synthesis of Ceramic Powders. in *Advances in Ceramics - Synthesis and Characterization, Processing and Specific Applications* (InTech, 2011). doi:10.5772/20472.
184. Liu, X., Wang, Z. & Zhang, S. Molten Salt Synthesis and Characterization of Titanium Carbide-Coated Graphite Flakes for Refractory Castable Applications. *International Journal of Applied Ceramic Technology* **8**, 911–919 (2011).
185. Le Bail, A., Duroy, H. & Fourquet, J. L. Ab-initio structure determination of LiSbWO6 by X-ray powder diffraction. *Materials Research Bulletin* **23**, 447–452 (1988).
186. Liu, Q. *et al.* Effect of titanium carbide coating on the microstructure and thermal conductivity of short graphite fiber/copper composites. *J Mater Sci* **48**, 5810–5817 (2013).
187. Dong, Z. J. *et al.* Tensile strength, oxidation resistance and wettability of carbon fibers coated with a TiC layer using a molten salt method. *Materials & Design* **50**, 156–164 (2013).
188. Morton, E. & Lewis, R. K. CONTRACT NO. NAW-663 FINAL REPORT PROPERTIES OF NON-STOICHIOMETRIC METALLIC CARBIDES. *Mendeley* https://www.mendeley.com/catalogue/contract-naw663-final-report-properties-nonstoichiometric-metallic-carbides/.
189. Frage, N., Levin, L., Manor, E., Shneck, R. & Zabicky, J. Iron-titanium-carbon system. II. Microstructure of titanium carbide (TiCx) of various stoichiometries infiltrated with iron-carbon alloy. *Scripta Materialia* **35**, 799–803 (1996).
190. Roger, J., Gardiola, B., Andrieux, J., Viala, J.-C. & Dezellus, O. Synthesis of Ti matrix composites reinforced with TiC particles: thermodynamic equilibrium and change in microstructure. *Journal of Materials Science* **52**, 4129–4141 (2017).
191. Fryt, E. Defect mobility in TiC1 − x at high temperatures. *Solid State Ionics* **101–103**, 437–443 (1997).
192. Dahan, I., Admon, U., Frage, N., Sariel, J. & Dariel, M. P. Diffusion in Ti/TiC multilayer coatings. *Thin Solid Films* **377–378**, 687–693 (2000).
193. Sarian, S. Diffusion of ^{44} Ti in TiC $_x$. *Journal of Applied Physics* **40**, 3515–3520 (1969).

194. Matsumoto, T., Fujii, H., Ueda, T., Kamai, M. & Nogi, K. Measurement of surface tension of molten copper using the free-fall oscillating drop method. *Meas. Sci. Technol.* **16**, 432–437 (2005).
195. Mortimer, D. A. & Nicholas, M. The wetting of carbon and carbides by copper alloys. *J Mater Sci* **8**, 640–648 (1973).
196. Eustathopoulos, N. & Drevet, B. Interfacial bonding, wettability and reactivity in metal/oxide systems. *Journal de Physique III* **4**, 1865–1881 (1994).
197. Sekimoto, H., Nose, Y., Uda, T. & Sugimura, H. Quantitative Analysis of Titanium Ions in the Equilibrium with Metallic Titanium in NaCl-KCl Equimolar Molten Salt. *MATERIALS TRANSACTIONS* **51**, 2121–2124 (2010).
198. Kreye, W. C. & Kellogg, H. H. The Equilibrium between Titanium Metal, TiCl2, and TiCl3 in NaCl - KCl Melts. *J. Electrochem. Soc.* **104**, 504–508 (1957).
199. Campbell, J. H. Modelling Platinum-Inclusion Dissolution in Phosphate Laser Glasses. *Glatech. Ber* **68**, 96–101 (1995).
200. Dynamic Viscosity of Potassium chloride from Dortmund Data Bank. http://www.ddbst.com/en/EED/PCP/VIS_C4577.php.
201. Sen, S. A study on kinetics of CrxC-coated high-chromium steel by thermo-reactive diffusion technique. *Vacuum* **79**, 63–70 (2005).
202. Roger, J., Audubert, F. & Le Petitcorps, Y. Thermal reaction of SiC films with Mo, Re and Mo–Re alloy. *Journal of Alloys and Compounds* **475**, 635–642 (2009).
203. Koyama, K., Hashimoto, Y. & Omori, S. Diffusion of Carbon in TiC. *Trans. JIM* **16**, 211–218 (1975).
204. Arai, T. Carbide coating process by use of molten borax bath in Japan. *Journal of Heat Treating* **1**, 15–22 (1979).
205. Roger, J., Audubert, F. & Le Petitcorps, Y. Thermal reaction of SiC films with tungsten and tungsten–rhenium alloys. *Journal of Materials Science* **43**, 3938–3945 (2008).
206. Albertsen, K. & Schaller, H.-J. Diffusion of C in TiC. *Berichte der Bunsengesellschaft für physikalische Chemie* **98**, 1224–1230 (1994).
207. Himbeault, D. D., Varin, R. A. & Piekarski, K. Carbon fibers coated with chromium carbide using the liquid metal transfer agent technique. *MTA* **20**, 165–170 (1989).
208. Fan, H. J., Gösele, U. & Zacharias, M. Formation of Nanotubes and Hollow Nanoparticles Based on Kirkendall and Diffusion Processes: A Review. *Small* **3**, 1660–1671 (2007).
209. Zhu, J., Tang, Y., Yang, C., Wang, F. & Cao, M. Composites of TiO2 Nanoparticles Deposited on Ti3C2 MXene Nanosheets with Enhanced Electrochemical Performance. *J. Electrochem. Soc.* **163**, A785–A791 (2016).
210. Lohse, B. H., Calka, A. & Wexler, D. Raman spectroscopy as a tool to study TiC formation during controlled ball milling. *Journal of Applied Physics* **97**, 114912 (2005).
211. Kang, Q. *et al.* Preparation of copper–diamond composites with chromium carbide coatings on diamond particles for heat sink applications. *Applied Thermal Engineering* **60**, 423–429 (2013).
212. Lyman, C. E. *et al.* Backscattered Electron Imaging. in *Scanning Electron Microscopy, X-Ray Microanalysis, and Analytical Electron Microscopy: A Laboratory*

Workbook (eds. Lyman, C. E. et al.) 51–54 (Springer US, 1990). doi:10.1007/978-1-4613-0635-1_8.

213. Booker, P. H., Kunrath, A. O. & Hepworth, M. T. Experimental determination of the ternary diagram of the Ti-Cr-C system. *Acta Materialia* **45**, 1625–1632 (1997).
214. Lin, T. *et al.* Effects of chromium and carbon content on microstructure and properties of TiC-steel composites. *International Journal of Refractory Metals and Hard Materials* **72**, 228–235 (2018).
215. Roach, J. D. Effect of Chromium on the Oxidation Resistance of Titanium Carbide. *J. Electrochem. Soc.* **98**, 160–165 (1951).
216. Arai, T. & Moriyama, S. Growth behavior of chromium carbide and niobium carbide layers on steel substrate, obtained by salt bath immersion coating process. *Thin Solid Films* **259**, 174–180 (1995).
217. Ghosh, G. Thermodynamic and kinetic modeling of the Cr-Ti-V system. *JPE* **23**, 310 (2002).
218. Fan, H. J. *et al.* Influence of Surface Diffusion on the Formation of Hollow Nanostructures Induced by the Kirkendall Effect: The Basic Concept. *Nano Lett.* **7**, 993–997 (2007).
219. Handbook of Refractory Carbides and Nitrides - 1st Edition. https://www.elsevier.com/books/handbook-of-refractory-carbides-and-nitrides/pierson/978-0-8155-1392-6.
220. Guo, L. *et al.* Ablation mechanism of WC-SiC double layer coating under oxyacetylene torch test. *Ceramics International* **42**, 16804–16812 (2016).
221. Zhao, M. *et al.* Interfacially reinforced carbon fiber/epoxy composites by grafting melamine onto carbon fibers in supercritical methanol. *RSC Adv.* **6**, 29654–29662 (2016).
222. Schubert, T. *et al.* Interfacial characterization of Cu/diamond composites prepared by powder metallurgy for heat sink applications. *Scripta Materialia* **58**, 263–266 (2008).
223. Zhang, Y., Zhang, H. L., Wu, J. H. & Wang, X. T. Enhanced thermal conductivity in copper matrix composites reinforced with titanium-coated diamond particles. *Scripta Materialia* **65**, 1097–1100 (2011).
224. Kong, B., Ru, J., Zhang, H. & Fan, T. Enhanced wetting and properties of carbon/carbon-Cu composites with Cr 3 C 2 coatings by Cr-solution immersion method. *Journal of Materials Science & Technology* **34**, 458–465 (2018).
225. Pan, Y., He, X., Ren, S., Wu, M. & Qu, X. High thermal conductivity of diamond/copper composites produced with Cu–ZrC double-layer coated diamond particles. *J Mater Sci* **53**, 8978–8988 (2018).
226. Sun, Y. *et al.* Enhanced tensile strength and thermal conductivity in copper diamond composites with B 4 C coating. *Sci Rep* **7**, 1–10 (2017).
227. Simchi, A. & Pohl, H. Direct laser sintering of iron–graphite powder mixture. *Materials Science and Engineering: A* **383**, 191–200 (2004).
228. Ma, Y. *et al.* On the study of tailorable interface structure in a diamond/Al12Si composite processed by selective laser melting. *Materialia* **5**, 100242 (2019).
229. Li, R., Shi, Y., Liu, J., Xie, Z. & Wang, Z. Selective laser melting W–10 wt.% Cu composite powders. *Int J Adv Manuf Technol* **48**, 597–605 (2010).

230. Aversa, A. *et al.* Microstructural and Mechanical Characterization of Aluminum Matrix Composites Produced by Laser Powder Bed Fusion. *Advanced Engineering Materials* **19**, 1700180 (2017).
231. Gu, D., Hagedorn, Y.-C., Meiners, W., Wissenbach, K. & Poprawe, R. Nanocrystalline TiC reinforced Ti matrix bulk-form nanocomposites by Selective Laser Melting (SLM): Densification, growth mechanism and wear behavior. *Composites Science and Technology* **71**, 1612–1620 (2011).
232. Gao, C. *et al.* Selective laser melting of TiN nanoparticle-reinforced AlSi10Mg composite: Microstructural, interfacial, and mechanical properties. *Journal of Materials Processing Technology* **281**, 116618 (2020).
233. Gu, D. *et al.* Densification behavior, microstructure evolution, and wear property of TiC nanoparticle reinforced AlSi10Mg bulk-form nanocomposites prepared by selective laser melting. *Journal of Laser Applications* **27**, S17003 (2014).
234. Leong, C. C., Lu, L., Fuh, J. Y. H. & Wong, Y. S. In-situ formation of copper matrix composites by laser sintering. *Materials Science and Engineering: A* **338**, 81–88 (2002).
235. Slocombe, A. & Li, L. Selective laser sintering of TiC–Al2O3 composite with self-propagating high-temperature synthesis. *Journal of Materials Processing Technology* **118**, 173–178 (2001).
236. Kumar, S. & Kruth, J.-P. Composites by rapid prototyping technology. *Materials & Design* **31**, 850–856 (2010).
237. AlMangour, B., Grzesiak, D. & Yang, J.-M. In-situ formation of novel TiC-particle-reinforced 316L stainless steel bulk-form composites by selective laser melting. *Journal of Alloys and Compounds* **706**, 409–418 (2017).
238. Signal noise ratio improvement technique for bulk thermal diffusivity measurement. *International Journal of Thermal Sciences* **129**, 385–395 (2018).
239. Azina, C., Cornu, I., Silvain, J.-F., Lu, Y. & Battaglia, J.-L. Effect of titanium and zirconium carbide interphases on the thermal conductivity and interfacial heat transfers in copper/diamond composite materials. *AIP Advances* **9**, 055315 (2019).
240. Constantin, L. *et al.* Design of tailored oxide-carbide coating on carbon fibers for a robust copper/carbon interphase. *Carbon* (2019) doi:10.1016/j.carbon.2019.11.032.
241. Bax, B., Rajput, R., Kellet, R. & Reisacher, M. Systematic evaluation of process parameter maps for laser cladding and directed energy deposition. *Additive Manufacturing* **21**, 487–494 (2018).
242. Rape, A., Liu, X., Kulkarni, A. & Singh, J. Alloy development for highly conductive thermal management materials using copper-diamond composites fabricated by field assisted sintering technology. *J Mater Sci* **48**, 1262–1267 (2013).
243. Park, S.-M. *et al.* Hybrid CuxO–TiO2 Heterostructured Composites for Photocatalytic CO2 Reduction into Methane Using Solar Irradiation: Sunlight into Fuel. *ACS Omega* **1**, 868–875 (2016).
244. Xie, Z. *et al.* Preparation of nano-sized titanium carbide particles via a vacuum carbothermal reduction approach coupled with purification under hydrogen/argon mixed gas. *RSC Advances* **7**, 9037–9044 (2017).
245. Donato, M. G. *et al.* High quality CVD diamond: a Raman scattering and photoluminescence study. *Eur. Phys. J. B* **20**, 133–139 (2001).

246. Constantin, L. *et al.* Effects of Laser Photolysis of Hydrocarbons at 193 and 248 nm on Chemical Vapor Deposition of Diamond Films. *Crystal Growth & Design* **18**, 2458–2466 (2018).
247. Constantin, L. *et al.* Additive Manufacturing of Copper/Diamond Composites for Thermal Management Applications. *Manufacturing Letters* (2020) doi:10.1016/j.mfglet.2020.03.014.
248. Contact angle evolution during selective laser melting. *Materials & Design* **139**, 304–313 (2018).
249. Kluczyński, J., Śnieżek, L., Grzelak, K. & Mierzyński, J. The Influence of Exposure Energy Density on Porosity and Microhardness of the SLM Additive Manufactured Elements. *Materials (Basel)* **11**, (2018).
250. Khairallah, S. A., Anderson, A. T., Rubenchik, A. & King, W. E. Laser powder-bed fusion additive manufacturing: Physics of complex melt flow and formation mechanisms of pores, spatter, and denudation zones. *Acta Materialia* **108**, 36–45 (2016).
251. Gunenthiram, V. *et al.* Experimental analysis of spatter generation and melt-pool behavior during the powder bed laser beam melting process. *Journal of Materials Processing Technology* **251**, 376–386 (2018).
252. McLouth, T. D. *et al.* The effect of laser focus shift on microstructural variation of Inconel 718 produced by selective laser melting. *Materials & Design* **149**, 205–213 (2018).
253. DePond, P. J. *et al.* In situ measurements of layer roughness during laser powder bed fusion additive manufacturing using low coherence scanning interferometry. *Materials & Design* **154**, 347–359 (2018).
254. Calignano, F., Manfredi, D., Ambrosio, E. P., Iuliano, L. & Fino, P. Influence of process parameters on surface roughness of aluminum parts produced by DMLS. *Int J Adv Manuf Technol* **67**, 2743–2751 (2013).
255. Li, R., Liu, J., Shi, Y., Wang, L. & Jiang, W. Balling behavior of stainless steel and nickel powder during selective laser melting process. *Int J Adv Manuf Technol* **59**, 1025–1035 (2012).
256. Influence of re-melting on surface roughness and porosity of AlSi10Mg parts fabricated by selective laser melting. *Journal of Alloys and Compounds* **792**, 574–581 (2019).
257. Yasa, E. & Kruth, J.-P. Microstructural investigation of Selective Laser Melting 316L stainless steel parts exposed to laser re-melting. *Procedia Engineering* **19**, 389–395 (2011).
258. Liu, F., Zhang, D. Z., Zhang, P., Zhao, M. & Jafar, S. Mechanical Properties of Optimized Diamond Lattice Structure for Bone Scaffolds Fabricated via Selective Laser Melting. *Materials* **11**, 374 (2018).
259. Leary, M. *et al.* Selective laser melting (SLM) of AlSi12Mg lattice structures. *Materials & Design* **98**, 344–357 (2016).
260. Sahoo, S. K., Das, M. K. & Rath, P. Application of TCE-PCM based heat sinks for cooling of electronic components: A review. *Renewable and Sustainable Energy Reviews* **59**, 550–582 (2016).
261. Maidin, S. & Azmi, N. F. DESIGN AND ANALYSIS OF HONEYCOMB STRUCTURE COOLING FIN. in (2015).

262. J. E. Field (ed.). The Properties of Natural and Synthetic Diamond. Academic Press, London 1992. £ 90.00. ISBN 0-12-255352-7. *Cryst. Res. Technol.* **28**, 602–602 (1993).
263. Ravi, K. V. Combustion synthesis: is it the most flexible of the diamond synthesis processes? *Diamond and Related Materials* **4**, 243–249 (1995).
264. Alers, P., Hänni, W. & Hintermann, H. E. A comparative study of laminar and turbulent oxygen-acetylene flames for diamond deposition. *Diamond and Related Materials* **2**, 393–396 (1993).
265. Haubner, R. & Lux, B. Diamond growth by hot-filament chemical vapor deposition: state of the art. *Diamond and Related Materials* **2**, 1277–1294 (1993).
266. Yalamanchi, R. S. & Harshavardhan, K. S. Diamond growth in combustion flames. *Journal of Applied Physics* **68**, 5941–5943 (1990).
267. Asmussen, J. *et al.* Multiple substrate microwave plasma-assisted chemical vapor deposition single crystal diamond synthesis. *APPL. PHYS. LETT., Applied Physics Letters Applied Physics Letters, Applied Physics Lettrs* **93**, (2008).
268. Donnet, J. B., Oulanti, H., Huu, T. L. & Schmitt, M. Synthesis of large single crystal diamond using combustion-flame method. *Carbon* **44**, 374–380 (2006).
269. Okabe, H. *Photochemistry of Small Molecules*. (John Wiley & Sons Inc, 1978).
270. Crim, F. F. Making Energy Count. *Science* **316**, 1707–1708 (2007).
271. Knox, B. E. & Palmer, H. B. Bond Dissociation Energies in Small Hydrocarbon Molecules. *Chem. Rev.* **61**, 247–255 (1961).
272. Kitahama, K. *et al.* Synthesis of diamond by laser-induced chemical vapor deposition. *Appl. Phys. Lett.* **49**, 634–635 (1986).
273. Goto, Y., Yag, T. & Nagai, H. Synthesis of Diamond Films by Laser-Induced Chemical Vapor Deposition. *MRS Online Proceedings Library Archive* **129**, (1988).
274. Kitahama, K. Reinvestigation of the carbon films prepared by ArF excimer laser-induced chemical vapor deposition. *Appl. Phys. Lett.* **53**, 1812–1814 (1988).
275. Tyndall, G. W. & Hacker, N. P. KrF Laser-Induced Chemical Vapor Deposition of Diamond. *MRS Online Proceedings Library Archive* **162**, (1989).
276. Zare, R. N. Laser Control of Chemical Reactions. *Science* **279**, 1875–1879 (1998).
277. Bronikowski, M. J., Simpson, W. R. & Zare, R. N. Effect of reagent vibration on the hydrogen atom + water-d reaction: an example of bond-specific chemistry. *J. Phys. Chem.* **97**, 2194–2203 (1993).
278. Zhu, L., Kellis, D. & Ding, C.-F. Photolysis of glyoxal at 193, 248, 308 and 351 nm. *Chemical Physics Letters* **257**, 487–491 (1996).
279. Lifshitz, Y. *et al.* The Mechanism of Diamond Nucleation from Energetic Species. *Science* **297**, 1531–1533 (2002).
280. Klein-Douwel, R. J. H., Spaanjaars, J. J. L. & ter Meulen, J. J. Two-dimensional distributions of C2, CH, and OH in a diamond depositing oxyacetylene flame measured by laser induced fluorescence. *Journal of Applied Physics* **78**, 2086–2096 (1995).
281. Luque, J., Juchmann, W. & Jeffries, J. B. Spatial density distributions of C2, C3, and CH radicals by laser-induced fluorescence in a diamond depositing dc-arcjet. *Journal of Applied Physics* **82**, 2072–2081 (1997).
282. Komaki, K., Yanagisawa, M., Yamamoto, I. & Hirose, Y. Synthesis of Diamond in Combustion Flame under Low Pressures. *Jpn. J. Appl. Phys.* **32**, 1814 (1993).

283. Miller, J. A. & Melius, C. F. Kinetic and thermodynamic issues in the formation of aromatic compounds in flames of aliphatic fuels. *Combustion and Flame* **91**, 21–39 (1992).
284. Redfern, P. C., Horner, D. A., Curtiss, L. A. & Gruen, D. M. Theoretical Studies of Growth of Diamond (110) from Dicarbon. *J. Phys. Chem.* **100**, 11654–11663 (1996).
285. Gruen, D. M., Redfern, P. C., Horner, D. A., Zapol, P. & Curtiss, L. A. Theoretical Studies on Nanocrystalline Diamond: Nucleation by Dicarbon and Electronic Structure of Planar Defects. *J. Phys. Chem. B* **103**, 5459–5467 (1999).
286. Shimada, M., Tynan, G. R. & Cattolica, R. Rotational and translational temperature equilibrium in an inductively coupled plasma. *Journal of Vacuum Science & Technology A* **24**, 1878–1883 (2006).
287. Kim, J. S. & Cappelli, M. A. Temperature measurements in low-pressure, diamond-forming, premixed flames. *Journal of Applied Physics* **84**, 4595–4602 (1998).
288. S. Fan, L. *et al.* Mass spectrometric investigation of the roles of several chemical intermediates in diamond synthesis. *RSC Advances* **5**, 4822–4830 (2015).
289. Asmussen, J. & Reinhard, D. *Diamond Films Handbook*. (CRC Press, 2002).
290. Liu, H. & Dandy, D. S. *Diamond Chemical Vapor Deposition: Nucleation and Early Growth Stages*. (Elsevier, 1996).
291. Ferrari, A. C., Robertson, J., Ferrari, A. C. & Robertson, J. Raman spectroscopy of amorphous, nanostructured, diamond–like carbon, and nanodiamond. *Philosophical Transactions of the Royal Society of London. Series A: Mathematical, Physical and Engineering Sciences* **362**, 2477–2512 (2004).
292. Bąk, G. W., Fabisiak, K., Klimek, L., Kozanecki, M. & Staryga, E. Investigation of biaxial stresses in diamond films deposited on a silicon substrate by the HF CVD method. *Optical Materials* **30**, 770–773.
293. Frenklach, M. & Spear, K. E. Growth mechanism of vapor-deposited diamond. *Journal of Materials Research* **3**, 133–140 (1988).
294. Wang, M. *et al.* Seed-Free Growth of Diamond Patterns on Silicon Predefined by Femtosecond Laser Direct Writing. *Crystal Growth & Design* **13**, 716–722 (2013).
295. Hamzah, E., Yong, T. M. & Mat Yajid, M. A. Surface morphology and bond characterization of nanocrystalline diamonds grown on tungsten carbide via hot filament chemical vapor deposition. *Journal of Crystal Growth* **372**, 109–115 (2013).
296. Kim, G.-H. Transmission electron microscope observation of diamond/WC interface. *Journal of Crystal Growth* **178**, 634–638 (1997).
297. Fan, L. S. *et al.* Synthesis of nitrogen-doped diamond films using vibrational excitation of ammonia molecules in laser-assisted combustion flames. *Journal of Laser Applications* **24**, 022001 (2012).
298. Okabe, H. Photochemistry of acetylene. *Can. J. Chem.* **61**, 850–855 (1983).
299. Okabe, H. & McNesby, J. R. Vacuum Ultraviolet Photochemistry. II. Photolysis of Ethylene. *J. Chem. Phys.* **36**, 601–604 (1962).
300. Zare, R. N. Laser Control of Chemical Reactions. *Science* **279**, 1875–1879 (1998).
301. Crim, F. F. Making Energy Count. *Science* **316**, 1707–1708 (2007).
302. Komaki, K., Yanagisawa, M., Yamamoto, I. & Hirose, Y. Synthesis of Diamond in Combustion Flame under Low Pressures. *Jpn. J. Appl. Phys.* **32**, 1814 (1993).

303. Miller, J. A. & Melius, C. F. Kinetic and thermodynamic issues in the formation of aromatic compounds in flames of aliphatic fuels. *Combustion and Flame* **91**, 21–39 (1992).
304. Kovács, T., Blitz, M. A. & Seakins, P. W. H-Atom Yields from the Photolysis of Acetylene and from the Reaction of C2H with H2, C2H2, and C2H4. *J. Phys. Chem. A* **114**, 4735–4741 (2010).
305. Irion, M. P. & Kompa, K. L. UV laser photochemistry of acetylene at 193 nm. *Appl. Phys. B* **27**, 183–186 (1982).
306. Balko, B. A., Zhang, J. & Lee, Y. T. 193 nm photodissociation of acetylene. *The Journal of Chemical Physics* **94**, 7958–7966 (1991).
307. Donnelly, V. M., Baronavski, A. P. & McDonald, J. R. ArF laser photodissociation of NH3 at 193 nm: internal energy distributions in NH2 X̃2B1 and Ã2A1, and two-photon generatin of NH A 3Π and b 1Σ+. *Chemical Physics* **43**, 271–281 (1979).
308. Pasternack, L. & McDonald, J. R. Reactions of C2(X 1Σ+g) produced by multiphoton uv excimer laser photolysis. *Chemical Physics* **43**, 173–182 (1979).
309. Sorkhabi, O. *et al.* Photodissociation of C2H at 193 nm: Branching ratios for the formation of C2 in the X 1Σg+, A 1Πu, and B′ 1Σg+ states. *The Journal of Chemical Physics* **107**, 9842–9851 (1997).
310. Nakayama, T. & Watanabe, K. Absorption and Photoionization Coefficients of Acetylene, Propyne, and 1-Butyne. *The Journal of Chemical Physics* **40**, 558–561 (1964).
311. Cromwell, E. F., Stolow, A., Vrakking, M. J. J. & Lee, Y. T. Dynamics of ethylene photodissociation from rovibrational and translational energy distributions of H2 products. *The Journal of Chemical Physics* **97**, 4029–4040 (1992).